Fundamental Studies of Adsorption Reactions in Organic Electrolytes and Electrocatalysis

Dissertation
zur
Erlangung des Doktorgrades (Dr. rer.nat)
der
Mathematisch-Naturwissenschaftlichen Fakultät
der
Rheinische Friedrich-Wilhelms-Universität Bonn

vorgelegt von

Ahmed Said Lotfy Elshatla

aus

Menoufia, Ägypten

Bonn, 2020

Angefertigt mit Genehmigung der Mathematisch-Naturwissenschaftlichen Fakultät der Rheinischen Friedrich-Wilhelms-Universität Bonn

Promotionskommission

Erster Gutachter: Prof. Dr. Helmut Baltruschat
Zweiter Gutachter: Prof. Dr. Thomas Bredow
Fachnaher Gutachter: Prof. Dr. Andreas Gansäuer
Fachfremder Gutachter: Prof. Dr. Gösta Hoffmann

Tag der mündlichen Prüfung: 21.12.2020

Erscheinungsjahr: 2021

Ich versichere, dass ich diese Arbeit selbständig verfasst und keine anderen als die angegebenen Quellen und Hilfsmittel benutzt sowie die Zitate kenntlich gemacht habe.

Bonn, 15.10.2020

Ahmed Said Lotfy Elshatla

For my Motherland (Egypt),
My Parents and
My beloved Wife

"A Person Who Never Made a Mistake, Never Tried Anything New"

Albert Einstein

Publications

Parts of this thesis have already been published in international, peer-reviewed journals:

4. **A. S. Shatla**, P. P. Bawol and H. Baltruschat, Adsorption of iodide and bromide on Au(111) electrode from aprotic electrolytes: role of the solvent, submitted to Journal of ChemElectroChem.

3. K. M. Hassan, **A. S. Shatla**, A.A. Abd-El-Latif, H. Baltruschat, M. Abdel-Azzem, Comparative studies of ethylene glycol electrooxidation on different conducting polymers supported Pt and Pd nanoparticles-DEMS study, submitted Journal of Electroanalytical Chemistry 878 (2020) 114624.

2. **A. S. Shatla**, A. A. Abd-El-Latif, S. Ayata, D. Demir and H. Baltruschat, Iodide adsorption at Au(111) electrode in non-aqueous electrolyte: AC-voltammetry and EIS studies, Electrochimica Acta 334 (2020) 135556.

1. **A. S. Shatla**, K.M. Hassan, A.A. Abd-El-Latif, A.A. Hathoot, H. Baltruschat, M. Abdel-Azzem, Poly 1,5 diaminonaphthalene supported Pt, Pd, Pt/Pd and Pd/Pt nanoparticles for direct formic acid oxidation, J. Electroanalytical Chemistry 833 (2019) 231-241.

Additionally, chapter 5 is a manuscript which is also prepared for submission to a journal.

A C K N O W L E D G E M E N T S

Foremost, I wish to express my sincere thanks to my research advisor Prof. Dr. Helmut Baltruschat for providing me with the opportunity and continuous support to complete the PhD study. This work could not have been possible without his guidance. I am grateful for his patience, motivation, enthusiasm and immense knowledge, as well as the financial support I received after finishing my scholarship. I am indebted to him more than he knows.

My appreciation is also extended to the other member of my thesis committee: Prof. Dr. Thomas Bredow, Prof. Dr. Andreas Gansäuer, and Prof. Dr. Gösta Hoffmann for their availability and eagerness to evaluate my thesis.

Also, I would like to thank Prof. Dr. Magdi Abdel Azzem, Prof. Dr. Abla Ahmed Hathoot, and Dr. Khaled Hassan for their support and encouragement during my study.

My sincere thanks also go to my colleagues Dr. Abd El Aziz for his great help in my work, and to the former and present members of our group, Shahid, Christoph B., Christoph M., Ehab, Mehdi, Hatem, Philip. R., Philipp H., Sevda, Soltani, Dilek, Martina, Jan, Akos, Ana, Pawol, Da, Sergi, Zan, Annchristin, Elina, Inhee, and Andreas for their help and support. In particular, I am grateful to Dr. Ernst and Dr. Manuel for their valuable discussions, Frau Rossignol for her help in administration and Frau Thome for her help in the lab.

I thank the members of mechanical, electronic and glass workshops, especially Mr. Königshoven, Mr. Paulig, and Mr. Koll for their help in designing and constructing the fine cells and repairing devices. Many thanks go to Mr. Knut Hintzen for his kind help in computer stuff.

I thank also the Egyptian Government (Ministry of High Education and Research - MOHE) for the financial support of this research for two years.

I would like to thank my mother, my sister, all of my family members and my friends in Bonn. They were always encouraging me and supporting me with their best wishes.

Special thanks to my beloved wife for her patience, love and motivational support that helped me reach all of my aims so far. She was always there carrying me up and stood by me through good and bad times. My lovely daughter (Lyan) and my little son (Youssef) helped me a lot.

Last but not the least, I dedicate this thesis to my dad for his, both physically and spiritually.

Ahmed Elshatla

Abstract

Adsorption processes have a vital influence on the features of heterogeneous electrochemical systems, like processes in electric double-layer capacitors and fuel cell systems. In order to study the fundamentals of such processes, the adsorption of iodide and bromide on Au(111) in aqueous and aprotic solvents has been investigated by cyclic voltammetry, AC-voltammetry, and electrochemical impedance spectroscopy. These techniques showed that the rate of adsorption of iodide is directly proportional to iodide concentration in propylene carbonate, where a complete layer of iodide is formed as in aqueous solution. The adsorption rate of iodide increases when the radii of solvated cations decreases, i.e. in this order: $K^+ > Na^+ > Li^+ > TBA^+$. The rate of adsorption of iodide and bromide on Au(111) and the point of zero charge of Au(111) and roughened Au(111) electrode is dependent on the type of aprotic solvent and water content. The decrease of the iodide adsorption rate in the order DMSO < DG < PC < H_2O. This order is related to the decreasing donor number of solvent in the order PC < DG < DMSO except for water. The extent of anion adsorption and thus the maximum coverage on Au(111) electrode decreases in the series of halides I^- > Br^- due to better solvation and in the solvent order PC > DG > DMSO. XPS measurements confirmed the results obtained from CV that iodide adsorption on Au(111) electrode in PC is stronger than in DMSO in terms of amounts of adsorbed iodide. The crystallographic structure of the electrode surface affects the pzc. Whereas anion adsorption shifts the pzc to a more negative potential, cation identity does not influence the pzc. That the adsorption of PC is enhanced on going to positive potential in presence of iodide has been investigated via ATR-SEIRAS measurements.

Oxidation of adsorbed CO molecules during Formic acid electrocatalysis is improved through bimetallic catalysts of Pt and Pd supported on conducting polymer of poly 1,5 DAN in comparison to the monometallic catalyst, as examined by using DEMS. It was found that Pt/Pd/p1,5–DAN exhibited greater current efficiency than Pd/Pt/p 1,5DAN/GC and monometallic catalysts. In addition, the kind of catalyst support (conducting polymers) plays an essential role in terms of electric conductivity and increased electroactive surface area of the catalyst for the enhancement of electrocatalysis of ethylene glycol on the binary catalyst of Pt and Pd. Using DEMS, it was found that Pt/Pd/p1,8-DAN showed higher current efficiency than Pt/Pd/p1,5-DAN and Pt/Pd/p1,2-DAAQ.

Contents

List of Figures

List of Tables

List of Notations

θ	Coverage	C_{DL}	Doubl105e-layer capacitance
Γ	Surface excess of adsorbed species	C_H	Helmholtz10 capacitance
Γ_{max}	Total surface excess of adsorbed species	C_d	Diffuse capacitance
ΔG_{ad}	Adsorption Gibbs energy	q_m	Metal charge
A	Current efficiency	R_{el}	Electrolyte resistance
A_{Geom}	Geometric surface area	C_{tot}	Total capacitance
E	Potential	α	Charge transfer coefficient
E_0	Initial potential	Å	Angstrom
E_u	Final potential	M_w	Molecular weight
F	Faraday constant, 96485 C·mol^{-1}	ρ	Density
I_F	Faradaic current	s	Proportionality constant
I_i	Ionic current	l	Electrocatalyst loading
j	Current density	I_p^d	Direct anodic peak current
K^*	Calibration const. of DEMS	I_p^{ind}	Indirect anodic peak current
ν	Potential scan rate	I_p^b	Backward direct peak
Φ	Work function	D	Diffusion coefficient
Q_F	Faradaic charge	k	Reaction rate constant
Q_{MS}	Ionic charge	n	Reaction order
u	Electrolyte flow rate	E_{onset}	Onset potential
z	The number of electrons transferred	ppm	Part per million
ϕ	Diameter	E_τ^N	normalized solvent polarity
R_{ad}	Adsorption resistance	μ	Dipole moment
C_{ad}	Adsorption capacitance	α_s	Polarizability
R_{ct}	Charge transfer resistance	R0	Reference potential reflectance
u_{ac}^0	Total ac voltage	f	Frequency
u_{ac}^{corr}	Corrected ac voltage	i_{ac}	Alternating current
$Y_{re-corr}$	Corrected real part of the admittance	i_{dc}	Direct current
$Y_{im-corr}$	Corrected imaginary part of the admittance	i_{ac-re}	Real part of the ac current
IZI	Absolute value of the impedance	i_{ac-im}	Imaginary part of the ac current
Z_{re}	Real part of the impedance	u_{ac}	AC voltage
Z_{im}	Imaginary part of the impedance	φ	Phase angle
ω	Angular frequency	C_{diff}	Differential capacitance

List of Abbreviations

EDL	Electrical double layer	p-1,2-DAAQ	poly-1,2 diamino anthraquinone
IHP	Inner Helmholtz plane	CV	Cyclic voltammetry
OHP	Outer Helmholtz plane	EIS	Electrochemical impedance spectroscopy
pzc	Potential of zero charge	ACV	Alternating current voltammetry
fcc	Face-centered cubic	EMS	electrochemical mass spectrometry
cps	Close-packed sphere	XPS	X-ray photoelectron spectroscopy
hcp	Hexagonally closed pack	SEM	Scan Electron Microscope
FCs	Fuel cells	EDX	Energy Dispersive X-ray spectroscopy
DMFC	Direct methanol fuel cell	RHE	Reversible hydrogen electrode
PEMFC	Proton exchange membrane fuel cell	TBAP	Tetra Butyl ammonium perchlorate
SOFC	Solid oxide fuel cell	MWCNTs	Molecular wall carbon nanotubes
MCFC	Molten carbonate fuel cell	ECSA	Electrochemical active surface area
PAFC	Phosphoric acid fuel cell	PC	Propylene carbonate
AFC	Alkaline fuel cell	DG	Diglyme
FA	Formic acid	DMSO	Dimethyl sulfoxide
FAO	Formic acid oxidation	DN	Donor number
MOR	Methanol oxidation reaction	AN	Acceptor Number
DEFC	Direct ethanol fuel cell	TG	Tetraglyme
FTIR-ATR	Fourier Transform Infrared – Attenuated Total Reflection	upd	Under potential deposition
NPs	Nanoparticles	GBL	Gamma-butyrolactone
DFAFC	Direct formic acid fuel cell	ACN	Acetonitrile
ATR-SEIRAS	Attenuated Total Reflection-Surface Enhanced infrared Absorption spectroscopy	STM	Scanning tunnel microscope
SERS	Surface-enhanced Raman spectroscopy	DMFc	Decamethylferrocene
EG	Ethylene Glycol	UHV	Ultra-high vacuum
EGO	Ethylene glycol oxidation	PCTFE	Polychlorotrifluoroethylene
DEMS	Differential Electrochemical Mass spectroscopy	BBCr	Bisbiphenylchromium
CPs	Conducting polymers	MA	Mass activity
PANi	Polyaniline	PPy	Polypyrrole
p-1,5-DAN	Poly1,5- Diamino naphthalene	p-1,8-DAN	poly-1,8-diaminonaphthalene

Chapter one: Introduction

1.1 General introduction

The challenge for modern society is to meet the rising energy demand. The electronic revolution, which is based on the widespread use of highly advanced mobile devices such as cell phones, laptops, and video cameras, and more, relies on the provision of high-energy-density, secure and cheap power sources. Non - renewable energy resources and CO_2 reduction can only be sustained by developing new systems for electrochemical energy storage such as secondary (rechargeable) batteries, fuel cells, and supercapacitors.

Metal-air batteries are assembled from the metal anode, which can be Li, Na, K, Ca, and Mg and oxygen as a cathode in a proper electrolyte. They have been used early to convert and store electrical energy efficiently in a variety of applications, including portable electronic devices and grid-scale storage extending to electric vehicles (EVs). Lithium-air batteries have captured worldwide attention in energy research among all kinds of batteries due to their extremely high theoretical energy density [1].

Besides the anode identity, the electrolyte nature is another essential component for ionic transport and stabilization of the cell. The identification of electrolytes not substantially consumed or decayed by air cathode during operation of the cell is an indispensable requirement for the development of rechargeable Li-air batteries with both high capacity and high cycle number. Various Li-air battery types have been developed based on the electrolyte used: aprotic solvents, ionic liquids, aqueous, and solid-state batteries. The majority of studies were focused on aprotic types among the four kinds of solvents due to their relatively high energy density.

Abraham and Jiang proposed the first aprotic $Li - O_2$ battery composed of a mixture of ethylene carbonate (EC) and propylene carbonate (PC) as solvent and $LiPF_6$ as salt [2]. Unfortunately, when carbonates based electrolytes were employed, $Li\text{-}O_2$ batteries were found to be unstable due to the formation of Li_2CO_3 as a by-product resulting in a higher charge overpotential.

Consequently, electrochemists used sulphoxide-based electrolytes due to possessing many features: high oxygen diffusion, low volatility, and particularly superoxide tolerability. Ether-based electrolytes were the most commonly used electrolyte for $Li - O_2$ batteries and stood out from different organic electrolytes due to having a high stable operation potential window, which is essential for the long cycling life of $Li - O_2$ batteries. The reason for this study is that not yet enough fundamental research in aprotic solvents has been conducted.

The common feature of metal-air batteries and fuel cells is the cathode (oxygen), which is ideally accessed from the ambient air. In the 1960s, only specialized applications like space missions, etc., were used for fuel cells, mainly because of their high costs. However, with science and technology progress over the past 50 years, the cost barrier has been lowered by almost 50%, and fuel cells are expected to become a significant energy source in the future. Fuel cells have shown significant efficiency ratings of between 40% and 45% and can achieve efficiencies of almost 80% when used with CHP (combined heat and power), while the existing internal combustion engines have a performance limit of about 30% [3]. Moreover, it is suitable for more extended operating periods because no moving parts are available. They have a quiet operation, i.e. low noise pollution, due to the lack of moving parts and energy conversion through the electrochemical reactions. The domestic and public transport system, both as a vehicular traction system and as an auxiliary power unit, is one of the significant applications for fuel cells. All these important and beneficial features make fuel cells an excellent choice for future electricity production.

1.2 Electrified interfaces structure

1.2.1 Electrode/electrolyte Interface and the Double Layer

There are two different types of operations in an electrochemical cell that can happen at an electrode surface. The first one is the faradaic processes which are non-adsorptive and result from the charge transfer reaction across the electrode/solution interface. The obtained charge transfer reaction of solution species is controlled by Faraday's first law which states that the amount of a chemical species, formed by electrolysis, is proportional to the quantity of electrical current utilized. Potential regions exist where no charge transfer reactions or no Faradaic processes take place because of its kinetic hindrance or thermodynamic impossibility at such potentials. The processes that lead to the electric current because of double-layer charging are called non- faradaic processes. These processes can result in a physical change in the electrode surface depending on applied potential or electrolyte solution concentration [4].

Reactions of charge transfer taking place at the electrode/solution interface occur in an environment different from that of the homogeneous bulk solution. In the latter, there is an absence of an electric field, and the species are in an isotropic environment. The breakdown of symmetry and the electric field at the electrode/solution interface lead to anisotropy. The influence of this anisotropic electric field on the species is depending on distance and increases with decreasing distance from the electrode surface [5].

The orientation of solvent molecules at the interface occurs as a result of the polarization of solvent dipoles and subsequently, a net ionic charge accumulates on the electrode. Then, the electrode attracts a layer of ions whose charge is of opposite sign and equal in quantity to its surface (negative electrodes draw positive ions and vice versa). This produced charge separation generated by the local arranging of the ions at the electrode/electrolyte interface is recognized as the *electrical double layer (EDL)*. **Figure 1.1** shows three structural representation of the double layer.

In the mid-19th century, charge separation at interfaces was investigated firstly when Helmholtz suggested that the interface structure among metal and a solution has resembled that of a capacitor of the parallel plate, i.e. an instrument fabricated from two metal sheets and these are separated by a dielectric material that is able to store charge. Nevertheless, this was to some degree a naive description as it is improbable that the charges on the solution side of the interface lie on an ordered single plane because thermal irritation leads to disorder. This concept of a diffuse layer of charge on the solution side of the interface was presented by Gouy and Chapman; it describes how the excess charge concentration is highest close to the electrode as this is the point where the electrostatic forces are largest. Their model predicted dependence of the measured capacity on both potential and electrolyte concentration. The concentration of charge gradually increases when the distance from this point toward the bulk solution decreases.

In the Gouy-Chapman model, there are also limitations. The suggestion that the ions are considered as point charges that can move toward the surface at any irregular point is unreasonable. Generally, ions have a defined radius and will be solvated. The distance of ions of closest approach will be larger than zero due to the presence of solvated ions and solvent molecules at the metal/electrolyte interface. This distance depends on the solvation shell around the ion, the electrostatic interaction, and the ionic radius. This is taken into account in Stern approach to investigating EDL structure.

The interface may comprise one layer of specifically adsorbed ions which have weakly linked solvation spheres and adsorbed molecules of solvent. As a consequence of Brownian movement, the real double layer is consisting of many layers, involving the ions which are specifically adsorbed in the inner layer and extending to the bulk solution [6]. The *inner Helmholtz plane* (IHP) is defined as the inner layer at the interface which contains the chemisorbed ions (specifically adsorbed). Anions have the ability to lose their solvation sphere and tightly bound to the solid surface are therefore included in the IHP. These anions like I^-, Cl^-

and Br^- are subject to a chemical reaction which involve covalent or ionic bond formation with the surface of the electrode after removal of their solvation sphere in the EDL.

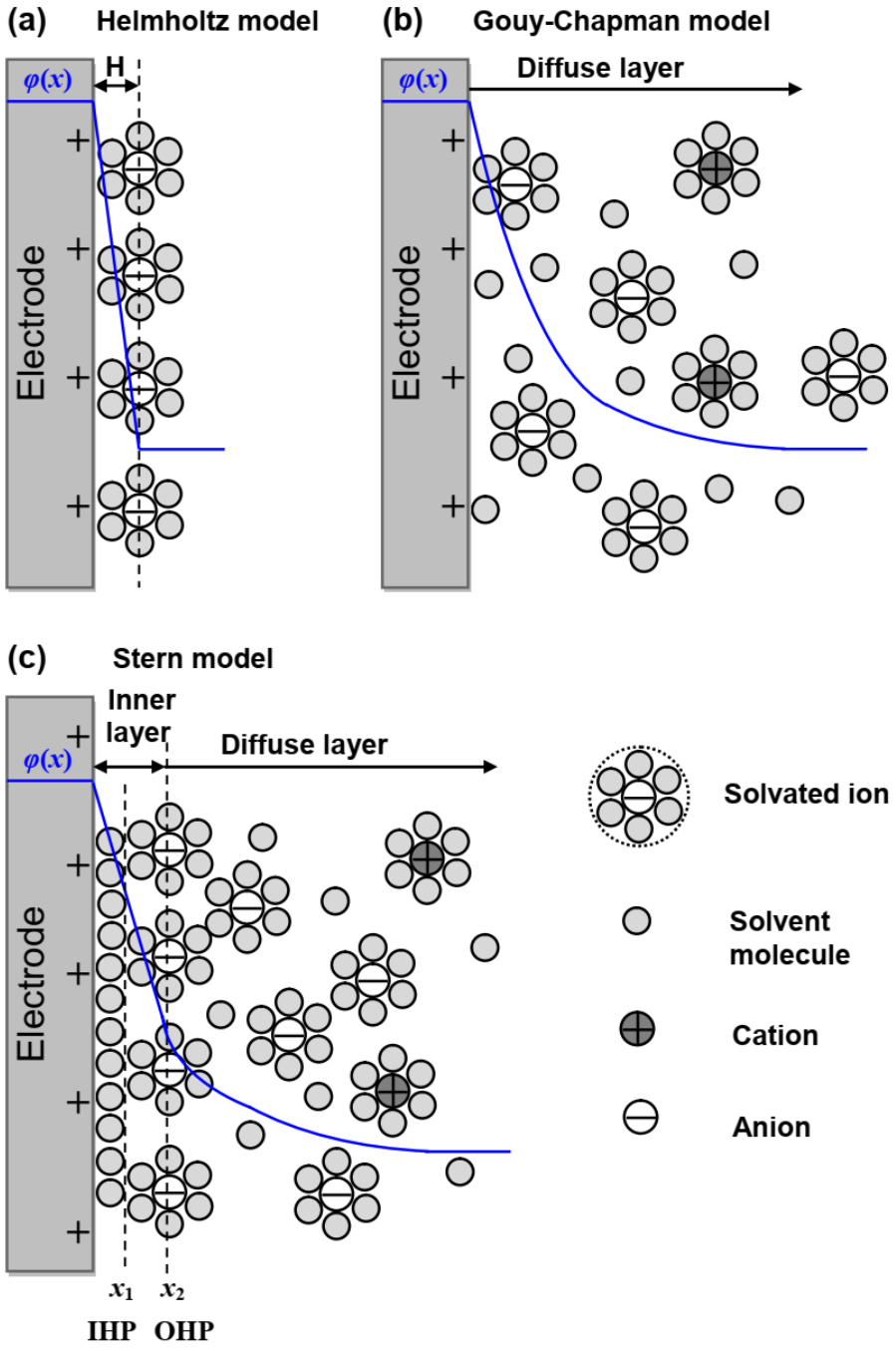

Figure 1.1: Structural representation of a double layer of (a) Helmholtz model, (b) Gouy-Chapman model, and (c) Stern model.

Throughout the diffuse layer of the interfacial zone, non-specifically adsorbed particles involve solvated cations, anions like F^-. Cations are easier to be solvated because of their low radii giving rise to large solvation energy. Solvated cations are less likely to give up their

solvation shell if the charge of the electrode is negative: subsequently, the inner solvent-coordination shell radius will affect the closest approach distance from the electrode. The coverage of non-specifically adsorbed ions rarely reaches 0.1 to 0.2 of a complete layer to create a typical potential drop of 1V. The *outer Helmholtz plane* (OHP) is described as the layer (that extends from inner to mass solution layer) consisting of solvated cations.

1.2.2 Potential of zero charge (pzc)

Pzc is a crucial electrochemical feature of a metal | electrolyte interface, plays an essential role in the investigation of EDL structure, and ions adsorption on the surface of the electrode. It is generally known as the potential where the electrode surface has no additional charge due to equality of cation and anions number, and several approaches have been developed to determine it. Pzc can be estimated directly from the maximum of the related electrocapillary graph in the case of liquid metal electrodes such as mercury and Gallium [7]. Whilst, pzc for silver and gold electrodes(noble metals) having a reasonably large DL charging region could be determined from differential capacitance measurements in the presence of low concentration solutions (1 – 5 mM), where a distinct minimum in DL capacitance is visible [8]. This method cannot be used for more reactive metals like transition metals, where adlayers or oxides of surface are produced across a broad potential limit.

Differential capacitance methodology is one of the experimental techniques for pzc determination. The background of this method can be clarified as follows:

$$\frac{1}{C_{DL}} = \frac{1}{C_H} + \frac{1}{C_d} \qquad (1.1)$$

It is understood that in low concentration solutions (concentration < 0.05 M) $C_H > C_d$, C_d which refers to diffuse capacitance is low enough to impact the DL capacitance (C_{DL}) greatly. When C_d is decreased, it becomes the dominating portion of the total capacitance. Therefore, the sharp minimum in the capacitance – potential curve defines the potential of the metal electrode ($q_m = 0$) at which the charge equals zero.

Since the Helmholtz capacitance (C_H) is independent of concentration in absence of chemisorption, it can be determined by a plot of $\frac{1}{C_{DL}}$ versus $\frac{1}{C_d}$ as calculated from The GC theory for various concentrations with a slope of unity (Parsons-Zobel plot). The ion adsorption affects the pzc value. Weak ions adsorptions will not result in major pzc changes. The strong adsorption of anions moves the pzc in the negative potential direction by 100 – 200 mV. The pzc decrease with increasing of anion adsorption in the series $F^- < Cl^- < Br^- < I^-$ [4, 9].

There are two types of charge, free and total charge. Frumkin and Petri could define two different values of pzc for hydrogen adsorbing electrodes, the potential of zero free charge (pzfc) and the potential of zero total charge (pztc) [10]. The potential of zero free charge comes from electronic charge lying on the electrode surface and then compensates due to the electrostatic attraction of the electrode surface towards electrolyte ions. The pzfc is equivalent to the pzc as measured by using the Gouy-Chapman theory which is used to determine the pzc for the Ag and Au electrodes in an aqueous medium [11].

The pztc refers to the total charge transferred including the electronic charge associated with the chemical bond formation due to the adsorption process. It can be determined by using CO displacement technique for platinum single crystal electrodes [12 - 17] and immersion technique for Au(111) and Pt(111) electrodes in aqueous solution [18]and for Au(100) electrode in ionic liquid [19]. A substantially higher value of pztc was found using the immersion experiments with immersing a UHV prepared Pt(111) crystal into 0.1 M perchloric acid in an inert atmosphere. A value for the pztc of 1.1 ± 0.2 V was obtained. This value is in good agreement with the value obtained theoretically from the work function value [18].

1.2.3 Single crystal surfaces: Au surfaces structure

For a deep understanding of surface reactions, using of single-crystal electrodes with well-characterized surfaces is needed. Polycrystalline structures, widely used throughout the early stages of electrochemical surface experiments, are too much difficult for a precise explanation on the atomic scale. Single crystal electrodes preparation and characterization of their composition is a complicated task in electrochemistry.

A crystalline electrode surface closely relates to its bulk structure. A crystal's atoms are organized in a periodic series creating the lattice. Very often, metals and metal alloys prefer to create a close-packed sphere (cps) configurations representing the isotropy of atomic interaction forces. Two probable configurations for cps exist, hexagonally closed pack (hcp) and face-centered cubic (fcc). The planes of maximum atomic density in both cases, (0001) and (111), respectively, possess the same two-dimensional (2D) arrangement at the surface.

A single crystal surface can be created through precise cut off of a three-dimensional (3-D) of the bulk structure of solid metal across a specific crystallographic plane and is typically identified through employing Miller indices (hkl), described by the reciprocal of plane intercepts at three axes of x-, y-, and z [20]. Au surface crystallizes in the (fcc) lattice and emerges in the elementary cell by indexing various lattice plains and characteristic planes. As a method for defining lattice planes and directions in a crystal, the Miller indices are employed.

The greater density of nodes of the crystal could be fulfilled in a few directions and planes and so that the dense planes can affect the crystal behaviour. The three popular low index planes (111), (110) and (100) are shaped by the chopping off a typical fcc lattice and are arranged atomically flat by the surface atoms in hexagonal, rectangle and square form respectively [21] (**Figure 1.2**). The fcc (111) plane is denser than the other planes and will have the minimum surface energy and greatest stability.

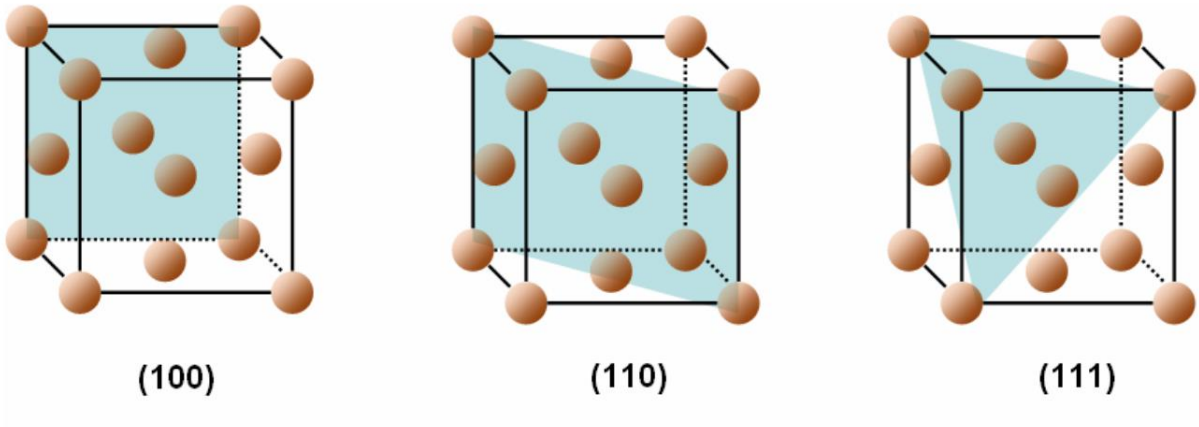

Figure 1.2: Unit cell of a fcc structure of the corresponding planes (100), (110), and (111) [22].

1.2.4 Surface reconstruction

Solid surface atoms are frequently located in places that vary distinctly from those expected for a perfect termination of the bulk. This disparity is the product of unbalanced forces at the surface where atoms are asymmetrically positioned relative to bulk atoms. Surface atoms are displaced sideways to create dramatically different surface structures in a number of cases. The reorganization of the location of the surface atoms leads to a decrease in surface energy and is called *surface reconstruction.* Surface stress is the forces responsible for the reconstruction of the single crystal surface [23, 24]. The rising in the density of the surface electron, which generates contractive surface stress was indicated by Marks and Heine [25, 26]. This effect was noticed under UHV circumstances. By changing electrode potential or using thermal conditions, surface reconstruction can occur.

It is well established that the low index gold surfaces in vacuum are subjected to reconstruction [27]. Reconstruction of gold (100), (110) and (111) surfaces also takes place at negative potentials in the solution, and once the electrode potential becomes positive, the reconstruction is lifted, and this phenomenon was observed by Hamelin [8], Kolb and Schneider [28, 29]. The potential and charge of the electrode surface affect the electrode surface stress.

Many groups have reported reconstruction of Au(111) [28 - 31]. It is known that the unreconstructed surface of Au(111) possesses a 4% lower atomic density than the reconstructed surface. The (1x23) reconstruction is established for Au(111), and this results in one direction in registration every 23rd atom with the fundamental bulk atoms (**Figure 1.3**). It is recognized that the reconstructed surface is characterized by distinctive stripes. When the Au reconstruction is lifted, the Au atoms are relaxed to establish the hexagonal structure.

Anion adsorption (especially halides) has a noticeable effect on the Au(111) crystallography, allowing the reconstruction to be lifted [25, 26]. When the reconstruction is lifted, the extra 4 % shifted above the surface and appeared as islands. This may modify the electrochemical attitude of the electrode. Close to the pzc where the anion concentration begins to increase on the electrode surface, the structural transformation from (1x23) reconstructed surface to the unreconstructed one (1x1) occurs.

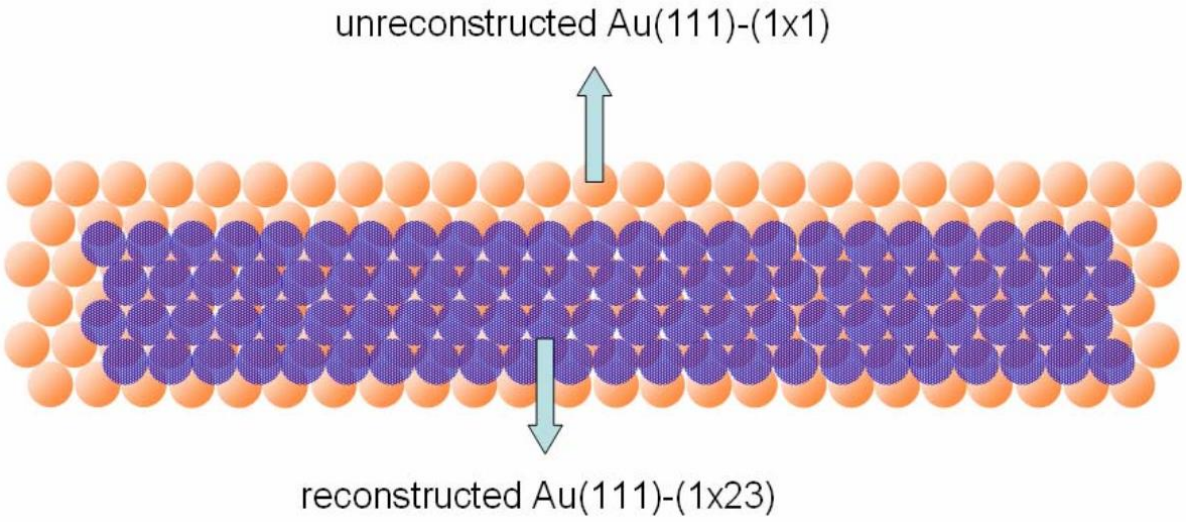

Figure 1.3: The reconstruction surface of Au(111) [32].

1.2.5 Adsorption

EDL interface structure often includes adsorption processes, as mentioned above. Specific adsorption is identified when an ion species concentration is greater than expected by electrostatic interactions. Almost all specific adsorptions are *chemisorption*, i.e. adsorption arising from electrochemical reactions between electrode and adsorbate. In certain situations, adsorption is induced by weak interactions like van der Waals forces and is called *physisorption.* The adsorption equilibrium can be readily established throughout physisorption; the adsorbate could still disperse and move whilst the electrode surface doesn't change. Typically, the reaction energy is around one order of magnitude greater through chemisorption,

the adsorbate is less mobile, whereas the electrode surface might even undergo reconstruction and be modified due to reactions with an adsorbate which can form a covalent or ionic bond.

The quantity of adsorbate is typically given in terms of coverage θ (e.g., the proportion of the electrode surface coated with adsorbate) and can be clarified as:

$$\theta = \frac{n_1}{n_2} = \frac{\Gamma}{\Gamma_{max}} \quad (1.2)$$

Where n_1 refers to adsorption sites number taken by adsorbed species, n_2 refers to overall adsorption sites number on the electrode surface and Γ, Γ_{max} refers to surface excess and total surface excess of adsorbed species, resp. When surface coverage equals one, complete monolayer formation of adsorbate has occurred. Many adsorption experiments are conducted on well-defined surfaces, which means on a particular surface plane of single-crystal [33].

The coverage relies on the concentration of the bulk in the electrolyte, regarding particles (A) adsorption. The relationships representing the difference of coverage with bulk concentration are classified as *adsorption isotherms*. Many adsorption isotherms models are existing, depending on various considerations. We will derive the corresponding relationship between θ and c_A by utilizing the total equilibrium rate principle.

$$\frac{\theta}{1-\theta} = c_A \exp(-\Delta G_{ad}/RT) \quad (1.3)$$

Where adsorption Gibbs energy (ΔG_{ad}) is the difference between molar Gibbs energy of particles A in the electrolyte and Gibbs energy of adsorbed species. It should be mentioned that the adsorption driving power reduces the free energy of the surface. When (ΔG_{ad}) is assumed to not depend on coverage (θ), *equation 1.3* is called *Langmuir isotherm*, which is used if the interaction among the adsorbed species is negligible (e.g. at low coverage) and when all adsorption sites are equal.

Usually, interactions between adsorbates are found, so the surface coverage affects significantly ΔG_{ad}. The *Frumkin isotherm* could be defined when adsorbed species repel or attract each other, with regard to the linear relationship $\Delta G_{ad} = \Delta G_{ad}^0 + \gamma\theta$, in which γ is constant and can be positive or negative value depending on the interaction kind between adsorbates.

$$\frac{\theta}{1-\theta} = c_A \exp(-\Delta G_{ad}/RT) e^{-g\theta} \quad (1.4)$$

Where ($g = \gamma/RT$) describes how the coverage θ modifies the adsorption energy. The potential of the electrode affects the Gibbs energy for cations, anions, and neutral species [4, 34].

1.3 Fuel cell electrocatalysis

Fuel cells (FCs) are exciting, emerging, and alternative technologies for power generation, which involves the production of electrical energy from chemical energy through an electrochemical reaction [35]. Fuel cell development focuses primarily on low-cost production, obtaining high efficiency of the FC system, and exploration of better and long-term materials. Nevertheless, the typical difficulties in the fuel cell system recently are high costs and low longevity [35]. There are many types of popular FCs technologies, involving direct methanol fuel cell (DMFC), proton exchange membrane fuel cell (PEMFC), solid oxide fuel cell (SOFC), molten carbonate fuel cell (MCFC), phosphoric acid fuel cell (PAFC), and alkaline fuel cell (AFC).

Hydrogen (H_2) is PMFC anode, and in light of fast oxidation kinetics and the high-power density is regarded to be the most suitable fuel for applications of FC. H_2 has to be formed from other supplies like electrolysis of water and reforming of natural gas, so it is not primary fuel [36]. Although it has good advantages of comfortable operating conditions and clean production, problems of storage and low range distributions prevented the broad application and commercialization of fuel cells based on H_2.

Formic acid (FA) is a natural simple acid which is found in ants bodies. FA is colorless and has a tremendous penetrating, pungent odour. Kinetics of FA oxidation (FAO) is fast compared to ethanol oxidation and this is attributed to the reduced number of electrons in FAO and the strong C-C bond in ethanol [37]. It can preserve the efficiency of operation in a wide limit of fuel concentration [38]. The low volumetric energy density (2104 WhL^{-1}) which is significantly smaller than that of clean methanol (4690 WhL^{-1}) is the main problem of using FA as fuel [38, 39].

Alcohols are regarded as promising alternative fuels to H_2 fuel. These alcohols are like methanol and ethanol. They have better characteristics such as simplicity of storage and distribution and being liquid at room temperature and ambient pressure as well as possessing a large energy density in the range of 6-9 KWh/Kg [40 - 42]. Because methanol has only one carbon its electrooxidation seemed simple, so it attained much interest at first. The toxicity of ethanol is lower than methanol. Ethanol can be produced in high amounts from some renewable sources. Besides, ethanol possesses a higher energy density than methanol (8 vs 6.1 KWh/Kg). Due to the faster kinetics of methanol oxidation reaction (MOR) than that of ethanol, the functional application of DMFC is more straightforward than direct ethanol fuel cell (DEFC).

The highest quality electrocatalysts used for achieving such reactions focused on platinum (Pt) and alloys based on Pt. The significant hindrances for developing this relevant

field are limited stock and the price of Pt. Comprehensive work of research has been conducted to design electrocatalysts of much active and cost-efficient.

1.3.1 Adsorption and oxidation of carbon monoxide (CO)

The CO adsorption and oxidation on electrocatalysts based on Pt are heterogeneous catalytic reactions. They belong to the most widely studied processes in surface chemistry related to applications of FC. In the case of low-temperature FCs utilizing H_2 as fuel, a significant problem is the poisoning of the Pt catalyst by a given amount of CO_{ads} (10- 100 ppm) [43]. Beden et al. also found adsorbed CO_{ads} in DMFC as an intermediate compound which blocks Pt catalyst using an in-situ IR spectroscopic approach. It is necessary to eliminate and oxidize CO_{ads} on Pt surface at the low potential in DMFC and Hydrogen FC.

Such reaction occurs on transition metal catalyst surface via the Langmuir-Hinshelwood mechanism (L-H) which was reported firstly by Gilman [44] or the Eley-Rideal mechanism. In acidic medium through the L-H mechanism, the net reaction is typically represented by the following steps:

Langmuir – Hinshelwood: $CO + * \rightarrow CO_{ads}$

$$H_2O + * \rightarrow OH_{ads} + H^+ + e^-$$

$$CO_{ad} + OH_{ad} \rightarrow COOH_{ads}$$

$$COOH_{ads} \rightarrow CO_2 + H^+ + e^- + 2^*$$

Where * refers to a free surface position

(L-H) mechanism consists of the following two separate electron transfer steps: adsorption of species containing oxygen which results from the oxidative decomposition of water which is reversible; irreversible reaction between adsorbed CO_{ads} and OH_{ads} to give a hydroxy carbonyl intermediate where this species was proposed based on FTIR-ATR techniques [45] to be broken down to yield CO_2 as the reaction product. For polycrystalline and single crystal surface platinum electrodes, the L-H principle for that reaction is commonly agreed [46, 47].

Eley – Rideal (E-R) mechanism has been observed on Pt/Ni electrode in alkaline conditions where the free hydroxyl group could take part in the reaction and subsequently eliminate CO_{ads} from the catalyst surface [48]. The overall reaction proceeds as follows:

$$CO_{ads} + 2\,OH^- \rightarrow CO_2 + H_2O + 2e^-$$

If the reaction proceeds between adsorbed CO and activated water molecules (oxygen contained species) in EDL, it means that MOR proceeds via an E–R mechanism. On the other

side, if the bifunctional catalyst with CO_{ads} and OH_{ads} adsorption sites is favoured, it indicates that the reaction follows an L–H mechanism.

The CO oxidation on Pt nanoparticles (NPs) produces voltammetric peaks at potentials depending on various parameters like particle size [49, 50], nanoparticle agglomeration [51, 52], grain boundaries [53], or specific surface crystallographic domains [54-60]. Two peaks have been shown ; one oxidation pre-peak in the potential range 0.3 – 0.6 V which has been detected for polycrystalline (PC) Pt [61], Pt single crystals [62, 63] and Pt nanoparticles [57, 58] and sometimes can be identified lower than 0.3 V based on surface defects of the Pt electrode [64], and the second main peak oxidation observed at higher potential [62]. While the OH adsorption potential in the potential limit of 0.68- 0.69 V was found to be independent on Pt NPs size.

Electrooxidation of adsorbed CO has been studied on cyanide modified Pt(111) by using DEMS and FTIR techniques [65]. As well as introducing a one or two metals to Pt (hkl) single crystal electrode to reduce the onset potential of CO oxidation has been conducted by using DEMS [66, 67]. The weakly adsorbed CO has a low heat of adsorption, and this is related to pre-peak oxidation. In contrast, the higher heat of adsorption of strongly adsorbed CO is responsible for the prominent peak in the presence of broad coverage of CO ($\theta_{CO} > 0.65$ ML) [62]. Because of the presence of the repulsion forces between CO molecules at high coverage led to the weak adsorption of CO molecules on the surface. Less amount of CO coverage decreases during CO oxidation at low potentials and the rest of the adsorbed CO relax on the surface and consequently become strongly adsorbed at the surface and oxidize at high potentials [46]. Wang et al. found that the rate-determining step (rds) for the oxidation of adsorbed CO changes with potential [68].

MOR on the platinum surfaces proceeds the dual pathway mechanism which suggested firstly by Bagotzky et al. [69] and later by Parsons et al [70]. This mechanism includes formation, adsorbed CO through the indirect pathway and soluble intermediates (formic acid and formaldehyde) [71, 72] through the direct pathway. The dual pathway mechanism for MOR at Pt (poly) electrode has been proved by using DEMS technique [73]. MOR has been studied on different platinum surfaces and it is concluded that the current efficiency of CO_2 hasn't influenced markedly with increasing step density but methanol oxidation can be enhanced [74].

Additional components to the Pt surface can change the electronic properties of Pt, resulting in a reduction of the bond strength of CO_{ads} to surface [75 - 77], and improve the OH adsorption by supplying more oxophilic places. [78, 79]. Pt-based electrocatalysts have been demonstrated to be highly effective than Pt alone for MOR, like PtRu [80, 81], PtNi [75, 82 -

84], PtAu [85], Pt-Pd [86 - 91]and PtAuRu [92]. In addition, some metal oxides like CeO_2 [76], SnO_2 [93], RuO_2 [78, 94, 95], and TiO_2 [96], and metal hydroxides like $Ni(OH)_2$ [79], have been exhibited CO tolerance enhancement.

The enhancement of MOR via the addition of one or two metals or metal oxide with Pt is ascribed to the bifunctional mechanism of CO_{ads} oxidation and reducing CO_{ads} oxidation potential [97, 98]. So, the MOR on PtRu alloy follows the bifunctional mechanism and ligand effect as shown in **Figure 1.4** [74, 99, 100].

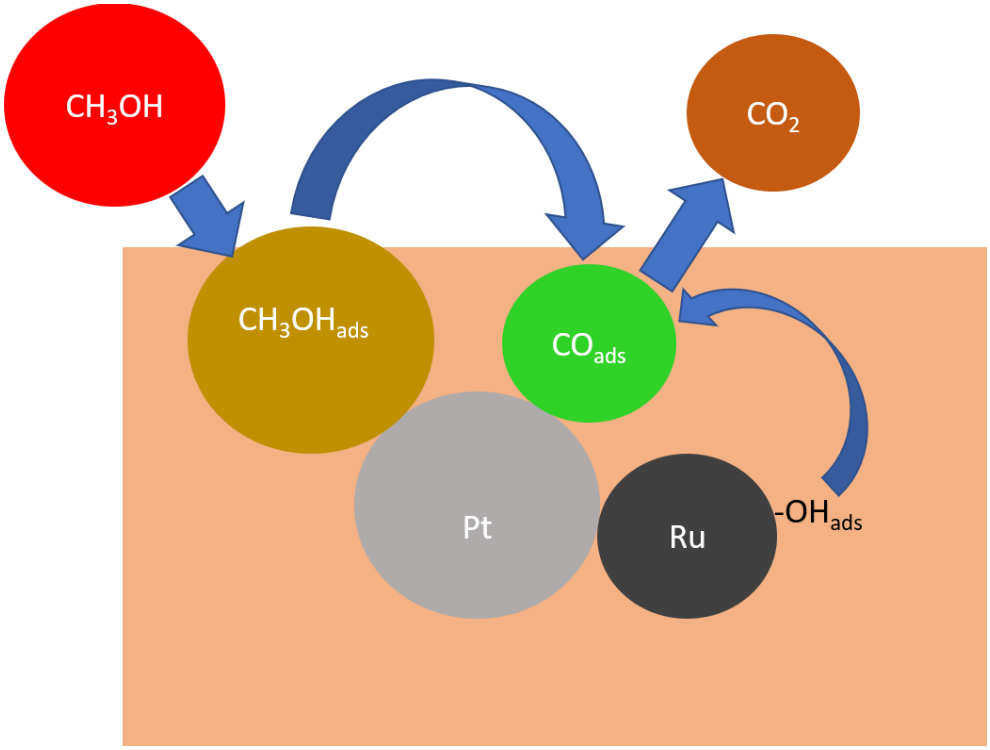

Figure 1.4: Bifunctional influence of Ru with Pt surface.

Methanol is first adsorbed on the Pt surface and then decomposed to CO_{ads}. Then oxygen-containing species like H_2O adsorb at potentials lower than 0.3 V and dissociate to OH_{ads} on the neighbouring Ru atoms. Consequently, the adsorbed CO_{ads} and oxygenated species mix together to produce carbon dioxide (CO_2) and refreshed sites on Ru and Pt surface. The ligand effect leads to a modification of the electronic properties of Pt by addition the second metal (Ru), and consequently, CO binding energy is decreased on the Pt surface.

1.3.2 Electrocatalysis of Formic Acid

Much interest and many studies have been received in electrocatalysis toward formic acid oxidation (FAO) based on Pt catalyst [101 - 107]. The great importance of direct formic acid fuel cell (DFAFC) lies in being a promising alternative to DMFC due to owing advantages; FA is non-flammable, non-toxic, and possessing permeability through the Nafion membrane of two orders of magnitude lower than methanol which results in increasing the cell efficiency [108]. Although FAO on Pt is regarded as a standard reaction in electrocatalysis because of the simplicity of its structure and involving only two electrons in the total oxidation to CO_2 formation, the reaction was found to be quite complicated.

The concept of dual-path mechanism is usually associated with the studies by Capon and Parsons [109] and Parsons and Vander Noot [70] in case of FAO. In contrast to MOR, the reason for the dual-path mechanism lies in the possibility of dehydration of the formic acid molecule on the catalyst surface. This is why the dual-path mechanism may be represented as a combination of the following reactions:

Direct path (dehydrogenation of the molecule)

$$HCOOH \rightarrow active\ intermediate \rightarrow CO_2 + 2\,H^+ + 2e^-$$

The indirect dehydration (CO Path)

$$HCOOH \rightarrow CO_{ads} \rightarrow CO_2 + H_2O$$

Initially, it was stated that in the direct path, the rate-determining intermediate is a COOH which adsorbs via its C atom [110] and appears at dehydrogenation of the molecule. However, later, through the ATR-SEIRAS method, Osawa and his group [111] detected the presence of bridge bonded formate HCOO adsorbed on a thin-layer Pt electrode chemically deposited on Si. At sufficiently high potentials, formate was also detected on Pd [112]. The discovery of adsorbed formate has awakened the active interest of several research groups in elucidating its role in FAO.

It deserves mention that HCOO is an active intermediate of FAO in ultrahigh vacuum [113]; moreover, the subsequent decomposition of HCOO turns out to be the limiting stage on Pt, whereas on Au this process is limited by the rate of HCOO formation.

Later, Cuesta et al. [114, 115] arrived at the conclusion that considers $HCOO_{ads}$ as the significant intermediate both in the dehydrogenation and dehydration pathways of FAO (**Figure 1.5**).

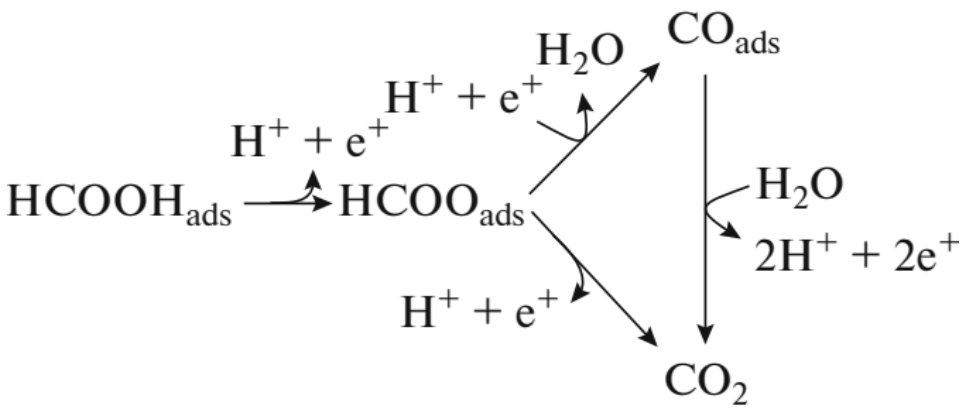

Figure 1.5: Scheme of the bifurcation point of adsorbed formate for two parallel pathways [115].

In this case, the presence of neighbouring free sites is not necessary. Thus, $HCOO_{ads}$ in its bridge form can be considered as the bifurcation point for the dual-path mechanism and also as the common precursor for the formation of CO_2 and CO. The conclusions of [115] agree with the results by Grozovski et al. [116] according to which the FAO current is directly proportional to the surface coverage with $HCOO_{ads}$. In [116], a scheme of triple path mechanism was proposed for FAO in which weakly adsorbed HCOOH molecules were considered as the active intermediate (**Figure 1.6**).

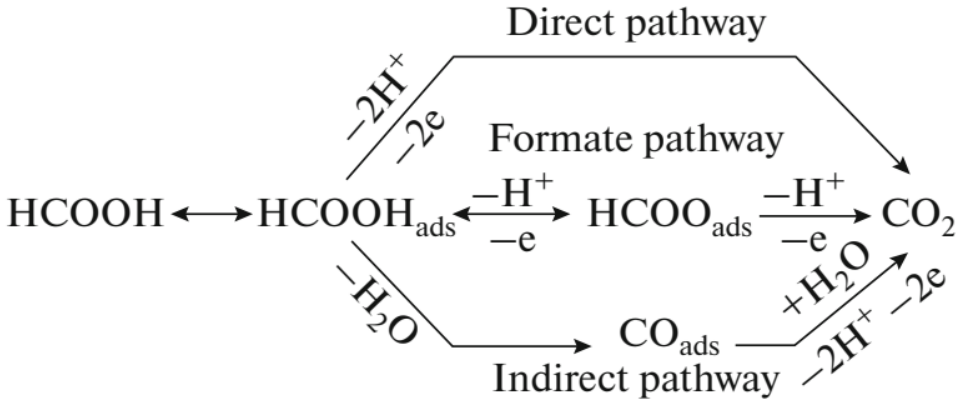

Figure 1.6: Triple path mechanism of FAO [116].

Wang et al. have shown based on periodic DTF computation [117] that more probably, $HCOO_{ads}$ is neither intermediate, nor spectator, but plays a template role that enhances FA adsorption in the CH arrangement which serve as precursors of CO_2 formation.

There is much interest to prohibit CO_{ads} formation which effectively blocks active sites on the electrode or to enhance its oxidation at low potential by, for instance using binary

electrocatalyst. The bimetallic surfaces with the second metal achieve prevention CO formation through bifunctional effect as mentioned above in detail [118]. Pt and Pd are quite well-known as the two more powerful catalysts towards FAO [119 - 121]. The CO_{ads} intermediates result in poisoning of the Pt surface through the dehydration pathway, while on Pd surface FAO occurs through a direct way to promote the rate of oxidation to form CO_2 [122 - 124]. However, under certain polarisation conditions, CO_{ads} is gradually accumulated, which results in inhibition of the catalyst activity and gradual decomposition of the catalyst [125, 126].Many studies have been reported that Pd improved FAFC technology due to possessing special features such as low price, and its presence in large amounts.

There are some methods to improve FAO effectiveness highly: (1)Mixing the advantages of Pd with additional metals to form alloy as Pd-Pt alloy [127], and Pd-Au [128]; (2) well developing of catalysts support such as conducting polymers and graphene to achieve good distribution, accumulation prohibition and enhancement of electrocatalytic of PdNPs [129](3) structural ordering like core-shell configuration [130].

1.3.3 Electrocatalysis of Ethylene Glycol

Ethylene glycol (EG) is utilized in many formulations due to being an antistatic agent in association with other organic compounds. EG is an effective energy carrier for FCs due to some features: it can be produced from biomass, has a low molecular weight, high power density, low vapour pressure (0.06 mmHg at 20°C), is easy to transport and has a lower toxicity than methanol [131, 132]. Miyazaki et al [131] stated that EG presents high conversion to CO_2 using Pt-based catalysts and as consequence it is considered as promising alternative to DMFC[133 - 136].

The total oxidation per EG molecule gives ten electrons to lead to the final product (CO_2) as shown in the equation:

$$C_2H_6O_2 + 2H_2O \rightarrow 2CO_2 + 10H^+ + 10e^-$$

Ethylene glycol oxidation (EGO) may occur via many sequential and parallel pathways, producing various intermediates compounds such as glycolaldehyde, glyoxal, glycolic acid, glyoxylic acid and oxalic acid through DEMS measurements on Pt catalyst which can be represented in the scheme [137] (**Figure 1.7**).

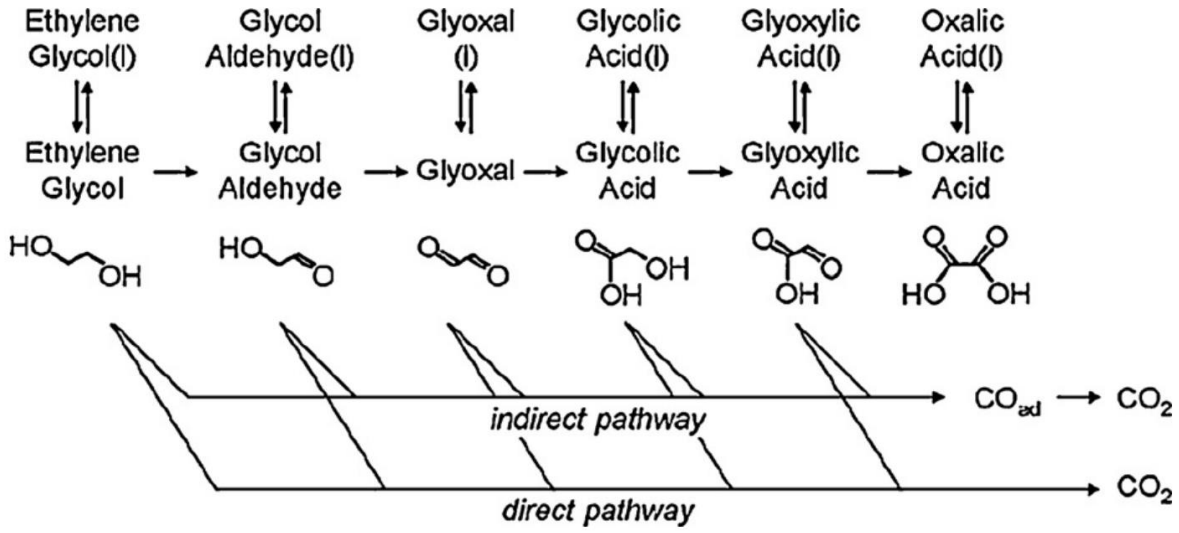

Figure 1.7: EG oxidation scheme [137].

The carbonyl group intermediates formed during EGO react strongly with Pt to facilitate C-C bond breaking and to decompose to adsorbed CO even at potentials of coverage of Pt surface with H_{upd} species. While the interaction between hydroxyl group intermediates and Pt surface is weak so that the decomposition rate of EG to CO_{ads} is slow where molecules containing hydroxyl group cannot adsorb or dissociate on the surface covered with H_{upd} species [137].

CO_{ads} is produced from cleavage of the C-C bond at 0.5 V which blocks the active sites of Pt surface at a lower potential, prohibiting EGO and reducing the efficiency of the fuel cell [138]. Oxidation of CO_{ads} occurs at higher potential [137]. EGO was elucidated on a Pt electrode by FTIR spectroscopy in acidic and basic medium. It was observed that the major products in the acidic medium are CO_2 and glycolic acid [139].

The activity of EGO on a Pt catalyst can be enhanced utilizing bimetallic catalysts such as PtRu/C [135, 140], Pt-Au [141] and PtPb [142] in basic medium. The bimetallic catalyst Pt-Pd with varying composition has been shown good activity toward EGO through a synergistic effect in basic medium, which is attributed to reducing the residue of EG strongly bound to surface [143]. Furthermore, a higher current density was obtained, and the onset potential of EGO was decreased about 70 mV upon introducing Bi to the Pt catalyst [144]. However, the ternary electrocatalyst did not affect the onset potential of EGO, improve the current density compared to the bimetallic catalyst of Pt–Bi/C [144].

1.3.4 Conductive polymers

Conducting polymers (CPs) are considered conjugated polymers; they can be described as organic materials that possess an extended π-bond system, through which electrons migrate through its polymeric chain from one end to the other [145]. CPs have optical and electrical features due to the existence of delocalized π- electrons on their backbone in addition to other characteristics like low cost, high charge density and lightweight[146]. They can be synthesized through two ways: (1) chemical polymerization, and (2) electrochemical polymerization, which is the method used in this work. Generally, there are applications of CPs in many fields such as batteries [147], sensors [148], fuel cells [149], solar cells [150], and supercapacitors [151]. Kinetics of electrode processes can be improved through the deposition of a thin layer of CP on it. The most intensely investigated CPs are polyaniline (PANi), polypyrrole (PPy), and their derivatives [152]. As an example of the mechanism of electropolymerization of polyaniline (PANi) has been described in **Figure 1.8** [152].

There is an increasing interest in using CPs as catalyst supports in the fuel cell such as PANi which has been used to reduce COads poisoning of platinum [153]. Choi et al. [154] and Kim et al. [155] electrooxidized methanol by using conducting polymer (PANi) supported for PtRu particles. Also, Kim et al. showed that the improved electrocatalytic activity of PtRu/PANi support is more effective than PtRu/carbon support and this attributed to some reasons: (1) faster ion diffusion, (2) higher surface area of the electrocatalyst, and higher electrical conductivity of PANi support [155].

Methanol oxidation and oxygen reduction reaction have been improved through using Pt/PANi/WC/C catalyst compared to Pt/C catalyst in the presence of methanol [156]. Also, Ruiwen Yan et al. found that the electroactivity of Pt-Pd/PANi/CNT catalyst towards MOR is more significant than in the absence of the polymer, and this proves that polymers behave as good matrices for better metallic particles distribution [157].

It was observed that FAO at Pt/poly (o-toluidine) is considerably faster than on Pt electrode [158]. Kelaidopoulou et al. [159] noticed that Pt particles incorporated in PANI enhanced the activity of oxidation of ethylene glycol oxidation as compared to Pt electrode. Besides, ethanol electrooxidation was significantly improved on NiNPs supported on PPy compared to free CP catalyst [160].

Step 1. Oxidation of aniline Monomer

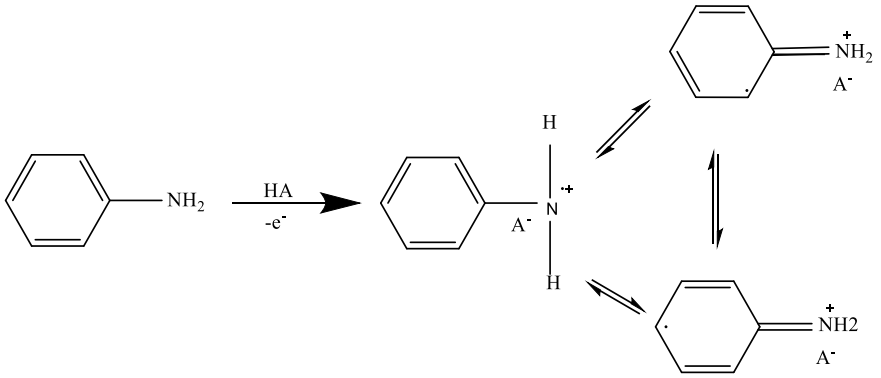

Step 2. Radical coupling of aniline

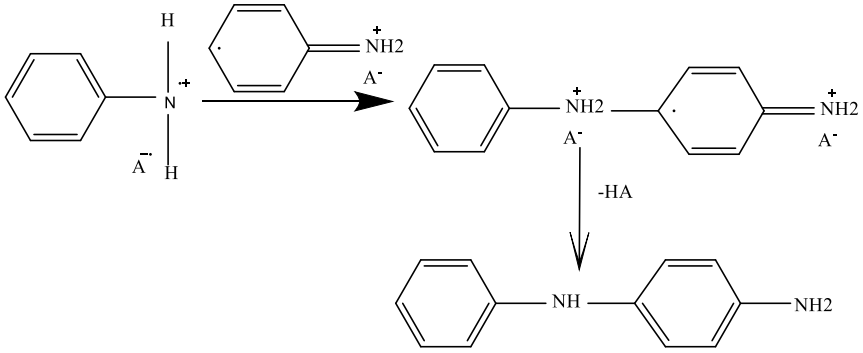

Step 3. Propagation of aniline

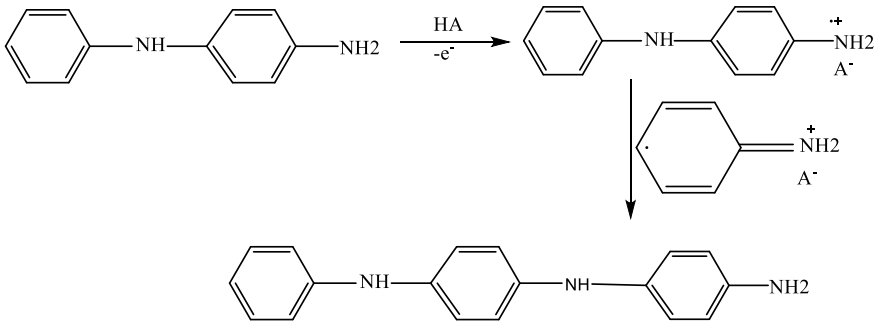

Step 4. Doping in Polyaniline

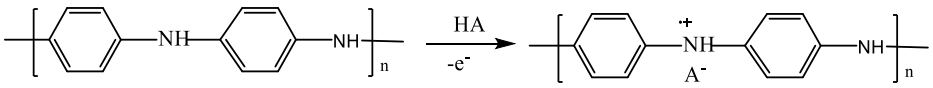

Figure 1.8: Mechanism of PANi electrolpolymerization [152].

1.4 Scope of the study

This work aims at investigating the adsorption rate of iodide and bromide ions on the Au(111) electrode in organic solvents and on studying the role of adsorbed CO molecules formed during the electrooxidation of formic acid and ethylene glycol on metal nanoparticles supported on conducting polymers. For the former, mainly EIS is used, for the latter mainly differential electrochemical mass spectrometry (DEMS). The chapters of this thesis are organized as follows:

Chapter one gives a brief introduction into the electrode/ electrolyte interface structure and fuel cell electrocatalysis.

Chapter two reports the experimental techniques used in work.

Chapter three talks about the adsorption of iodide on Au(111) electrode in propylene carbonate compared to adsorption in the aqueous medium. **(Published)**

Chapter four reports on the adsorption of iodide and bromide on Au(111) electrode in different aprotic solvents**. (Submitted)**

Chapter five describes the determination of the point of zero charge of Au(111) in aprotic solvents and studying the parameters which affect the pzc, as well as, investigation the electrode/electrolyte interface of gold in propylene carbonate by ATR-SEIRAS technique. **(In preparation to be submitted)**

Chapter six reports on electrooxidation of formic acid on Pd/p1,5-DAN/GC and Pt/ p1,5-DAN/GC, Pt/Pd/p1,5-DAN/GC, and Pd/Pt/p1,5-DAN/GC in acidic medium using DEMS**. (Published)**

Chapter seven reports on electrooxidation of ethylene glycol on different conducting polymers supported to the metal nanoparticle of Pd and Pt in the acid medium using DEMS. **(Published)**

Chapter eight gives a summary of the experimental findings presented in this thesis and outlook for future work.

Chapter two: Experimental techniques

This chapter discusses methods of measurements with the present work, including cyclic voltammetry (CV), alternating current voltammetry (AC-voltammetry), electrochemical impedance spectroscopy (EIS), differential electrochemical mass spectrometry measurements (DEMS), X-ray photoelectron spectroscopy (XPS), Scan Electron Microscope and Energy Dispersive X-ray spectroscopy (SEM & EDX), and Fourier– Transform Infrared Spectroscopy (FTIR).

2.1 Cyclic Voltammetry

Cyclic voltammetry (CV) is the most versatile electrochemical methodology. Its versatility and effectiveness lie in providing information about thermodynamics and kinetics of electron transfer processes on the electrode surface. These processes include the electron transport through the interface, ion adsorption, and order modifications of the adsorbed layer. It is also useful for the investigation of catalysis reactions which are initiated by electron transfer. A standard three-electrode experimental configuration composing of reference, a working and a counter electrode has been employed for CV.

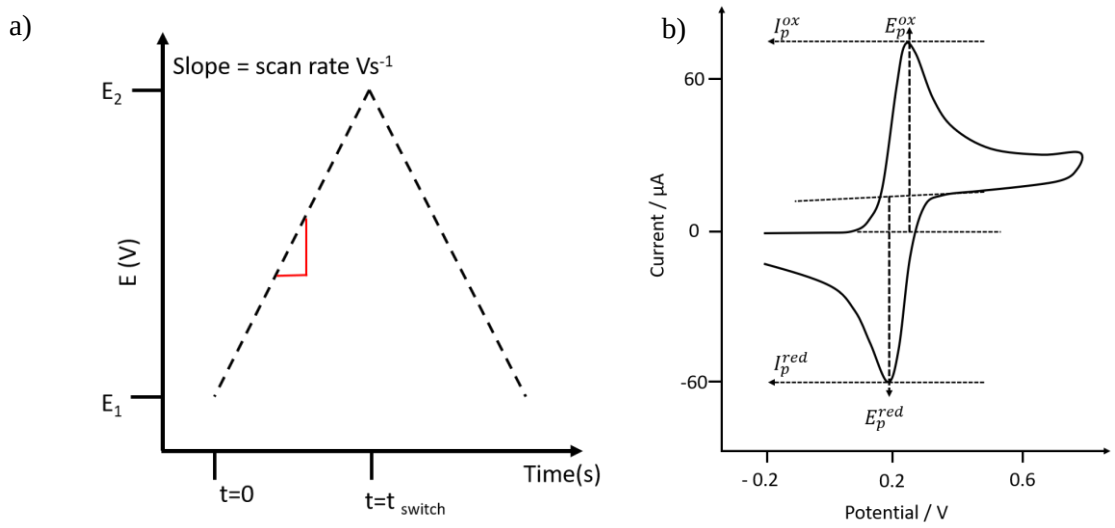

Figure 2.1: Classic diagram CV depiction. **a)** The potential-time waveform. **b)** The resulting cyclic voltammogram [161].

A potential E is ramped linearly from E_1 to E_2 between the working and reference electrode and upon reaching to specific potential value E_2, the direction is inverted, and the voltage keeps

going in the inverted path (**Figure 2.1**a). During the entire process, the resulting current between the counter and working electrode is recorded.

During a reversible process, the most straightforward reaction of one-electron transfer, the initial voltage, E_1, is selected in a voltage area where the analyte reaction cannot happen. Optimally, there is no faradaic current close to E_1, but as the potential is ramped to E_2 with a fixed scan rate, a rise in faradaic current is detected suggesting analyte oxidation (**Figure 2.1**b). After that, the highest current, I_p^{ox}, is determined. The potential path is then changed in the other direction, and the redox analyte reduction is likewise determined, generating another peak–the lowest current, I_p^{red}. The inverted sweep seeks to assess the oxidized molecules stability as well as the reaction reversibility since the unstable molecules may be transformed to other molecules and therefore used up in the vicinity of the electrode, and thus cannot contribute to the current in the reversed scan.

The Nernst equation (**Equation 2.1**) illustrates how the applied potential is relating to electrode surface concentrations of redox species [161].

$$E_{eq} = E^0 + \frac{RT}{nF}\ln\frac{a_{ox}}{a_{red}} \qquad (2.1)$$

Where $\alpha_{ox/red}$ are the activities of redox species, R is the gas constant, and T represents the absolute temperature. E^0 is the standard electrode potential, n is the number of electrons number exchanged during the redox reaction, and F is the Faraday constant (96.485 C. mol^{-1}).

The difference between the anodic and cathodic peak for the reversible system(ΔE_p) at 25°C is close to 2.3RT/nF 0.0.059/n V [4]. Besides a redox couple's reversibility, CV can also give details, based on the Randles-Sevcik **Equation 2.2**, on diffusion coefficient, the surface area of the electrode, and species concentration.

$$i_p = 2.69\ x\ 10^5\ n^{3/2}\ A\ D^{1/2}\ C\ \nu^{1/2} \qquad (2.2)$$

Here i_p represents the highest current (A), n is the electron number transferred per molecule, A represents the electrode area (cm^2), D is the diffusion coefficient ($cm^2\ s^{-1}$), C is the concentration of molecules (mol cm^{-3}) and ν the sweep rate (V s^{-1}).

Adsorbed species can induce changes in CV shape. Specifically, if only adsorbed species are involved in the solution and have fast kinetics, the resultant voltammogram is symmetrical, with peaks of oxidation and reduction taking place at about the same potential. (**Figure 2.2**)

When kinetics slow down, peak separation is observable. The peak currents are still proportional to the scan rate as in **Equation 2.3**, compared with $\nu^{1/2}$ in **Equation 2.2**).

$$i_p = \frac{n'\alpha_c\ n\ F^2\ \nu\ A\ \Gamma_{o,i}}{eRT} \qquad (2.3)$$

Where $\Gamma_{o,i}$ is surface coverage of adsorbed species [161].

The surface excess of adsorbed species could be estimated from charge transfer (integration of the area under the peak as in **Equation 2.4**):

$$\Gamma_{o,i} = \frac{Q}{nFA} \qquad (2.4)$$

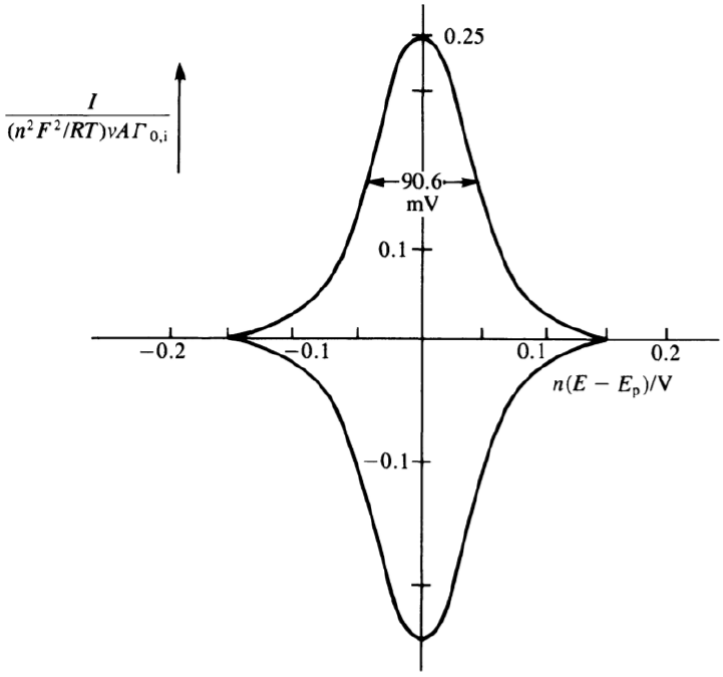

Figure 2.2: An example of a cyclic voltammogram of the reversible response of a surface adsorbed species. $E_p = E^0$ from the Nernst equation [161].

2.2 Alternating Current Voltammetry (AC-voltammetry)

Alternating current voltammetry is a frequency domain approach involving the superimposition of a low amplitude AC voltage on a DC -potential during the typical voltammetric process upon the potential scan or potential step measurements. AC voltammetry is an expansion to conventional linear sweeping methods such as cyclic voltammetry. It is essentially a faradaic impedance methodology [4]. It enables us to characterize the electrode processes quantitatively.

The alternating potential has a frequency of 10-100 Hz and an amplitude of 3 mV applied to the working electrode. As a consequence, the resultant AC current and its phase angle are measured as seen in **Figure 2.3**. The purpose of the phase-sensitive detector is to isolate and show the real and imaginary current contribution based on the potential [162]. The produced AC current is measured at the same frequency (f) of AC potential. Precaution should be taken

to adjust the signal in the lock-in amplifier since phase-sensitive detectors commonly sense only the root mean square signal of processing frequency.

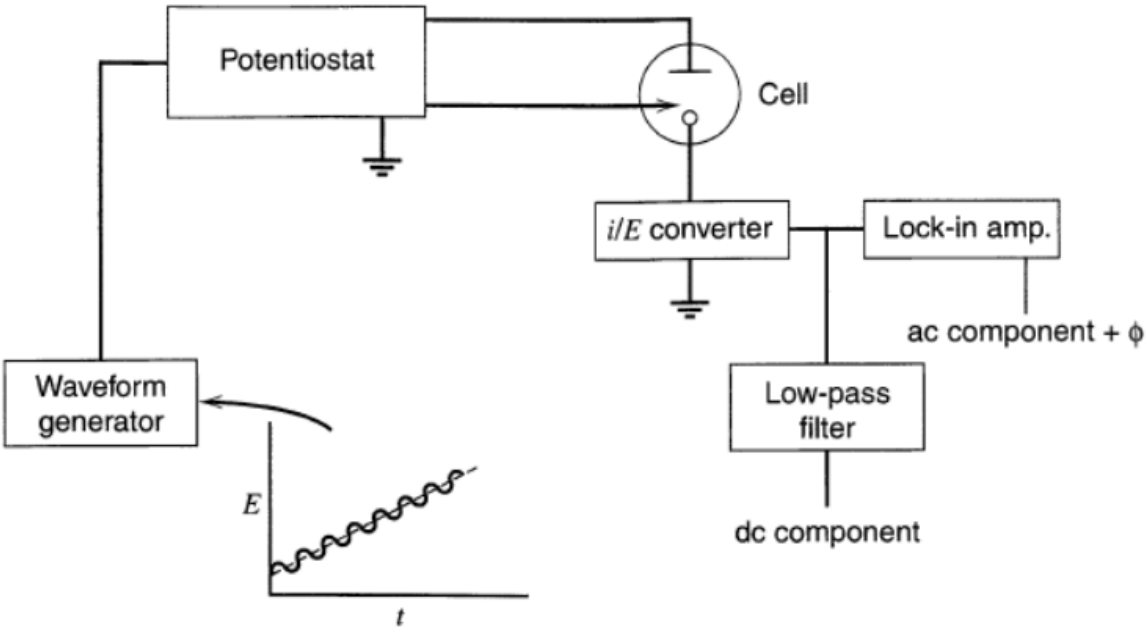

Figure 2.3: Graphical representation of an AC voltammetry experiment. Adopted from Ref. [4].

2.3 Electrochemical Impedance Spectroscopy (EIS)

Impedance spectroscopy is a simplified practical approach to investigate electrochemical systems and processes. Its power lies in its capability to interrogate the phenomenon of relaxation whose time constants extend over numerous orders of magnitude [163]. In EIS, the frequency dependency of the examined electrochemical system e.g. reactions occurring on the electrode | solution interface or the double layer (DL) itself, is examined by overlaying a sinusoidal disturbance potential $E_{WE,p}(t) = Ep \sin(\omega t)$ to certain fixed potential E^0_{WE}, where Ep is perturbation amplitude and ω is the radial frequency ($\omega = 2\pi f$). The measuring current response $I(t) = I_r \sin(\omega t+\varphi)$ with the phase shift (φ) among $E_{WE,p}(t)$ and I(t), where I (t) is the current at a given time and I_r is the current amplitude. **Figure 2.4** exhibits a sinusoidal potential perturbation ($E_{WE,p}(t)$) and current response (I (t)).

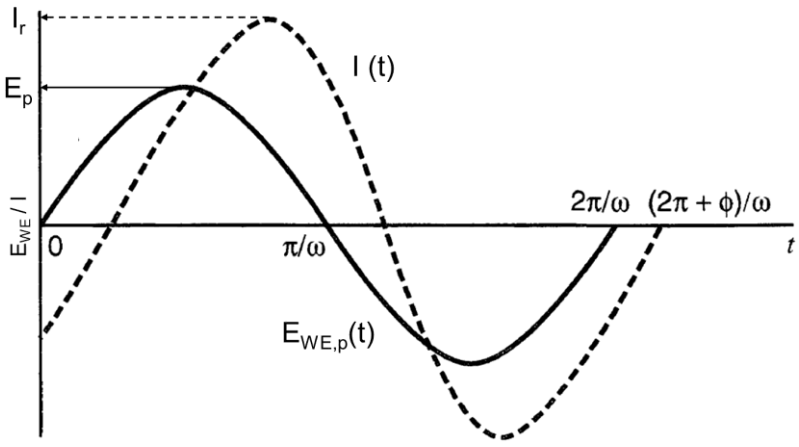

Figure 2.4: Sinusoidal potential perturbation and current response. Adopted from Ref. [4].

The ratio of sinusoidal potential disturbance and the current response I (t) gives the complex impedance Z(ω) of the system, comprising of a real part Z_r and an imaginary part Z_i with $i = \sqrt{-1}$.

$$Z(\omega) = \frac{E_{WE,p}}{I(t)} = Z_r + Z_i \qquad (2.5)$$

The real and imaginary components of the complex impedance are connected by the phase variation between sinusoidal potential perturbation ($E_{WE,p}(t)$ and response current (I (t)).

$$\tan\varphi = \frac{Z_i}{Z_r} \qquad (2.6)$$

The complex impedance description in polar form (**Figure 2.5**) can be described:

$$Z = |Z|\,(\cos\varphi + i\sin\varphi) \qquad (2.7)$$

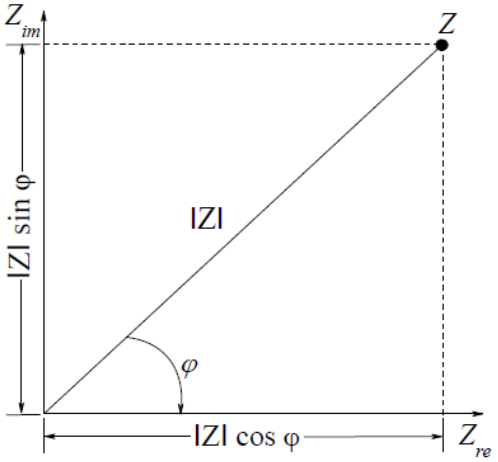

Figure 2.5: Impedance display in the complex plane.

When angular frequency changes, it results in an impedance spectrum over the examined frequency limit. Two standard plots of this kind of impedance spectrum could be seen in **Figure 2.6**.

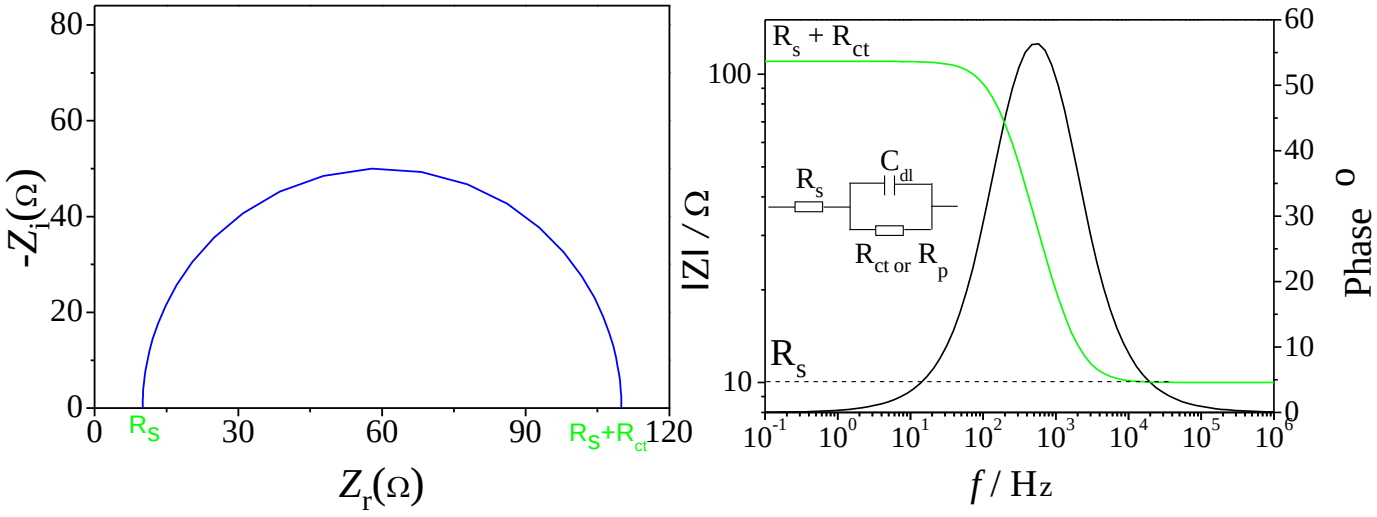

Figure 2.6: Left: Nyquist plot of the impedance spectrum of the Eq. circuit presented in the inset, Right: Bode plot. R_S = 10 Ω, R_P = 100 Ω, C_{DL} = 10 µF.

On the left side of the Nyquist diagram, $-Z_i$ plotted against Z_r , whereas the Bode plot is on the right side, the impedance |Z| and phase shift are plotted versus frequency f. The impedance of a resistor with resistance R and a capacitor with a capacitance C are provided by:

$$Z_{resistor}(\omega) = R$$

$$Z_{capacitor}(\omega) = \frac{i}{\omega C} = \frac{1}{i\,\omega C} \qquad (2.8)$$

2.4 Differential electrochemical mass spectrometry (DEMS)

Differential Electrochemical Mass Spectrometry (DEMS) is an ultimate analytical tool that integrates electrochemical half-cell experiments with mass spectrometry. It is not only suitable for recognizing gaseous products produced throughout electrooxidation of organic species on the electrode surface or intermediates of successive faradaic processes by utilizing galvanostatic and potentiostatics techniques. However, it also identifies sub-monolayer quantities of adsorbed species generated on single crystal and polycrystalline electrode surfaces byways of their desorption. The association of the faradaic electrode current and the resulting mass ion current of the electrolyte flow can explain unclear electrochemical reactions.

In 1971 Gadde and Bruckenstein were initially able to use in situ electrochemical mass spectrometry (EMS) to examine electrochemical processes using a PTFE interface [164].

Wolter and Heitbaum further developed the DEMS technique in 1984 by enhancement of the vacuum system to measure the volatile product quantitatively and with high sensitivity [165]. The expression "differential" was selected to differentiate between the time-and potential-resolved relation of mass signal and electrode faradaic current [165] from unresolved integration methods [164, 166]. Bruckenstein and Gadde had a substantial delay time of 20 s [165] between electrochemical production and species mass spectrometric identification, Wolter and Heitbaum's method reduced the time delay between ionic signal detection and faradaic reaction at the electrode also allowed them to investigate dynamic processes.

There are many cell configurations in a DEMS setup which have been studied in-depth in the literature [167 - 169]. Baltruschat et al. built a thin layer cell for massive electrodes with smooth and single crystals faces [170 - 172]. A new revelation of dual thin layer cell in conjunction with quartz crystal microbalance has been developed by Baltruschat and collaborators [166]. The Faradaic reactions in this cell that must be carried out under the continuous electrolyte flow are uniquely suited due to the fast consumption of reactants in the thin layer cell. The characteristic aspect is also that the produced molecules are pushed by steady convection from the top compartment to the bottom across six capillaries then transferred to the mass spectrometer through the Teflon membrane.

Figure 2.7 displays a graphical description of the dual thin layer flow cell employed in this study. The cell design is also described in ref. [169]: First, the electrolyte passes through a thin layer compartment (electrochemical compartment) comprising the working electrode positioned on a four thick (ca. 50 µm)Teflon ring spacers (Gore-Tex ®), average cavity size 0.02µm, inside diameter of 6 mm, 50 percent porosity leaving a 200 µm electrolyte layer thickness. Then, the electrolyte passes to the second thin layer compartment through 6 capillaries whose diameter equals 0.5 mm. The porous Teflon membrane is supported by a stainless-steel frit and is used as an interface between the electrolyte and vacuum.

A peristaltic pump regulated various electrolyte flow rates at the cell outlet. The current output is well distributed, and the ohmic resistance is declined in dual thin layer cell via employing two platinum wires as counter electrodes where one with high resistance (100 kΩ) is attached at the inlet of the cell, and low resistance one (1100 Ω) is contacted at the outlet.

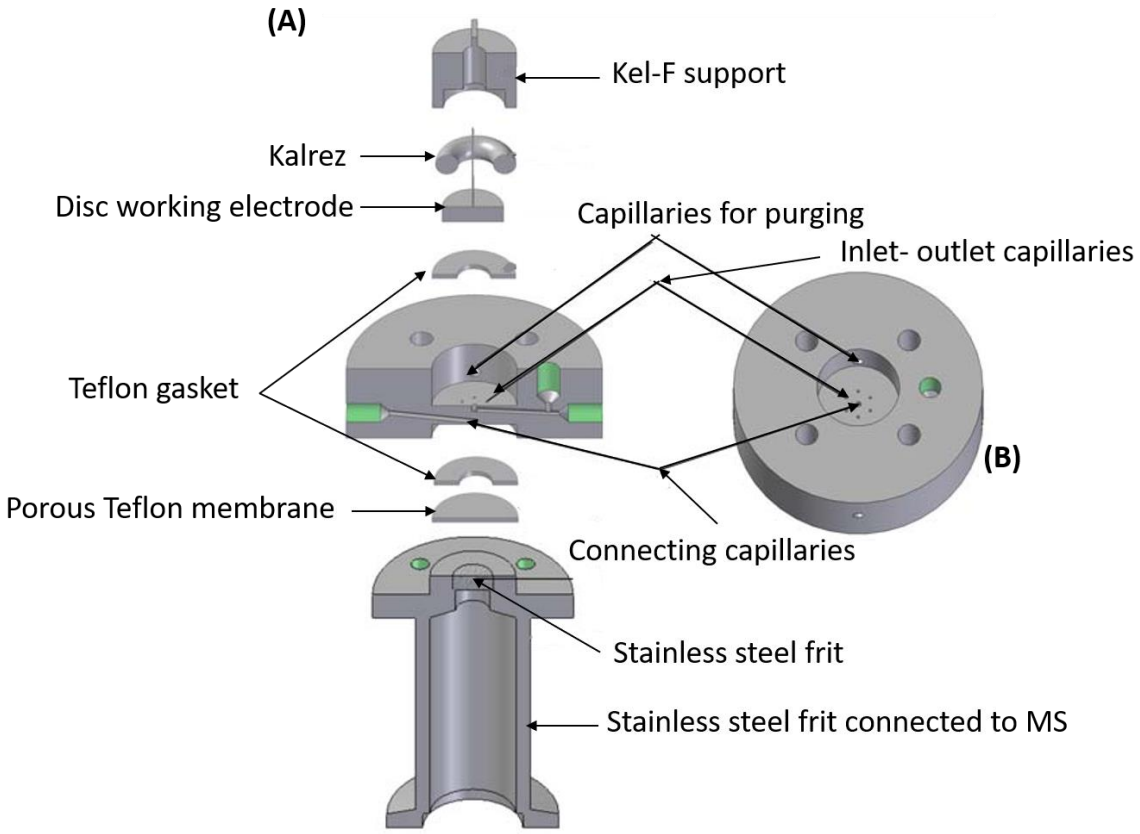

Figure 2.7: Dual thin- layer cell for experiments under constant flow through (Kel-F). (A) Side view of Kel-F body of the cell, (B) Top view of the cell. Adopted from [169].

2.5 X-ray photoelectron spectroscopy (XPS)

XPS is an outstanding technique used for the analysis of surface chemistry of the sample. It can measure the electronic, chemical state of elements within the sample, and the elemental composition of the material. XPS spectra can be obtained by irradiating the solid surface with X- rays under UHV conditions. The electrons that are occupying various energy states in the sample are excited with beams of x-ray while simultaneously measuring the kinetic energy and number of electrons that are emitted from the top 1-10 nm of the sample being analyzed. Direct identification of each element that is placed on the top layers of a sample can be revealed from the peaks in XP spectra. The peak positions (binding energy) correlate with specific electron configurations within the atoms (e.g. 1s, 2s, 2p, etc.) and the element amount within the irradiated area can be directly identified from the peak area, taking into account the atomic sensitivity factors.

XPS measurements (made by P. Bawol in our lab) were used to investigate adsorbed iodide quantitatively on Au(111) electrode from DMSO and PC based electrolytes. These XPS measurements involve the following steps: (1) The Au(111) crystal attached to the stainless-

steel crystal holder which can be attached to the UHV manipulator is annealed; (2) The electrochemical adsorption of iodide on Au(111) attached to the holder is performed in the electrochemical H-cell; (3) After the electrochemical adsorption of the iodide in the organic electrolyte, the electrode is removed from the electrochemical cell under potential control and rinsed with high purity MilliQ water (R=18.2 MΩ) to remove residual electrolyte; (4) The transfer of the electrode is done through the air and takes no longer than 3 min; (5) XPS measurements were carried out in a UHV chamber (base pressure 5·10-10 mbar) with a non-monochromatized Mg Kα (1253.6 eV) source. Due to highly accurate stepper motors at the manipulator, the same XPS position is approached in every experiment, thereby the intensity of the peaks in the spectrum is not distorted. As an electron analyzer, a hemispherical electron analyzer (Omnicron NanoTechnology EA 125) is used. The binding energy is referred to the Au 4f7/2 core level excitation (83.95 eV) [173]. Survey spectra are recorded with an energy resolution of 0.5 eV and a pass energy of 50 eV. For the high-resolution spectra, a resolution of 0.1 eV and an averaging over 4 spectra are chosen.

2.6 Scanning Electron Microscopy and Energy Dispersive X-ray spectroscopy (SEM & EDX)

SEM uses electron beams which interact with Nano or Micro-scale samples to obtain information about the sample. The significant required signals for detection are the backscattered and secondary electrons, which produce SEM images of the sample at various magnifications. It is equipped with an EDX unit, which is used for qualitative and quantitative analysis. This unit can identify the type and percentage of the elements in the peaks of the EDX spectrum. The SEM instrument is used to examine morphology and surface topographies of Pd/PDAN/GC, Pt/PDAN/GC, Pt/Pd/PDAN/GC, and Pd/Pt/ PDAN/GC modified electrodes. The catalysts are prepared in an electrochemistry lab (University of Menoufia, Egypt) within the project ″Electrochemical and differential electrochemical mass spectrometry studies of novel biofuel cell based on Nano metal dispersed in conducting polymers‟ of Alexander von Humboldt Foundation. The instrument used is the SEM Model QUANTA FEG 250 at National Research Center – Cairo – Egypt.

2.7 Fourier– Transform Infrared Spectroscopy (FTIR)

2.7.1 Infrared Spectroelectrochemistry

Demand to more detailed structure or chemical knowledge of solid | liquid interface is the main motivation for FTIR measurements. In situ spectroelectrochemistry has been a

promising instrument to characterize interface structures on electrode substrates, described as a particular association of traditional electrochemical techniques with spectroscopic surface-sensitive methods.

In situ Fourier Transform Infrared spectroscopy (in situ-FTIR) was commonly being one of the most famous spectroelectrochemical approaches as it is structure-specific, non-destructive, easy-to-operate, quick-detect. It gives proper structure and chemical knowledge of adsorbed species on electrode surfaces. This work will concentrate on applying ATR-SEIRAS in characterizing electrode/electrolyte interface on gold electrodes.

2.7.2 Notation on FT-IR techniques

For electrochemical purposes, FT-IR spectroscopy generally employs three techniques: Transmission, external and internal reflection [174]. Owing to the restrictions on the small thickness of the mini-grids of metal and on reduced sensitivity to adsorbed molecules on the electrode surface, the transmission technique is not appropriate to detect signals at the interface [174]. Reflective configuration techniques are commonly used in measurements of electrochemical FT-IR spectroscopy.

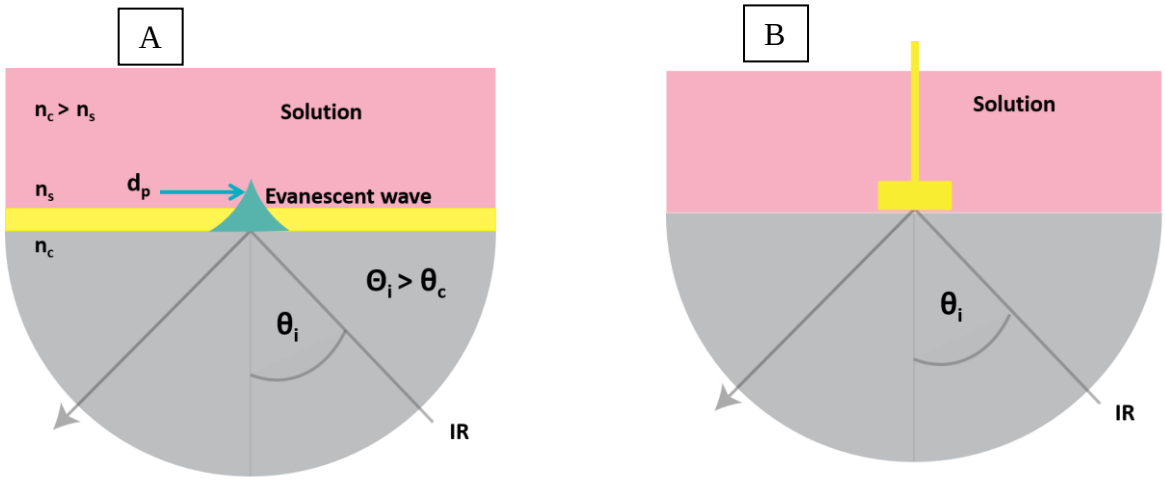

Figure 2.8: Different modes of FTIR, (A) internal reflection where the prism could be Si, Ge or ZnSe, and (B) external reflection where the prism could be CaF_2.

External reflection is the most commonly used technique, where reducing of solvent absorption is occurred via trapping a thin layer of electrolyte (1– 50µm) [174] between an IR-transparent window of the prism and the reflective working electrode (**Figure 2.8B**). SNIFTIRS (subtractively normalized interfacial FTIR spectroscopy) and IRRAS (infrared reflection absorption spectroscopy) are examples of the external reflection mode. Such a configuration of

the thin layer aims at reducing the interference associated with solvent infrared absorption, which is typically more significant than the interfacial signal of molecules adsorbed on surface [175, 176]. If gas formation occurs, it becomes stuck in the thin layer and irritates spectral as well as electrochemical measurements [177]. The large resistance of the thin layer often inhibits a fast device response to externally imposed potential modifications [178]. External reflection is only appropriate for slower kinetic measurements, as opposed to internal reflection approaches like attenuated total reflection (ATR) (**Figure 2.8A**).

The work under study relies on the application of an ATR approach, where it depends on the total reflection of the infrared beam at the internal interface of the transparent prism (internal reflection element) with an extensive refractive index (n_c)like Si, Ge, ZnSe [179, 180]. The internal reflection element in many spectroelectrochemical measurements is commonly a crystal (prism) covered on the top with a smooth layer of metal (gold or silver). This sort of film electrodes, generally evaporated on the surface to construct a continued thin layer composition, demonstrates either features of quasi- single crystal surface or roughened surface but a marked IR cross-section surface enhancement. ATR is predominantly labeled as Kretschmann design [181], who employed this configuration (**Figure 2.8A**) to excite the waves of surface plasma through the heterogeneous light wave produced by total reflection.

The total reflection takes place in the internal reflection element at a suitable incident angle more magnificent than the critical angle θ_c. Refractive indices of FTIR prism and electrolyte affect the critical angle θ_c as follows in **Equation 2.9**:

$$\theta_c = \sin^{-1}(n_s/n_c) \qquad (2.9)$$

Where n_s and n_c is the refractive index of sample and crystal, respectively, the characteristics of the thin film of metal should be transparent to the infrared radiation. Even though the occurrence of the total reflection, a part of the beam penetrates into the electrolyte and consequently the evanescent wave is produced that can't propagate or sustain a resonance. Its intensity decays exponentially with depth into the second medium (**Figure 2.8A**). The penetration depth d_p is a guideline for the appropriate vicinity of the species to the interface. It is described as the distance from the interface to the extent to which the electromagnetic field amplitude at the interface is equal to 1/e (~37 percent) amplitude of incoming beam. The penetration depth d_p (**Equation 2.10**) relies on three factors: incident angle θ, wavelength λ, and the variation of refractive indices between the optically thick material (ATR crystal) and the thinner optically component (e.g. sample) $n_{sc} = n_s/n_c$.

$$d_p = \frac{\lambda}{2\pi\sqrt{n_1^2 sin^2\,\theta - n_{sc}^2}} \quad (2.10)$$

n_c = refraction index of ATR crystal
n_s = refraction index of sample

The significant solvent absorption is reduced when the path length is decreased. The incident IR beam goes within the sample (transmitted) when the incident angle is lower than the critical angle $\theta_i < \theta_c$. FTIR spectrometers have a simple collection method of data which could frequently be through used. When the electrode potential is ramped between two potentials of E_{ref}, background potential at which no reaction occurs and E_i, adsorption potential of given species, the resulting spectra is demonstrated as reflectance [174] :

$$\Delta R/R = (R_{E_i} - R_{E_{ref}})/R_{E_{ref}}) \quad (2.11)$$

Or absorbance A [182]

$$A = \log(R_{E_{ref}}/R_{E_i}) \quad (2.12)$$

Where the variance between the reflectance R of two single beams at E_{ref} and E_i is correlated to reflectance at E_i. Infrared bands which are positive-going indicate a rise of the related molecules at E_i relative to the reference potential (E_{ref}). In contrast, depletion of molecules is indicated at negative-going IR bands. The aim of calculating this variance (normalized) spectra is for obtaining spectra of intermediates attached to the surface.

2.7.3 Surface-Enhanced Infrared Spectroscopy (SEIRAS)

The intensity of the infrared absorption on the thin-layer film of metals can be increased significantly between 10 -1000 times compared to the traditional infrared methods in Surface-Enhanced Infrared Spectroscopy (SEIRAS). The phenomenon is commonly discussed for surface enhancement in Raman spectroscopy (SERS) which is focused on a similar approach [4]. It was employed firstly by using Raman spectroscopy through investigation of pyridine adsorption on Ag electrodes by Fleischmann et al [183]. Hartstein et al. [184] extended this for IR spectra in the Kretschmann-ATR configuration, subsequently termed surface-enhanced infrared absorption in 1980, and progressed experimentally and theoretically by many authors [185 - 189]. Osawa et al. pioneered the SEIRAS technique application to electrochemical interfaces [190, 191].

The impact of an enhanced IR intensity was detected and manipulated in the geometry of the internal reflection element for example, Ag surface [185, 192 - 195], Au electrode surface [192, 196 - 198] and metals of Pt-Group [198, 111] and also in case of element morphology in external reflection like Ag surface [199] and Pt electrode [200, 201].

The surface enhancement mechanism in SEIRAS is assumed to include two parts: an electromagnetic and chemical mechanism which are similar to the surface-enhanced Raman spectroscopy (SERS) mechanism [186, 191, 202 - 205].

The electromagnetic mechanism arises from the excitation of surface- plasmon resonance in the electrode metal surface by electromagnetic field associated with incident IR beam [202, 206]. This mechanism greatly relies on surface morphology (size and shape), mostly small size of the metal islands show greater enhancement than the bigger one [202, 203, 207, 208]. Whereas in the context of chemical impact, it is linked to charge transfer through adsorption, wherein some particular cases a given IR band can be enhanced through the vibrionic coupling of vibrational modes with the transfer of charge across the surface of the metal and adsorbate[191, 206]. The kind of adsorption of species affects the vibronic intensity where the intensity of chemisorbed species is more significant than physisorbed ones [203, 209]. The adsorbed molecules are aligned in case of chemisorption, and consequently, a significant intensity is obtained when the dipoles of molecules are aligned parallel to the surface normal [203].

2.7.4 Principle of FTIR

The FTIR approach is commonly employed in different areas of science, in the industry as well as in other purposes for efficient and systematic structural examinations of chemical substances, electrode solution interface and observation of processes [182, 210, 211]. In the early 1980s, the FTIR technique has been employed to investigate electrochemical surface processes. FTIR spectroscopy provides characteristic advantages. The capability of FTIR to evaluate spectra with the significant signal to noise ratio is one of the key advantages with respect to dispersive IR spectrometers. Also, it experiences a wavenumber precision of ± 0.01 cm^{-1} (reproducibility) and multiplex advantage where the addition of more scans together is such way to improve the signal to noise ratio of the measured spectrum (S/N α $\sqrt{N}$, where N is the number of spectra) [212]. The advancement of the Fourier Transform (FT) techniques diminished acquisition time considerably.

The optical device is the heart of the FTIR spectrometer and is called an interferometer. The interferometer consists of two mirrors one of which is placed at a fixed position, and the other is movable. It splits the single light beam into two light beams and then the two light beam move in various paths (D_1 and D_2), and after this journey of traveling, the two light beams recollect into one beam and finally leaves the interferometer as shown in **Figure 2.9**.

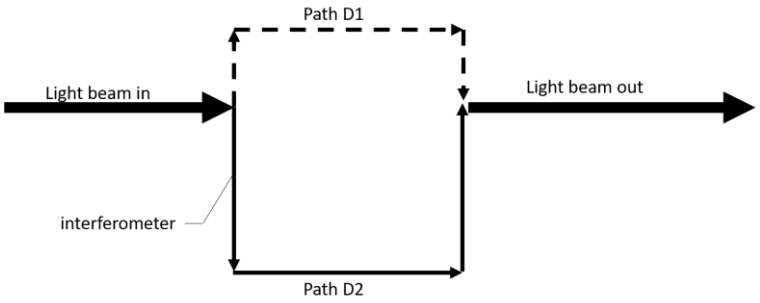

Figure 2.9: A simplified scheme of an interferometer.

There is a variety of interferometer configurations employed in FTIR measurements, but Michelson one is the outdared and most common type [213, 214]. An optical system titled a beam splitter is at the core of the interferometer. A beam splitter is constructed to transfer some of the incident light, and another part of the incident light is reflected. The light emitted by the splitter goes to the stationary mirror, and the reflected light is sent to the movable mirror, as seen in **Figure 2.10**. The light beams drive back to the beam splitter where they are reconstituted into a single light beam that exits the interferometer, interferes with the analyte, and hits the detector.

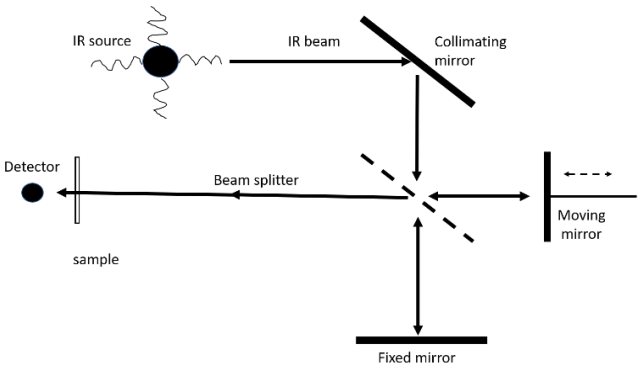

Figure 2.10: A scheme of Michelson interferometer [213].

2.7.5 Setup of FTIR electrochemical cell

A designed in situ electrochemical cell setup scheme for FTIR measurements built in this research is provided in **Figure 2.11** [215]. The cell of FTIR measurements constructed from glass consists of three compartments for working, counter and reference electrodes. The hemispherical prism in frame) acts as the cell window with the thin layer of the substrate. The window material of the prism should have distinctive features such as being IR transparent and having broad reflective indices like Si. The IR beam generating from the source is reflected through a mirror which has a smooth gold layer under an angle of 30° with respect to the optical axis of the system or 75° with respect to the surface normal of the mirror. The resulting incident

angle of the reflected IR beam on Si prism with respect to the surface normal is 60 ° which leads to total reflection. Finally, the IR beam transferred from the Si prism is reflected by the second mirror and directed to the detector. The cell design and thin gold film preparation were described in detail in reference [185, 193, 215].

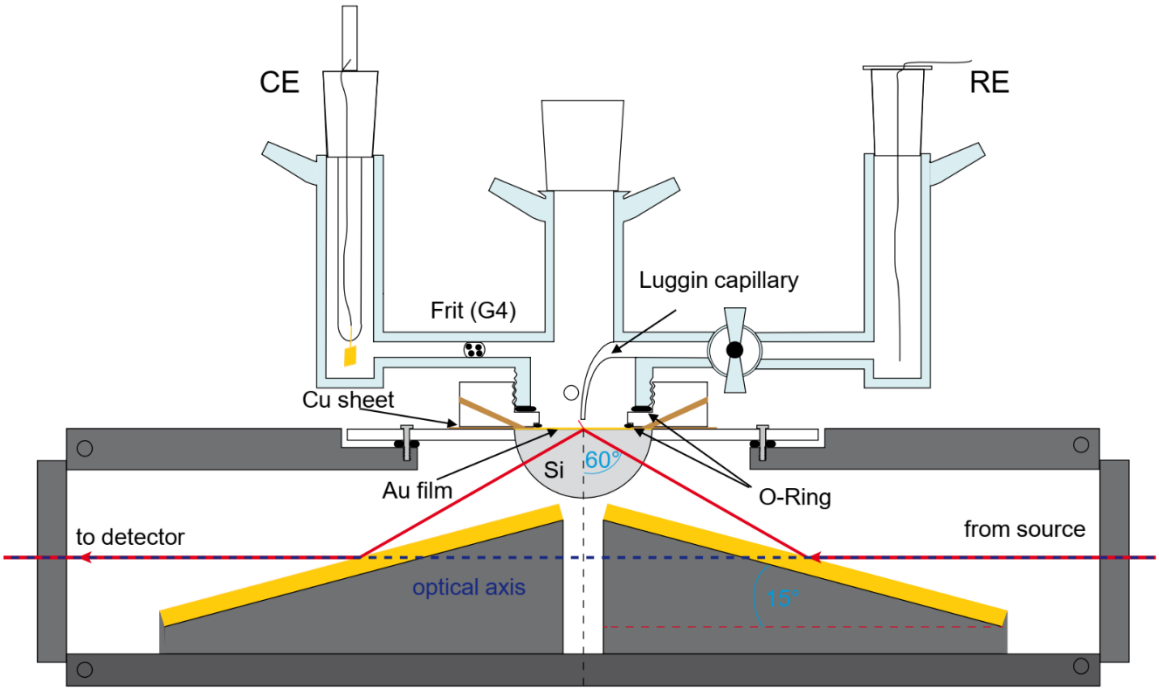

Figure 2.11: A sketch of the custom- made in situ electrochemical cell setup for FTIR measurements [215].

Chapter three:

Iodide adsorption at Au(111) electrode in non-aqueous electrolyte:AC-voltammetry and EIS studies

A. S. Shatla [a,b], A. A. Abd-El-Latif [a,c], S. Ayata [d], D. Demir [d] and H. Baltruschat [a]

[a] Institut für Physical and Theoretical Chemistry, Bonn University, Römerstraße 164, D-53117 Bonn, Germany.
[b] Permanent address: Menoufia University, Faculty of Science, Chemistry Dept., Shebin Elkoom, Egypt.
[c] Permanent address: National Research Centre, Physical Chemistry Dept., El-Bohouth St. Dokki, 12311 Cairo, Egypt.
[d] Permanent address: Dokuz Eylul University, Faculty of Science, Chemistry Dept., İzmir, Turkey.

Received: August 26, 2019
Published online: December 27, 2019

Reprinted (adapted) with permission from
A. S. Shatla, A. A. Abd-El-Latif, S. Ayata, D. Demir and H. Baltruschat, Electrochim. Acta **2020**, 334, 135556.
 DOI: 10.1016/j.electacta.2019.135556

Acknowledgments

Financial support by the German Federal Ministry of Education and Research (BMBF) of the "LuCaMag" project (Fkz: 03EK3051A) under the framework of "Vom Material zur Innovation" program is acknowledged. A. S. S. wishes to thank MoHE (Egypt).

3.1 Abstract

The adsorption/desorption of iodide ions on the Au (111) single crystal plane in propylene carbonate has been investigated by cyclic voltammetry, AC-voltammetry, and electrochemical impedance spectroscopy for various electrolyte compositions. In non-aqueous electrolyte (propylene carbonate), two broad reversible peaks are present in the cyclic voltammetry due to the adsorption/desorption of iodide at the electrode surface; they are broader than in the corresponding aqueous electrolyte. AC voltammetry shows sharp peaks of the iodide adsorption/desorption process at the same potential. Similar to the aqueous solution, the adsorption charge is in the range of 80 μC cm^{-2} and thus corresponds to a complete monolayer. The rate of iodide adsorption increases with iodide concentration in the solution as expected for a simple charge transfer. When hexafluorophosphate(PF_6^-) is the anion in the supporting electrolyte, the rate is also larger than when it is perchlorate (ClO_4^-). When the cation is changed, the rate also decreases (the adsorption resistance increases) by more than an order of magnitude in the sequence $K^+ > Na^+ > Li^+ > TBA^+$ and, thus, in the same sequence as the radii of the solvated ions.

3.2 Introduction

Within the context of research on high energy density storage systems, in particular, lithium-air batteries and supercapacitors, a new interest in fundamental research on the interface between a metal (or carbon) electrode and non-aqueous electrolytes is arising. In particular, for the oxygen reduction and evolution in an aprotic electrolyte, the importance not only of the solvent but also of the electrode material and its surface structure have been demonstrated [216, 217, 218]. This led to a merging of battery research with electrocatalytic and interfacial electrochemical research.

Organic solvents have important electrochemical applications: in metal-ion and metal-air batteries, in the electrodeposition of metals, alloys, and semiconductors, and in the electro-synthesis of organic compounds and polymers. Electrochemists are interested in non-aqueous electrolytes because of the wide range of potentials that can be reached before solvent decomposition occurs as compared to aqueous systems [219, 220]. Many of these applications depend on charge transfer across the electrode/electrolyte interface. The structure and properties of the electric double layer determine the rate and mechanism of the charge transfer and thus are key factors for controlling electrochemical reactions.

On the other hand, studies of the interface between a metal and organic electrolyte have a long tradition. Often, such studies have been done using mercury, because its surface can be continuously regenerated during an experiment and thus is less prone to contaminants. In addition, direct measurements of the surface tension can be used for the thermodynamic determination of

adsorbate coverages. Most of the thermodynamic relationships that relate to interfacial surface tension and capacity of the electrode and even the composition of the double layer were, therefore, developed and experimentally verified for mercury electrodes, both in aqueous and non-aqueous electrolytes. Surface excesses of halogenides in aqueous solution were determined from surface tension measurement of mercury electrodes [221]. The adsorption of halogenides on a mercury electrode in an acetonitrile electrolyte was studied by Schirmer and Baumgärtel [222].

Huge progress in the studies of the interfacial electrochemistry of metal surfaces has been accomplished in aqueous electrolytes when it was shown, that clean electrochemistry was possible even using single-crystal electrodes of Au [223] or Pt [224]. Adsorption processes of halides at gold single crystals were studied by capacitance measurements using AC-voltammetry [225 - 228]. A complete thermodynamic analysis of iodide adsorption at gold single crystal electrodes has been done using chronocoulometry. It was found that at low charge densities and coverages, the bond polarity is determined by the ability of free electrons to screen the dipole formed by the adsorbed anion but at high charge densities and coverages, the chemisorption bond has a predominantly covalent character [229, 230].

Halogenide adsorbate layers were also characterized ex-situ (e.g. in UHV [231 - 233] or in-situ by STM [234 - 236]. X-ray scattering was used to investigate the structure of well-ordered monolayers of iodide, which changes from a ($\sqrt{3}\ x\ \sqrt{3}$) over a ($p\ x\ \sqrt{3}$) to a rotated-hexagonal phase [237, 238]. In these studies, the use of halogenide ions as adsorbates certainly helped in maintaining the surface clean. Therefore, in our current work in non-aqueous electrolytes, we also started studying the adsorption of iodide, in particular, the rate of adsorption.

Besides, ‘simple’ outer sphere electron transfer adsorption reactions are conceptually the simplest charge transfer reactions consisting of only one reaction step. Similar to its analogue, the adsorption of hydrogen from protic electrolytes, the adsorption of I^- is a prototype for such a reaction [34]:

$$I^- \rightarrow I_{ad} + e^-$$

Corresponding reaction rates can be studied by electrochemical impedance spectrometry (EIS). Whereas the adsorption of hydrogen from acidic solutions on Pt is extremely fast, depending on the surface orientation [239 - 244], its adsorption rate in alkaline solutions is readily accessible by EIS [239, 242]. The adsorption rate of iodide, as well as that of other anions, is extremely fast and hardly measurable at Pt(111) [239, 242, 245] and Bi(001) [246], but also readily accessible on Au(111)[247, 248].

To our knowledge, there are few double-layer studies on massive electrodes in aprotic electrolytes. The pzc of polycrystalline gold in propylene carbonate (conventional electrolyte in Li-ion batteries) containing 0.1M $NaClO_4$ has been determined by Van Huong [219]. The effect of the Au monocrystalline surface structure on the pzc has been reported in propylene carbonate using electroreflection spectroscopy [249]. Halide adsorption on polycrystalline Ag electrodes was studied using impedance by Falciola et al. [250].

As far as it concerns fundamental studies on the double layer on single crystalline electrodes, there recently seem to be much more studies for ionic liquids than for other aprotic systems, e.g. [251 - 255]. Thus, the adsorption of iodide was studied on Bi(111) from ionic liquids [256, 257].

The goal of the present manuscript is the systematic investigation of the anion adsorption (iodide) from a non-aqueous electrolyte (propylene carbonate) at Au-electrodes (low index Au(111) single crystal). The effect of anions, cations and iodide ion concentration will be studied in detail. Different electrochemical techniques are used in this study such as cyclic voltammetry combined with AC-voltammetry and electrochemical impedance spectroscopy (EIS). The AC voltammetry and the Electrochemical Impedance Spectroscopy (EIS) can give a deeper understanding of the electrochemical processes and electrode/electrolyte interface because these techniques can differentiate much better between capacitive and faradaic currents.

3.3 Experimental

3.3.1 Chemicals, materials, and electrolyte

The chemicals used in this work are potassium iodide (KI, ≥ 99.5%, MERCK), potassium hydroxide (KOH, ≥ 99.98%, ACROS), potassium perchlorate ($KClO_4$, ≥ 99%, SIGMA-ALDRICH), potassium hexafluorophosphate (KPF_6, ≥ 99%, ACROS), lithium perchlorate ($LiClO_4$, ≥ 99%, SIGMA-ALDRICH), lithium hexafluorophosphate ($LiPF_6$, ≥ 99%, SIGMA-ALDRICH), lithium iodide (LiI, ≥ 99%, SIGMA-ALDRICH), tetrabutyl ammonium perchlorate (TBAP, ≥ 99%, SIGMA-ALDRICH), silver nitrate ($AgNO_3$, ≥ 99%, SIGMA-ALDRICH), H_2SO_4 spectra pure grade (Merck), propylene carbonate (PC, 99.7%, SIGMA-ALDRICH) and acetonitrile (ACN, 99.8%, ACROS). All aqueous solutions were prepared with 18.2 MΩ·cm Milli-Q Millipore water. The electrolytes were deaerated with highly pure argon (99.999%, AIR LIQUIDE).

Glassware, Teflon and "PCTFE" parts are cleaned by 5 M potassium hydroxide to remove organic contamination. In addition, inorganic impurities are removed by immersion in a chromic acid bath.

The Au(111) single crystal (ϕ =10 mm) electrode was cleaned electrochemically before flame annealing by sweeping the potential between 0.03-1.8 V vs. RHE in 0.1 M H_2SO_4 solution at

50 mV s^{-1}. Sometimes a high potential (10 V between the Au electrode and a counter electrode) had to be applied for a few seconds to form an oxide film [20] at the electrode surface which was dissolved afterward in concentrated HCl.

The single-crystal electrode surfaces were prepared according to Clavilier's method by flame annealing. Au(111) electrode was heated over a butane flame until it turned to a light pink colour (≈ 600 ^{o}C). Thereafter, the electrode was kept at that temperature for thirty seconds before being transferred into a glass cell, under Ar atmosphere to cool down for 4 min.

Using the hanging meniscus configuration of Au(111) in the supporting electrolyte (0.1M H_2SO_4), the quality of the preparation was checked by a cyclic voltammogram in the potential range of 0.03 to 1.2 V (cf. **Figure S3.1**). The potential should not exceed 1.2 V because of the electrode surface being oxidized and roughened at higher potentials.

A classical 3-compartment glass cell was used for the electrochemical measurements with the Au(111) crystal in the hanging meniscus configuration. A silver wire in 0.1 M $AgNO_3$ dissolved in ACN was used as the reference electrode and was connected to the working electrode compartment via a Luggin capillary and separated by a roughened stop cock. A reversible hydrogen electrode (RHE) was used as a reference electrode in aqueous electrolytes. A Pt disk of 1 cm diameter was used as a counter electrode and it was mounted in parallel to the working electrode and separated by a glass frit.

All these steps were repeated in non-aqueous electrolytes. Distinctly, the single crystal electrode was allowed to cool down in an Argon stream in the dry conventional H-cell and then quickly transferred to another cell containing the non-aqueous electrolyte. Water content has been measured using Karl Fischer titration and was around 35 ppm after the measurements, except for $NaClO_4$ in propylene carbonate where it was around 47 ppm.

3.3.2 Instruments and data evaluation

CV and AC voltammetry measurements were carried out using an EG&G potentiostat (model 273A) in combination with LabVIEW software (National Instruments GmbH, Munich, Germany) for recording cyclic voltammograms (CV).

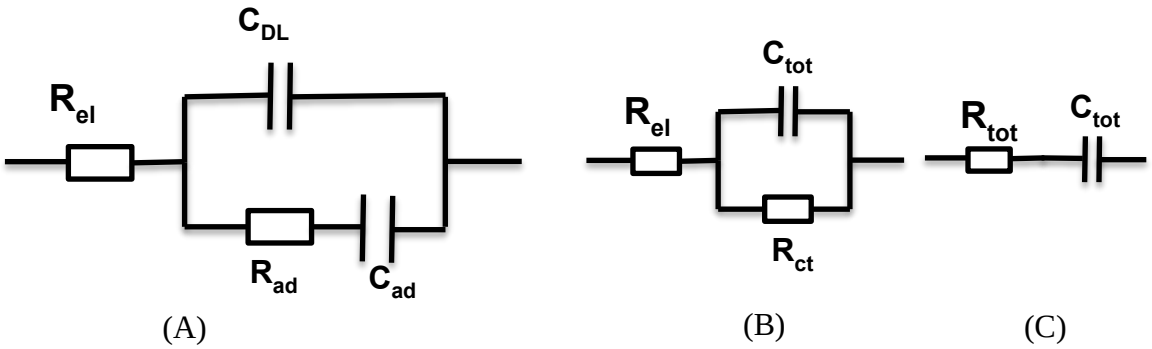

(A) (B) (C)

Figure 3.1: Equivalent circuits: (A) for the evaluation of the adsorption process from EIS data (B) for the evaluation of EIS data at potential limits (C) for the evaluation of the AC voltammetry.

All electrochemical impedance spectra measurements were carried out with an EG&G potentiostat (model 273) connected to a Solartron Impedance /Gain-Phase analyzer (Model SI 1260) in combination with LabVIEW software (National Instruments GmbH, Munich, Germany). A sine wave of 3 mV amplitude has been applied over a frequency of 100 kHz to 0.1 Hz. Zplot and Zview programs have been used for data collection and analysis using the equivalent circuit of **Figure 3.1A**. In the absence of specific adsorption R_{ad} and C_{ad} were omitted, and, in particular, close to the limits of the stability window of the electrolyte, replaced by R_{ct} (cf. **Figure 3.1B**). Although slightly better fits of the impedance data might have been obtained using additional elements in the equivalent circuit, we did not include those, because physically they would not make sense for the systems studied here. Deviations from ideal fits might e.g. be due to edge effects in the hanging meniscus arrangement. Impedance spectra were quite reproducible; also, subsequent measurements (without new crystal preparation) and cyclic voltammetry after recording the impedance spectra gave identical results to those immediately after single crystal preparation. Some scatter in the values of R_{ad} is due to differing positions of the electrode with respect to the Luggin capillary.

Impedance spectra were measured directly after a recording of the AC-voltammograms, starting with the lowest potential. The potential was then changed in anodic direction to a value, where the next impedance measurement was performed. After the measurement at the most positive potential, the potential was sequentially changed stepwise in cathodic direction for further impedance measurements. Before each impedance measurement, the potential was held constant for 1 minute. Impedance measurements recorded directly after each other at constant potential gave identical results.

In AC-voltammetry measurements, the resulting complex AC current was measured by a Lock-in amplifier (EG&G, model 5210). At sufficiently low frequencies, such as the 10 Hz used here for AC-voltammetry, the equivalent circuit of **Figure 3.1A** can be simplified to that of **Figure**

3.1C. Here, R_{tot} is the sum of R_{el} + R_{ad} and the capacitance C_{tot} represents the sum of double-layer and adsorption capacitance (C_{DL} + C_{ad}). (The parallel resistance R_{ct} (**Figure 3.1B**) only plays a role close to the stability limit of the electrolyte.)

The AC frequency for AC voltammetry should be low enough that the capacitance largely determines the overall impedance. In particular, it should be so low that its impedance is large compared to any adsorption resistance; see below. 10 Hz proved to be best for the systems shown here. The time constant settings were 300 ms and amplitude u_{ac}^{0} was 3 mV. The capacitance $C_{tot}(E)$ was calculated from the imaginary part of the complex impedance $Z(E) = u_{ac}/i_{ac}(E)$.

For a better comparison of the cyclic voltammetric currents with the capacitance determined by AC voltammetry or impedance spectrometry, the former was converted to capacitance values using C= j/v. Capacitance data obtained during variation of the potential in the negative direction are plotted in the negative direction of the y-axis, thus maintaining the shape of the CV.

3.4 Results

3.4.1 Adsorption of iodide in aqueous (KOH) on Au (111) pH 11

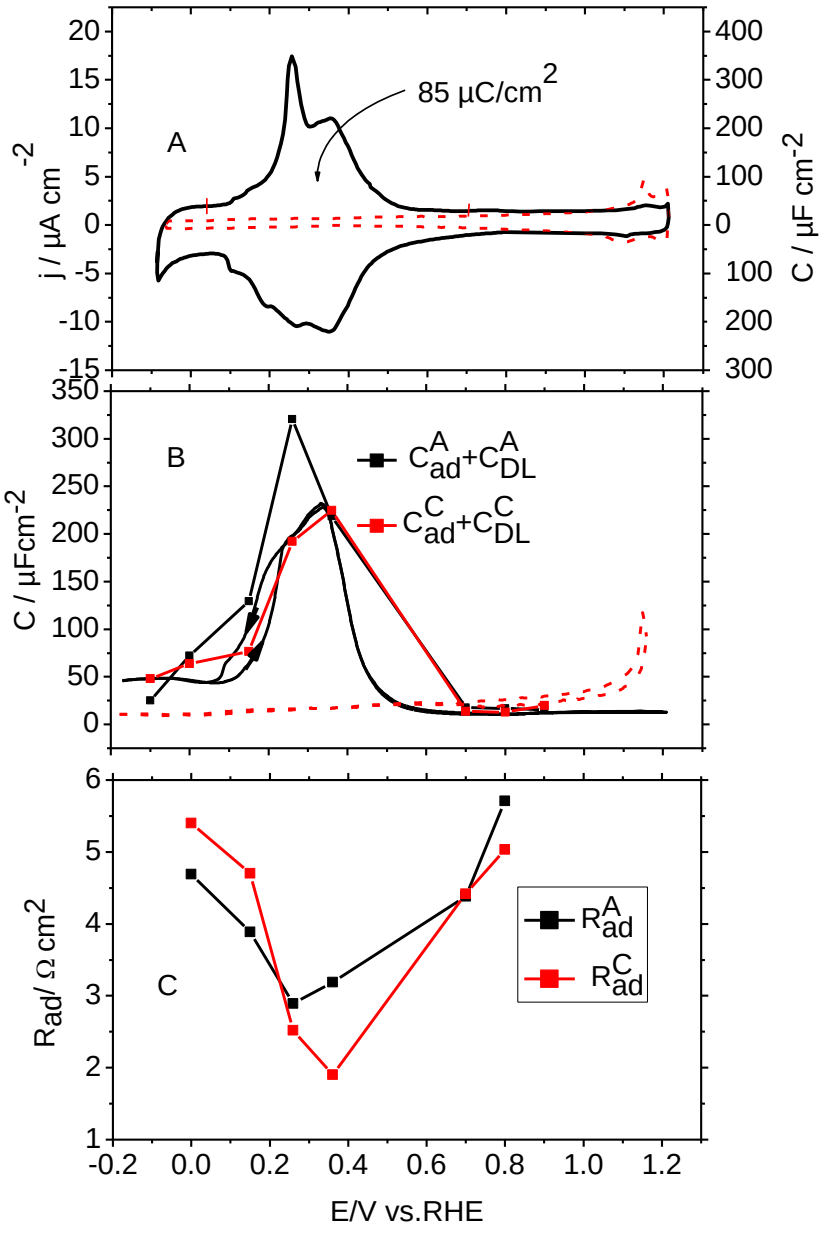

Figure 3.2: (A) CVs recorded at a Au(111) in 0.45 M KPF_6 + 1mM KOH (dashed line) and 0.45 M KPF_6 + 10 mM KI (PH 11) solutions (solid line) at a sweep rate of 50 mV s^{-1}. Right axis: current density converted into capacity; (B) (Solid line) Differential capacitances determined using an AC perturbation of 10 Hz frequency, 3 mV r.m.s. the amplitude at a sweep rate of 10 mV s^{-1} and (■) the sum of capacitances C_{ad} + C_{DL} (as measured by impedance spectroscopy); (C) potential dependence of adsorption resistance. All straight lines serve as a guide to the eye only. Black symbols represent data obtained after potential variation in anodic direction; red symbols those in cathodic direction.

For comparative purposes, the adsorption of iodide was first studied in aqueous electrolyte. In order to shift the potential window to values where iodide desorption is occurring, alkaline electrolyte had to be used. The electrode surface was characterized by cyclic voltammetry. The cyclic voltammogram for Au(111) in 10 mM KI + 0.45 M KPF_6, pH 11 is shown in **Figure 3.2A** together with that in the supporting electrolyte. It agrees with that reported in the literature [230, 258].

The small peak at the potential of 1.15 V in the positive potential scan in the supporting electrolyte in **Figure 3.2A** is due to the adsorption of hydroxyl ions (OH^-) at the Au (111) surface [230]. Upon addition of KI to the solution, three peaks are observed: The one at E ≈ 0.25 V (RHE), appearing only in the anodic sweep, is related to the iodide-induced lifting of the (1×23) reconstruction of the Au (111) surface [238, 259 - 261]. The second one is reversible and situated at 0.35 V (RHE); it reflects the formation of a regular $(p \times \sqrt{3})$ iodide adlayer. The last one near 1.14 V (RHE) is weak and related to the phase transition between the $(p \times \sqrt{3})$ and the rotated hexagonal structure of the iodide adlayer. The corresponding coverages between 0.36 and 0.41 (for the $(p \times \sqrt{3})$ phase), corresponding to adsorption charges between 80 and 90 µC cm^{-2}, and 0.41 to 0.44 (for the rot.hex. structure) [238] , corresponding to 90 to 98 µC cm^{-2}, agree with our experimental value of 85 µC cm^{-2} (without background subtraction). Here, the charge values were calculated by multiplying the coverage with the theoretical charge of 1 electron per surface Au atom (223 µC cm^{-2} = electron charge x number of surface Au atoms per cm^2). The lifting of the reconstruction is similar to that observed in the much more often studied Au(111)/ H_2SO_4 system (also cf. **Figure S3.1**). The reconstructed surface is usually slowly re-established at about 100 mV more negative potential.

The differential capacitance curve shown in **Figure 3.2B** (shown together with capacitance data from impedance spectra, see below) agrees with the shape of the CV. The peaks related to the lifting of the reconstruction are less clear in the capacitance curves than in the CV because of the slow kinetics of the surface reconstruction. The difference between potentials at which reconstruction is lifted and re-established leads to the hysteresis in the capacitance curve.

The adsorption of iodide in aqueous solution was confirmed by electrochemical impedance spectroscopy measurements under the same conditions.

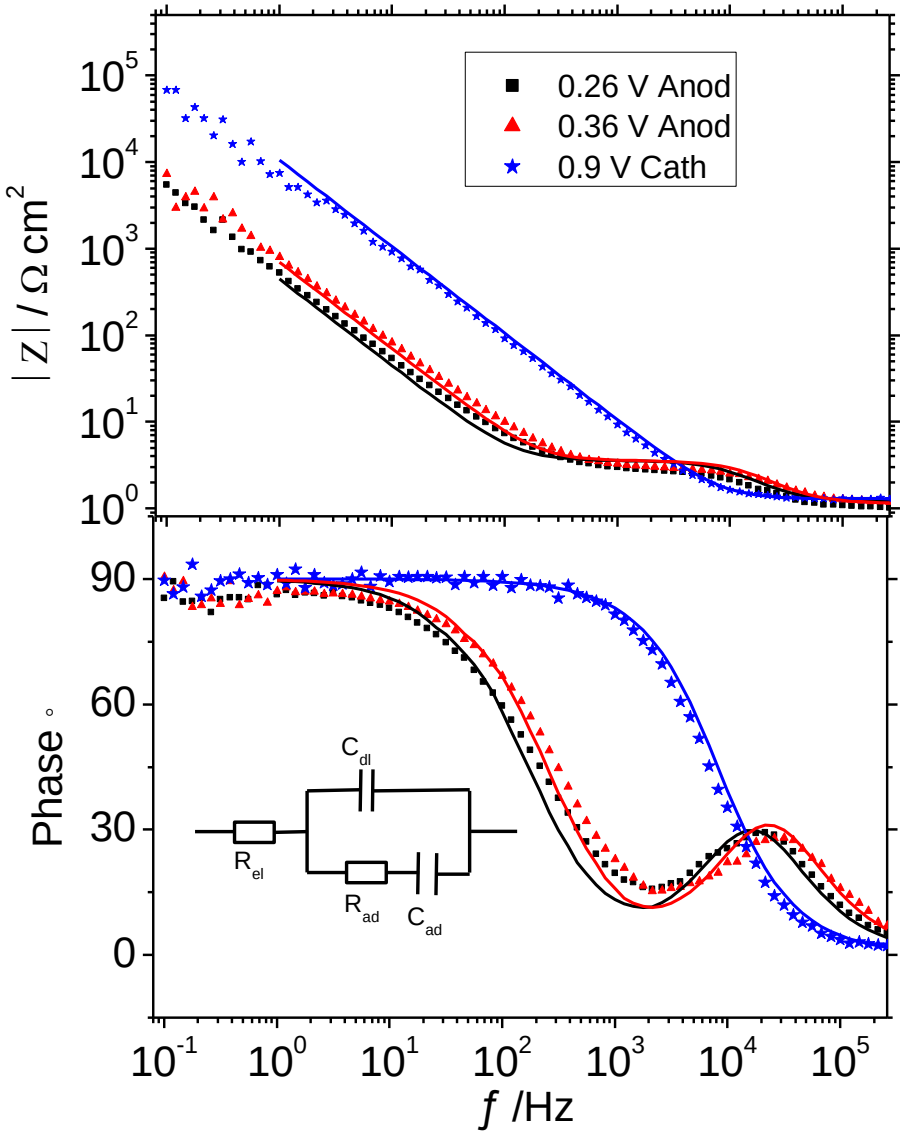

Figure 3.3: Examples for impedance spectra of the Au (111) disk electrode at the indicated potentials in 10 mM KI with 0.45 M KPF_6 in 1 mM KOH solution, the lines are the fitting curves. The inset shows the equivalent circuit employed for the fitting of the impedance curves. R_{el}: electrolyte resistance; C_{DL}: double-layer capacitance; R_{ad}: adsorption resistance; C_{ad}: adsorption capacitance. (Surface area (A) =0.785 cm^2).

Table 3.1: The fitting data for EIS on Au(111) for 0.45 M KPF_6 + 10 mM KI (pH 11) solution using the equivalent circuit of **Figure 3.1A**. When there was no indication for an adsorption process, R_{ad} and C_{ad} were omitted.

Potential /V vs. RHE	**R_{el} / (Ω cm^2)**	**C_{DL} / (μF cm^{-2})**	**R_{ad} / (Ω cm^2)**	**C_{ad} / (μF cm^{-2})**
-0.1 anodic	1.4	26.5		
0	1	2.1	4.7	73.6
0.15	1.1	2.7	3.9	128.4
0.26	1.2	3.9	2.9	318
0.36	1.2	2.9	3.2	216
0.7	1	4.2	4.4	16.3
0,8	1	3.6	5.7	15
0.9	2.7	10.2		
0.9 cathodic	1.3	21.3		
0.8	1	3.2	5	11.2
0.7	1.3	2.8	4.4	12.2
0.36	1.4	2.6	1.9	224
0.26	1.5	2.7	2.5	191
0.15	1.5	1.6	4.7	74.6
0	1.2	1.7	5.4	63
-0.1	1.2	48		

Figure 3.3 shows typical impedance spectra obtained in the potential regions of iodide adsorption. For E = 0.9 V, the spectra can be fitted well by an equivalent circuit consisting of the double-layer capacity C_{DL} in series with the solution resistance R_{el} (RC model). For E = 0.26 and 0.36 V in anodic and cathodic directions, the spectra agree well with that expected for an adsorption process; they can be fitted with the corresponding equivalent circuit (the electrolyte resistance (R_{el}) in series with a parallel combination of the double-layer capacitance (C_{DL}) and the adsorption resistance (R_{ad}) in series with adsorption capacitance (C_{ad}), (cf. **Figure 3.1A**). Small variations of

the electrolyte resistance are caused by the slightly changing meniscus from measurement to measurement. It is also obvious that the adsorption resistance determines the total impedance between 1 kHz and 10 kHz, but is negligible at 10 Hz at which frequency the AC measurements are performed. From the data given by Kerner et al. [248], a minimum adsorption resistance of about 3 Ω cm^2 is estimated for Au(111) in a solution of 1 mM KI in 0.1 M $KClO_4$, which is comparable to our minimum value of about 2 Ω cm^2, although the effect of the different electrolyte concentration is unclear at this point.

Astonishing is the very small double layer capacitance of a few µF cm^{-2} at potentials, where iodide adsorption takes place (cf. **Table 3.1**). This had been observed before already for Pt(111) in iodide solutions [242]. Whereas for a complete layer of iodide one might expect a decreased (DL) capacitance because the iodide acts as an insulating layer (12 µF cm^{-2} at 0.9 V vs. ca. 30 µF cm^{-2} at – 0.1 V), the low (DL) capacitance for partial iodide coverages is hard to understand and deserves further attention. Given the ideal shape of the impedance spectra and the clearly different time constants, an artifact due to non-optimal fit seems highly improbable. In particular, a fit with a fixed, assumed value for C_{DL} of 20 µF cm^{-2} results in a shift of the corresponding peak in the phase (now at around 20 kHz) to unreasonably low values not consistent with the experimental data.

Figure 3.2B and **3.2C** show the potential dependence of adsorption capacitance and adsorption resistance. As expected [242], the adsorption resistance has its minimum (around 2 Ω cm^2) where the adsorption capacitance is largest. Thus, the adsorption rate is fast, similar to the case of iodide adsorption on a Pt electrode [239]. Values determined during a potential change in anodic direction differ from those obtained during the potential variation in cathodic direction. The reason is the reconstruction of the Au(111) surface, which is lifted at more anodic potentials than being re-established. Remarkable is the agreement of the total capacitance determined by EIS in anodic direction with that calculated from CV (cf. right axis of **Figure 3.2A**) at the potential of the anodic peaks. The same is true for the capacitance data determined by EIS in cathodic direction and the cathodic CV. Particularly at the peak corresponding to the lifting of the reconstruction at 0.26 V in anodic direction, the capacitance from AC voltammetry is lower because the frequency of 10 Hz is too high in this case. Certainly, the iodide desorption/ adsorption process is connected to the reconstruction and its lifting.

3.4.2 Adsorption of iodide at Au (111) in propylene carbonate and the effect of iodide concentration

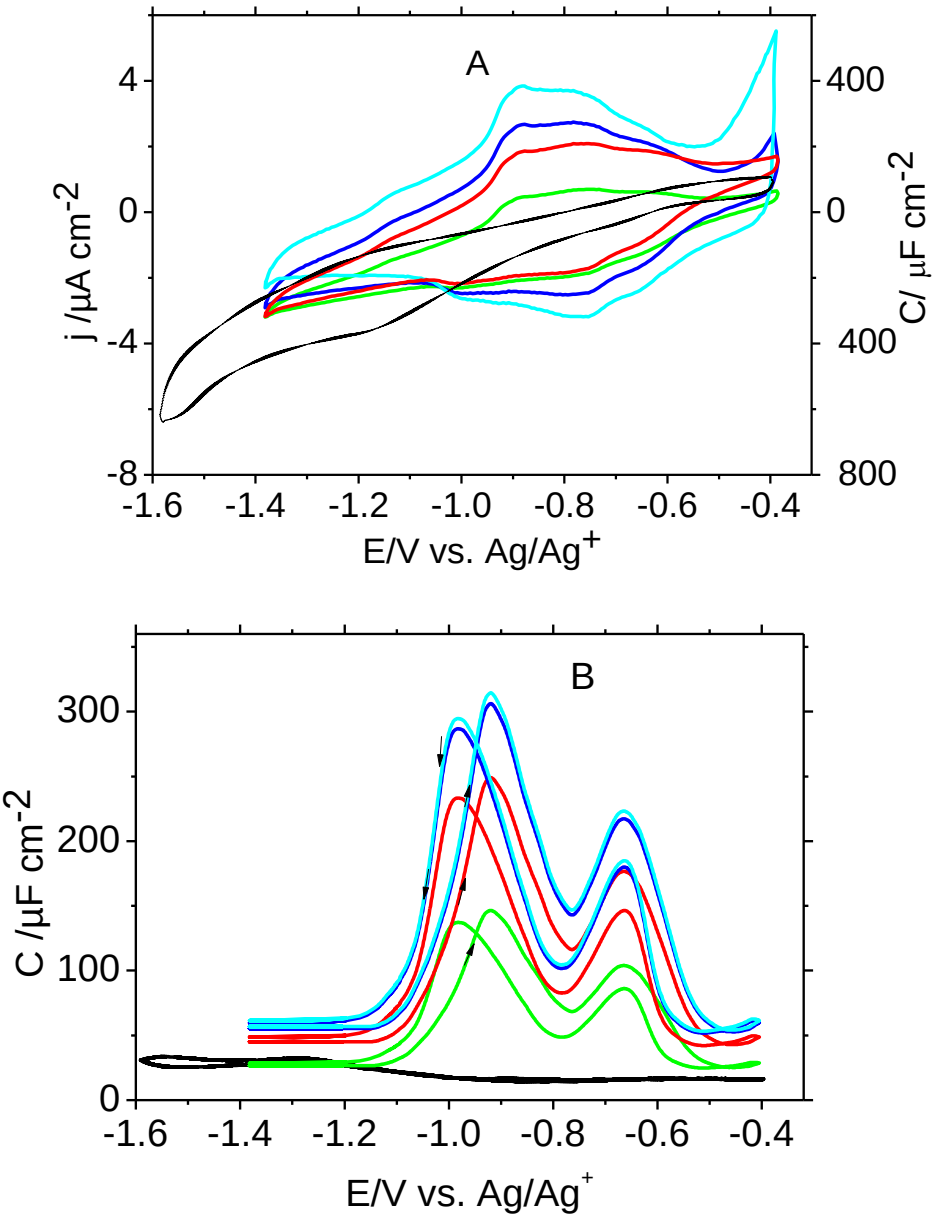

Figure 3.4: (A) Cyclic voltammograms at a sweep rate of 10 mV s^{-1} for Au(111) in propylene carbonate + 0.5 M KPF_6 for different concentrations of KI: (—) 0.0, (—)1.0, (—) 10, (—)50, and (—)100 mM, for comparison, the right scale gives the corresponding capacitance calculated according to C= j/v; (B) capacitance - potential curves determined using an AC perturbation of 10 Hz frequency, 3 mV r.m.s. amplitude at a sweep rate of 10 mV s^{-1}.

Figure 3.4A displays cyclic voltogramms for different concentrations of KI. No peak is observed in the absence of iodide (black curve). The tilted background corresponding to a parallel resistance of about 300 kΩ cm^2 has been observed in the literature and is probably due to the

reduction of impurities in the organic electrolyte [262, 263]. With increasing concentration, an increase in the peak current is observed in both anodic and cathodic direction. These peaks can be interpreted as adsorption and desorption of iodide. (The anodic current around -0.4 V may be related to oxidation of highly concentrated iodide.)

These adsorption peaks resemble those in the aqueous electrolytes, although they are much broader. Because of the similarity, we assume that in the anodic going sweep, the peak around -1.05 V corresponds to the lifting of the reconstruction, the broad peak between - 1.0 and - 0.6 V to the completion of iodide adsorption. The total adsorption charge (between -1.1 and -0.5 V) increases with iodide concentration (40, 73, 82 and 89 μC cm^{-2}, resp.); for the highest iodide concentration, it, therefore, is close to that expected for a closed packed iodide layer with a coverage of 0.44 (adsorption charge of 98 μC cm^{-2} for a one-electron transfer) [230, 264]. An examination of the influence of the scan rate on adsorption of iodide at Au (111) in propylene carbonate shows a linear dependence of the peak currents on the sweep rate as expected for an adsorption process and no dependence of the peak potential on scan rate, (cf. **Figure S3.2** in the supplementary information (SI)). Only at the highest sweep rate, the peaks in the cathodic sweep merge.

Capacitance curves are shown in **Figure 3.4B**. The variations of the peak height and also of the total charge are similar to those observed in cyclic voltammetry. Their decrease with decreasing iodide concentration is similar to the results reported by Trasatti and coworkers [250] for halogenides on polycrystalline Ag in aprotic solvents. As we will discuss below, this is not due to the slow adsorption. Obviously, for very low iodide concentrations, full iodide coverage is not achieved. Astonishingly, a change of concentration does not lead to a clear shift of the peak potentials, as e.g., in the case of sulfate adsorption on Pt(111) or bromide on Ag(111), where a change of the concentration leads to a peak shift of ca. 60 mV/decade, as expected from the Nernst equation and an electrosorption valency of one [228, 265]. A complete thermodynamic analysis would help in elucidating possible reasons for this behaviour.

The specific capacitance shows a good agreement between the data determined by AC voltammetry and cyclic voltammetry (**Figure 3.4B**). Two sharp pseudo-capacitive peaks at - 0.93 and - 0.65 V (in anodic direction) correspond to the broad peaks in cyclic voltammetry. As for the aqueous system, the peak potentials of anodic and cathodic peak agree much better for the more positive one (iodide adsorption) than for the more negative one, which is due to reconstruction. The charge in the differential capacitance curve from -1.2 V to - 0.5 V for the different concentrations of KI in anodic direction was found to be 36, 62, 72 and 81 μC cm^{-2}. These values are similar to those calculated from cyclic voltammetry.

The effect of concentration of KI on iodide adsorption on Au (111) was confirmed by electrochemical impedance spectroscopy measurements (cf. **Figure 3.5**). As before in the aqueous electrolyte, spectra obtained in the potential range of the peaks are well fitted using the typical equivalent circuit for adsorption processes (shown in **Figure 3.1A**), spectra obtained outside of this region are fitted by a series of capacitance (C_{tot}) and the electrolyte resistance, paralleled by a large resistance R_{ct} representing the electrolyte decomposition at the limits of the potential window (cf. **Figure 3.1B**). The large parallel resistance in the range of several hundred $k\Omega \cdot cm^2$ which is responsible for the tilted background in the CV curves, would only show up at frequencies below 10^{-2} Hz.

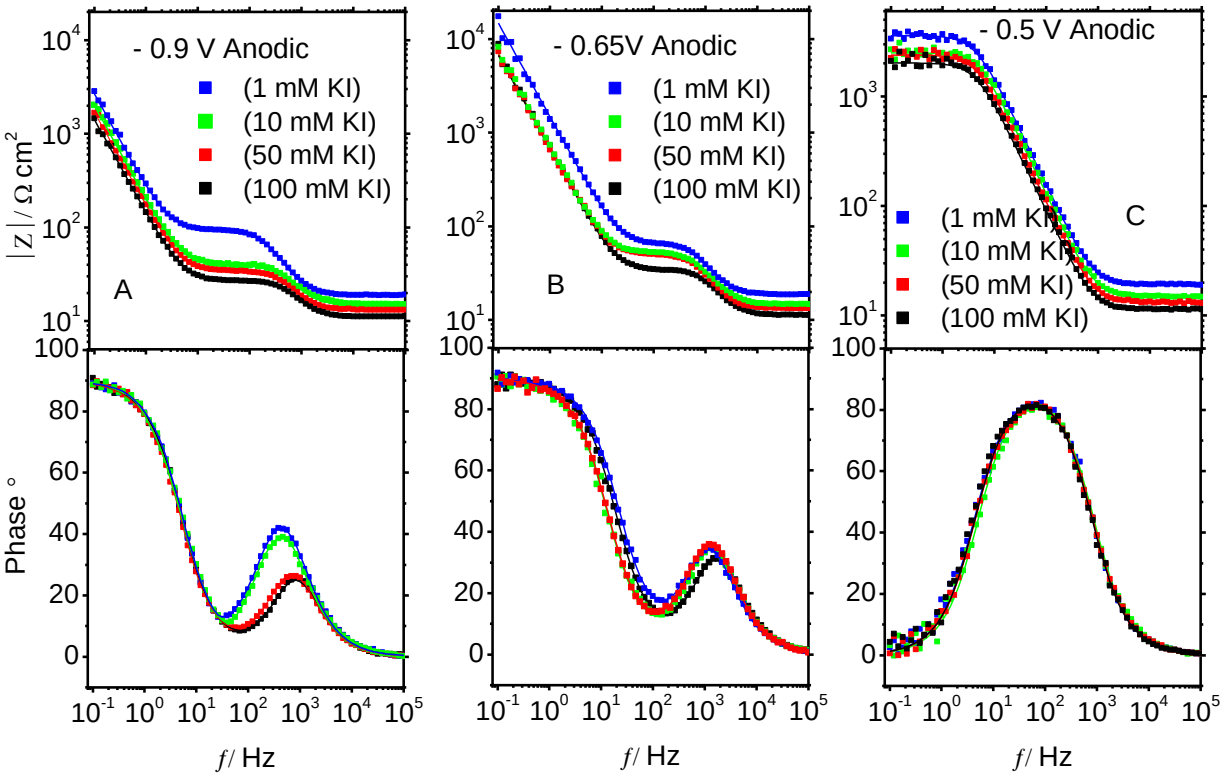

Figure 3.5: Impedance plots for the iodide desorption process on Au (111) in different concentrations of 1, 10, 50 and 100 mM KI with 0.5 M KPF_6 in propylene carbonate, recorded at (A) peaks of adsorption potentials at -0.9 V, (B) peak potential of -0.65 V in anodic direction and (C) -0.5 V in the anodic direction where there are no adsorption-peaks. The curves of the measured spectrum are shown by symbols. The fitting curves are shown as a full line.

Table 3.2: The fitting data for EIS on Au(111) using equivalent circuit 2R and 2C model and RCR model for different concentrations of KI with 0.5 M KPF_6 in propylene carbonate.

Concentration @ -0.9 V anodic	**R_{el} / (Ω cm^2)**	**C_{DL} / (μF cm^{-2})**	**R_{ad} / (Ω cm^2)**	**C_{ad} / (μF cm^{-2})**	**C_{ad} /(μF cm^{-2}) From AC voltammetry**
1 mM	19	10.7	77	155	151
10 mM	15	13.8	25.9	323	252
50 mM	13.2	16.8	21.4	345.8	308
100 mM	11.2	18.4	16.3	356.8	317

Concentration @ -0.65 V anodic	**R_{el} / (Ω cm^2)**	**C_{DL} / (μF cm^{-2})**	**R_{ad} / (Ω cm^2)**	**C_{ad} / (μF cm^{-2})**	**C_{ad} / (μF cm^{-2}) from AC voltammetry**
1 mM	18.8	6.57	75.3	131.1	104
10 mM	14.8	7.51	56.7	265	176
50 mM	13.3	8.14	47.9	279.8	216
100 mM	11.3	9.1	36.8	286.8	224

Concentration @ -0.5 V anodic	**R_{el} / (Ω cm^2)**	**C_{DL} / (μF cm^{-2})**	**R_{ct} / (Ω cm^2)**
1 mM	19.1	10.3	3569
10 mM	14.9	12.5	2477
50 mM	13.2	15.2	2379
100 mM	11.4	17.7	2009

Table 3.2 shows that the adsorption resistance increases with decreasing the concentration of KI. Assuming kinetics according to the Butler Volmer equation, the adsorption resistance should be proportional to $1/c^{\alpha}$, where α is the charge transfer coefficient [239, 242]. From **Table 3.2** one can estimate a value of α= 0.2 to 0.3, which is reasonable for ion transfer reactions in light of the asymmetric free energy curves. [34, 266, 267] It has to be taken into account, though, that at least for the more cathodic peak, the rate of reconstruction (or its lifting) might also play a role and that the coverage is decreased for the lowest concentrations, as discussed above. Despite the importance

of this kind of adsorption reactions, we are not aware of similar determinations of the concentration dependence of R_{ad} even in aqueous electrolyte. The value of the adsorption capacitance C_{ad} increases with increasing the concentration of KI similar to the charge calculated from voltammetry or the capacitance curves. The capacitance from AC voltammetry is somewhat lower than that determined from EIS; the reason is that due to the slow adsorption, the impedance at the AC frequency of 10 Hz is largely determined by the large adsorption resistance and, therefore, the calculated capacitance is somewhat inexact. The decrease of the iodide adsorption charge with decreasing concentration (observed before on polycrystalline Ag in organic electrolytes [250]) is astonishing, as is the independence of the peak position. Since the peak current is proportional to the scan rate (cf. **Figure S3.2**), and since the time constant of adsorption as given by R_{ad} and C_{ad} is below 0.1 s, the reason is not the slow adsorption at low concentration. Rather we have to assume that propylene carbonate is adsorbed so strongly that it cannot be displaced completely by iodide when the iodide concentration is low. Furthermore, we have to assume that the potential of iodide adsorption is determined by the competitive adsorption/desorption of propylene carbonate and of course, the interference with the surface reconstruction. Further work is necessary to clarify this.

Figure 3.6 shows a measurement where the cyclic voltammetry is compared to the potential dependence of the adsorption capacitance and the adsorption resistance together with the AC-voltammetry for 10 mM KI at Au(111). (The corresponding impedance data are shown in the SI, cf. **Figure S3.3**). These data confirm what was mentioned above, but also demonstrate the good agreement between cyclic voltammetry and capacitance data from the impedance. Only at very low potentials, the pseudocapacitance from voltammetry is too large, possibly due to electrolyte decomposition. As for the aqueous system (and as expected), the adsorption resistance is lowest when the adsorption capacitance is the largest.

Such measurements have also been conducted on Au (111) using 0.5 M $KClO_4$ as a supporting electrolyte (cf. **Figure 3.7**, all impedance data are shown in SI). As expected, all values are very similar to those when using PF_6^- as an anion. The only clearly remarkable effect is that the peak separation is less: whereas the first peak in anodic scan direction remains at - 0.9 V, the second is now at -0.75 V instead of -0.65 V.

The charge determined by integration of the CV between -1.2 to -0.4 V in anodic direction was found to be 72.2 and 81.2 µC cm^{-2} for KPF_6 and $KClO_4$ supporting electrolytes, respectively. These values are close to the adsorption charge of iodide as given above and in an aqueous medium. The charge in the differential capacitance curve from potential -1.2 V to -0.5 V in the anodic going sweep was determined to be 55 and 50 µC cm^{-2} in PF_6^- and ClO_4^- supporting electrolytes, respectively.

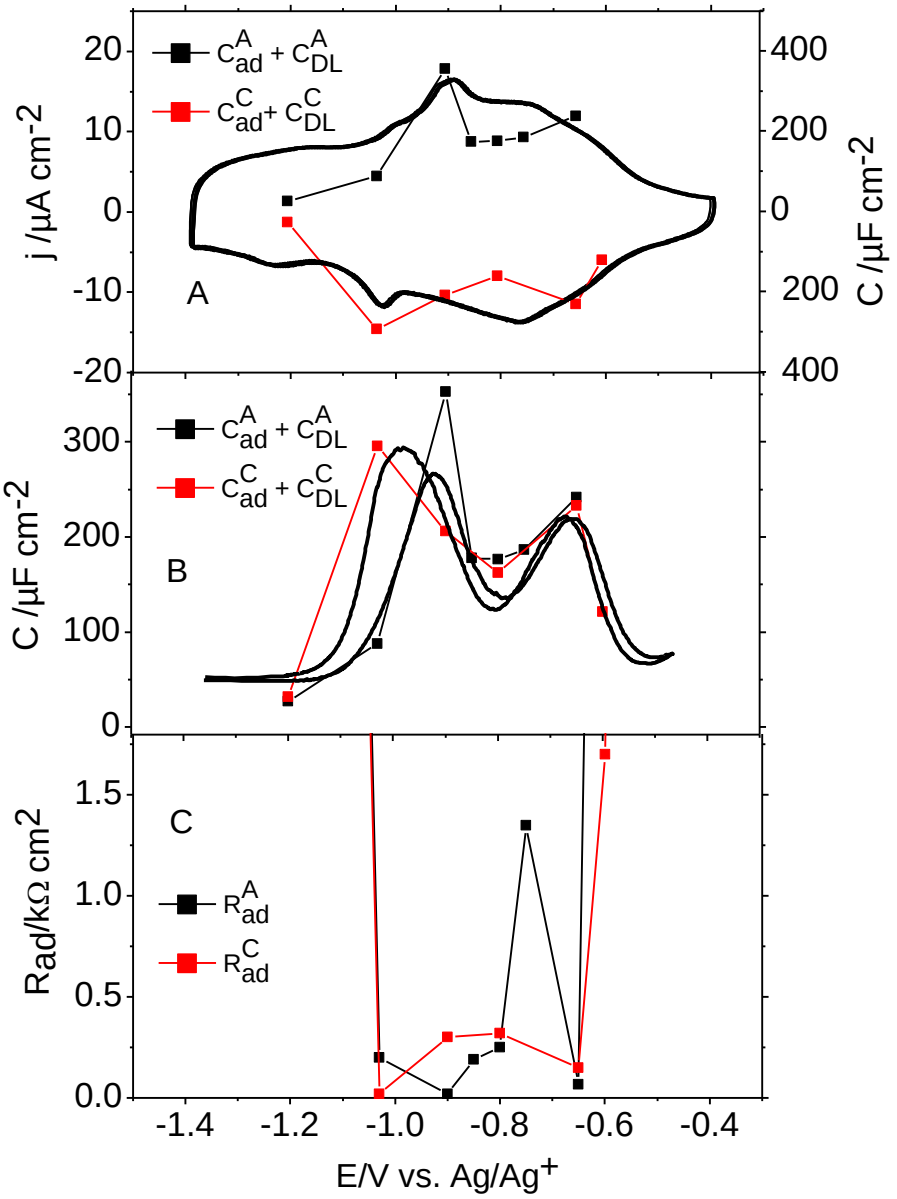

Figure 3.6: Au(111) in 0.5 M KPF_6 + 10 mM KI in propylene carbonate:

(A) CV (v =50 mV/s, the baseline is corrected; right scale: current density converted into capacity using C= j/v) compared to C_{ad} + C_{DL} measured by impedance spectroscopy (black squares: anodic and red squares: cathodic variation of the potential, plotted as capacitance in the negative direction for better comparison with the CV)

(B) Differential capacitance curves recorded using an AC perturbation of 10 Hz frequency, 3 mV rms. the amplitude at a sweep rate of 10 mV s^{-1}; squares: C_{ad}+ C_{DL} measured by impedance spectroscopy (black: anodic and red: cathodic variation of the potential)

(C) Potential dependence of R_{ad} measured by EIS.

. **Figure 3.7C** shows that, as expected, the two maxima of the capacitance coincide with the minimum values of the adsorption resistance, similar to the aqueous system. The data are tabulated in the SI together with the impedance spectra **(**cf. **Figure S3.4** and **Table S3.2**).

3.4.3 Influence of cations

The general structure of the CV is maintained when other cations are used in the supporting electrolyte. This is shown in **Figure 3.7** to **3.10** for K^+, Na^+, Li^+, and TBA^+ with perchlorate as the anion. In all cases, two peaks can be identified in the anodic scan, but in the cathodic scan, only one peak is clearly discernible except for K^+. The currents are comparable, and so is the resulting charge. Thus, the above interpretation of the peaks, namely the lifting of the reconstruction and electrosorption of iodide, also holds here. The charge was calculated from the CV by integrating the area under the adsorption of iodide in the anodic direction between the potential limit of -1.2 to -0.4 V for $KClO_4$, $NaClO_4$, $LiClO_4$ and TBAP supporting electrolytes and was found to be 81.2, 76, 83 and 67 μC cm^{-2}, respectively. These values are close to the value of the charge of adsorption of iodide in the aqueous medium.

The capacitances determined from the impedance spectra are also included in **Figure 3.7** to **3.10** where black squares are capacitances measured during potential increments in anodic direction and the red squares in the cathodic direction. The values of these capacitances from impedance spectra are lower than those from dc current, but the two peaks in the capacity are also visible in cathodic direction. This will be discussed below.

Figure 3.7 to **3.10** compare the cyclic voltammetry with the capacitances from AC voltammetry and impedance measurements and also give the potential dependence of the adsorption resistance for the perchlorate supporting electrolyte with different cations (K^+, Na^+, Li^+ and TBA^+).

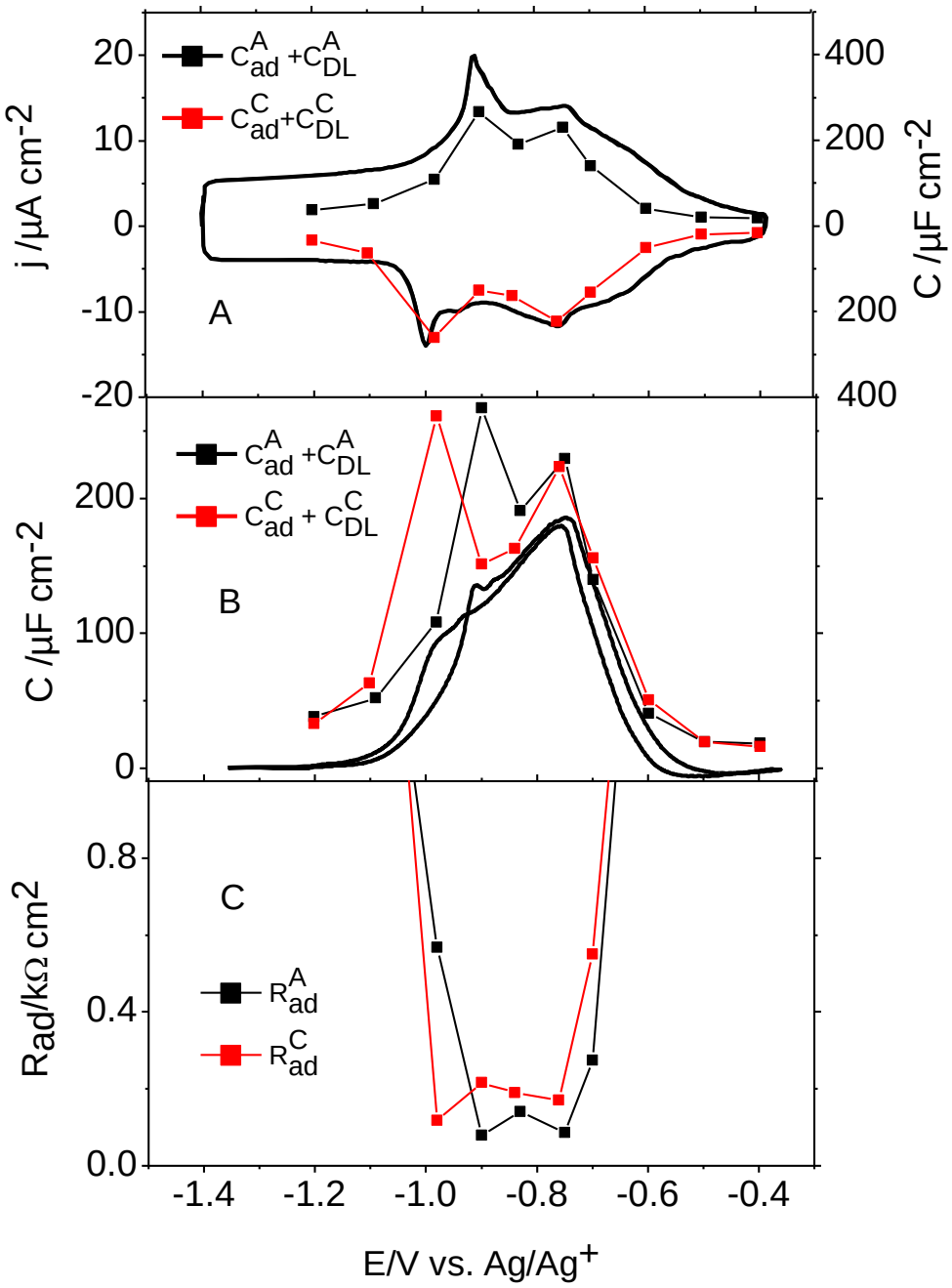

Figure 3.7: Au(111) in 0.5 M $KClO_4$ + 10 mM KI in propylene carbonate, otherwise the same in **Figure 3.6**.

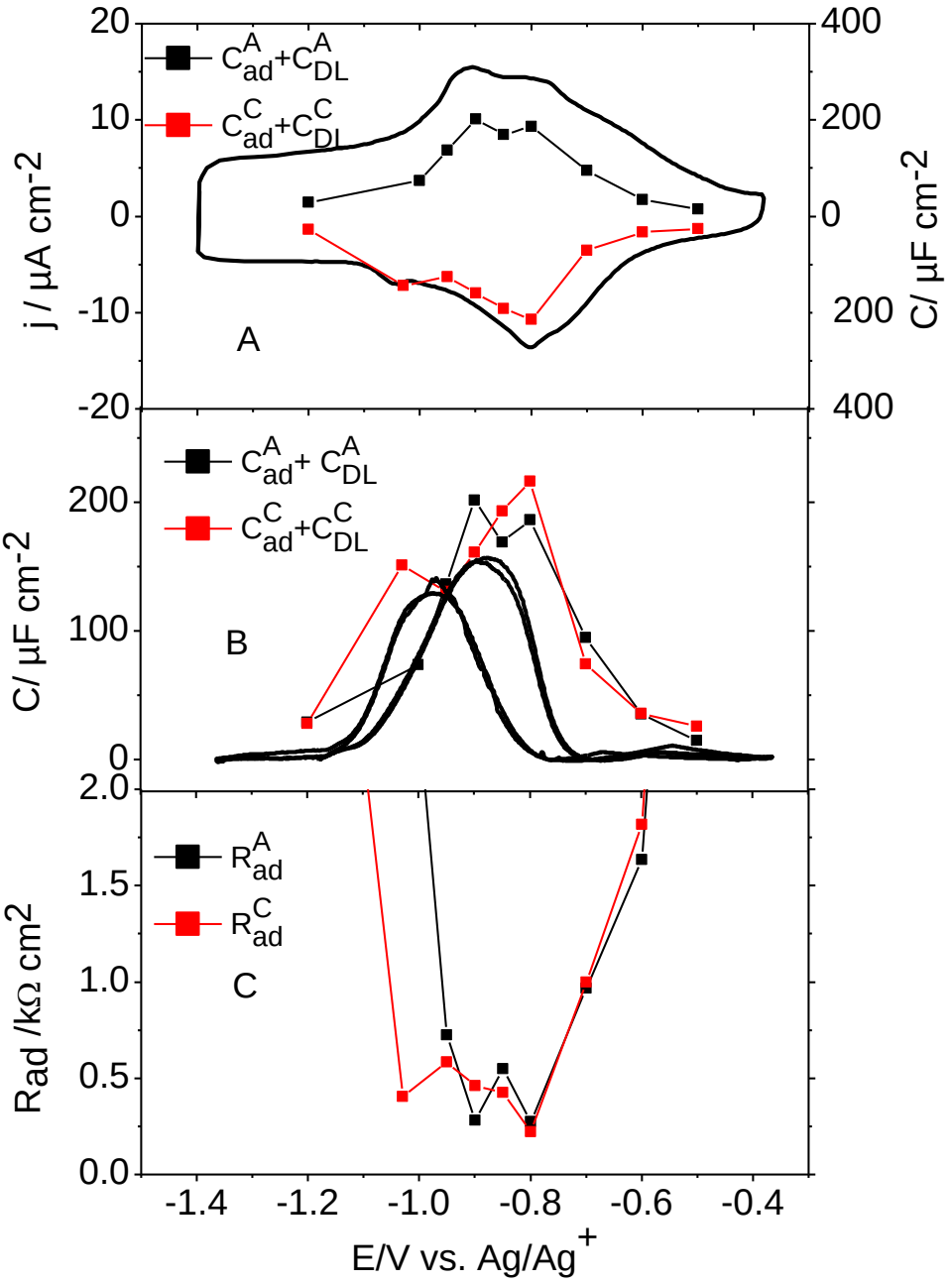

Figure 3.8: Au(111) in 0.5 M $NaClO_4$ + 10 mM NaI in propylene carbonate, otherwise the same in **Figure 3.6**.

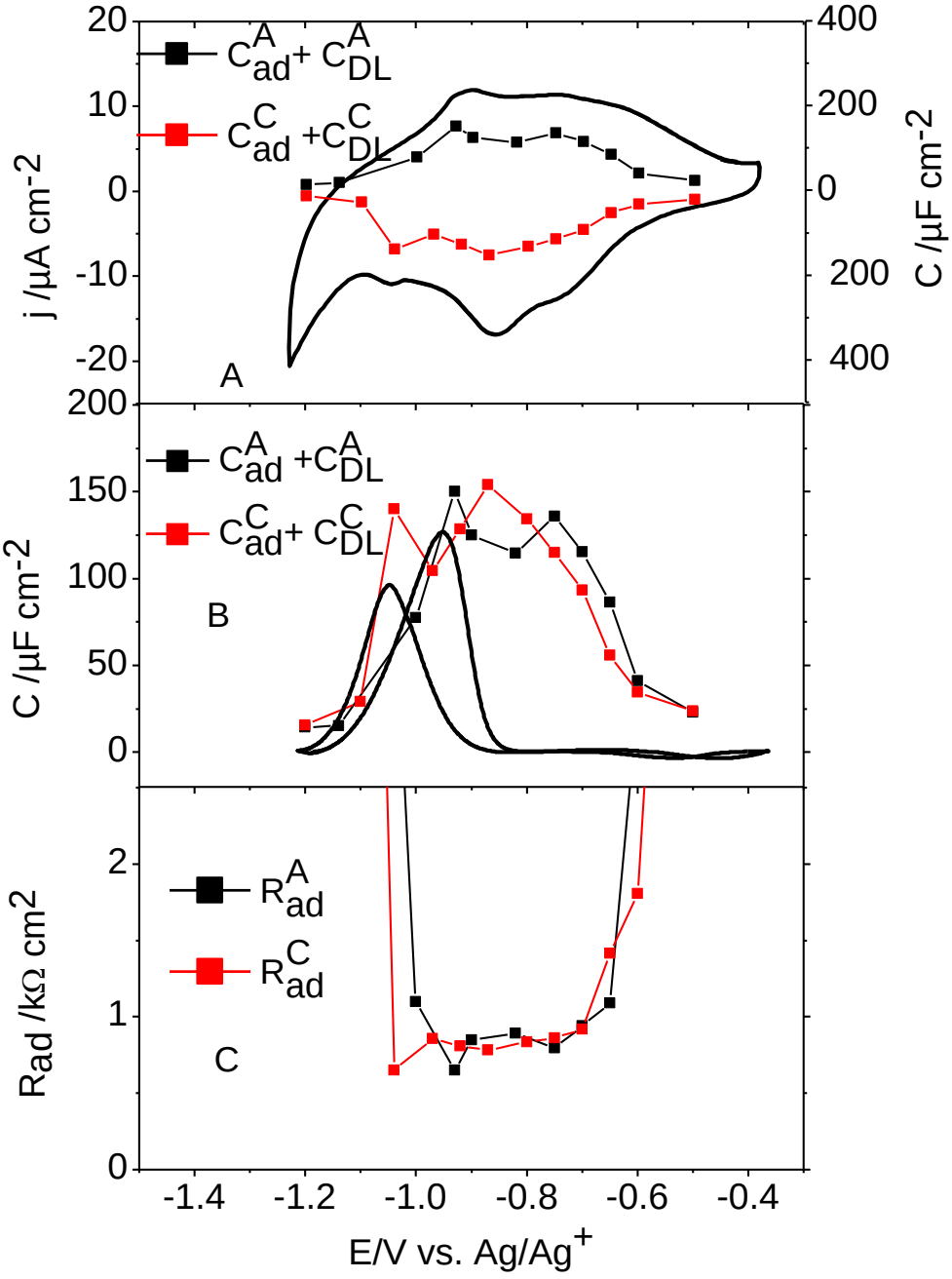

Figure 3.9: Au(111) in 0.5 M $LiClO_4$ + 10 mM LiI in propylene carbonate, otherwise the same in **Figure 3.6**.

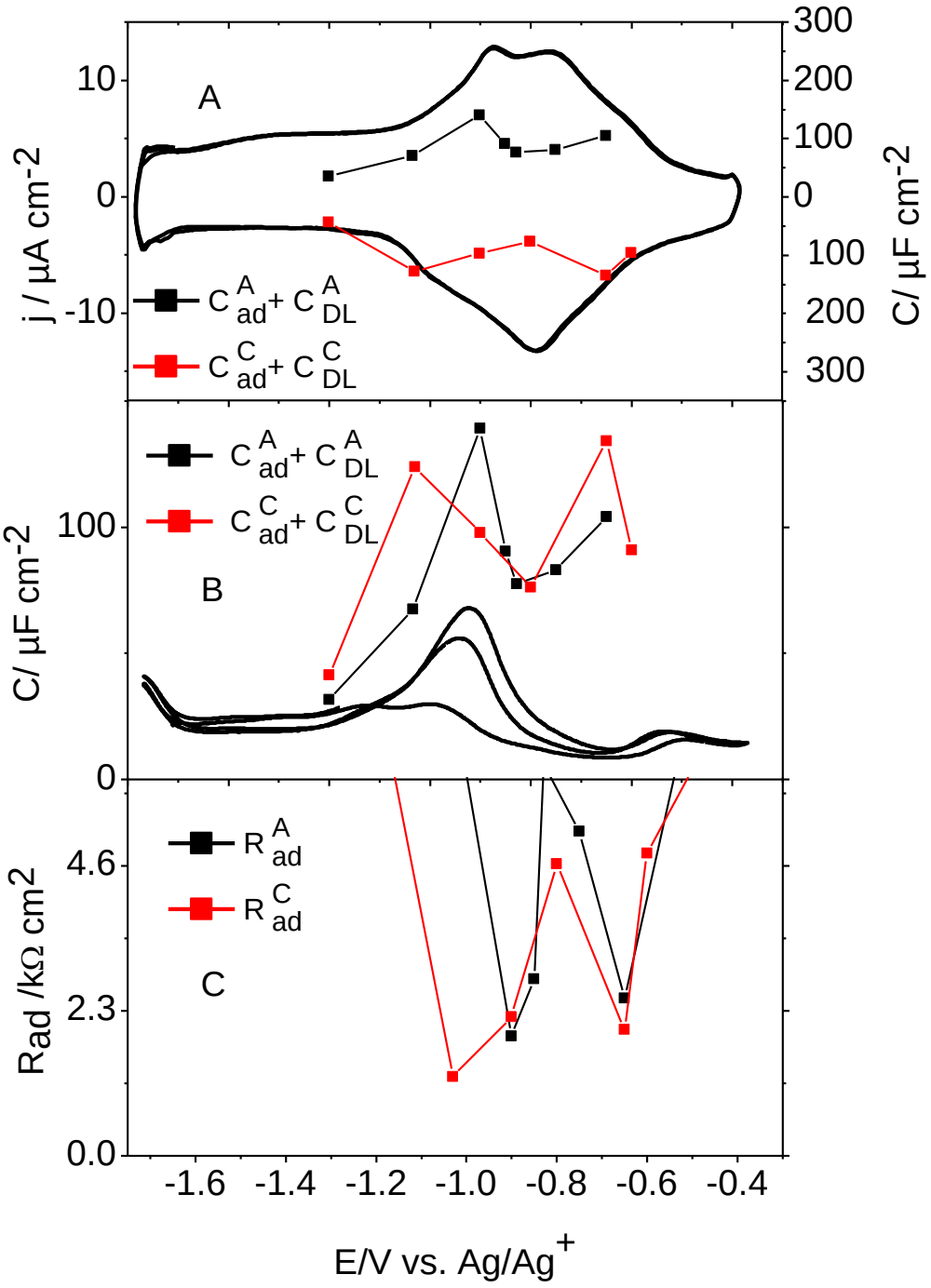

Figure 3.10. Au(111) in 0.5 M TBAP + 10 mM KI in propylene carbonate, otherwise the same in **Figure 3.6**.

There are remarkable differences in these capacitance curves as compared to those obtained in presence of K^+ (**Figure 3.7B**): Only the first one at -0.9 V is clearly visible, the second peak, which is visible in cyclic voltammetry, is not visible in AC voltammetry. The reason becomes clear from the impedance measurements (see SI): Whereas in the case of K^+ the impedance is already influenced by the adsorption capacitance at the frequency of 10 Hz (**Figure S3.5** to **S3.7**), for the

other cations the frequency of 10 Hz is too high to determine the adsorption capacitance, which therefore in these cases can only be determined from the complete frequency spectrum. As mentioned before in the context of **Figure 3.7** to **3.10**, two maxima in the adsorption capacitance result from the analysis of the impedance spectra. The analysis of the adsorption resistance shows again that these capacitance maxima correspond to minima in the adsorption resistance. However, their values largely differ depending on the cation: Whereas for the second peak the adsorption resistance amounts to only 86 Ω cm^2 for K^+ (at -0.75 V) it is 274 Ω cm^2, 796 Ω cm^2 and 2500 Ω cm^2 (all at - 0.65 V) for Na^+, Li^+ and TBA^+ , respectively. The same trend is visible for the first peak at - 0.9 V, cf. **Table 3.3**. These large values of the adsorption resistance result in a shift of the increase of the impedance on the low-frequency side to lower frequencies, thus making the adsorption capacitance 'invisible' at 10 Hz.

Table 3.3: Comparison of the resistance and capacitance data for iodide adsorption at Au(111) in various electrolytes (p^1 denotes the first anodic peak and p^2 denotes the second anodic peak).

System	E_A^{p1} / (V)	C_{ad}^{p1} / ($\mu F.cm^{-2}$)	R_{ad}^{p1} / ($k\Omega.cm^2$	E_A^{p2} / (V)	C_{ad}^{p2} / ($\mu F.cm^{-2}$)	R_{ad}^{p2} / ($k\Omega.cm^2$	Q_A^{CV} / ($\mu C.cm^{-2}$)	Q_A^{Cap} / ($\mu C.cm^{-2}$)
0.5M KPF_6 + 10 mM KI	- 0.9	334	0.02	- 0.65	228	0.07	72.2	55
0.5M $kClO_4$ + 10 mM KI	- 0.9	255.95	0.078	- 0.75	217	0.086	81.2	50
0.5M $LiPF_6$ + 10 mM LiI	- 0.9	206	0.27	- 0.65	190	0.261	72.52	38.84
0.5M $LiPF_6$ + 10 mM KI	- 0.9	245	0.24	- 0.65	203	0.235	58	32.5
0.5M $LiClO_4$ + 10 mM LiI	- 0.93	142.65	0.651	- 0.75	126.7	0.796	83.71	20
0.5M $LiClO_4$ + 10 mM KI	- 0.9	157	0.337	- 0.65	132	0.62	76	32
0.5M $NaClO_4$ + 10 mM NaI	- 0.9	193.63	0.281	- 0.8	178.3	0.274	76	40
0.5M TBAP + 10 mM KI	- 0.9	126	1.9	- 0.65	96	2.5	67	21

Table 3.3 also includes data for 10 mM LiI in 0.5 M $LiPF_6$. A comparison of the resistance data with those for KI/KPF_6 confirms the above- mentioned effect of the cation. They also confirm the effect of the anion, namely the lower adsorption resistance in presence of PF_6^- as the anion. Also, a mixture of $LiPF_6$ or $LiClO_4$ with 10 mM KI results in the expected effect on the adsorption resistance: even small amounts of K^+ lead to a notable decrease of the adsorption resistance.

The charge in the differential capacitance curve between -1.2 V and -0.5 V in the case of K^+ and TBA^+ and from -1.2 V to -0.7 V in the case of Na^+ and Li^+ in the anodic going sweep was calculated and found to be 50, 40, 20 and 21 µC cm^{-2} for K^+, Na^+, Li^+ and TBA^+, respectively. The

value of charge calculated from AC voltammetry is lower than calculated from cyclic voltammetry. This is obviously due to the increased adsorption resistance in this order and the incomplete determination of the adsorption capacitance by AC voltammetry.

3.5 Discussion

The rate of adsorption of iodide in different electrolytes with the same anion increases in the order $TBA^+ < Li^+ < Na^+ < K^+$. It therefore follows (nearly) the same order as the radius of solvated cations, which decreases from 5.44, 5.86, 5.14, to 4.26 Å for these ions in propylene carbonate. The large TBA^+ cation is hardly solvated, whereas the small Li^+ is strongly solvated and thus has a similar radius [268]. K^+ with the smallest solvated ion radius leads to the fastest adsorption rate of iodide. This is quite different from the effect of cations on the oxygen reduction in aprotic solvents: there TBA^+ behaves similarly to K^+ in that the main reduction product is the superoxide and not the peroxide as for Li^+ [216]. Although that effect is certainly related to the stability of the formed peroxide, the process seems to be kinetically controlled and a decisive characteristic seems to be the acceptor number of the cation [269].

The other obvious effect is that of the anion in the supporting electrolyte. In PF_6^- containing electrolytes the adsorption rate is faster than in ClO_4^- electrolytes by roughly a factor of two, although the difference of their effective radii as obtained from conductivity measurements is minor (2.8 vs. 2.66 Å) [268]. On the other hand, decisive might also be the mere ion radius, which is 2.95 and 2.4 Å, resp. Here, the radius has an opposite effect than for the cations.

Two possibilities can be envisaged as a cause of this effect:

First, the different size of the double layer. The iodide adsorption is occurring at the potentials negative of the pzc of the supporting electrolyte. The double-layer and its extension into the electrolyte, therefore, is mainly defined by the cations. The I^- ion with an effective radius of 2.67 Å, therefore, may reach the middle of the double layer (with its extension over 4 to 6 Å) before being discharged. The effective Galvani potential difference for the charge transfer, therefore, is only about half of the total potential difference; this effect is similar to the Frumkin effect. Thus, effective overpotential is decreased and is the smallest for the largest cation. In addition to this, the concentration of iodide ions is decreased within the double layer due to the negative potential, again similar to the Frumkin effect. Also, this effect is largest for the larger cations. The resulting is a net decrease of the rate of adsorption with the cation radius, which is indeed observed experimentally. The situation is however more complicated, because of the effect of the anions, which partially counterbalance the effect of the cations.

Second, there may be an effect on the activation barrier of adsorption cf.[34]. This barrier, which is due to the interaction of the adsorbing ion with the solvent molecules, is certainly decreased by ion-pair formation with counter ions, which itself can be assumed to be the largest for smaller ions. Again, this leads to the effect observed experimentally.

It is probable that both effects play a role. More data are necessary to elucidate these effects in more detail. Moreover, calculations from computational chemistry are highly important. It also should be noted that the adsorption rate in propylene carbonate is much lower than in the aqueous electrolyte. The dependence on the electrolyte will be the topic of a forthcoming paper.

3.6 Conclusion

The joint use of cyclic voltammetry, AC-voltammetry, and electrochemical impedance spectroscopy allowed us to obtain a conclusive picture of the adsorption of iodide on Au(111) in an aprotic solvent and the effect of the electrolyte composition thereupon. We found that a complete layer of iodide is formed similar to the aqueous solution. The adsorption rate, however, is much smaller by one order of magnitude. The concentration dependence of the rate confirms that the adsorption process is a simple charge transfer reaction. The rate decreases by another order of magnitude when the radius of the (solvated) cation is increased from $K^+ < Na^+ < Li^+ < TBA^+$. This effect is probably related to the differing sizes of the double layer. This also demonstrates the importance of the structure and composition of the double layer on charge transfer reactions.

3.7 Supporting Information

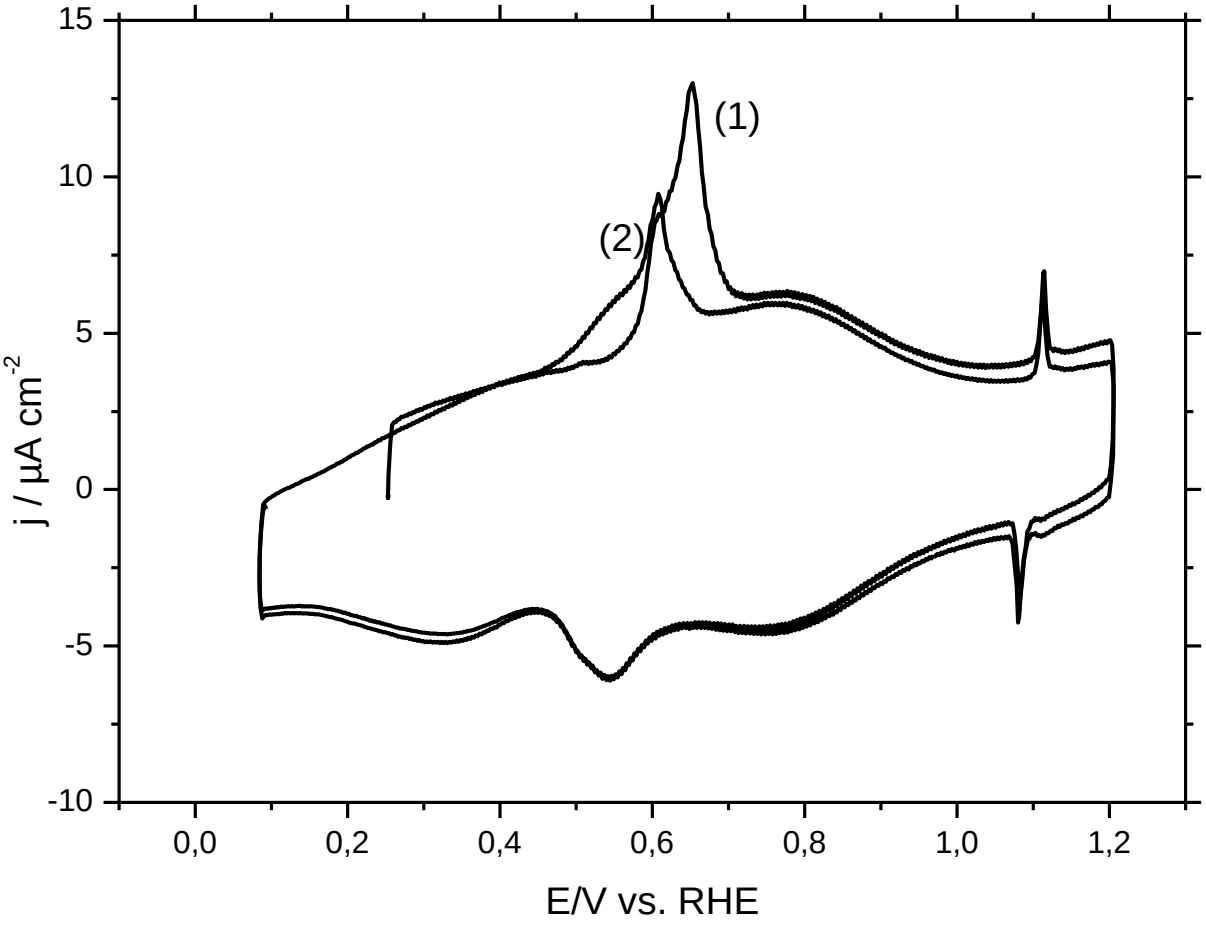

Figure S3.1: CV of Au(111) in 0.1 M H_2SO_4 solution saturated with Ar in H-cell at 50 mV s^{-1} with the first scan (1) and second scan (2).

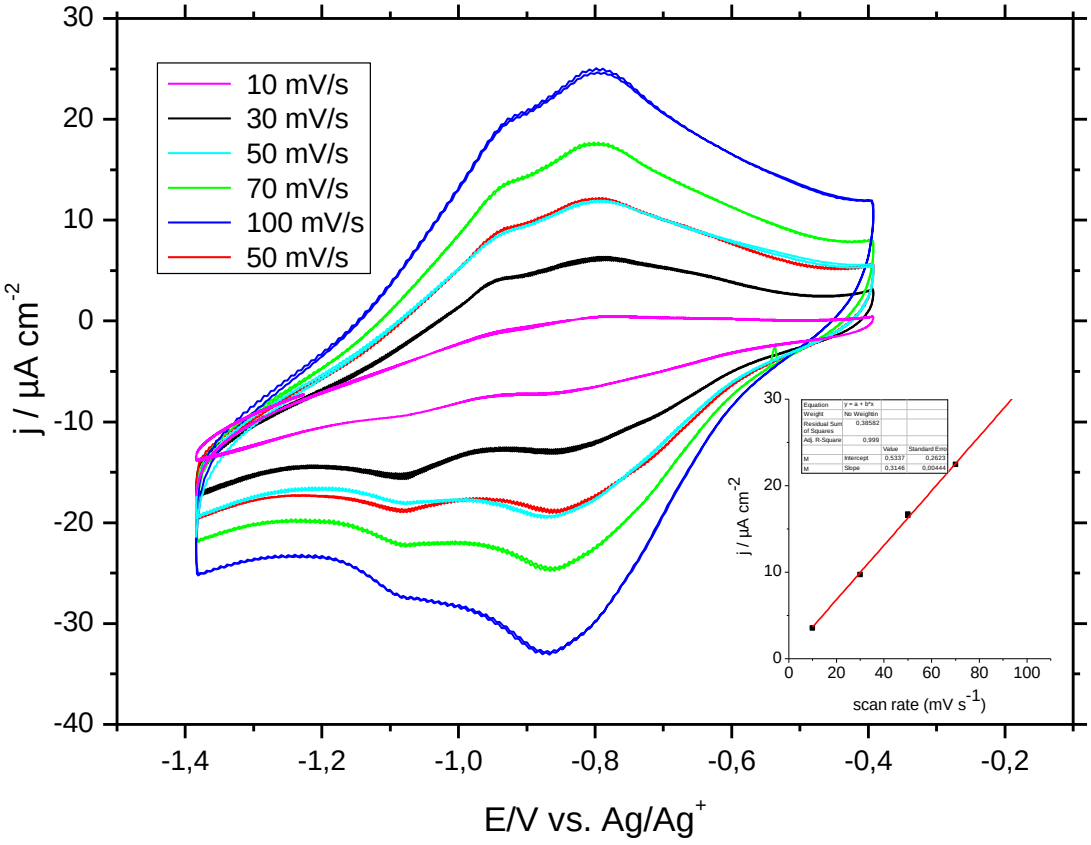

Figure S3.2: Cyclic voltammograms for Au(111) in propylene carbonate + 0.5 M KPF_6 +10 mM KI in different scan rate: (a) 10, (b) 30, (c) 50, and (d) 70 and (e) 100 mV s^{-1}. The inset shows the relation between scan rate and the peak current after subtracting the base line.

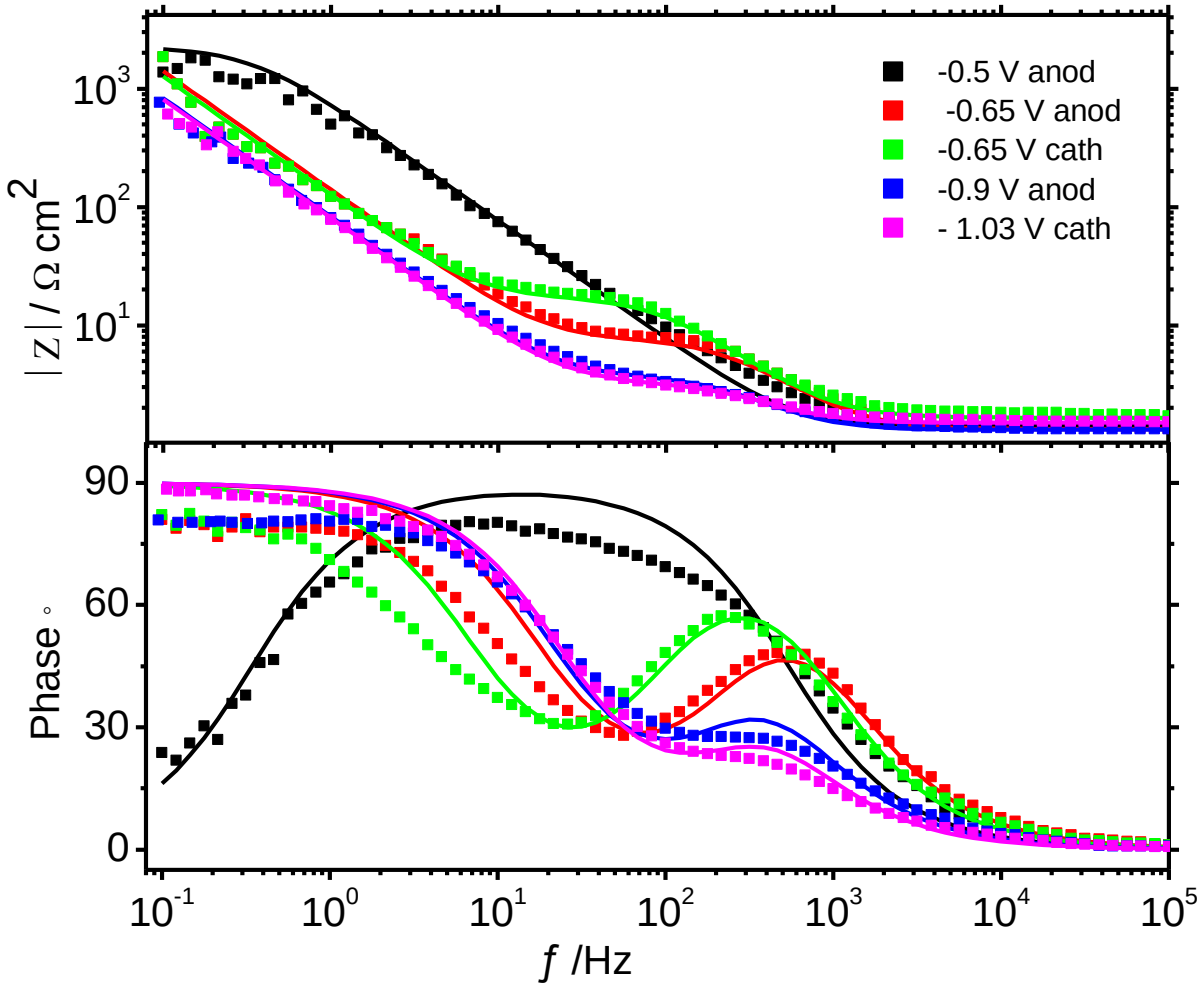

Figure S3.3: Examples for impedance spectra of the Au (111) disk electrode at the indicated potentials in 10 mM KI with 0.5 M KPF_6 in propylene carbonate, the lines are the fitting curves

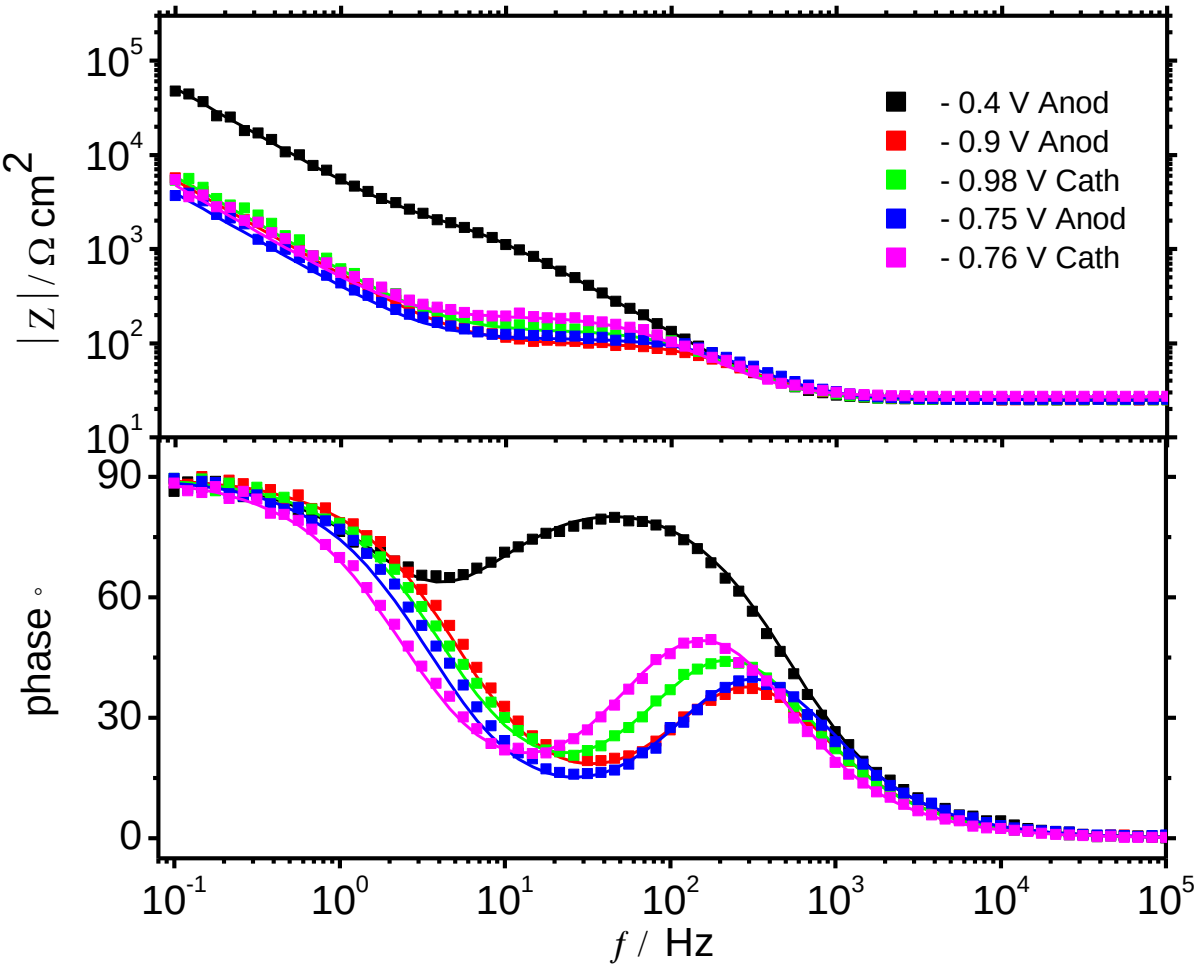

Figure S3.4: Examples for impedance spectra of the Au (111) disk electrode at the indicated potentials in 10 mM KI with 0.5 M $KClO_4$ in propylene carbonate, the lines are the fitting curves

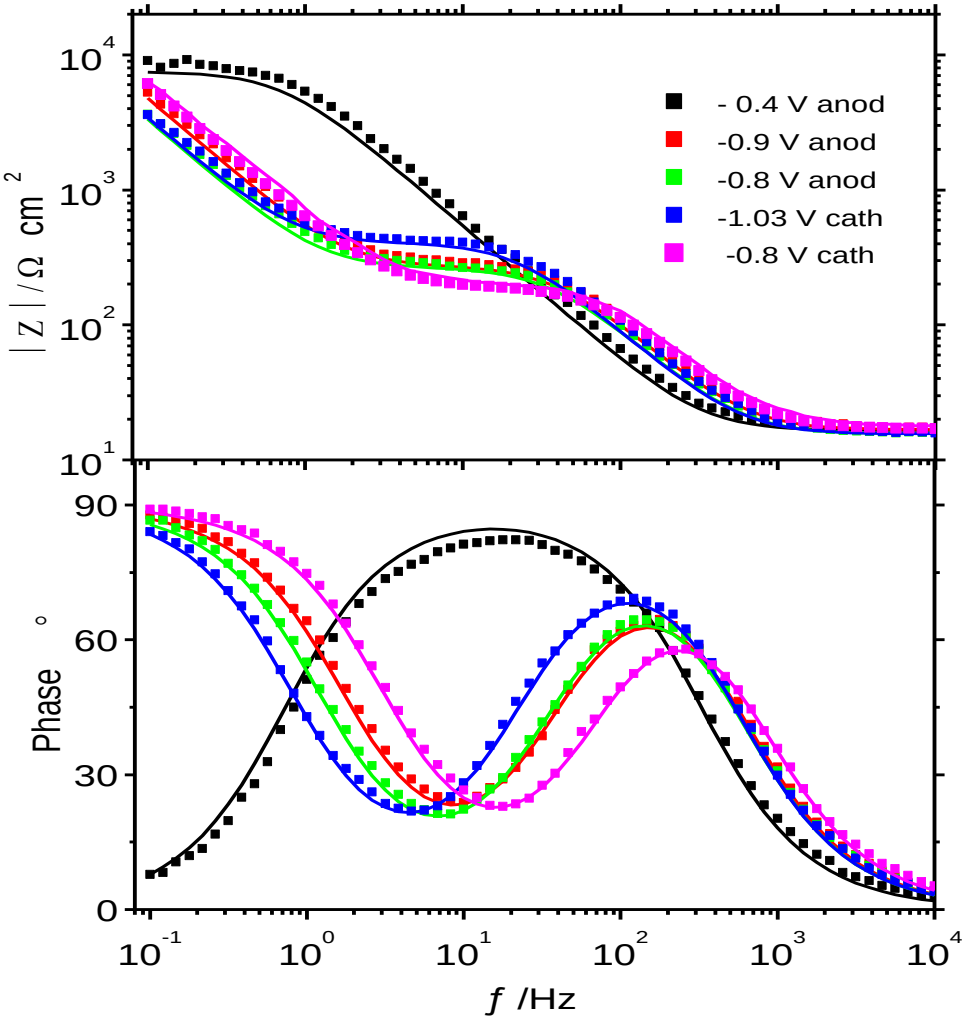

Figure S3.5: Examples for impedance spectra of the Au (111) disk electrode at the indicated potentials in 10 mM KI with 0.5 M $NaClO_4$ in propylene carbonate, the lines are the fitting curves.

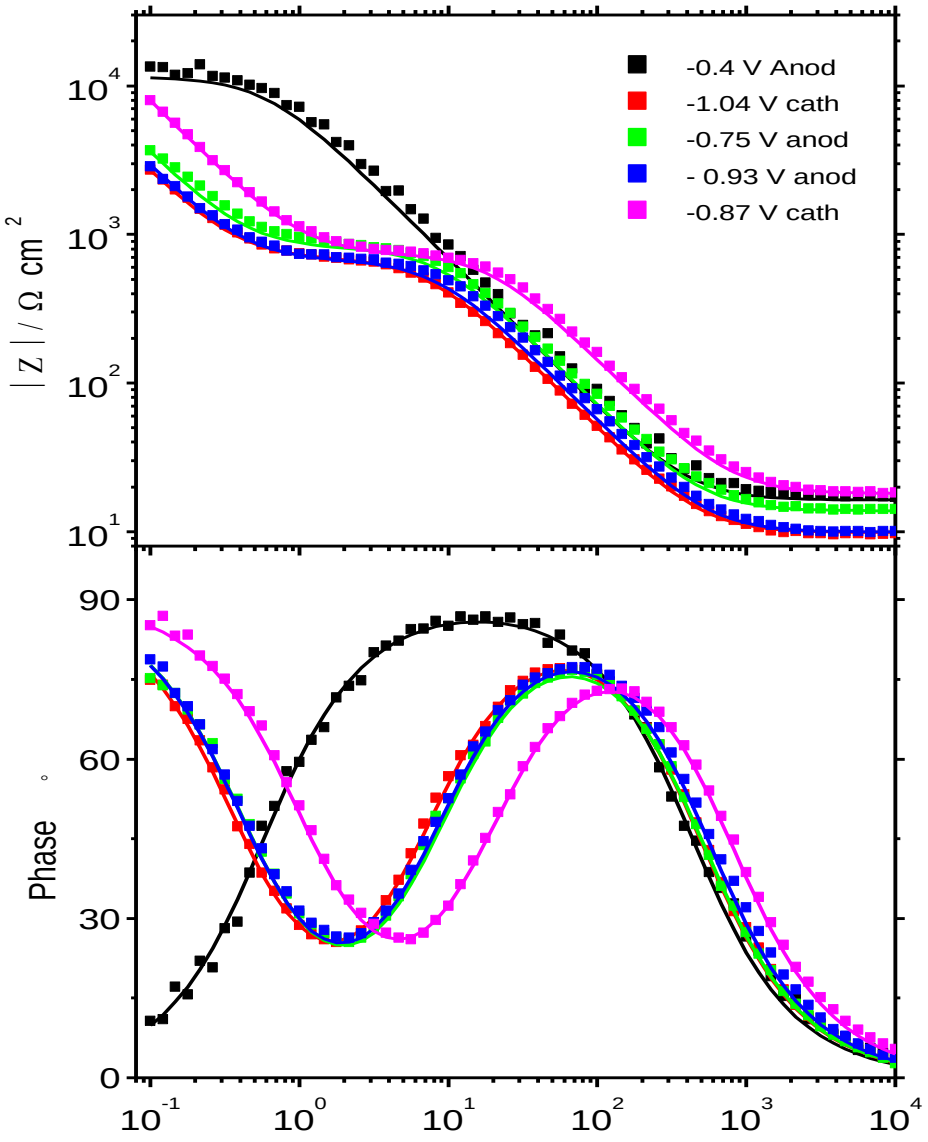

Figure S3.6: Examples for impedance spectra of the Au (111) disk electrode at the indicated potentials in 10 mM KI with 0.5 M $LiClO_4$ in propylene carbonate, the lines are the fitting curves.

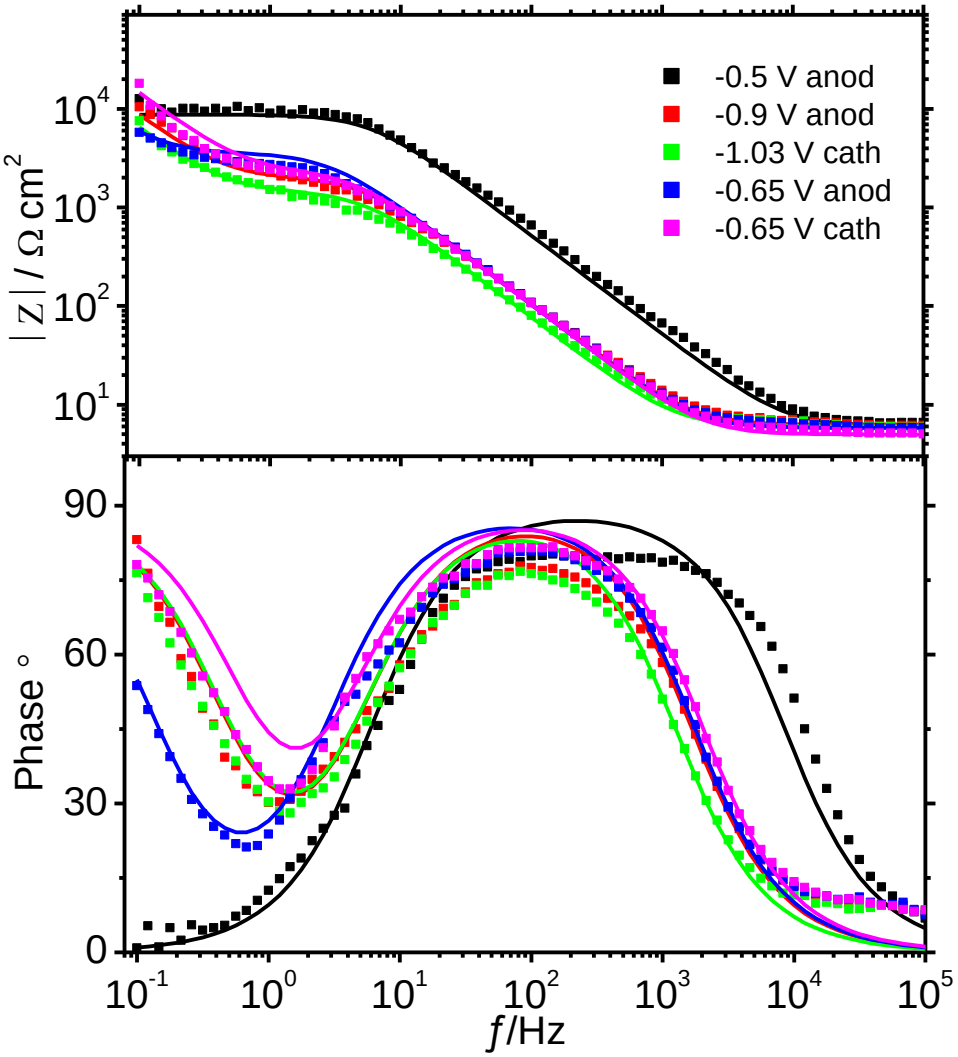

Figure S3.7: Examples for impedance spectra of the Au (111) disk electrode at the indicated potentials in 10 mM KI with 0.5 M TBAP in propylene carbonate, the lines are the fitting curves.

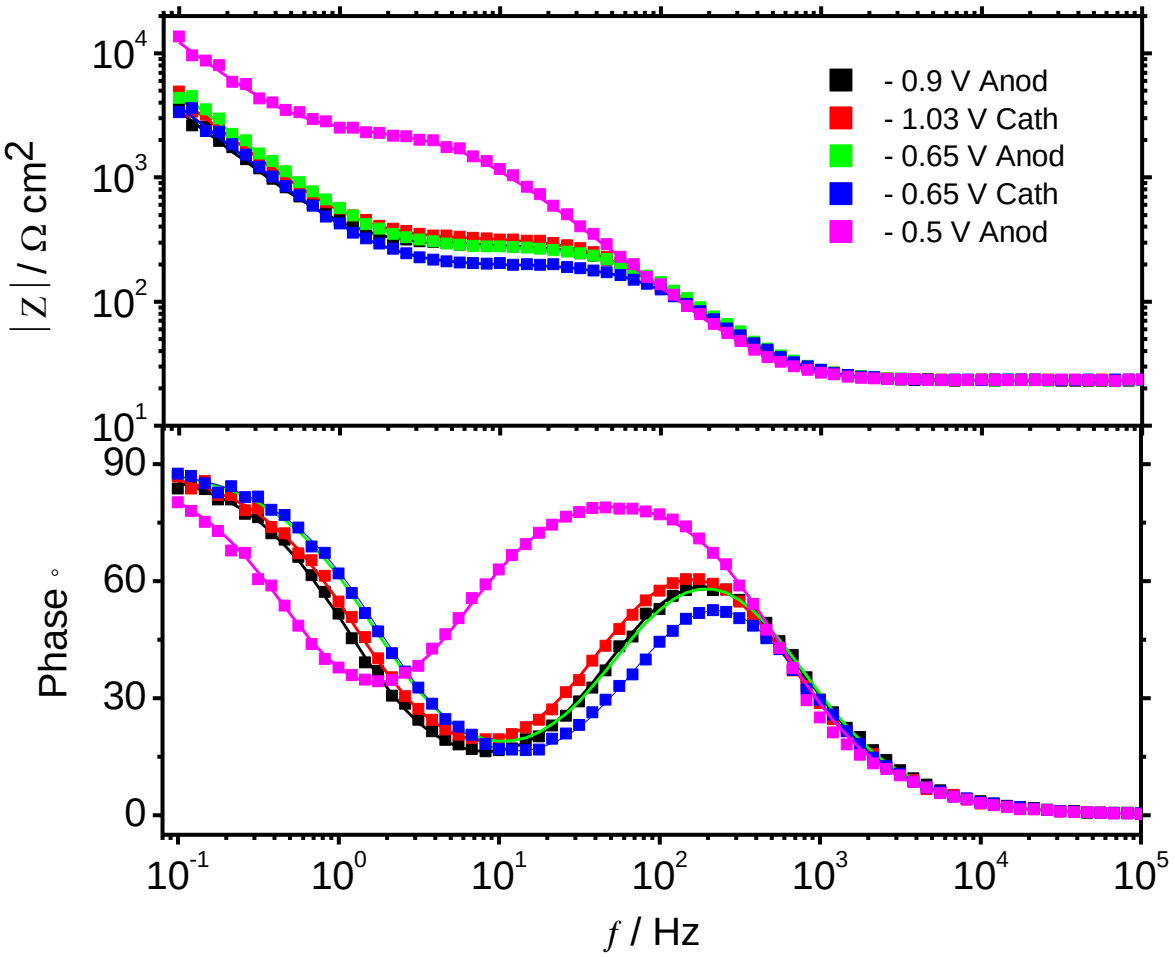

Figure S3.8: Examples for impedance spectra of the Au (111) disk electrode at the indicated potentials in 10 mM liI with 0.5 M $LiPF_6$ in propylene carbonate, the lines are the fitting curves.

Table S3.1: The fitting data for EIS on Au (111) using equivalent circuit 2R and 2C model for 10 mM KI + 0.5 M KPF_6 + PC.

Potential /V vs. Ag/$AgNO_3$	**R_{el} / (Ω cm^2)**	**C_{DL} /(μF cm^{-2})**	**R_{ad} / (Ω cm^2)**	**C_{ad} / (μF cm^{-2})**
-1.2 Anod	14	19.7	18798	5
-1.03	14.2	11.5	200.6	78
-0.9	13.1	15.4	20	334
-0.85	14	12	190.2	164
-0.8	14	10.5	251.5	165
-0.75	14.5	11.5	1349.2	175
-0.65	14	11.2	70	228
-0.5	13.8	11.7	3050	
-0.5 Cath	13.9	12.6	2980	
-0.6	14.3	8.3	1700	103.5
-0.65	13.8	10.9	150	220
-0.8	14.5	13	320	149.6
-0.9	13.8	10	300	197.5
-1.03	13.5	16.4	18	282.6
-1.2	14	19.8	17552	10

Table S3.2: The fitting data for EIS on Au(111) using equivalent circuit 2R and 2C model which is called Randles equivalent circuit for 10 mM KI + 0.5 M $KClO_4$.

Potential /V vs. Ag/$AgNO_3$	**R_{el} / (Ω cm^2)**	**C_{DL} /(μF cm^{-2})**	**R_{ad} / (Ω cm^2)**	**C_{ad} / (μF cm^{-2})**
-1.2 Anod	27.47	19.1	2370.7	16.2
-1.09	28.26	11.46	1727	38.7
-0.98	26.69	12	568.34	98.14
-0.9	25.2	14	78,5	255.95
-0.83	27.47	11.4	141.3	179.78
-0.75	25.12	12.4	86,3	217.34
-0.7	27.47	11.4	274.75	128.66
-0.6	26.69	10.3	2041	31.84
-0.5	28.26	13.24	2245.1	6.3
-0.4	25.12	12.9	3295.4	5.6
-0.4 Cath	24.33	10.82	3350.4	6.2
-0.5	27.47	10.57	2276.5	9.9
-0.6	25.9	10.7	2119.5	40.76
-0.7	26.69	14.2	549.5	142.7
-0.76	27.47	16.5	170	209.5
-0.84	26.69	11.1	190.3	153
-0.90	24.33	12.3	215.8	140.2
-0.98	25.12	14.5	117.7	247.7
-1.1	28.26	12.2	2211.3	50
-1.2	26.69	16.5	2433.5	15.7

Table S3.3: The fitting data for EIS on Au(111) using equivalent circuit 2R and 2C model which is called Randles equivalent circuit for 10 mM NaI + 0.5 M $NaClO_4$.

Potential /V vs. Ag/$AgNO_3$	**R_{el} / (Ω cm^2)**	**C_{DL} /(μF cm^{-2})**	**R_{ad} / (Ω cm^2)**	**C_{ad} / (μF cm^{-2})**
-1.2 Anod	14.91	6.36	4725.7	20.38
-1	15.7	6.87	2370.7	65.31
-0.95	14.13	10.95	725.34	128.34
-0.9	14.91	10.57	281.2	193.63
-0.85	14.13	10.06	549.5	160.5
-0.8	13.56	9.68	274.75	178.34
-0.7	14.13	8.78	965.55	86.3
-0.6	15.7	9.29	1634.4	26.75
-0.5	14.91	9.68	5652	6.36
-0.4	14.13	10.82	7072.8	
-0.4 Cath	14.13	9.8	7080.7	
-0.5	14.91	10.31	6295.7	15.2
-0.6	14.13	10.82	1815.7	25.47
-0.7	12.56	10.31	999.3	63.69
-0.8	15.34	9.29	219.8	206.36
-0.85	14.13	9.8	425.4	183.43
-0.9	14.91	10.19	460	150.8
-0.95	14.13	11.08	584.82	118.15
-1.03	14.91	11.33	405.8	136
-1.2	14.13	7.13	4749.25	20

Table S3.4: The fitting data for EIS on Au(111) using equivalent circuit 2R and 2C model for 10 mM LiI + 0.5 M $LiClO_4$.

Potential /V vs. Ag/$AgNO_3$	**R_{el} / (Ω cm^2)**	**C_{DL} /(μF cm^{-2})**	**R_{ad} / (Ω cm^2)**	**C_{ad} / (μF cm^{-2})**
Anod -1.2	12.56	8.53	13345	5.1
-1.14	11.77	5.85	10990	9.8
-1	12.56	6.49	1099	70.1
-0.93	10.1	7.38	651.55	142.65
-0.9	13.34	8.4	850	115.74
-0.82	12.56	8.78	894.1	105.54
-0.75	13.77	8.66	796	126.74
-0.70	12.56	8.78	942	106.22
-0.65	13.34	9.29	1091.2	77.1
-0.6	12.56	9.29	3061.5	31.84
-0.5	11.77	9.55	3454	14
-0.4	15.77	11.59	10990	
Cath -0.4	13.56	11.71	8674.3	
-0.5	11.77	11.71	7693	12.7
-0.6	11.77	9.68	1805.5	25.47
-0.65	12.56	9.42	1413	44.58
-0.7	13.34	9.17	918.45	84.27
-0.75	11.77	9.17	861.93	105.97
-0.8	11.77	9.17	832.8	125.16
-0.87	15.9	9.29	784	144.62
-0.92	11.77	8.91	810	119.15
-0.97	11.77	8.66	855.65	95.3
-1.04	10.2	8.4	650	130,93
-1.1	12.56	9.55	9336	20
-1.2	12.56	8.66	13188	4.7

Table S3.5: The fitting data for EIS on Au (111) using equivalent circuit 2R and 2C model for 10 mM KI + 0.5 M TBAP.

Potential /V vs. Ag/$AgNO_3$	**R_{el} / (Ω cm^2)**	**C_{DL} /(μF cm^{-2})**	**R_{ad} / (Ω cm^2)**	**C_{ad} / (μF cm^{-2})**
-1.2 Anod	8.6	2.3	11.98	29
-1.03	8.4	3.1	7.48	65
-0.9	8.6	12.7	1.9	126
-0.85	8.2	12.36	2.8	78.26
-0.82	8.7	14.2	6.2	63.8
-0.75	8.6	8.91	5.14	74.9
-0.65	8.3	8.28	2.5	96
-0.5	8.3	7.64	7.28	
-0.5 Cath	8.6	9.55	6.12	
-0.6	8	8.53	4.8	82.35
-0.65	8.2	12.76	2	121
-0.8	8.8	13.2	4.63	63.12
-0.9	8.9	7.6	2.2	90.4
-1.03	8	3.8	1.26	120
-1.2	8	3.8	7.52	37

Table S3.6: The fitting data for EIS on Au(111) using equivalent circuit 2R and 2C model for 0.5 M $LiPF_6$ in propylene carbonate + 10 mM LiI solution.

Potential /V vs. Ag/AgNO$_3$	**R_{el} / (Ω cm^2)**	**C_{DL} /(μF cm^{-2})**	**R_{ad} / (Ω cm^2)**	**C_{ad} / (μF cm^{-2})**
Anod -1.2	30.61	11.2	4684	15.92
-1	25.12	10.3	94.,7	80
-0.9	23.33	11.2	270	206
-0.85	23.55	9.2	449	164.91
-0.8	25.90	8.5	570.2	140
-0.75	26.69	9.2	622.3	160
-0.65	23.55	10.9	261	190
-0.5	23.55	12.6	2512	63.69
Cath -0.5	29.83	13.2	2747.5	50
-0.6	26.69	10.2	1648.5	100.52
-0.65	23.55	11.6	180	211
-0.8	25.12	9.2	550	149
-0.9	23.55	10.3	470	170
-1.03	23.55	12.2	310	210
-1.2	30.61	10.2	4702.9	20

Chapter four:

Adsorption of iodide and bromide on Au(111) electrode from aprotic electrolytes: role of the solvent

A. S. Shatla [a,b], P. P. Bawol [a] and H. Baltruschat [a]

[a] Institute of Physical and Theoretical Chemistry, University of Bonn, 53117 Bonn, Germany.
[b] Permanent address: Menoufia University, Faculty of Science, Chemistry Dept., Shebin Elkoom, Egypt.

Submitted to journal of **ChemElectroChem**

Acknowledgments

Financial support by the German Federal Ministry of Education and Research (BMBF) of the "LuCaMag" project (Fkz: 03EK3051A) under the framework of "Vom Material zur Innovation" program is acknowledged.

4.1 Abstract

The adsorption of iodide and bromide ions on a Au(111) single crystal electrode in three organic solvents (propylene carbonate (PC), diglyme (DG), and dimethyl sulfoxide (DMSO)) was studied using differential capacity measurements, cyclic voltammetry (CV), X-ray photoelectron spectroscopy (XPS) and electrochemical impedance spectroscopy (EIS). The anion adsorption charge in DMSO is approximately half as large as in propylene carbonate and that in water. Quantification of the adsorbed iodide amount from XPS spectra confirms the coverage estimated from the adsorption charge in CVs. As expected, the rate of anion adsorption on Au(111) is higher for I- than for Br- due to better solvation of the latter. The extent of anion adsorption on the Au(111) electrode decreases and the corresponding adsorption rate decreases in the solvent order H2O > PC > DG > DMSO. Since the donor number (DN) of the solvent increases in the same order (PC < DG <DMSO), we assume that it plays a decisive role since it determines the chemical interaction of the solvent with the metal surface. Moreover, the adsorption rate of iodide and the extent of its adsorption is increased with increasing water content in the PC and DMSO. This effect and the much higher adsorption rate in water is explained by the closer approach of the solvated halogen ion to the surface and the resulting stronger interaction of the transition state with the electrode.

4.2 Introduction

Due to the current interest in high energy batteries, research on electrochemical processes in aprotic solvents is becoming more and more important. Fundamental studies on oxygen reduction and evolution in the context of metal-air battery research showed that surface processes are particularly important and that not only the kind of electrode material but also the atomic surface structure plays a large role [216, 270 - 272]. These studies also showed that the reaction rate and mechanism are largely influenced by the type of solvent and additives [273, 274]. Moreover, it is well known that the electrochemical reactivity of a metal electrode is strongly influenced by adsorbed anions. Such surface modification has significant implications in electrosynthesis, electrocatalysis, corrosion, galvanic deposition and battery research.

We therefore decided to examine the adsorption of iodide and bromide in different aprotic solvents, namely propylene carbonate, diglyme and DMSO, in particular the rate of adsorption, as a model for a simple elementary reaction. The reason to choose these solvents stems from the fact that their chemical nature differs considerably and that they play a large role in battery research: PC is a standard electrolyte for Li-ion batteries [275], DMSO seems to

be best suited for Li-oxygen batteries [270, 276 - 279], and glymes like DG or tetraglyme (TG) seem to be well suited for Mg deposition as necessary in aprotic Mg-batteries [280 - 283]. Halides (except fluoride) are known to strongly adsorb on electrode surfaces ("specific adsorption"), i.e. the amount of anions in the double layer exceeds that expected from electrostatics. This adsorption often has been studied by determining the potential dependent double layer capacity. e.g. by AC voltammetry[226], also a detailed determination of the thermodynamic Gibbs surface excess was reported for several systems [229, 230, 284, 285] [286]. On single-crystal surfaces, the adsorbed ions usually form an ordered adlayer phase, with a structure and packing density depending on potential, as shown by LEED, STM and SXS [231, 233, 235 - 238, 287 - 291].

Much fewer studies dealt with the rate of the adsorption process, particularly on single crystal surfaces. Whereas the metallic adsorption systems ("underpotential deposition", upd) is typically characterized by an attractive interaction between the adsorbed atoms, the adsorption of anions (and also hydrogen) is characterized by repulsive interaction, giving rise to broader adsorption peaks in cyclic voltammetry. Correspondingly, the rate of adsorption of upd systems often is examined by potential step experiments [292 - 295] demonstrating the nucleation and growth process as well as the role of steps for the rate of monolayer deposition. Opposed to that, we introduced electrochemical impedance spectroscopy for the determination of the adsorption rate of anions on single crystal surfaces [239, 242, 248, 296].

Such studies using well defined single crystal surfaces are a prerequisite for any theoretical modelling. But in addition to the crystallographic structures of electrodes also the dielectric properties and chemical composition of electrolyte have an outstanding effect on the electrical double structure and adsorption kinetics of ions, therefore a knowledge of its influence on thermodynamics and kinetics of adsorption also is of great importance for a better, theory-based understanding. The adsorption of simple ions, in particular that of the monoatomic halide ions, is an ideal, simple model for a charge transfer reaction within the inner Helmholtz layer, and, as an elementary reaction, a model for the single steps of the more complicated electrocatalytic reactions. The influence of the solvent molecules is twofold: on the one hand, the solvation strength and interaction between the solvent and the ion influences the thermodynamics of the adsorption and also the kinetics via the solvent reorganization energy, on the other hand, the solvent interaction with the surface competes with the ion adsorption depends on the adsorption.

There is a large number of studies examining the adsorption of halides from non-aqueous solvents on mercury electrodes [222, 297 - 299] and other liquid electrodes [300 - 304]. The strong chemical interaction with DMSO molecules in the Helmholtz-layer has been observed on Ga and (In-Ga) electrodes [297, 305]. Emets et al. found that the adsorption strength of halide ions decreased in the sequence $I^- > Br^- > Cl^-$ on (Cd-Ga) electrode while it increased in the opposite sequence on Hg/DMSO interface [306]. On polycrystalline silver in organic solvents, the strength of halogen adsorption decreased in the order $I^- > Br^-$ and in the solvent order DMF > PC >ACN [250]. Weaver and coworkers studied the adsorption of CO in non-aqueous solvents using FTIR spectroscopy [307] and found that the cation nature in the double layer can affect the structure of CO adsorption on a polycrystalline platinum surface.

Quite in general, the number of studies using single crystal electrodes in non-aqueous electrolytes is quite limited. Van Huong characterized the double layer of gold single crystal electrodes in propylene carbonate by AC voltammetry and electroreflectance measurements [308]. The adsorption of halides was also studied on single crystal electrodes of Bi in non-aqueous solvents [309 - 311]. Gibbs energy of iodide adsorption at Cd(0001) and Bi(hkl) single-crystal electrodes was determined (increase in the sequence H_2O < MeOH < EtOH < EC < PC < gamma-butyrolactone < ACN), but there was no clear separation of the adsorption process from faradaic iodide oxidation [312].

Anion adsorption has been investigated on Bi(hkl), and Cd(0001) surfaces in ionic liquid by electrochemical impedance method as well as differential capacitance measurements[312]. The specific adsorption of iodide on an Au(111) electrode surface in the ionic liquid was examined via voltammetric analyses, XPS, and STM [313]; $\left(\sqrt{3} \times \sqrt{3}\right)$ and $\left(p \times \sqrt{3}\right)$ was found similar to the aqueous system [237].

This work is a continuation of our previous publication, in which we studied the influence of iodide concentration and various cations on the adsorption rate and extent of adsorption in propylene carbonate [314]. Here this research aims to investigate the effect of solvent characteristics on the adsorption kinetics (adsorption rate) of iodide and bromide in propylene carbonate, dimethyl sulphoxide and diglyme on Au(111) single crystal electrode. Electrochemical impedance spectroscopy, AC-voltammetry, XPS and cyclic voltammetry are used to compare the anion adsorption in the different organic solvents.

4.3 Experimental

4.3.1 Chemicals and materials

Potassium iodide (KI, ≥ 99.5%, MERCK), Potassium bromide (KBr, 99+ %, ACROS), potassium hexafluorophosphate (KPF_6, ≥ 99%, ACROS), propylene carbonate (PC, 99.7%, SIGMA-ALDRICH), Diethylene glycol dimethyl ether (Diglyme, DG, 99.5%, anhydrous, dried over molecular sieve), Dimethyl sulfoxide (DMSO, 99.7%, over molecular sieve, Acros Organics) and acetonitrile (ACN, 99.8%, ACROS) were used as received. Silver nitrate ($AgNO_3$, ≥ 99%, SIGMA-ALDRICH) was used for the preparation of the reference electrode, H_2SO_4 spectra pure grade (Merck) was used for cleaning the Au(111) electrochemically. The aqueous solutions were prepared with 18.2 MΩ·cm Milli-Q Millipore water. All electrolytes were purged with highly pure argon (99.999%, AIR LIQUIDE).

The cleaning and preparation of the Au(111) electrode were described before in detail [314]. The electrochemical measurements have been conducted in the classical H-cell of a three-electrode cell setup with a hanging meniscus configuration of Au(111). The counter electrode was a gold sheet and it was placed in parallel to the working electrode to have better current distribution and separated by glass frit. The reference electrode is a silver wire in 0.1 M $AgNO_3$ dissolved in ACN when the electrolytes in the working part are PC and DG, whereas silver nitrate is dissolved in DMSO. In order to avoid contamination of the working electrolyte with silver-ions during the measurements, the reference electrode was connected via a Luggin capillary, which had contact with the reference electrolyte through the wet surface of a closed, rough glass stopcock. The potential scale of reference electrode was calibrated using decamethylferrocene (DMFc) and $E_{1/2}$ (vs. Ag/Ag^+ in DMSO or ACN) for $DMFc^+$/DMFc in DMSO, PC, and DG is -0.342, - 0.484, and - 0.317 V, respectively [315]. The water content was calculated using Karl Fischer titration and was approximately 35 ppm in PC, 31 ppm in DMSO and 45 ppm in DG after measuring.

4.3.2 Instruments and data evaluation

The cyclic voltammetry and differential capacitance curves measurements (recorded by AC voltammetry) were used to investigate the electrochemical characteristics of the Au(111) | electrolyte system utilizing an EG&G potentiostat (model 273A) in integration with LabVIEW software (National Instruments GmbH, Munich, Germany).

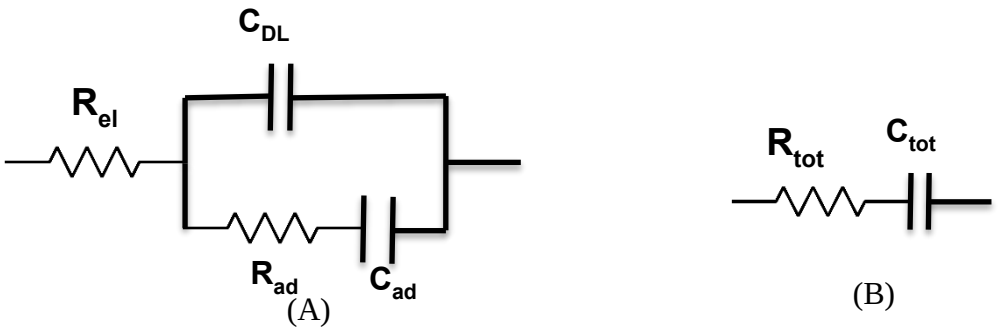

Figure 4.1: Equivalent circuit used for fitting the experimental impedance of the anion adsorption (A) and equivalent circuit for the calculation of the AC voltammetry (B).

Electrochemical Impedance experiments were performed using an EG&G potentiostat (model 273) connected to a Solartron Impedance /Gain-Phase analyzer (Model SI 1260) in collection with LabVIEW software (National Instruments GmbH, Munich, Germany) and Zplot and Zview programs used for data collection and analysis. Impedance spectra were measured within AC frequency range from 10^{-1} to 10^{5} Hz with 3 mV AC modulation amplitude. They were fitted by the equivalent circuit shown in **Figure 4.1A**, where R_{el} is the electrolyte resistance, R_{ad} the adsorption resistance (proportional to the reciprocal of the adsorption rate), C_{ad} is the adsorption capacitance (related to the change of coverage with potential) and C_{DL} is the double layer capacitance (a high-frequency component of the capacitance).

Measurements of impedance were quite reproducible; also subsequent measurements after the impedance analysis (without fresh preparation of crystal) and cyclic voltammetric tests brought the same findings as immediately following the preparation of the single crystal. Impedance spectra, starting with the lowest potential, were acquired right after recording the AC-voltammograms. The potential was then stepped to a value, where the next impedance analysis was carried out. The potential in the negative-going scan for further impedance measurements was sequentially changed after the most positive potential measurements. The potential was maintained constantly for 1 minute before each impedance measurement. Impedance measurements reported at a constant potential, immediately after each other, provided similar results.

In differential capacitance measurements, the real and imaginary components of admittance of AC current was measured under equilibrium conditions using a Lock-in amplifier (EG&G, model 5210). The equivalent circuit of **Figure 4.1A** at relatively low frequencies, like the 10 Hz utilized for AC-voltammetry, can be extended to that of **Figure 4.1B**. The capacitance

C_{tot} is the sum of double-layer and adsorption capacitance (C_{DL} + C_{ad}), and R_{tot} represents the total of R_{el} + R_{ad}.

The frequency of AC voltammetry should be sufficiently small to determine the total impedance by the capacitance. It should be particularly small to achieve a high impedance relative to any adsorption resistance; see below. For the systems shown here, 10 Hz turned out to be preferable. The time constant was 300 ms with amplitude u_{ac}^{0} being 3 mV. Based on the imaginary part of the complex impedance $Z(E) = u_{ac}/i_{ac}(E)$, the total capacitance $C_{tot}(E)$ was determined.

In XPS measurements, the Au(111) electrode is attached to a stainless-steel crystal holder which can be attached to the UHV manipulator. Due to highly accurate stepper motors at the manipulator the identical XPS position is approached in every experiment, thereby the intensity of the peaks in the spectrum is not distorted. The Au(111) crystal is also annealed attached to the stainless-steel crystal holder and the electrochemical experiments are also performed attached to it. After the electrochemical adsorption of the iodide in the DMSO or PC based electrolyte, the electrode is removed from the electrochemical cell under potential control and rinsed with high purity MilliQ water (R=18.2 MΩ) to remove residual electrolyte. The transfer of the electrode is done through the air and takes no longer than 3 min. XPS measurements were carried out in a UHV chamber (base pressure 5·10-10 mbar) with a non-monochromatized Mg Kα (1253.6 eV) source. As an electron analyzer, a hemispherical electron analyzer (Omnicron NanoTechnology EA 125) is used. The binding energy is referred to the Au 4f7/2 core level excitation (83.95 eV) [173]. Survey spectra are recorded with an energy resolution of 0.5 eV and a pass energy of 50 eV. For the high-resolution spectra, a resolution of 0.1 eV and an averaging over 4 spectra are chosen.

4.4 Results

4.4.1 Voltammetric analysis

Figure 4.2A displays cyclic voltammograms for adsorption of iodide on the gold single crystal electrode in three different organic solvents. There are no peaks when there is no iodide in the solution (the black curve is an example for PC). The inclined background has often been observed in literature and is presumably due to a reduction of organic impurities in the electrolyte and edge effects [262, 263, 314]. The shape of CVs in three organic solvents are similar. There are two peaks in the case of PC and DG: the first one is a narrow peak, which is attributed to the lifting of the Au(111) reconstruction similar to the aqueous system [230, 238,

314]; this peak is not visible in DMSO. A second broad peak is related to the completion of iodide adsorption in the anodic direction. The increased current density in the CVs in comparison with the blank curve of the potential range -1.13 to -0.43 V is thus due to adsorption and desorption of iodide on the Au(111) electrode. These adsorption peaks are identical to those in the aqueous medium but are much wider [230, 314]. The anodic current at the anodic potential limit may be associated with the beginning bulk iodide oxidation. An examination of the influence of the scan rate on adsorption of iodide at Au (111) in DMSO shows a linear dependence of the peak currents on the sweep rate as expected for an adsorption process and no dependence of the peak position on scan rate, cf**. Figure S4.1**.in the supplementary information (SI).

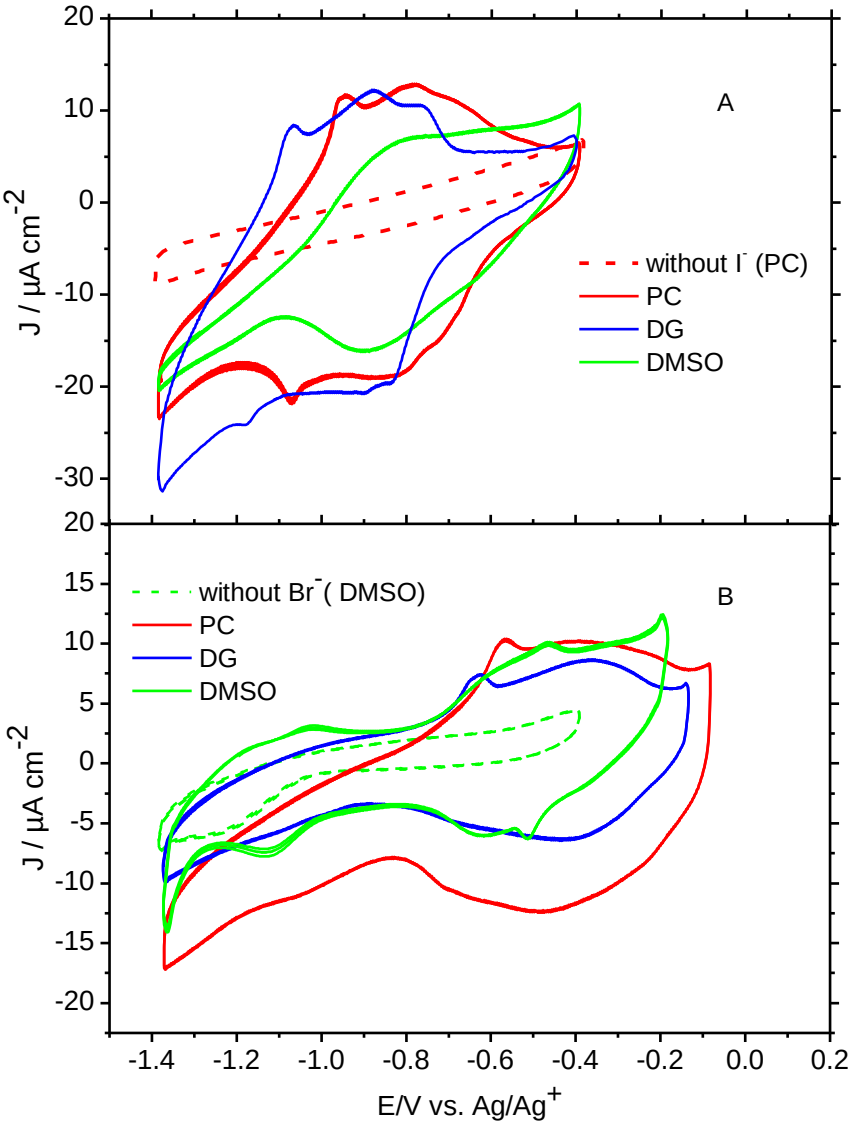

Figure 4.2: CVs for a Au(111) electrode in electrolytes with different organic solvents (propylene carbonate, diglyme and DMSO as indicated in the figure); (A) 10 mM KI + 0.5 M KPF_6 and (B) 10 mM

KBr + 0.5 M KPF_6; sweep rate 50 mV s^{-1}. The broken lines are examples of the CV without specifically adsorbing ion (blank).

The total charge (after background subtraction) of the adsorption peaks (between -1.05 and -0.43 V in PC, between -1.13 and -0.5 V in DG and between -1.0 and -0.46 V in DMSO) is 73, 57.2, and 30.2 µC cm^{-2}, respectively. Adsorption charges increase in this order: DMSO < DG < PC. The corresponding coverages for iodide adsorption on Au(111) for PC, DG, and DMSO, resp., are 0.33, 0.26 and 0.14, calculated by dividing the charge by the theoretical charge for 1 electron per surface Au atom, i.e. 223 µC cm^{-2}. These values are lower than the experimental value in aqueous solution (85 µC cm^{-2} corresponding to coverage of 0.38) [314] to be compared to the coverage of 0.36 and 0.41 corresponding to the $\sqrt{3}x\sqrt{3}$ and ($p\ x\ \sqrt{3}$) phase just before the transition to the rot hexagonal phase) [238].

Cyclic voltammograms of the Au(111) | 10 mM KBr system in three organic solvents are shown in **Figure 4.2B**. The behavior is similar to the case of iodide adsorption, again reconstruction and adsorption of the anion appear at the lowest potential for DG, whereas the adsorption charge is highest in PC. For the three different organic solvents, the voltammetric response is similar. There is no peak without bromide ion in the electrolyte (black curve). At the potential limit between -0.9 and -0.15 V, the Au(111) electrode shows similar behavior for PC, DG, and DMSO with a small sharp peak at -0.56, -0.62, and -0.46 V resp., and a broad peak more positive indicate completion of bromide adsorption.

These results resemble CVs in an aqueous medium which published in literature [29, 229, 316]. The potential region from -0.9 to -0.15 V was integrated to calculate the adsorption charge, as shown in **Table 4.1**. The trend of charge obtained from bromide adsorption in different organic solvent resembles the iodide adsorption in the same electrolytes.

4.4.2 AC- voltammetry and electrochemical impedance spectroscopy

In **Figure 4.3A**, the differential capacitance curves for Au(111) electrode in 0.5 M KPF_6 + 10 mM KI in three different organic solvents are shown. A comparison of the differential capacitance curves measured for non-aqueous solvent mixed electrolyte systems shows some similarities. The C, E curves have typical maxima for all electrolytes containing iodide ions. At more negative potentials, low capacitance values were measured. The similarity of the curves obtained in the anodic and cathodic scan, which almost overlap, reveals that the adsorption process of halides is quite reversible. The adsorption charge of iodide on the Au(111) electrode

obtained by integration evidently increases in order DMSO < DG < PC. There are some variations in the C - E- curves: A comparison with the cyclic voltammograms shows that in PC the peak ascribed to the reconstruction (ca. -1V in PC and -1.1 in DG) shows up as a large peak in the AC-Voltammogram, but only as a shoulder in DG, where the adsorption process (or its completion) leads to a larger peak than in PC (ca. -1 V in DG and -0.65 in PC). The capacitance values obtained in DMSO are significantly lower than in the other solvents, reflecting the lower current density in **Figure 4.2A**.

The C - E curves measured for Au(111) in a bromide solution (0.5 M KPF_6 solutions + 10 mM KBr) in the three different solvents (**Figure 4.3B)** reveal again a similar shape. The process ascribed to the lifting of the surface reconstruction only shows up as a shoulder for both PC and DG. The maxima height decreases in the sequence: PC > DG > DMSO, similar to the charge of bromide adsorption.

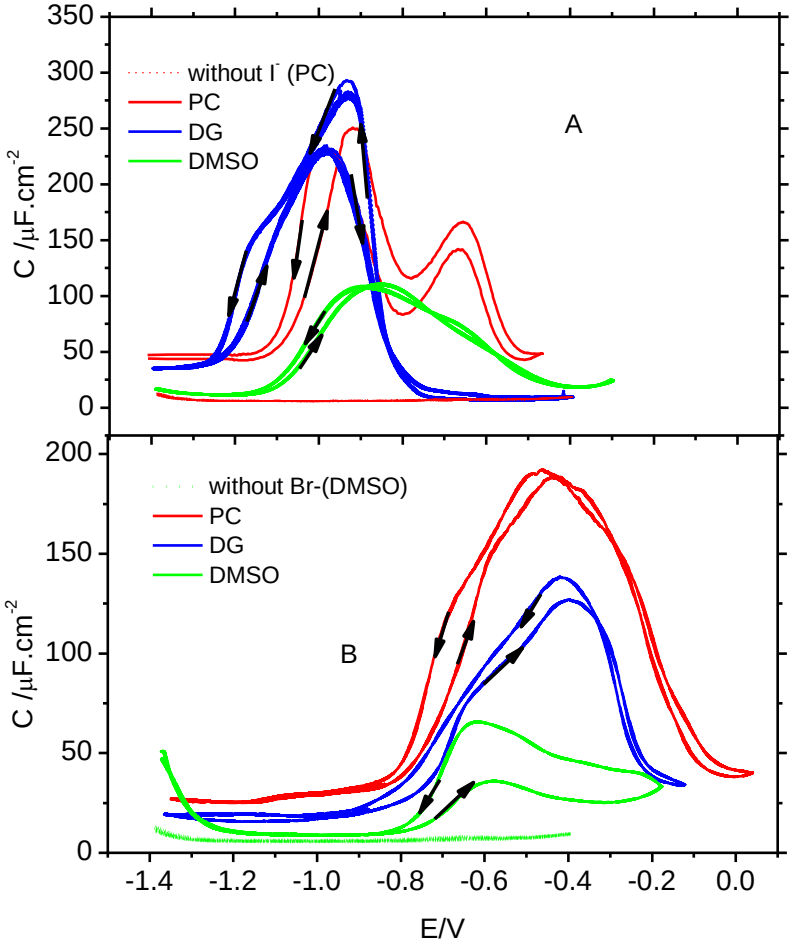

Figure 4.3: Curves of differential capacitance for Au(111) electrode in various solvents (the figure contains solvent names) in solutions 0.5 M KPF_6 + 10 mM KI (A) and 10 mM KBr (B) measured

utilizing an AC signal of 10 Hz frequency, 3 mV r.m.s. The amplitude with 10 mV s^{-1} of scan rate. The dotted line curve is the blank.

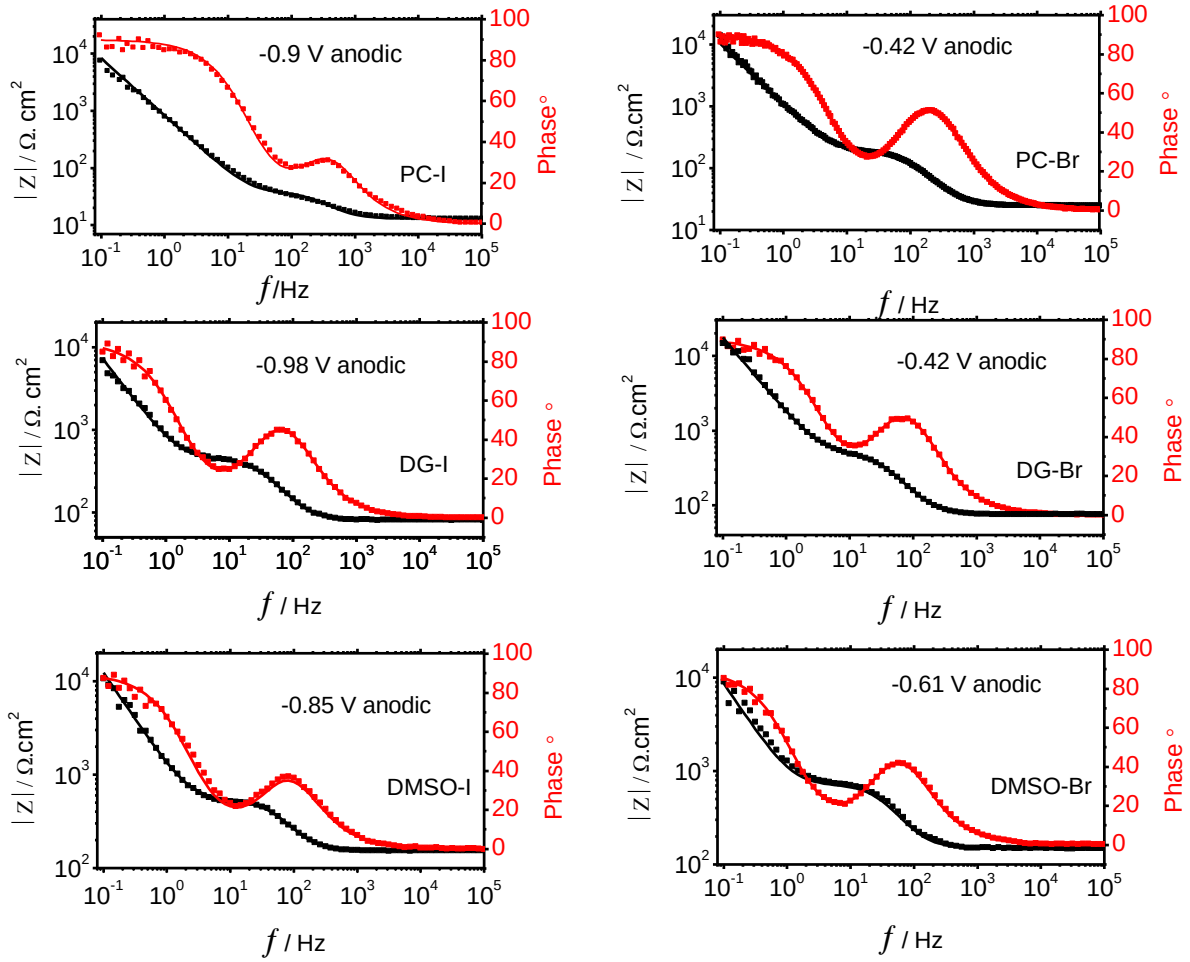

Figure 4.4: Impedance spectra for the iodide or bromide adsorption on Au(111) in three various solvents measured at peak potentials vs. (Ag/Ag^+) of the adsorption. The measured spectra (squares) and of the fitting (thin line) are also reported.

Impedance spectra of the iodide and bromide adsorption in a frequency range from 10^{-1} – 10^{-5} Hz on Au(111) in the three organic solvents were measured at potentials close to the maxima of the above capacitance curves (**Figure 4.3**). Those obtained when the potential was changed in anodic direction are reported in **Figure 4.4,** spectra were recorded after a cathodic potentials variation are shown in **Figure S4.2** and fitting data in **Table S4.1**.

The spectra were fitted by using an equivalent circuit (RCRC) as shown in **Figure 4.1A**. R_{el}, describing the solution layer resistance between the Lugging capillary and the electrode, only depends on their distance and the electrolyte conductivity. The double-layer capacitance C_{DL} is paralleled by a series of adsorption resistance R_{ads} and the adsorption capacitance C_{ads}.

The latter describes the change of the adsorption isotherm with potential, whereas the first is the charge transfer resistance of an adsorption process and thus related to the (reciprocal) rate of iodide and bromide adsorption on the Au(111) electrode surface. This circuit has been proposed [228, 239, 317] to represent a double layer where ion adsorption/desorption occurs at a measurable rate, i.e. where halide ion adsorption/desorption is slow and adsorption kinetics is the limiting factor. This equivalent circuit adequately describes the measured spectra (**Figure 4.4)**. Data are summarized in **Table 4.1** which shows that adsorption capacitance and rate increase in the order: DMSO < DG < PC < H_2O. Also, the adsorption rate for bromide is lower than for iodide in the three different organic solvents. Values obtained for I^- adsorption in PC are similar to those reported in our previous publication [314]. The adsorption capacitance determined from EIS is always larger than that determined from AC voltammetry. A close inspection of the EIS spectra shows that at the frequency of 10 Hz, which is used in the AC measurements, the total impedance is largely determined by the adsorption resistance and the determination of the value of the adsorption capacitance at this single frequency therefore is less reliable, but it reveals the potential dependence of the adsorption process. (Lower frequencies for AC measurements would require unpractically low sweep rates). **Table 4.1** also lists the adsorption potentials. In all solvents, the adsorption of iodide occurs at 0.35 to 0.4 V more negative than that of bromide, similar to the aqueous system. We also include the adsorption potentials (peak potentials) with respect to the pzc in the respective solvent, using values for the pzc determined from the capacitance minima in dilute solutions which will be reported in our forthcoming paper [315].

Table 4.1: Fitting values of the elements of the equivalent circuit (**Figure 4.1A**) used for the impedance spectra and charge(C) of halide adsorption on Au(111) electrode obtained from the voltammetry or AC voltammetry.

	PC				**DG**				**DMSO**		**H_2O**			
	I^-		**Br^-**		**I^-**		**Br^-**		**I^-**	**Br^-**	**I^-**		**Br^-**	
E/V vs. Ag/Ag^+ for EIS	-0.9	-0.65	-0.42		-0.98		-0.42		-0.85	-0.61	-0.19 [a]	-0.08 [a]	-	
R_{sol} /Ω.cm^2	15	15.3	24		81		76		150	153	1.2	1.2	-	
C_{dl} /µF.cm^{-2}	13.9	7.7	13.9		16.6		12.6		9.91	10	3.9	2.9	-	
R_{ads} /Ω.cm^2	30	61	171		393		497		504	601	2.9	3.2	-	
C_{ads} /µF cm^{-2}	317	205	178		204		115		111	34	318	216	-	
Q_{CV} /µC.cm^{-2}	73		68		57.2		55		28.5	29	85		90 $(\sqrt{7} \times \sqrt{7})$[286]	
Q_{AC} /µC.cm^{-2}	60		64.5		55.5		54		33	15	64			
Coverage	0.33		0.3		0.26		0.25		0.15	0.13	0.38		0.4 [318]	
E_P^A vs. Ag/Ag^+(V) (anod)	-0.94	-0.79	-0.58	-0.40	-1.06	-0.87	-0.62	-0.36	-0.81	-0.44	-0.19 V [a]	-0.08 V [a]	0.19 V [a] [229]	0.34 V [a] [229]
E_P^A V vs. pzc	-0.84	-0.69	-0.48	-0.30	-1.37	-1.18	-0.93	-0.67	-0.80	-0.43	-0.75	-0.65	-0.37	-0.22

Values of Br^- adsorption potentials in aq. solution from literature [229], pzc of Au(111) in water = 0.56 V vs. SHE [8], [a] vs. SHE.

In order to elucidate why the anion coverage varies that much in different solvents, we performed experiments in which iodide was adsorbed from an aqueous solution where the coverage is well known, inserted the iodine covered crystal into the PC or DMSO electrolyte at a potential positive of the iodine adsorption peak. The subsequent potential cycles are shown in **Figure S4.4**. The charge for iodide desorption in the first cathodic sweep is larger now and corresponds to a full iodide monolayer also in DMSO, whereas subsequent sweeps are identical to the CVs shown in **Figure 4.2**.

4.4.3 Effect of water on adsorption rate

Since water is a major impurity in aprotic solvents, it is essential to study the impact of water content on the adsorption capacitance and the rate of adsorption. Investigation of the variation of water content on values of adsorption capacitance and adsorption rate of iodide on gold single crystal (111) was carried out in propylene carbonate and DMSO containing KPF_6 as supporting electrolyte in presence 10 mM KI by cyclic voltammetry, AC voltammetry and EIS measurements.

Figure 4.5A shows cyclic voltammograms recorded for the Au(111) in 10 mM KI with 0.5 M KPF_6 in propylene carbonate solutions with different water contents together with the corresponding AC-capacitance curves in **Figure 4.5**B. With increasing water content, the CVs become sharper and ultimately resemble that in aqueous solution [314]. The adsorption charge increases with increasing water content to be 53, 72, 79, 83.2 and 88 ($\mu C / cm^2$) with respect to the water content of 11, 35, 240, 620, and 1100 ppm, respectively. Charges obtained from capacitance curves were 61, 68, 77.5 and 82.6 $\mu C\ cm^{-2}$ and thus similar to those from cyclic voltammetry. The increase in the capacitance with increasing water content is similar to the results reported by Friedl and coworkers on Au (111) in ionic liquid interface [319] and on polycrystalline gold in perchlorate containing propylene carbonate [219].

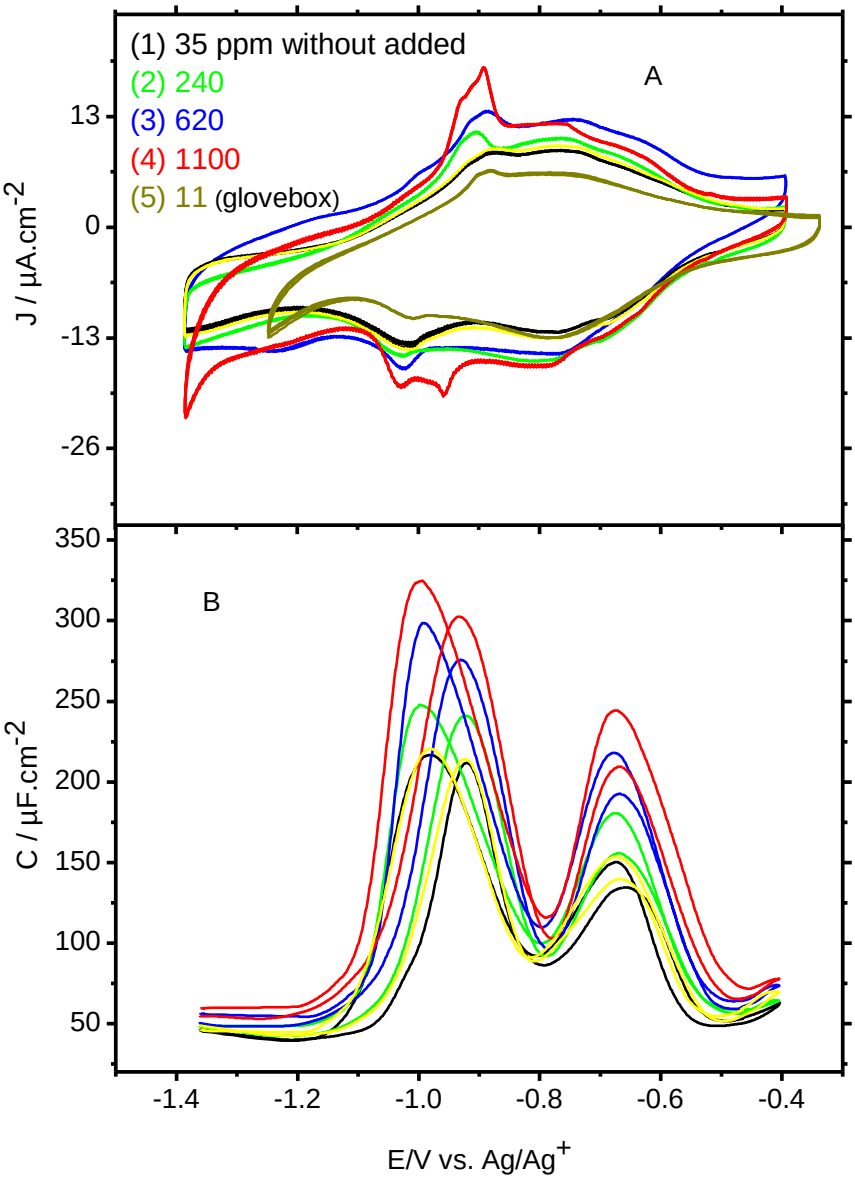

Figure 4.5: (A) Cyclic voltammograms for Au(111) in propylene carbonate + 0.5 M KPF_6 +10 mM KI in different water content: (1) without added water, (2) 240, (3) 620, (4) 1100, and (5) 11 (measurement inside glovebox) ppm at a sweep rate of 50 mV s^{-1}. (B) Differential capacitance curves determined using an AC perturbation of 10 Hz frequency, 3 mV r.m.s. the amplitude at a sweep rate of 10 mV s^{-1}. The yellow line is a control experiment.

The effect of water content on the rate of adsorption was studied by using EIS in the same solutions at the potential of maximum capacity. The results are represented as the Bode plot, as shown in **Figure 4.6 (A and B)**. The fitting results (again using the equivalent circuit shown in **Figure 4.1**A) are shown in **Table 4.2**. It is obvious that the capacitance and rate of

adsorption increase with increasing water content, but a clear effect is only observed for very large water contents.

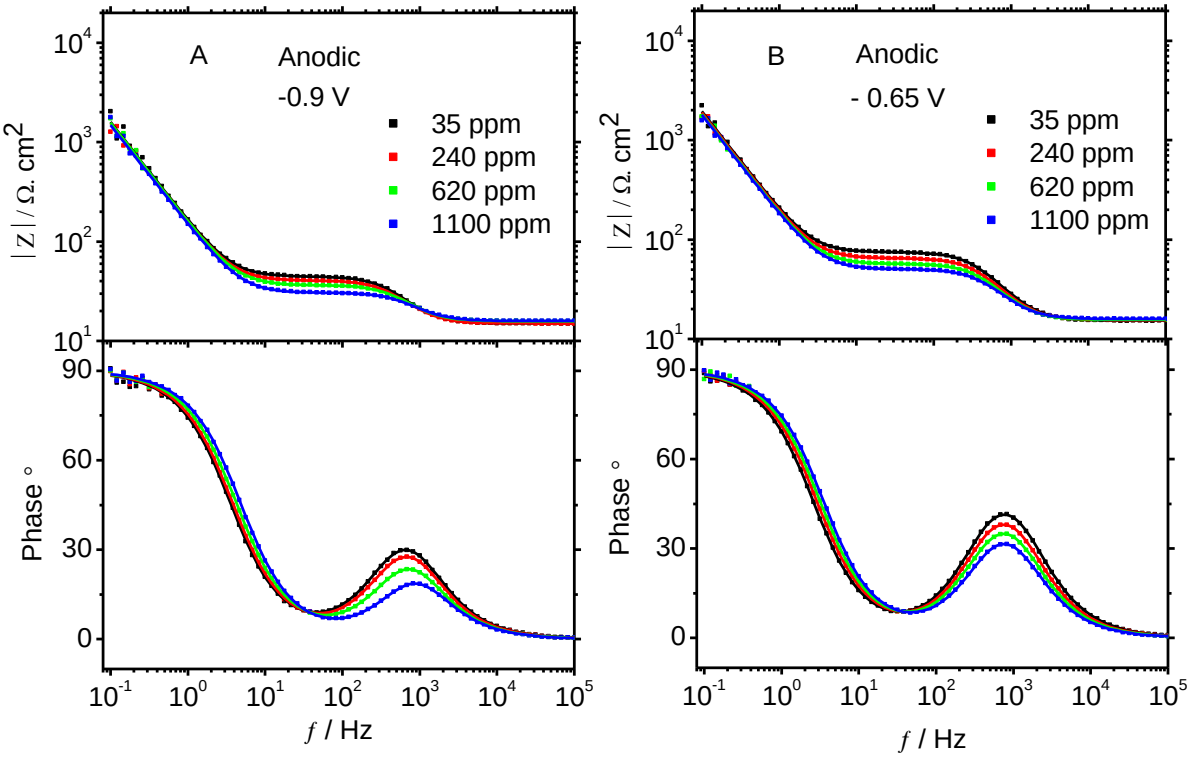

Figure 4.6: Impedance spectra for the iodide adsorption on Au(111) in propylene carbonate measured at peak potentials of (A) -0.9 V and (B) -0.65 V anodic. The measured spectra (squares) and of the fitting (thin line) are also reported.

Table 4.2: Fitting values of the elements of the equivalent circuit (**Figure 4.1A**) used for the impedance spectra in 10 mM KI+ 0.5 M KPF_6 in PC on Au(111) electrode with different water content.

	35 ppm (2.3 mM)		**240ppm (16 mM)**		**620 ppm (41mM)**		**1100 ppm (73 mM)**	
	-0.9 V	**-0.65 V**	**-0.9 V**	**-0.65 V**	**-0.9 V**	**-0.65 V**	**-0.9 V**	**-0.65 V**
R_{sol} / Ω.cm^2	15	15.3	15	15.5	15.8	15.6	15.9	15.9
C_{DL} /µF.cm^{-2}	13.9	7.7	14.8	8.8	15.9	9.7	16.7	10.6
R_{ads} / Ω.cm^2	30	61	25.5	49.5	20.3	41.6	15.4	31.4
C_{ads} /µF.cm^{-2}	317	205.4	325.5	230	334	257.5	340	260
Charge (Q/µC cm^{-2})from CV	72		79		83		88	

The influence of water content was also investigated in iodide containing DMSO. **Figure 4.7A and B** show the effect of added water on the cyclic voltammogram and differential capacitance curves of Au (111) in 10 mM KI + 0.5 M KPF_6. The charge of the adsorption region increases with the addition of water to around 1210 ppm from 40 to 53 $\mu C.cm^{-2}$ in the potential limit from -1.13 to -0.4 V in the CV and from 33 to 39 $\mu C.cm^{-2}$ in AC voltammetry. It is obvious that the tilted baseline in CV is due to the water content. The adsorption charge in glovebox (11ppm) is 24 $\mu C.cm^{-2}$.

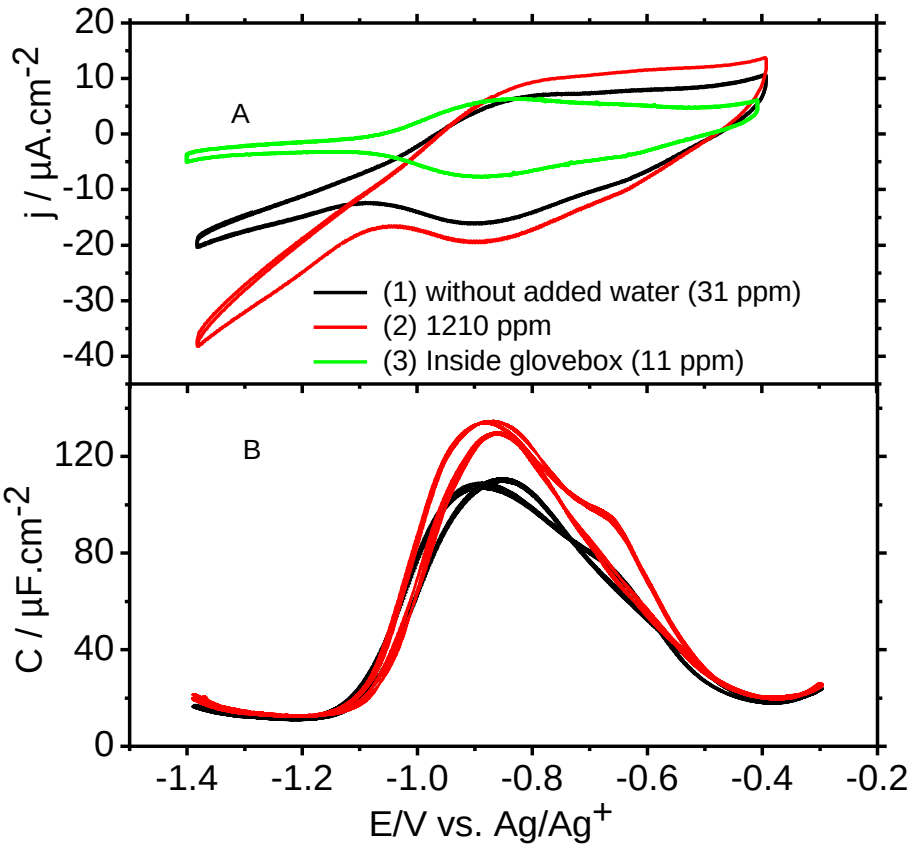

Figure 4.7: (A) Cyclic voltammograms for Au(111) in DMSO + 0.5 M KPF_6 +10 mM KI in different water content: (1) without added water, (2) 1210 ppm, and (3) 11 ppm (inside glove box) at a sweep rate of 50 mV s^{-1}. (B) Differential capacitance curves determined using an AC perturbation of 10 Hz frequency, 3 mV r.m.s. the amplitude at a sweep rate of 10 mV s^{-1}.

Impedance spectra recorded at the capacitance maxima are shown in **Figure 4.8** for the two different water contents; fitting results are given in **Table 4.3**. The rate of adsorption and the adsorption capacitance increases with rising water content as before in propylene carbonate. Both for PC and DMSO the increase of adsorption capacitance and adsorption rate with increasing water content is less than the apparent increase in adsorption charge as obtained from

CV or AC-CV. Particularly in the case of PC the capacitance determined from AC-CV is too low at low water content because at 10 Hz it cannot completely be separated from the total impedance which is largely determined by the adsorption resistance; at higher water content the latter is decreased and the capacitance is better separated and therefore the values are higher. The increase in capacitance and therefore also the charge could therefore in part also be an artefact. It is also interesting to note that the capacitance determined in DMSO with the lowest water content from CV at higher sweep rates is 120 $\mu F.cm^{-2}$ and therefore agrees well with those determined by EIS even at higher water content.

The amount of water added is in the same order of magnitude as the concentration of iodide. This may well explain that the shape of the CV in PC approaches that of the aqueous system with increasing water content. The iodide ion will be largely solvated by water molecules, but it is also obvious that in DMSO the shape is not changing much, although its acceptor number which describes the interaction between the anion and the solvent is much lower.

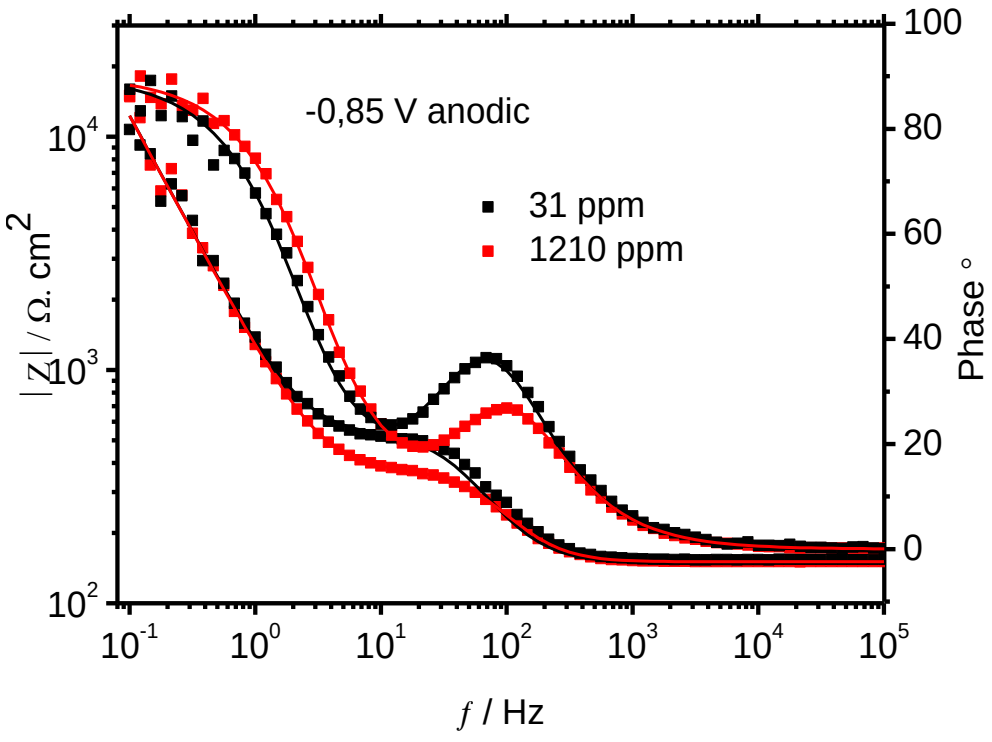

Figure 4.8: Impedance spectra for the iodide adsorption on Au(111) in DMSO recorded at a peak potential of - 0.85 V anodic. The measured spectra (squares) and of the fitting (thin line) are also reported.

Table 4.3: Fitting values of the elements of the equivalent circuit (**Figure 4.1A**) used for the impedance spectra in 10 mM KI+ 0.5 M KPF_6 in DMSO on Au(111) electrode with different water content.

	31 ppm (1.9 mM)	**1210 ppm (73.3 mM)**
	-0.85 V	**-0.85 V**
R_{sol} / Ω.cm^2	150	150.6
C_{DL} /µF.cm^{-2}	9.9	10.6
R_{ads} / Ω.cm^2	504	393
C_{ads} /µF.cm^{-2}	111	136
Charge (Q / µC cm^{-2}) (CV)	40	53

4.4.4 XPS measurements

Evaluation of the CV and differential capacitance data has shown that the adsorption charge of iodide and thus the amount of adsorbed iodide is smaller in DMSO based electrolyte than in PC based electrolytes. This observation was also confirmed by XPS as follows: After the electrochemical adsorption of iodide on Au(111) from the PC, DMSO and water-based electrolytes, the electrode was washed with H_2O and transferred to UHV. The high-resolution spectra of the 3d core-level excitations of iodine are shown in **Figure 4.9**, a survey spectrum is shown in **Figure S4.3**.

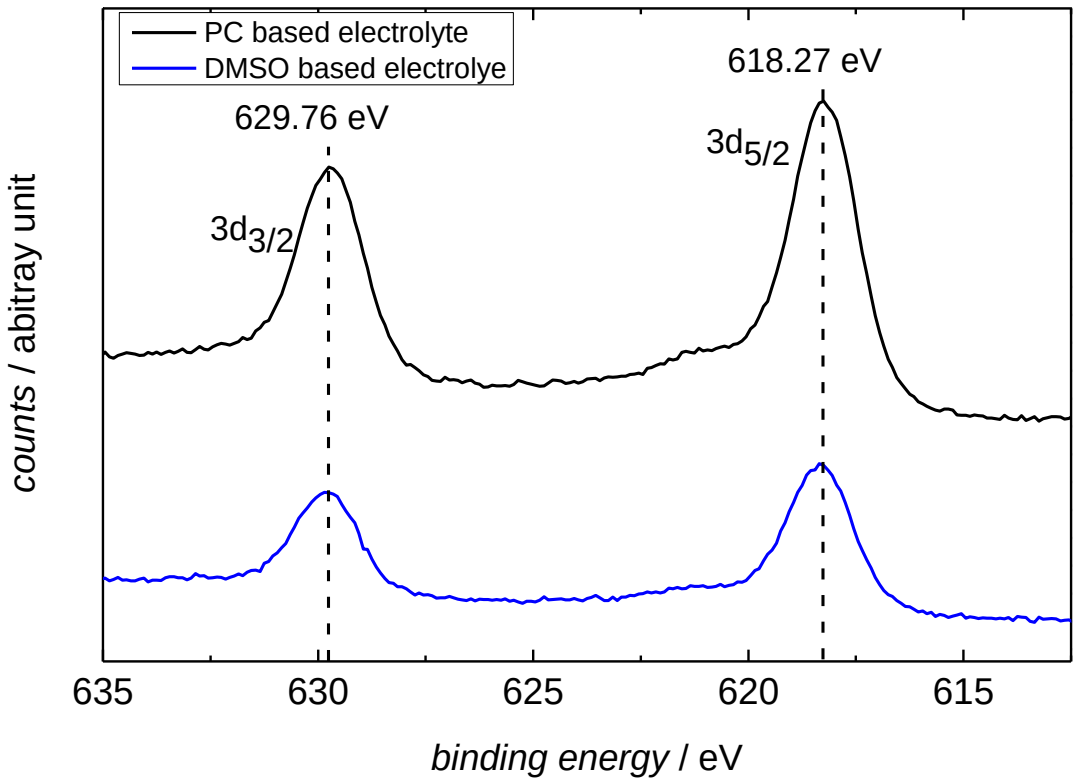

Figure 4.9: Binding energy region of the 3d core-level excitation of iodine.

After adsorption of I^- during 3 cycles in 0.1 M $KClO_4$ +10 mM KI between -1.4 and -0.4 V the potential was stopped at -0.45 V during the anodic sweep. Then, the electrode is removed from the cell under potential control and rinsed with MilliQ water to remove residual electrolyte.
Black: PC as a solvent; Blue: DMSO as a solvent. The spectra are shown on the same intensity scale.

The intensity of the 3d doublet in **Figure 4.9** shows that less iodide was adsorbed from the DMSO based electrolyte than from the PC based electrolyte. The ratio of the areas under these peaks shows that only about half as much iodide was adsorbed from DMSO which is in good agreement with the charge values obtained from the CVs. Since the intensity might be influenced by the thickness of a layer of adventitious carbon (which is well-known contamination in XPS experiments and leads to some attenuation of the signal intensity) it is important to note that the amount of carbon is comparable in both measurements, cf. the C1s core level excitations in the survey spectra (see **Figure S4.3** in the supporting information). We could not detect any sulfur peak, which would indicate adsorbed DMSO molecules, but this is probably due to its low atomic sensitivity factor. The amount of adsorbed iodide in the PC based electrolyte is also comparable to the adsorption of iodide from aqueous solution, which is

known to result in a coverage of 0.4 at the chosen potential of 0.3V vs. Ag/AgCl [238], (see survey spectra in **Figure S4.3** in the supporting information).

The binding energy of the 3d5/2 core level excitation, observed in the DMSO and PC-based electrolyte of 618.27 eV is in good agreement with the reported value for the adsorption of iodide in aqueous solution (618.4±0.5 eV) [320, 321]. As the binding energy is also a measure for the chemical oxidation state of the investigated element, this confirms the previously reported zero valency of adsorbed I also for adsorption from the organic solvent and therefore little ionic character between the Au surface and the adsorbed I [320, 321].

4.5 Discussion

Besides demonstrating that reliable electrochemical data on single crystal electrodes can be gained in non–aqueous electrolytes and besides elucidating factors influencing rates of a simple model reaction, the main issue of this work and our preceding paper [314] was to find out whether commonly-used concepts (or models) for describing ionic adsorption from aqueous electrolytes also hold in aprotic solvents. These concepts consist in the use of the Stern model (together with the Gouy-Chapman theory) for the description of ionic adsorption in the absence of strong surface - ion interaction (non -specific adsorption) on the one hand. The interaction with the surface is governed by electrostatics, and adsorption is very fast. On the other hand, strong, specific adsorption, governed by the chemical interactions between ion and electrode metal, is usually described by models involving the Langmuir, Frumkin or similar isotherms. The latter involves a nearly complete discharge of the adsorbing ion and a potential-dependent equilibrium constant for the adsorption reaction, leading to a typical shift of the adsorption potential (e.g. the potential of half coverage) in the range of 60 mV/z (where z is the charge number) for a change of the concentration in a solution by a factor of 10. (For a detailed discussion of the charge number and the electrosorption valency the reader is referred to [229, 230]. The maximum coverage corresponds to a closed packed layer of the (largely discharged) ions. Due to the stripping of the solvation shell upon discharge and formation of the bond with the surface, there is an activation barrier for this process leading to a limited rate of this process. Examples are the adsorption of iodide, bromide and sulfate on Pt and Au single crystal electrodes [229 - 231, 233, 248, 289, 322 - 325]. Also upd systems and proton adsorption e.g. on Pt belong to this category. The potential dependence leads to adsorption peaks in cyclic voltammograms (or capacitance peaks in AC-voltammetry), the peaks of which shift by ca. 60 mV/z for a concentration change by one order of magnitude. Also in the first case (solely

electrostatic interaction), such peaks may be observed in capacitance curves: positive or negative of the capacitance minimum at the pzc (at low concentrations), the capacitance increases and then falls again to a lower value due to saturation effects and repulsion in the double layer. At high concentrations, peaks for anions and cations merge. The integration of these capacitance peaks leads to values much below a monolayer.

Since iodide and bromide belong to the most strongly adsorbing anions in aqueous systems, we had expected a similar behavior typical for strongly adsorbing systems also in the organic electrolytes examined here. This, however, is only partially true:

- The cyclic voltammograms and AC voltammograms in PC resemble those in the aqueous system. The total adsorption charge has a similar magnitude which only increases little when water is added. Even a peak corresponding to the (lifting of the) reconstruction is clearly visible. However, this latter feature evolves considerably when adding water, and therefore might require the accumulation of residual water in the double layer. Also, in the case of DMSO the shape is quite different.
- The total adsorption charge and thus the estimated iodide and bromide coverage in DMSO is at least a factor of two smaller than in PC. Whereas the iodine coverage in PC of about one third might correspond to a $\left(\sqrt{3} \times \sqrt{3}\right)$ adlayer structure also observed in an aqueous environment, to explain the much lower packing density in DMSO we would have to assume a mixed adlayer of the halogen with solvent molecules.
- An even stronger indication that in organic solvents iodide and bromide do not behave as strong adsorbates (as defined for aqueous systems above) is the dependence on iodide concentration reported in our previous paper [314].
- On the other hand, the slowness of the adsorption reaction also indicates that the ions are discharged upon adsorption. At least a mere electrostatic interaction of the halides with the surface can be excluded.

In order to elucidate possible solvent characteristics which influence the behavior, we summarize some characteristic values in **Table 4.4** and compare them with our experimental data. The adsorption potentials of iodide and bromide with respect to the pzc value (to be reported in our forthcoming paper [315]), also cf. **Table S4.2**) decrease in the order H_2O > DMSO > PC > DG. This is the same order in which the acceptor number (AN) decreases. This is not astonishing since the AN describes the interaction strength of a Lewis acid (here the solvent) with a Lewis base (the anion) [326]. The free enthalpy of iodide or bromide is lower

(more negative) in water (high AN) than in DG (low AN) and therefore adsorbed only at higher potentials in water than in DG.

The adsorption rate of iodide and bromide increases in the series DMSO < DG < PC < H_2O. The same trend is followed by the adsorption charge and the maximum adsorption capacitance. Differently from the dependence of the coverage on the solvent (as discussed above), a dependence of the adsorption rate on solvent properties could certainly be expected, because the solvation shell of the ion has to be partially stripped off upon contact adsorption. At first instance, it was expected that this behavior can be related to the dielectric constants or the dipole moments of the organic solvents. However, no such correlation exists. The same is true for the permittivity parameter on which the rate of charge transfer should depend according to the Marcus theory (e.g. [327]). Another factor which might affect the adsorption rate of halide on Au(111) is the E_τ^N value which describes the normalized solvent polarity [328] and which successfully described the influence of solvents and additives on oxygen reduction in aprotic solvents [274] but obviously is not applicable here. Particularly for the latter two values, one expects a decrease of the rate with increased permittivity parameter or polarity, whereas rather the contrary is observed.

Of course, for an adsorption reaction, the situation is quite different from a 'simple' charge transfer: the activation barrier is not just related to the reorganization energy, but the (partial) stripping of the solvent [33, 329]. The corresponding energy certainly is related to the reorganization energy. Another factor which may determine the activation barrier and therefore may well influence the adsorption rate is the strength of the interaction of the solvent with the metal surface. As a descriptor for this interaction strength, the donor number (DN, [330]) has been discussed in a number of papers on the influence of the solvent on the double layer capacity and the point of zero charge on liquid metals (Hg, Ga and various alloys thereof) [301, 331 - 335]. The DN is the negative enthalpy value in the non-coordinating solvent 1,2-dichloroethane with zero DN between a Lewis base and the typical Lewis acid $SbCl_5$ in dilute solution[326]. DN evaluates a solvent's ability to solvate Lewis acids and cations. In the above papers, however, only the thermodynamic aspects are addressed, not the rate. But from the linear free enthalpy relationship, one can conclude that also the activation barrier for solvent displacement should increase with an increased donor number. Our data show indeed that the adsorption is slowest in the solvent with the highest DN, namely DMSO. But it is also obvious, that this is not the whole story: For the other solvents, the DN only varies little, whereas the adsorption rate changes by an order of magnitude. Furthermore, it is interesting to note that the DN of

DMSO is larger than that of iodide (DN=28.9) or bromide (DN=33.7)[336], therefore both strongly compete for sites on the surface. The potential dependence will also be determined by that of the interaction of DMSO with the surface, which at the pzc is expected to be substantial and also in the absence of a strongly adsorbing anion will change its orientation only at more negative potentials [301]. In the other solvents studied here, this effect, which may also be the cause for the wide potential range over which the adsorption is occurring, is smaller due to the lower DN. Only water is different. One difference is the much larger acceptor number (AN), which lowers the effective DN of the halide anion in solution; but this can hardly explain the observed effects. Another difference is the much smaller size of the water molecule. In [314] we had observed that the rate of iodide adsorption is largely dependent on the size of the double layer: it is smallest in the presence of large solvated cations and largest for small cations. The reason is, that for the small size of the double layer the iodide ion – the reactant – is outside of the DL and therefore subject to the complete potential drop in the reaction, whereas for a large extension of the DL the iodide ion enters the DL and only a part of the potential drop causes the reaction, similar to the Frumkin effect. The effect of the solvent on the adsorption rate then is due to the different radius of the solvated cation. An even more important effect could be the closer approach of the halogenide ion to the surface before losing the solvation sphere: the energy barrier is located much closer to the surface, thus the electronic interaction in the transition state is increased, leading also to an increased pre-exponential factor. An alternate view is that an ion pair is formed [337] leading to the stabilization of iodide or bromide with a smaller solvated cation in the DL. Further studies with a non-solvated cation like TBA^+ would be necessary to clarify this. This might also explain the effect of added water: a few hydrated cations might reduce the size of the double-layer locally at some places of the surface, where iodide ions are discharged and adsorbed at a high rate.

Table 4.4: Physical properties of organic solvents.

Solvent	**PC**	**Diglyme**	**DMSO**	**Water**
Dielectric constant ε_s [338, 339]	69	7.4	46.7	80.2
Permittivity parameter $\gamma = (1/\varepsilon_{op} - 1/\varepsilon_s)$ [327]	0.48	0.368	0.44	0.55
Dipole moment μ / D [340]	4.9	1.97	3.96	1.8546
10^{-3} polarizability α_s / nm^3 [341, 342]	9	-	10.5	1.5
E_τ^N Normalized solvent polarity [328]	0.472	0.244	0.444	1
Donor number [281, 338]	15.1	19.5	29.8	18
Acceptor number AN [326, 343]	18.3	9.9	19.3	54.8

4.6 Conclusion

The cyclic voltammetry, differential capacitance, XPS and impedance characteristics of the Au(111)/electrolyte interface have been studied to determine the effect of solvent nature on the extent and rate of adsorption of bromide and iodide in PC, DG, DMSO in comparison to water. The adsorption charge of halides from cyclic voltammetry and C, E curves increases in the order: DMSO < DG < PC < water. The adsorption rate of halides follows the same trend. This is largely determined by the donor number of the solvent, which can be assumed to describe the metal-solvent chemisorption interaction energy: The solvents with high DN like DMSO molecules are strongly chemisorbed in the Helmholtz layer, with their negative (oxygen) ends directed to the electrode surface. This competitive adsorption – the DN of DMSO and iodide are similar – leads to less than full monolayer coverages of the halide.

Another factor playing a role seems to be the size of the double layer: The much higher rate in the case of water cannot be explained by its DN. Rather, we assume an effect similar to the Frumkin effect: the halide ion, still being outside of the DL formed by the solvated cations, approaches the surface more closely before being discharged. For larger solvent molecules and correspondingly large solvated cations, the halide ion enters the double layer and then is not subject to the complete potential drop. A further, maybe even more important effect is the distance of closest approach of the ion, leading also to a closer distance of the transition state from the surface and thus stronger electronic interaction. Also added water leads to an increased

adsorption rate. This may be well understood in this context, because cations will be preferentially solvated by water, thus the size of the DL will be (locally) reduced.

4.7 Supporting information

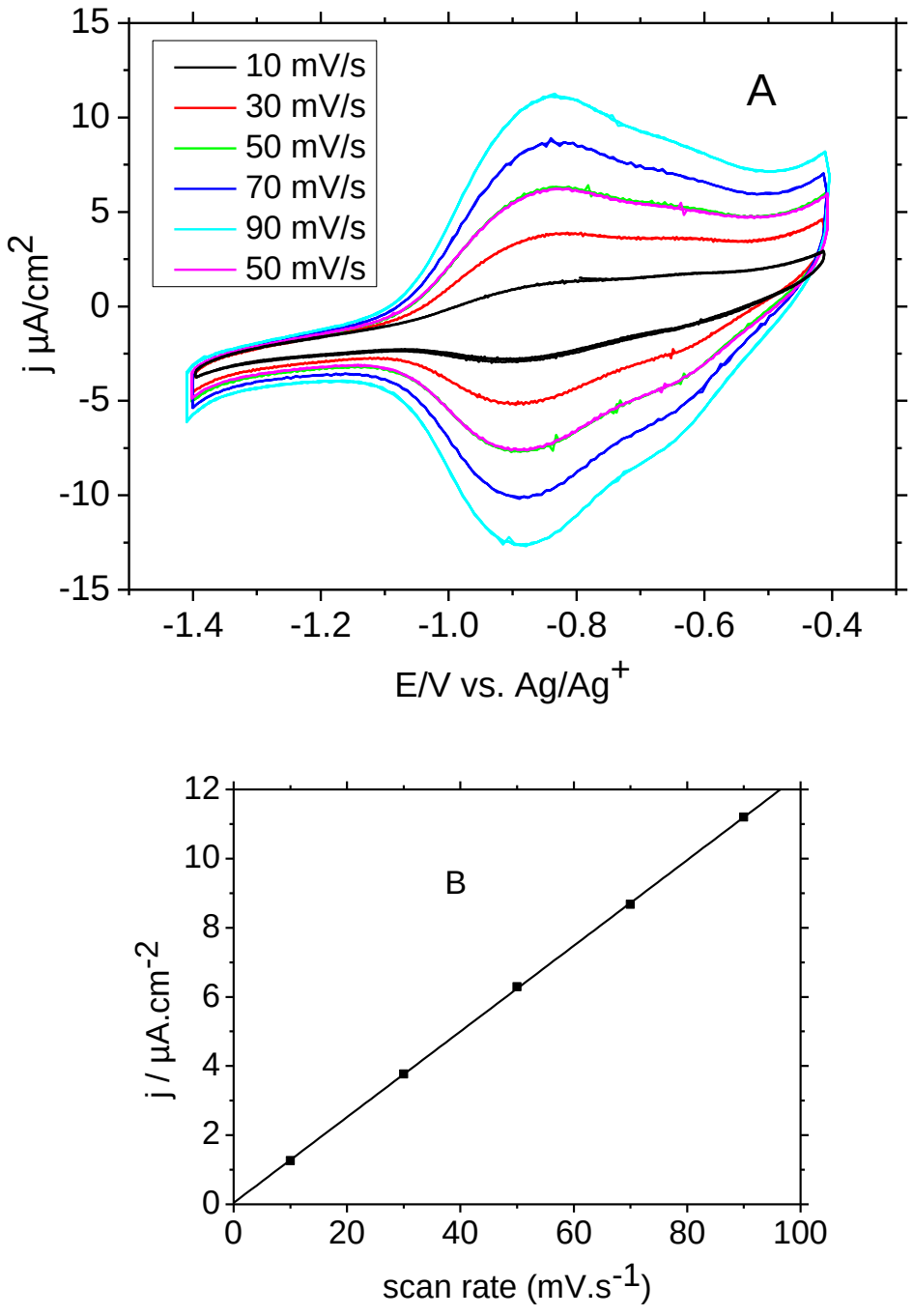

Figure S4.1: (A) Cyclic voltammograms for Au(111) in DMSO + 0.5 M KPF_6 +10 mM KI in different scan rate: (a) 10, (b)30, (c) 50, and (d) 70 and (e) 90 mV s^{-1}, (B)The relation between scan rate and the peak current after subtracting the base line.

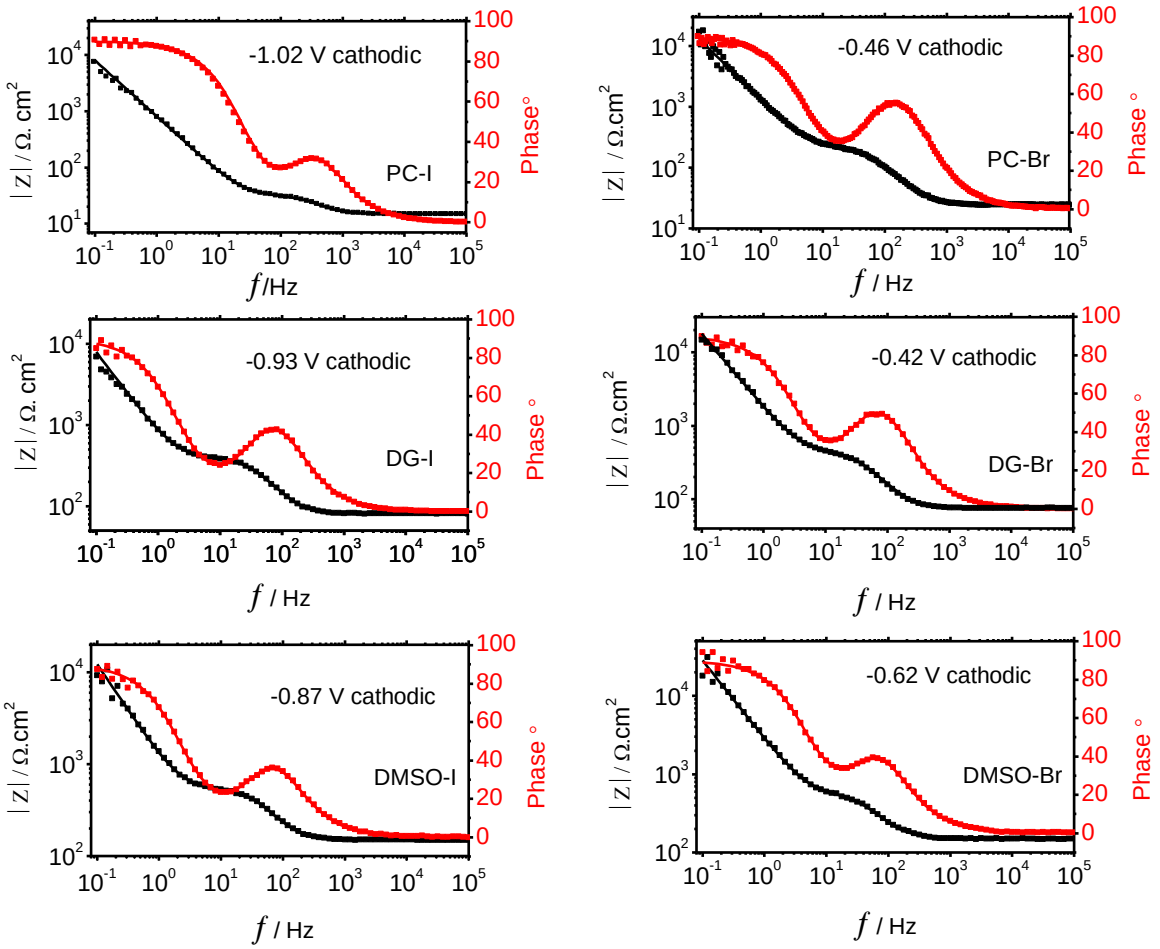

Figure S4.2: Impedance spectra for the iodide or bromide adsorption on Au(111) in three various solvents measured at cathodic peak potentials Vs. (Ag/Ag^+) of the adsorption. The measured spectra (squares) and of the fitting (thin line) are also reported.

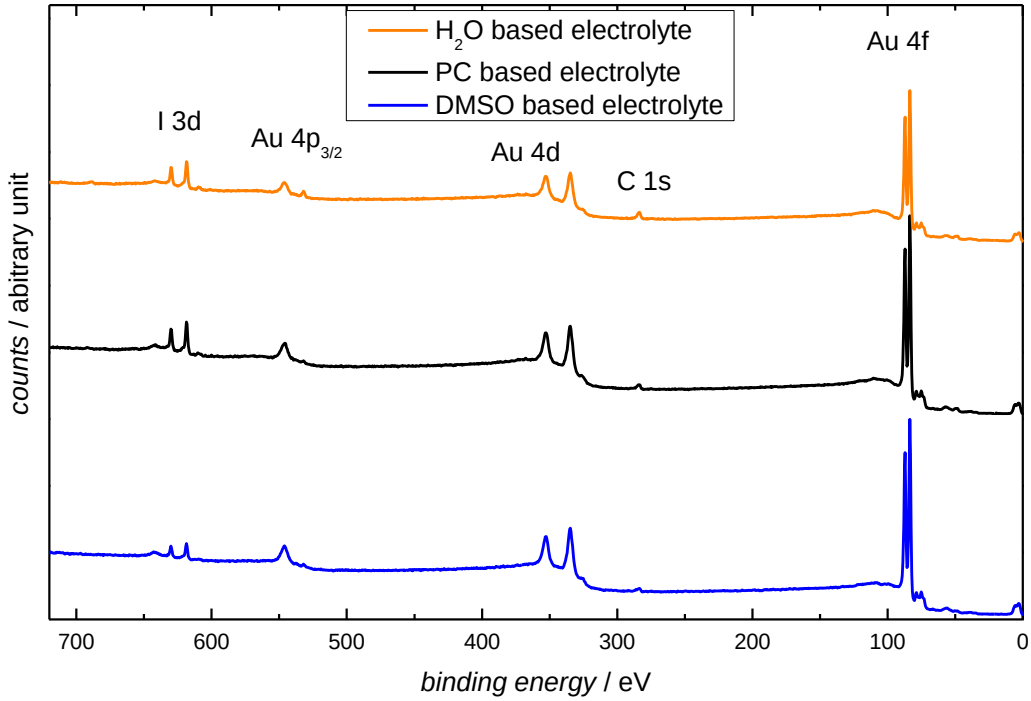

Figure S4.3: Survey XP spectra of the Au(111) electrode after iodide adsorption in aqueous solution 0.1 M $KClO_4$ + 10 mM KI + 1mM KOH (orange trace measurement), 0.1 M $KClO_4$ + 10 mM KI in PC (black traced measurement) and in 0.1 M $KClO_4$ + 10 mM KI in DMSO (blue traces measurement). After adsorption of I^- during 3 cycles in iodide containing PC and DMSO between -1.4 and -0.4 V vs. Ag/Ag^+ the potential was stopped at -0.45 V during the anodic sweep. Adsorption of iodide in aqueous solution is done between 0.2 and 1.2 V vs. RHE, the potential was stopped at 1.15 V during the anodic scan. Then, the electrode is removed from the cell under potential control and rinsed with MilliQ water to remove residual electrolyte.

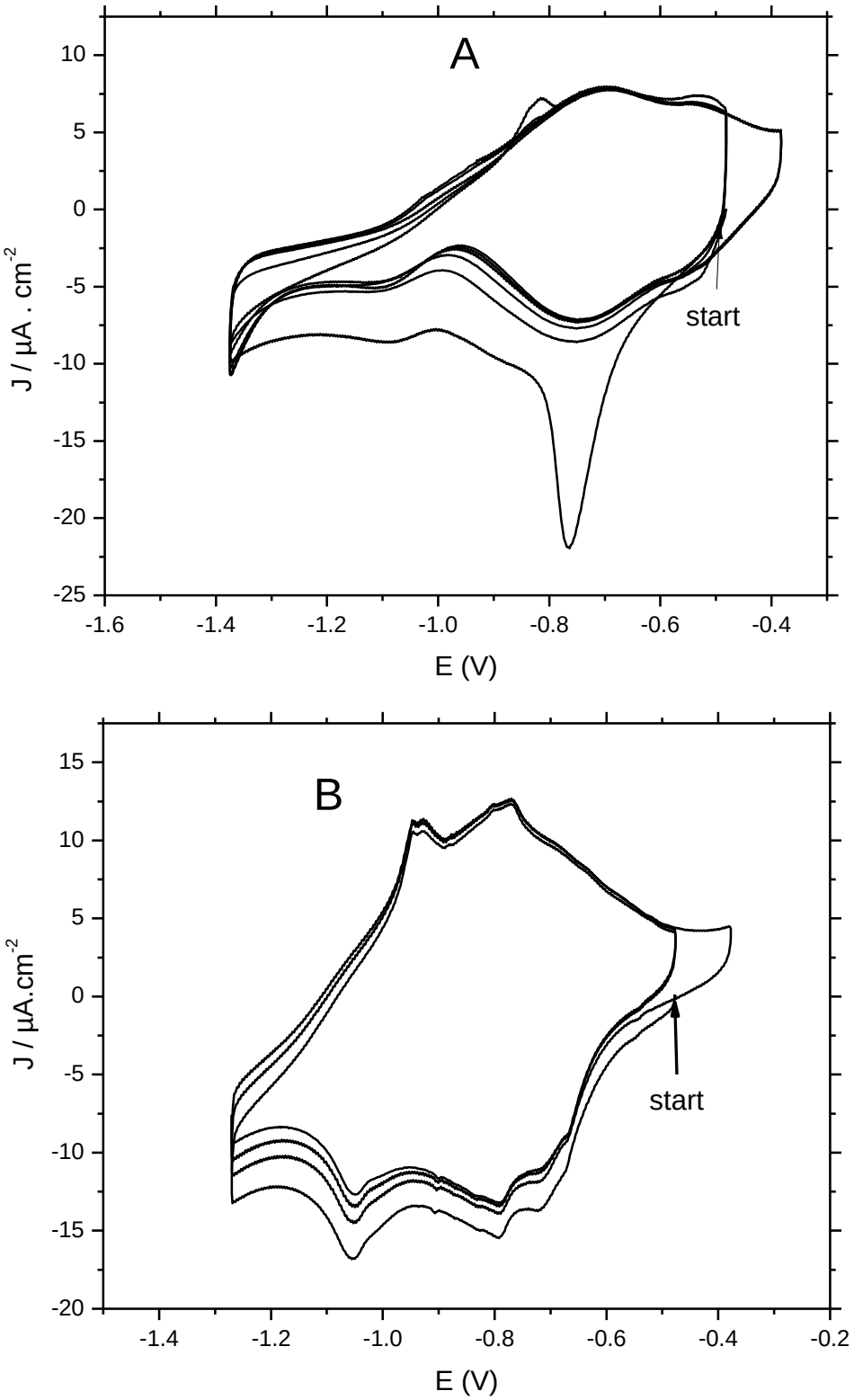

Figure S4.4: CVs for a Au(111) electrode pre-covered by a monolayer of iodide, sweep rate 50 mV s^{-1}.(A) 10 mM KI + 0.5 M KPF_6 in propylene carbonate and (B) 10 mM KI + 0.5 M KPF_6 in DMSO.

The Au(111) electrode was prepared by flame annealing and cooling under an argon atmosphere, then inserted into the electrode in aqueous iodide solution (0.45 M KPF_6+ 10 mM KI [pH

11]) to form an adsorbed layer of iodide; after 3 cycles between 0.2 and 1.2 V vs. RHE, the potential was stopped at 1.14 V in anodic direction. Then, the iodide modified electrode was inserted into the iodide containing the organic solution of propylene carbonate and DMSO under potential controlled (-0.48 V) and the scan in the cathodic direction was started.

Table S4.1: Fitting values of the elements of the equivalent circuit (**Figure 1A**) used for the impedance spectra of halide adsorption (cathodic peak potentials) on Au(111) electrode.

Parametrs	**PC**		**DG**		**DMSO**	
	I^-	**Br^-**	**I^-**	**Br^-**	**I^-**	**Br^-**
R_{sol} / Ω.cm^2	13.6	24.5	81.1	75.7	150	153
C_{DL} /µF.cm^{-2}	16.4	14.5	14.8	12.1	10.5	9.87
R_{ads} / Ω.cm^2	18	220	337.8	430	417	512
C_{ads} /µF.cm^{-2}	282	175	216.6	119.7	116	62.7

Table S4.2: Adsorption potentials of anions versus pzc in different aprotic solvents.

Solvent		**PC**	**DG**	**DMSO**	**H_2O**
E_1^a V vs. Ag/Ag^+	I^-	-0.94	-1.06	-0.81	-0.19[a]
	Br^-	-0.58	-0.62	-0.44	0.19 [a]
E_2^a V vs. Ag/Ag^+	I^-	-0.78	-0.87	-	-0.08 [a]
	Br^-	-0.40	-0.36	-	0.34 [a]
$E_{1/2}$ V for DMFc* vs. Ag/Ag^+		-0.48	-0.32	-0.34	-
E_1^a V vs. DMFC	I^-	-0.46	-0.74	-0.47	-0.19[a]
	Br^-	-0.1	-0.3	-0.09	0.19 [a]
E_2^a V vs. DMFC	I^-	-0.30	-0.55	-	-0.08 [a]
	Br^-	0.08	-0.04	-	0.34 [a]
pzc vs. Ag/Ag^+		-0.1	0.31	-0.01	0.56 [a]
pzc vs. DMFc		0.38	0.63	0.33	0.51
E_1^a V vs. pzc	I^-	-0.84	-1.37	-0.80	-0.75
	Br^-	-0.48	-0.93	-0.43	-0.37
E_2^a V vs. pzc	I^-	-0.69	-1.18	-	-0.65
	Br^-	-0.30	-0.67	-	-0.22
E_1^a V vs. Ag/Ag^+ (AC)	I^-	-0.91	-1.1	-0.86	-0.22 [a]
	Br^-	-0.58	-0.64	-	-
E_2^a V vs. Ag/Ag^+ (AC)	I^-	-0.65	-0.98	-0.6	-0.11 [a]
	Br^-	-0.42	-0.4	-	-
E_{onset} V vs. Ag/Ag^+ (@ 10% of Cap.)	I^-	-1.09	-1.2	-1.06	-0.29 [a]
	Br^-	-0.77	-0.75	-0.74	-
E_{onset} V vs. pzc (@ 10% of Cap.)	I^-	-0.99	-1.51	-1.05	-0.85
	Br^-	-0.67	-1.06	-0.73	-

[a] vs. SHE.

Chapter five:

The pzc of Au(111) in aprotic solvents

A.S. Shatla [a,b] and H. Baltruschat [a]

[a] Institute of Physical and Theoretical Chemistry, University of Bonn, 53117 Bonn, Germany.
[b] Permanent address: Menoufia University, Faculty of Science, Chemistry Dept., Shebin Elkoom, Egypt.

The results presented in this chapter have not been published yet. This chapter describes the determination of the pzc of Au(111) in aprotic solvents and studying the parameters which affect the pzc, as well as, investigation the electrode/electrolyte interface of gold in propylene carbonate by ATR-SEIRAS technique.

5.1 Abstract

The voltammetric and Gouy-Chapman capacitance minimum measurements were conducted on a Au(111) and roughened Au(111) electrode in aprotic electrolytes in the absence and presence of specifically adsorbed ions for concentrations ranging from 0.001 to 0.5 M. Negative of the point of zero charge (pzc), the capacitance maximum increases in the order $Ca^{2+} < Li^{+} < K^{+}$, but the pzc value is independent of cation nature. The capacitance values have a slight dependence on cation type at a more negative potential. The pzc is not correlated with the dielectric constant of the aprotic solvent despite its dependence on the kind of solvent. The pzc value of Au(111) is influenced by metal-solvent interactions and donor number for different solvents. The pzc moves to more positive values with increasing water content. Specific anion adsorption shifts the pzc to more negative values. The pzc value is more negative for the roughened electrode compared to the single crystal electrode. Propylene carbonate (PC) adsorption in the presence of perchlorate and iodide was examined on gold film by surface-enhanced infrared absorption spectroscopy (SEIRAS).

5.2 Introduction

Within the framework of recent research for better energy storage systems like batteries, and fuel cells based on non-aqueous electrolytes with their wider potential range are becoming more and more important. A deeper understanding of the electrochemical interface is a requirement for further development of these systems and the underlying processes. The properties of electrode/ electrolyte interface structure are influenced by some factors such as kind and concentration of ions [344, 345], nature of solvent molecules, and atomic structure of the electrode [346]. For instance, different cations can result in a redistribution of the potential drop in the interfacial double layer and improvement of the anion adsorption rate [314, 347]. Besides variation of organic solvents affects the intensity of double-layer capacitance through differences in electrolyte resistance and relaxation time constant of an electrical double layer (EDL) [348, 349].

The potential of zero charge (pzc) is of fundamental significance in surface electrochemistry and its importance lies in providing information about the structure of the electrode/electrolyte interface. Several techniques are available for the determination of the pzc. One of these consists in measurements of capacitance curves and location of the capacitance minimum caused by the diffuse double layer contribution to the total differential capacitance in dilute solutions (according to the Gouy-Chapman-Stern model). The correlation with the

electronic work function of the electrode is clearly established. [350, 351]. Frumkin and Petri have proposed two different pzcs to determine the fundamental magnitudes of Pt/electrolyte interface and are potential of zero total charge (pztc) and potential of zero free charge (pzfc) [10]. The pztc has been observed and measured due to transferring the total charge involving the transferred charge during the chemisorption of e.g. hydrogen atoms. While the pzfc (electronic charge lying on the electrode) is observed in absence of adsorption of species and is equivalent to pzc for simplicity [352].

Although several capacitance data were provided on the single crystal electrodes in aqueous interface such Au (111) [8, 18, 28, 229, 353 - 356] and Ag (111) [225, 344, 354, 357 - 362], measurements of the pzc of the Au(111) or other single crystal surfaces in aprotic electrolytes in absence and presence of specific adsorption has not yet been extensively reported except for[249, 363].

The pzc has been determined in organic solvents on polycrystalline electrodes such as Au electrode [219, 341, 364], silver electrode [352, 365], and platinum electrode [366]. In addition many studies have been reported for mercury [298, 367 - 373], gallium and indium-gallium alloys [300, 301, 305, 332, 334, 335, 374 - 377], bismuth [300, 309, 378].

In-situ SERS together with capacitance –potential curves were used to estimate the pzc on polycrystalline Ag electrode in a Br^- containing DMSO electrolyte [379]. Recently the influence of cations of perchlorate salts on adsorption of acetonitrile on gold film was investigated by using SEIRAS [215].

The properties of the electrical double layer in various ionic liquids on many polycrystalline and single crystal electrodes were reviewed in detail [380]. In situ surface-enhanced Raman spectroscopy connected with differential capacitance measurements was established to estimate the pzc values for several ionic liquids on the silver electrode [381]. It has been determined for a variety of ionic liquids by using capacitance –potential measurements on Au, Hg, GC, and Pt electrodes [382, 382].

The goal of this study is to elucidate the influence of the solvent properties on the position of the pzc of a well-oriented Au(111) and a roughened electrode. Also, the influence of the water content, and cation and anion identity on the point of zero charge of the Au (111) electrode will be studied. We furthermore characterize the interface using SEIRAS. This is a continuation of our efforts to elucidate the influence of the solvent on the extent and rate of ionic adsorption. A more general aim of this paper is to elucidate whether and to demonstrate that, such surface-sensitive measurements are possible at single crystals in aprotic solvents.

5.3 Experimental

5.3.1 Chemicals and materials

Potassium perchlorate ($KClO_4$, ≥ 99%, SIGMA-ALDRICH), potassium hexafluorophosphate (KPF_6, ≥ 99%, ACROS), (KBr, ≥ 99.5%, MERCK), lithium perchlorate ($LiClO_4$, ≥ 99%, SIGMA-ALDRICH), calcium perchlorate tetrahydrate (99 %, Sigma Aldrich) was dried under reduced pressure and T= 83 °C in a Büchi-oven for 48h prior to further use), silver nitrate ($AgNO_3$, ≥ 99%, SIGMA-ALDRICH), decamethylferrocene ($Me_{10}Fc$, 97%, SIGMA-ALDRICH), H_2SO_4 spectra pure grade (Merck), propylene carbonate (PC, 99.7%, SIGMA-ALDRICH) and acetonitrile (ACN, 99.8%, ACROS), Diethylene glycol dimethyl ether (Diglyme, DG, 99.5%, anhydrous, dried over a molecular sieve), Dimethyl sulfoxide (DMSO, 99.7%, over molecular sieve) were used. All aqueous cleaning solutions were made with 18.2 MΩ·cm Milli-Q Millipore water. The electrolytes have been deaerated with very pure argon (99.999%, AIR LIQUIDE).

Glasses, Teflon, and PCTFE materials have been treated with 5 M KOH solution to remove organic pollutants, as well as inorganic contaminants are eliminated by immersion into chromic acid.

5.3.2 Electrochemical conditions and instrumentation

All tests were conducted at room temperature in a three-compartment electrochemical cell. The working electrode was a gold single crystal disk electrode (Au(111)) (ϕ =10 mm) and was electrochemically cleaned by cycling in 0.1M sulfuric acid solution in the potential range between 0.03 to 1.8 V vs. RHE. It was annealed by gas flame and cooled in an inert gas (Ar), as described previously [314]. The accuracy of the preparation was examined by cyclic voltammetry between 0.03 and 1.2 V in hanging meniscus configuration in 0.1 M H_2SO_4. An Au sheet acted as the counter electrode for cyclic voltammetry and differential capacitance measurements. For the measurements in the non-aqueous electrolytes, the Au(111) electrode was quickly cooled down in an Argon stream, and then rapidly was moved to the cell, which set for non-aqueous electrolytes. Potentials were recorded versus an $Ag|Ag^+$ reference electrode in either DMSO or ACN containing 0.1 M $AgNO_3$ depending on the type of electrolyte in the working electrode compartment connected to the cell by a Luggin capillary.

The water content was determined by Karl Fischer titration and was approximately 35 ppm in PC, 31 ppm in DMSO, 20 ppm in ACN, and 45 ppm in DG after the electrochemical experiments.

The potential scale of the reference electrode was calibrated using decamethylferrocene (DMFc) (SI **Table S5.1**) as a reference redox system, and its potential is regarded as more solvent independent than that of the Fc+/Fc couple [384]. Thus we report pzc values of Au(111) electrode versus the $DMFc^+$/DMFc reference system for comparability. $E_{1/2}$ (vs. Ag/Ag+) for $DMFc^+$/DMFc in DMSO, PC, ACN, and DG is -0.342, - 0.484, - 0.457, and - 0.317 V, respectively. Electrode potentials were controlled with an EG&G potentiostat (model 273A) (National Instruments GmbH, Munich, Germany). The cyclic voltammograms were recorded using LabVIEW software. In situ FTIR spectroscopic measurements were conducted on Nicolet iS50 FTIR spectrometer fitted with a liquid nitrogen-cooled MCT-A detector in conjunction with a single-reflection mirror adapter prepared for spectrum acquisition. The incident angle of the IR beam was at 60 °. Parker Balston adsorption dryer cleaned the accessories of the optical bench and mirror attachment with dry, CO_2-free air. A 4 cm^{-1} spectral resolution, resulting in a final data spacing of 0.5 cm^{-1} was used for all measurements. The spectrum is an average of 32 interferograms. Results are shown as absorbance, log (R0/R), where R0 is the reference potential reflectance which is demonstrated in each measurement. As a consequence, elevated peaks signify gain or enhanced adsorption of particles, while decreased bands (downward) reflect species reduction. The spectroelectrochemical cell used for SEIRAS measurements was previously described in detail [215].

5.3.3 Differential capacitance measurements and data analysis

The capacitance-potential curves for the Au(111) | interface were was determined by measuring the in-and out - of phase components of the interfacial impedance using a Lock-in amplifier (EG&G, model 5210). At a constant frequency of 10 Hz, the real and imaginary parts of the impedance were determined, and the potential was swept with 10 mV per second from -1.0 to 0.8 V versus Ag $|Ag^+$. Measured impedance values of the impedance were evaluated using the equivalent circuit shown in **Figure 5.1**. It is composed of a resistance (R_{el}), which represents the electrolyte resistance in series with a parallel combination of a capacitance (C_{DL}), which represents the double-layer capacitance, and another resistance (R_{ct}) which represents the charge transfer resistance. The time constant was set to 300 ms and the amplitude u_{ac}^0 was 3 mV.

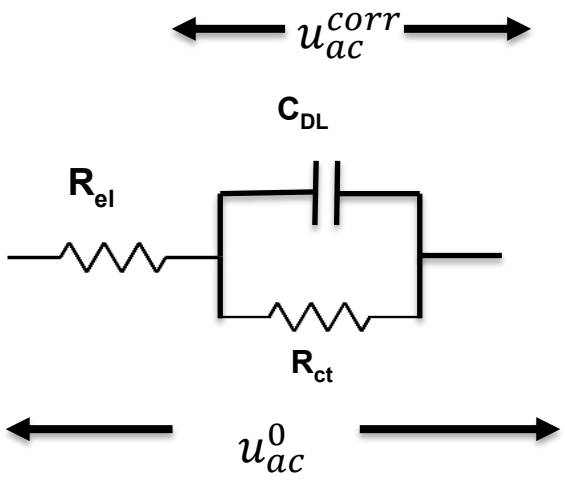

Figure 5.1: The equivalent circuit used for the simulation of C vs. E curves from AC voltammetry.

As described before [385] [386], particularly for electrolytes with low conductivity, the superimposed AC potential has to be corrected for $i_{ac}R$ potential drop as follows:

$$u_{ac}^{corr} = u_{ac}^{0} - R_{el} i_{ac} \tag{5.1}$$

Where, $i_{ac} = i_{ac}^{re} + j i_{ac}^{im}$

Here, i_{ac}^{re} and i_{ac}^{im} are the real and imaginary parts of the ac current, respectively. Dividing i_{ac} by i_{ac}^{corr} gives:

$$\frac{i_{ac}}{u_{ac}^{corr}} = \frac{i_{ac}^{re} + j i_{ac}^{im}}{u_{ac}^{0} - R_{el}\,(\, i_{ac}^{re} + j i_{ac}^{im}\,)}$$

$$= \frac{i_{ac}^{re}\,(u_{ac}^{0} - i_{ac}^{re}\,R_{el})}{(u_{ac}^{0})^2 - 2\,u_{ac}^{0} R_{el}\, i_{ac}^{re} + (\,R_{el} i_{ac}^{re}\,)^2 + (\,R_{el} i_{ac}^{im}\,)^2} + j\,\frac{i_{ac}^{im}\,(u_{ac}^{0} - i_{ac}^{im}\,R_{el})}{(u_{ac}^{0})^2 - 2\,u_{ac}^{0} R_{el}\, i_{ac}^{re} + (\,R_{el} i_{ac}^{re}\,)^2 + (\,R_{el} i_{ac}^{im}\,)^2}$$

$$= Y_{re-corr} + j\, Y_{im-corr} \tag{5.2}$$

Here, $Y_{re\text{-}corr}$ and $Y_{im\text{-}corr}$ are the corrected real and imaginary parts of the admittance.

$$C_{diff} = \frac{Y_{im-corr}}{\omega}\,, \qquad R_{ct} = \frac{1}{Y_{re-corr}} \tag{5.3}$$

Hence by utilizing $Y_{im\text{-}corr}$ for determining C_{diff} , it is possible to get the real value of the differential capacitance.

5.4 Results and discussion

5.4.1 Effect of solvent

The double-layer capacity for different concentrations of KPF_6 on Au(111) electrode in the range 3 to 100 mM in DMSO and in the range 5 to 500 mM in PC, DG, and ACN is exhibited as a function of the potential in **Figure 5.2** (**A, B, C, and D**), respectively. From the minima, at the lowest concentrations we obtain the pzc values. They differ between the anodic and cathodic scan because during the anodic scan the surface is reconstructed. The reconstruction is lifted at positive potentials, and therefore the pzc values obtained in the cathodic sweep refer to the unreconstructed Au(111). In DMSO the difference is much less than in the other cases. Probably the anodic potential limit is not positive enough for a lifting of the reconstruction to be achieved. The pzc values in the positive direction which refer to freshly prepared reconstructed surface is higher than in the negative direction (unreconstructed surface) because the unreconstructed surface has a lower work function than the reconstructed one[387, 388] The pzc values relative to DMFc scale changes as follows: ACN > DG > H_2O > PC > DMSO (**Table 5.1)**.

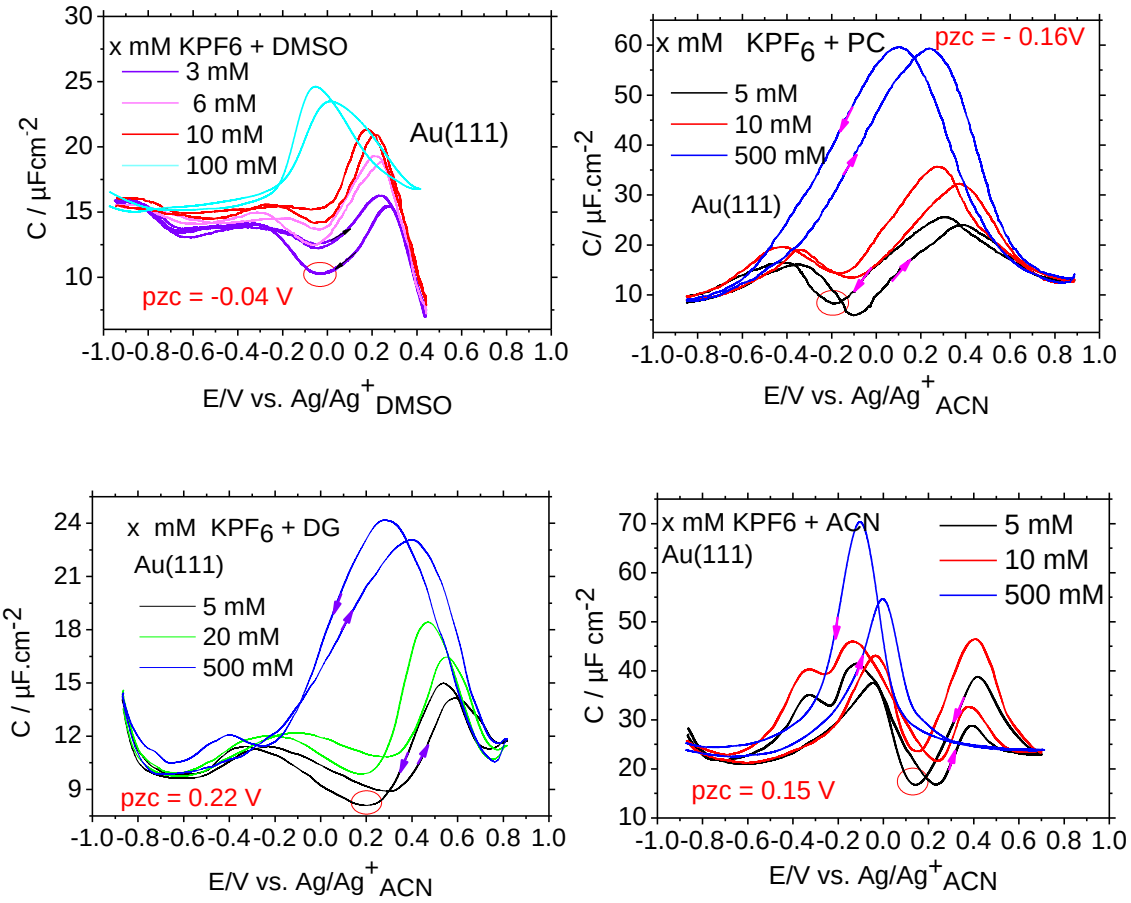

Figure 5.2: The differential capacity of the double layer at Au(111) electrode in different concentrations solutions of KPF_6 in propylene carbonate (PC) (A), dimethyl sulfoxide (DMSO) (B), diglyme (DG) (C), and Acetonitrile (ACN) (D) at 10 Hz frequency, 3 mV r.m.s. the amplitude at a sweep rate of 10 mV s^{-1}.

Thus, the pzc is most positive in ACN and most negative in DMSO, and this behaviour is in good agreement with the pzc of polycrystalline gold in aprotic solvents [341] where E_{min} values of gold (poly) and other metals (calibrated versus bisbiphenylchromium (BBCr(I/0) scale and mainly obtained from capacitance measurements) were summarized from literature data. For polycrystalline Au, they increase in the order MeOH < H_2O < DMSO < dimethylformamide < PC < ACN. The value of pzc of Au(111) in KPF_6 containing DMSO is - 0.04 V (vs. Ag/Ag+) which is slightly different from that reported by Borkowska [363] on the same electrode in DMSO containing $LiClO_4$ (pzc ~ 0.01 V vs. Ag/Ag^+).

Table 5.1: Physico-chemical properties of some organic solvents at 25 °C (KPF_6).

Solvent	**pzc vs. Ag/Ag^+**		**pzc vs. DMFc* (V)**		**ε[338, 339]**	**Donor number [281, 338]**	**10^{-3} polarizability α_s / nm^3 [341, 342]**	**Dipole moment μ / D [340]**
	Anod	Cath	Anod	Cath				
DMSO	- 0.01	-0.04	0.33	0.3	46.7	29.8	10.5	3.96
PC	- 0.1	-0.16	0.4	0.32	69	15.1	9	4.9
DG	0.31	0.22	0.6	0.54	7.23	19.5	-	1.97
ACN	0.24	0.15	0.7	0.61	27.7	14.1	4.48	3.92519
H_2O[8]	-	*0.56*[a]	-	*0.51*	80.2	18	1.5	1.8546

[a] vs. SHE, [a] vs. SHE, pzc value in water vs. Fc/Fc^+ = - 0.06 V (0.56 -0.624 [389]) and then it is converted vs. DMFc as following: = -0.06 + 0.57 (0.57 V is this is difference between $E_{1/2}$ for Fc and DMFc as in the literature [390]) .

It is observed that the pzc values correlate neither with the dielectric constant of solvents nor with the solvent polarizability. Other factors like specific metal-solvent interactions and related to this, the donor number of the solvent will also play a role [300, 369, 378]. A more detailed analysis involving the determination of the inner layer capacitance and in particular solvent contribution would be necessary, as done for liquid metal electrodes like Hg in [378, 391-393].

5.4.2 Effect of cations

It is well established that the thickness of the interfacial double layer is dependent on cation size [347, 394]. The differential capacitance curves measured for organic solutions of monovalent cations (Li^+ and K^+) and divalent cation (Ca^{+2}) with the same anion (ClO_4^-) of salt in contact with acetonitrile are presented in **Figure 5.3** (**A, B, and C**), respectively.

The curves practically converge at the negative potentials limit independent of the cation with a value of about 10 μC cm^{-2}. At less negative charges, the capacity (maximum) increases in the order $Ca^{2+} < Li^+ < K^+$ in accordance with corrected Stokes radii derived by Nightingale [395], (**Table 5.2**). The capacitance value at more negative potentials has a slight dependence on the cation like at the Hg | DMSO interface for 0.1 M solutions [370] and at the Hg interface with aqueous electrolytes (0.1 N) [396]. The data of the C(E) curves are summarized in **Table 5.2**. The capacitance (C) at large negative charges (C ~ 10.5 μF cm^{-2}) compares closely values obtained for other electrodes materials (Bi, Ln + Ga, and Hg) in ACN [300]. The values of pzc are practically independent of the cation similar to observed on Au(111) in aqueous solution

[397]. As shown in Fig. 3C, the left maximum capacitance is very small, and therefore, Ca^{+2} is probably very large indicating large solvation shells [398]. Since 250 mM and 500 mM almost no longer differ, the salt is not completely dissociated.

Table 5.2: Radii of alkali and alkaline cations ($XClO_4$+ACN).

Cation	$r_{cStockes}$[a]	$C_{max\ (5\ mM)}$	pzc V vs. DMFc (Cath)
Li^+	3.82	19.2	0.67
K^+	3.31	26	0.68
Ca^{+2}	4.12	16.3	0.66

[a] Corrected Stokes radius of the ion as described in Ref [395]

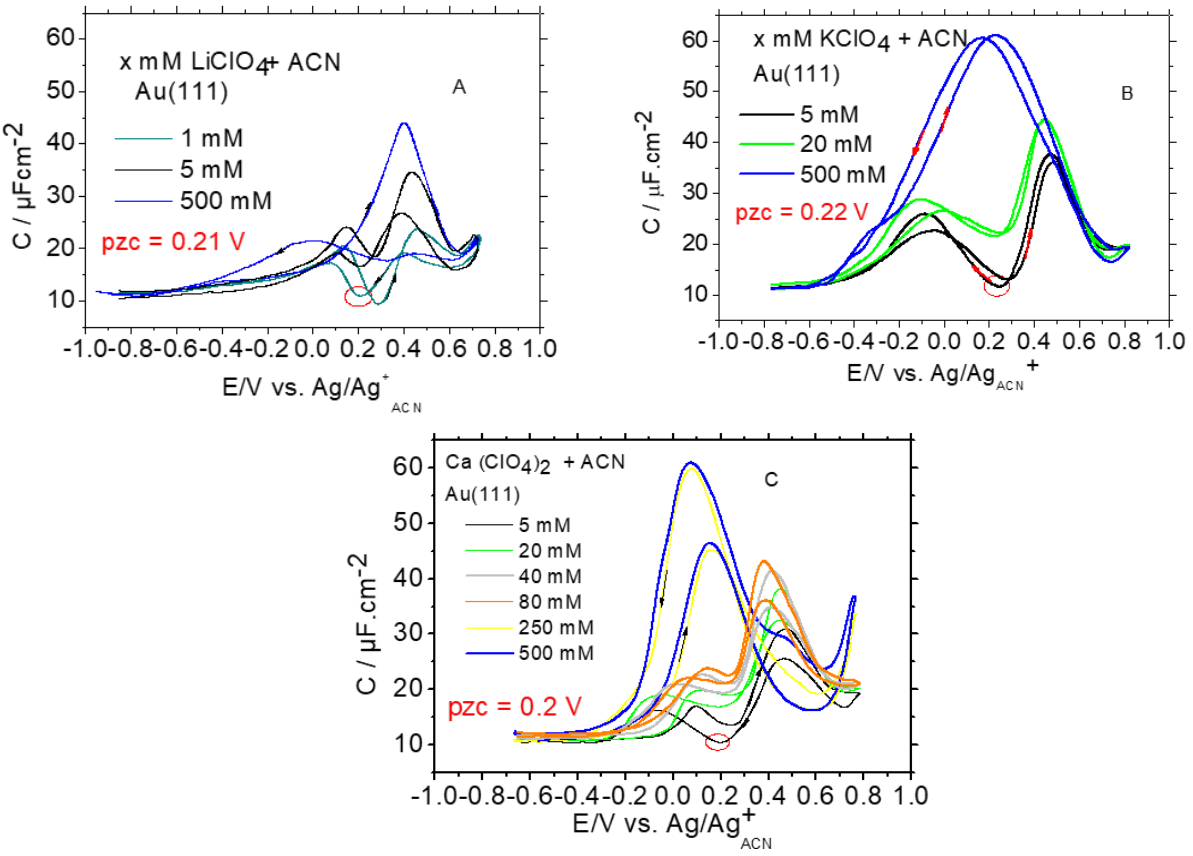

Figure 5.3: C(E) curves for Au(111) electrode in acetonitrile (ACN) containing different cations : (A) Li^+, (B) K^+, and (C) Ca^{2+} at 10 Hz frequency, 3 mV r.m.s. amplitude at a sweep rate of 10 mV s^{-1}.

5.4.3 Effect of anions

The effect of the specific anion adsorption on Au(111)|electrolyte interface in the organic solvent (DMSO) was studied with potassium salts in DMSO. The results obtained are shown in **Figure 5.4** (**A and B**). The negative shift of the pzc in the case of Br- adsorption compared to that for PF_6^- is typical for strong adsorption. The peak positive of the pzc is attributed to the adsorption of Br^- and PF_6^- (-0.5 and 0.28 V vs. Ag/Ag^+, respectively) [399]. In the case of KBr salt, the molar volume of anion and cation have a similar size because the two capacitance maxima are almost the same. So one can conclude that monovalent cation and anions in DMSO have the same partial molar volume. Compared to KPF_6 salt in aqueous solution on Ag(110) [399]: At 0.01 M left, C (max) ~ 50 µF.cm^{-2} (cation), while at 0.01 M of KBr in DMSO, the left C(max) ~30 µF.cm^{-2} (cation). From this, it can be concluded that the partial molar volume of cations in DMSO is much larger than in water.

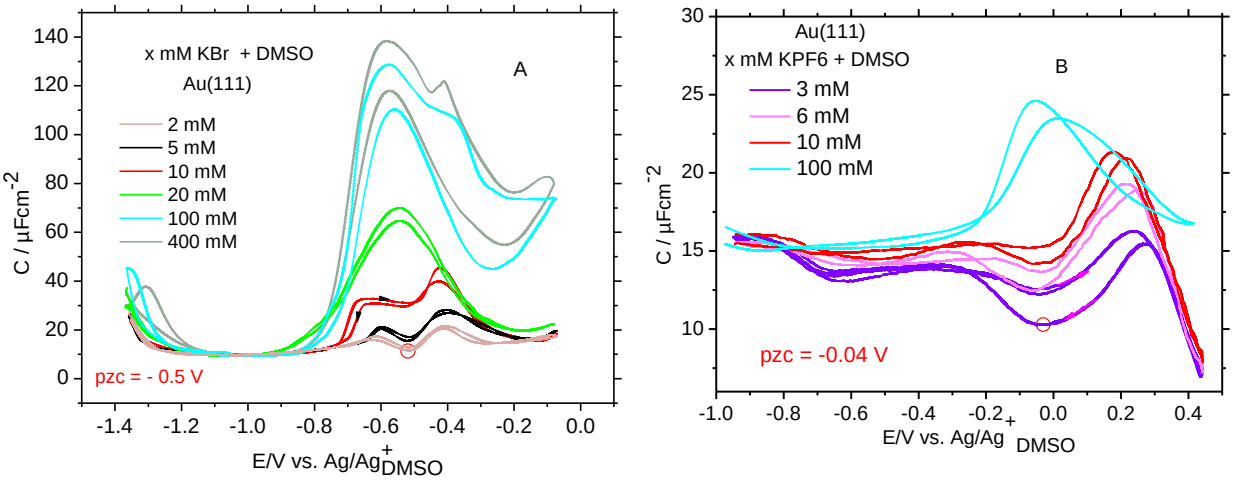

Figure 5.4: C(E) curves for Au(111) electrode in DMSO containing different anions : (A) Br^- and (B) PF_6^- at 10 Hz frequency, 3 mV r.m.s. the amplitude at a sweep rate of 10 mV s^{-1}.

Similar to Au(111) electrodes in aqueous solutions [226, 247], the anodic capacitance maximum increases in the order: $Cl^- < Br^- < I^-$ and this is attributed to adsorption strength. This trend is like anion adsorption activity on Bi(hkl) in organic solvents [312]. Bromide is more specifically adsorbed than PF_6^- so pzc shifts to a more negative potential. While the pzc of Au(111) in the case of ClO_4^- is quite similar to PF_6^- as shown in **Figure 5.5**.

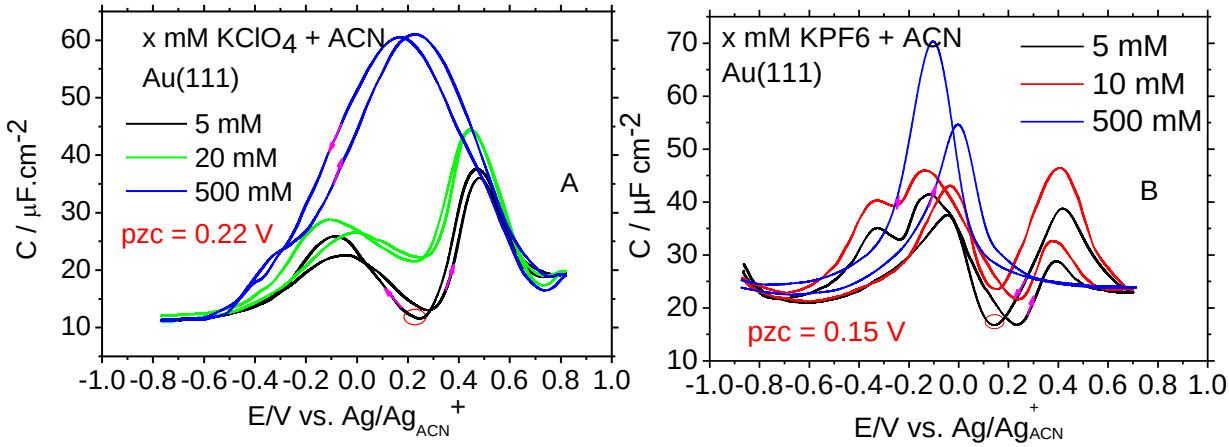

Figure 5.5: C (E) curves for Au(111) electrode in ACN containing different anions : (A) ClO_4^- and (B) PF_6^- at 10 Hz frequency, 3 mV r.m.s. the amplitude at a sweep rate of 10 mV s^{-1}.

5.4.4 Effect of water on pzc

Because water is the key impurity in aprotic solvents, investigating its effect on the interfacial capacities in general and particularly the capacitance is crucial. As seen in **Figure 5.6**, capacity values increase with raised water concentrations from 1.17 to 58 mM whereas the shape remains largely unchanged. The potential of the capacity minimum i.e., the pzc, changes to more positive values. This trend is identical to that obtained by Petrii and Khomchenko on Pt (poly) /acetonitrile [366] and on Au (poly) in PC [219]. Such capacitances increase with rising water content, were also be observed for the Au(111) electrode in the ionic liquid in the positive potential region [319].

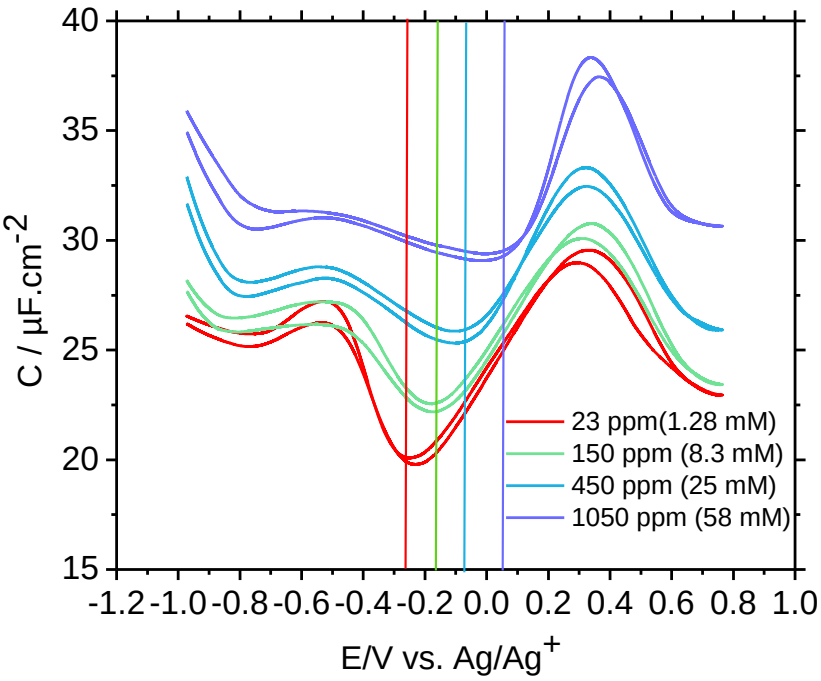

Figure 5.6: Curves of the differential capacity of the roughened Au (111) electrode in propylene carbonate solutions of 10 mM KPF_6, and with additions of 150, 450, and 1050 ppm of water using an AC perturbation of 10 Hz frequency, 3 mV r.m.s. the amplitude at a sweep rate of 10 mV s^{-1}.

5.4.5 Effect of the surface structure of the Au electrode on pzc

The effect of the atomic arrangement of the electrode surface on the double layer characteristics is well established [359, 363, 387]. The capacitance-potential curves for the gold (111) and roughened (111) surfaces in acetonitrile and propylene carbonate at various $LiClO_4$ and KPF_6 concentrations are presented in **Figures 5.7 and 5.8**, respectively. Also, C, E curves for Au(111), and polycrystalline gold electrode in different concentrations of KPF_6 containing DMSO are exhibited in **Figure 5.9**.

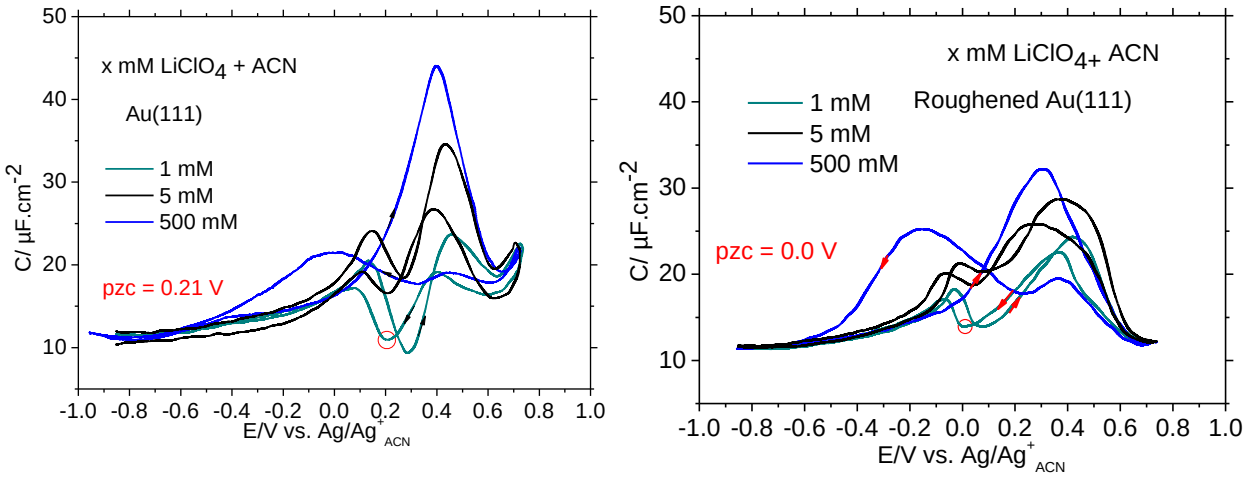

Figure 5.7: C(E) curves for Au(111) and roughened Au(111) electrode in ACN solutions in different concentrations of x mM $LiClO_4$ (as shown in the figure) using an AC perturbation of 10 Hz frequency, 3 mV r.m.s. the amplitude at a sweep rate of 10 mV s^{-1}.

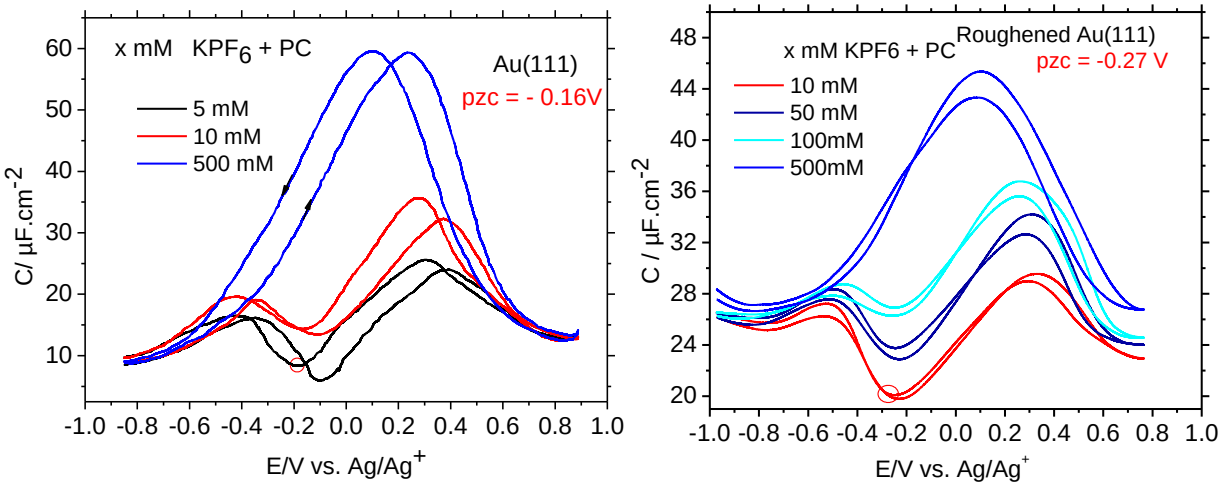

Figure 5.8: Same as in **Figure 5.7**, but in KPF_6 + Propylene carbonate.

Both electrodes display similar behavior. For both, the capacitance curves show a minimum at low concentrations. The same trend is found for KPF_6 in DMSO solutions. At a minimum, capacitance grows with salt concentration due to the concentration-dependent contribution of the diffuse portion of the double layer, confirming that the minimum can be regarded as pzc [357, 363]. The potential (E_{pzc}) varies from experiment to experiment within ± 11 mV for independent experiments for changing salt concentration, which displayed no systemic variability with the salt concentration. The pzc remains approximately constant with

concentration variation as reported in the literature for Au(111) and Ag (111) electrode in aqueous solution [225, 397].

The capacitance value at the minimum, C_{min}, varies from one surface to other (for instance minimum capacitance for Au (111) and polycrystalline-Au equal 10.2 and 16.6 µF.cm^{-2} (KPF_6 containing DMSO), resp.), and this behavior is similar to observed at faces (111, 100, and 110) of silver electrode| electrolyte interface system [359].

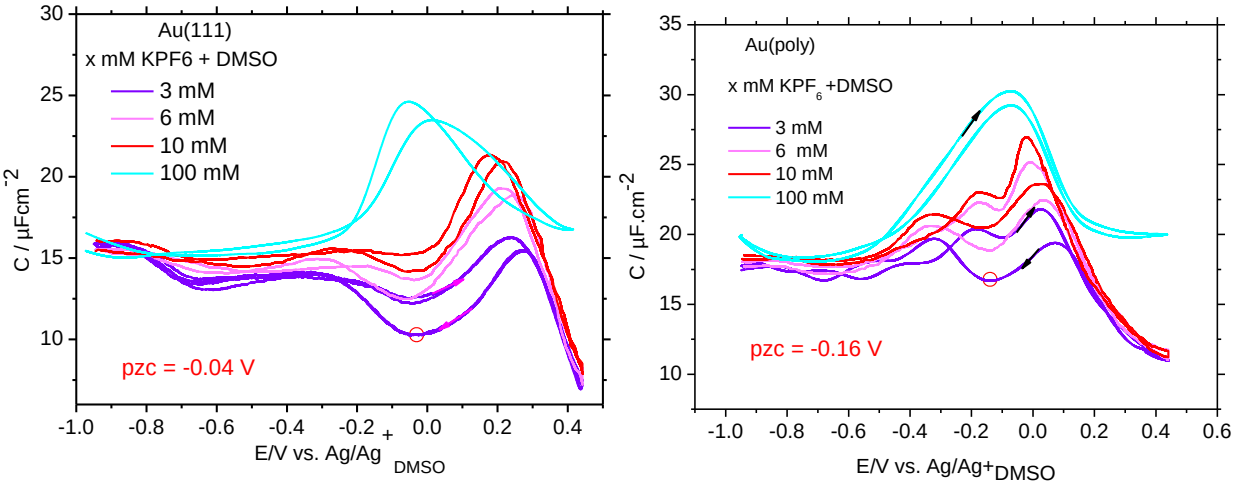

Figure 5.9: C (E) curves for a (111) and polycrystalline gold electrode. Concentration dependence in KPF_6 solutions in DMSO.

It is well known that the pzc of metal electrode and the work function ϕ_M are directly interrelated [400, 401]. The difference in the potential of zero charge between the Au (111) and the roughened Au (111) electrodes in $LiClO_4$ containing ACN ($E_{\sigma=0}$ = 0.21V and 0.0 V, respectively) , in KPF_6 containing PC ($E_{\sigma=0}$ = -0.16V and -0.27 V, respectively) and in KPF_6 containing DMSO ($E_{\sigma=0}$ = -0.04V and -0.16 V, respectively) corresponds closely to the difference in the work functions of the reconstructed (111) gold surfaces and polycrystalline gold electrode ($\phi_{Au\text{-}PC}$ = 5.11 and $\phi_{Au(111)}$ = 5.3) [388, 402].**Table 5.3**. Summarizes the values of pzc of Au(111) electrode in different organic solvents,referenced against standard reference electrode (DMFc) to minimize complications due to uncertain liquid junction potentials.

Table 5.3: Values of pzc of Au (111) and roughened electrode in different organic electrolytes.

Electrolyte	Solvent	Electrode	pzc / V vs. Ag/Ag^+ (Cath)	pzc / V vs. DMFc* (Cath)
KPF_6	PC	Au(111)	-0.16	+0.32
KPF_6	PC	r. Au(111)	-0.27	0.21
KPF_6	DMSO	Au(111)	-0.04	0.3
KBr	DMSO	Au(111)	- 0.5	-0.16
KPF_6	DG	Au(111)	0.22	0.54
KPF_6	ACN	Au(111)	0.15	0.61
$LiClO_4$	ACN	Au(111)	0.21	0.67
$LiClO_4$	ACN	r. Au(111)	0.0	0.46
$LiClO_4$	PC	Au(111)	- 0.17	0.31
$Ca(ClO_4)_2$	ACN	Au(111)	0.2	0.66
$KClO_4$	ACN	Au(111)	0.22	0.68
$KClO_4$	PC	Au(111)	- 0.21	0.27
KPF_6	DMSO	poly.(Au)	-0.16	0.18

* r means a roughened electrode

5.4.6 Surface-enhanced infrared absorption spectroscopy (SEIRAS)

The electrode/ electrolyte interface was investigated in an organic solvent by using SEIRAS technique. Infrared spectra of PC adsorbed on a gold surface at different potentials in the presence of 0.1 M $KClO_4$ are shown in **Figure 5.10** (**A and B**). The corresponding cyclic voltammogram of the system is exhibited in **Figure 5.10C**. The reference spectrum has been taken at 0.4 V. The bipolar band at about 1805 cm^{-1} corresponds to the C-O vibration of PC which was measured on silver electrodes in presence of NaI in SERS measurement [403]. With more negative potentials, it shifts to lower wavenumbers. The intensity increases with more negative potential due to the increasing field strength and the resulting stronger orientation of the PC molecules. The negative band due to the substraction of the reference spectrum becomes more prominent at more negative potentials because of the larger frequency shift. The system behaves reversibly. Except for a small broad peak at −0.2V (i.e. in the vicinity of the pzc), the resulting CV at the potential limit 0.4 – 1.0 V is fairly featureless. The band at 2338 and 2364 cm^{-1} in **Figure 5.10**B corresponds to the asymmetrical stretching vibration band of CO_2 in the

gas phase; this is caused by the changing CO_2 content in the spectrometer setup. **Figure 5.11** (**A and B**) shows IR spectra for gold thin layer film covered by iodide at two different reference spectra (-0.4 and -1.8 V, resp.) and recording cyclic voltammogram recorded during spectra obtaining (**Figure 5.11C**). The presence of iodide in the electrolyte (**Figure 5.11**) shifts the pzc to -1.1 V. Changing the potential in a more positive direction leads to a stronger field and, thus, stronger alignment of the PC molecules. The absence of a negative band in **Figure 5.11B** suggests that the intensity at -1.8 V is very small. Also in **Figure 5.10B**, the absorbance decreases from its maximum value around -1.0 V to lower values. We expect that the status of the surface with and without iodine is the same at the negative potential limit because no anions are adsorbed. Further experiments, e.g. with varied cations, might solve this question.

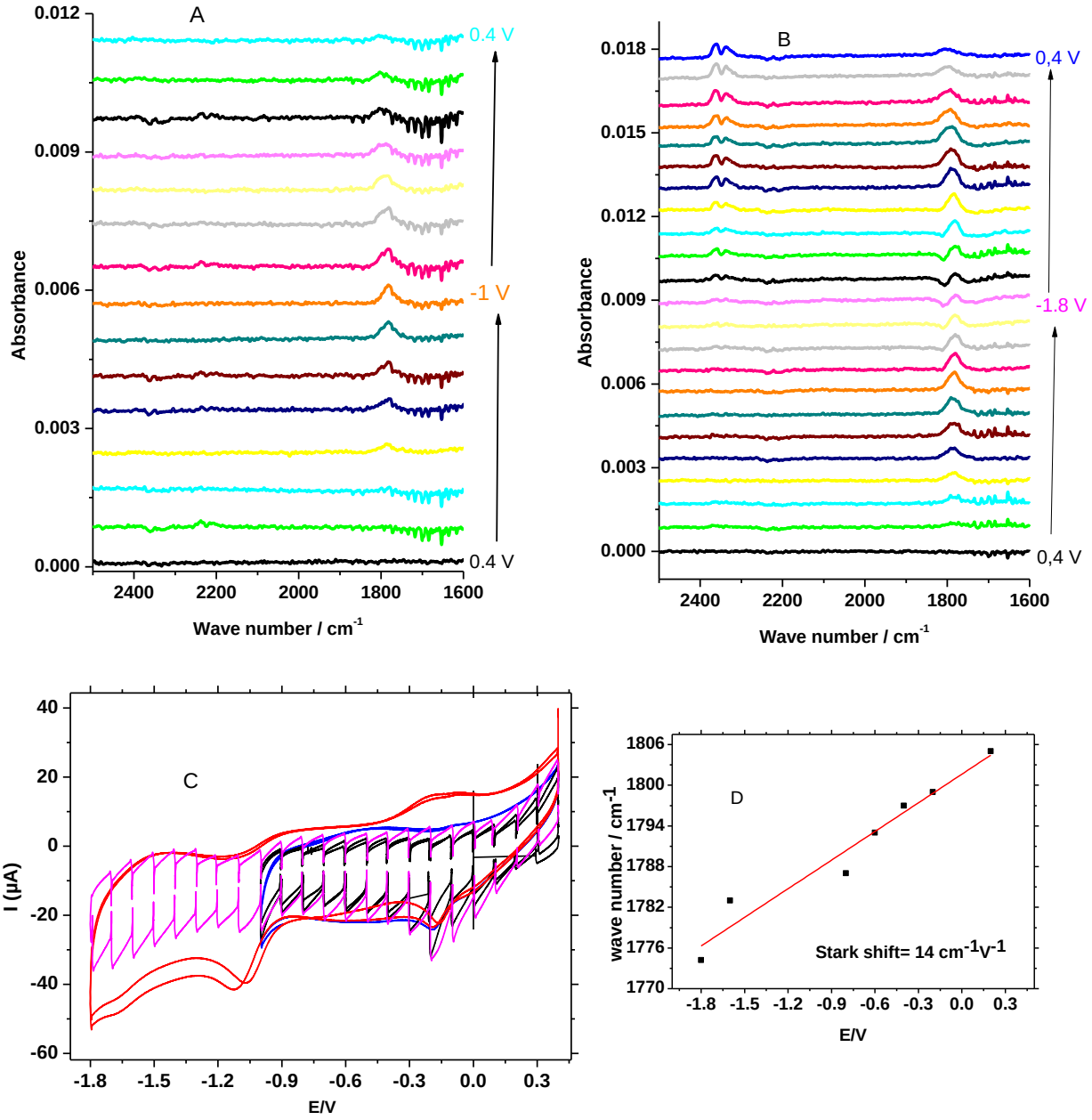

Figure 5.10: IR-spectra of propylene carbonate adsorbed on gold consisting of 32 interferograms with a resolution of 4 cm^{-1}. (A) IR-Spectra recorded in the potential limit from 0.4 to -1.0 V, (B) IR-Spectra recorded in the potential range from 0.4 to -1.8.0 V, (C) Corresponding CV. Electrolyte: 0.1 M $KClO_4$ in PC and (D) Shift of the wavenumber with the applied potential. The reference spectrum is collected at +0.4 V.

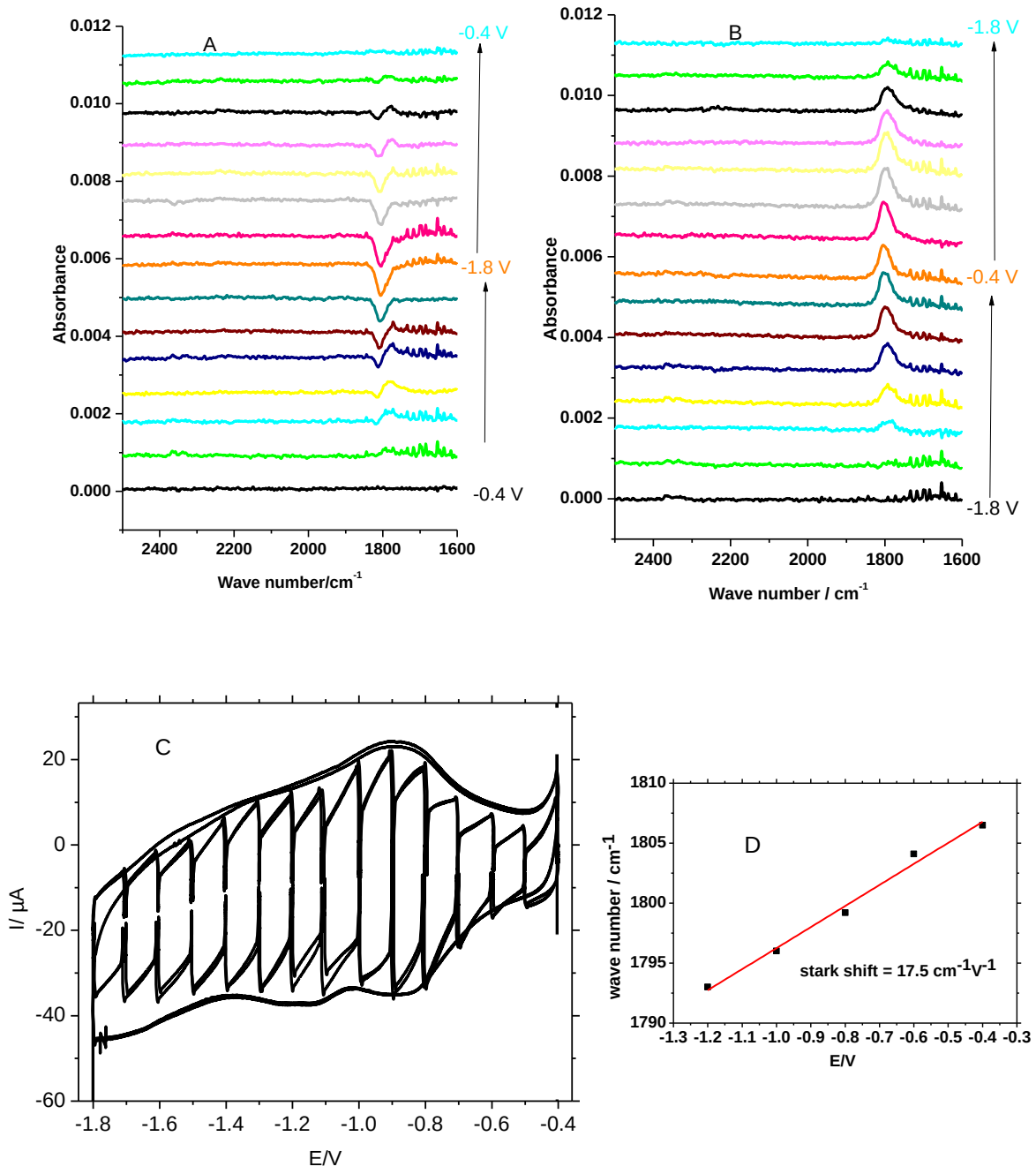

Figure 5.11: SEIRAS spectra recorded for Au thin film electrode in 10 mM KI + 0.1 M $KClO_4$/PC electrolyte at various reference potentials. (A) The reference potential was taken at -0.4 V, (B) It collected at -1.8 V, and (C) the corresponding CV at scan rate 10 mV/s and (D) Shift of the wavenumber with the applied potential.

5.5 Conclusion

The interfacial double-layer structure on a gold single crystal and a roughened gold electrode in aprotic solvents has been investigated by using cyclic voltammetry and differential capacitance measurements. The most densely packed face (111) has a more positive zero charge potential (pzc) than the roughened gold (111) electrode. Correspondingly, for gold, the differential capacitance at pzc increase from the roughened Au (111) to the Au (111) electrode. The pzc shifts to more positive potential and capacitance raises upon increasing water content from 1.17 to 58 mM on the roughened Au(111) electrode. The cation identity hasn't any effect on the pzc value, although the capacitance of hump at a low negative potential of pzc increases in the order $Ca^{2+} < Li^{+} < K^{+}$. When we look at various solvents in interaction with the same metal electrode and the salt, pzc vs. DMFc shifts as follows: ACN > DG > H_2O > PC > DMSO, and this order is not related to the dielectric properties of aprotic solvent, but this might be affected by the metal-solvent interaction and the donor number of the solvents. The pzc on the same electrode metal and solvent in different anions decreases in the order $PF_6^{-} > Br^{-}$. During SEIRAS measurements, it was concluded that the presence of iodide results in shifting the pzc to a more negative potential, and consequently changing the potential in a more positive direction leads to a stronger field and thus a more substantial alignment of the PC molecules. It is observed that a stronger electrical field with decreasing potential in absence of iodine leads to higher absorbance of PC molecules on the surface.

5.6 Supporting Information

Table S5.1: Reduction potentials of decamethyl ferrocene ($DMFc^{+/0}$) couples in various solvents.

Reference	Electrolyte	E_a / mV	E_c / mV	ΔE/ mV	$E_{1/2}$ / mV
0.1 M $AgNO_3$ in **DMSO**	1 mM DMFc* in 0.1 M $LiClO_4$ in **DMSO**	-310	-374	-64	-342
0.1 M $AgNO_3$ in **ACN**	2 mM DMFc* in 0.1 M $LiClO_4$ in **PC**	-451	-518	-67	-484.5
0.1 M $AgNO_3$ in **ACN**	3 mM DMFc* in 0.1 M $LiClO_4$ in **ACN**	-423	-491	-68	-457
0.1 M $AgNO_3$ in **ACN**	4 mM DMFc* in 0.1 M $LiClO_4$ in **DG**	-263	-371	-108	-317

Chhapter six:

Poly 1,5 diaminonaphthalene supported Pt, Pd, Pt/Pd and Pd/Pt Nanoparticles for direct formic acid oxidation

A. S. Shatla [a,b,*], K. M. Hassan [b] , A. A. Abd-El-Latif [a,c], A.A. Hathoot [b], H. Baltruschat [a] and M. Abdel-Azzem [b]

[a] Institute of Physical and Theoretical Chemistry, Bonn University, Römerstraße 164, D-53117 Bonn, Germany.
[b] Permanent address: Menoufia University, Faculty of Science, Chemistry Department, Menoufia, Egypt.
[c] Permanent address: National Research Centre, Physical Chemistry Dept., El-Bohouth St. Dokki, 12311 Cairo, Egypt.
[d] Permanent address: Menoufia University, Faculty of Electronic Engineering, Physics and Mathematics Engineering Department, Research Chemistry Laboratory Menoufia, Egypt.

Received: May 14, 2018
Published online: November 9, 2018

Reprinted (adapted) with permission from
A. S. Shatla, K. M. Hassan, A. A. Abd-El-Latif, A.A. Hathoot, H. Baltruschat and M. Abdel-Azzem, Journal of Electroanalytical Chemistry **2019**, 833, 231-241.
 DOI: 10.1016/j.jelechem.2018.11.005

Acknowledgments

The authors appreciate Alexander von Humboldt Foundation for the financial support of project No. 30260067.

6.1 Abstract

Comparative studies were carried out on the direct electrooxidation of formic acid at palladium (Pd), platinum (Pt), Pt/Pd and Pd/Pt nanoparticles (NPs) supported on poly 1,5-diaminonaphthalene (PDAN)-modified glassy carbon electrode. Metal electro-deposition was carried out using potentiodynamic technique. Cyclic voltammetry (CV), scanning electron microscopy (SEM), energy dispersive X-ray spectroscopy (EDX) have been used to investigate the electrochemical behavior, surface morphology and chemical composition of the studied electrodes. Electrode's electroactive surface area has been determined by electrooxidation of pre-adsorbed CO monolayer using the coupling of the dual thin layer flow through cell with mass spectrometer. Electrooxidation of formic acid (FA) at different modified electrodes have been studied using the differential electrochemical mass spectroscopy (DEMS) protocol and the current efficiencies with respect to CO_2 evolution were calculated. NPs incorporated PDAN polymer films improved the electrocatalytic efficiency towards the electrooxidation of FA. Among the studied electrodes, Pt/Pd/PDAN/GC shows the best metal dispersion and highest electrocatalytic activity towards formic acid oxidation (FAO).

6.2 Introduction

Electrochemistry offers an effective method for the direct formic acid oxidation (FAO) using metal catalysts. Platinum was generally utilized for formic acid oxidation [404-406]. There are several difficulties faces the marketable application of formic acid fuel cells, including the poisoning effect of intermediates, unsatisfactory durability and elevated expense of the frequently used Pt catalysts. To overcome these challenges, addition of secondary noble metal to Pt, for example, Pt/Au [407 - 410], Pt/Pd [411 - 418], Pt/Ru [419, 420], and Pt/Bi [421, 422] were utilized. Among the Pt/M catalysts, Pt/Pd bimetallic catalyst is the most promising candidate because of its high stability against poisoning. Since the primary use of pure Pd as an anode catalyst of direct FA fuel cells in 2004, Pd, the most Pt-like metal [423] with a reasonable abundance has attracted broad consideration because of its excellent electrocatalytic activity on initial FAO reaction compared with platinum [424 - 426]. The oxidation of FA on Pd progresses mostly within a preferred direct dehydrogenation route without developing poisonous adsorbed CO species. Nevertheless, the catalytic performance of pure Pd is hampered due to its instability after some time, especially when it is operated with FA at elevated concentrations. This is maybe due to the fast advanced dissolution of Pd in an oxidized state and sluggish adsorption of intermediates under acidic operating conditions, which impedes its use in the fuel cells [427,

428]. Blending Pt with another metal to manufacture a bimetallic catalyst is an effective approach to enhance the cell performance [423 - 426]. Up to the present time, a lot of bimetallic materials with synergistically improved performances have been considered based on Pt in a blend with its neighboring transition metals. Among these materials, the Pt/Pd catalyst is more stable than the other bimetallic catalysts at high potentials [423 - 426].

Recently, disperse metal particles on the conductive substrates such as conducting polymers (CPs) were utilized due to their porous structures and high surface areas [429, 430]. Various CPs such as polyaniline [431, 432], poly (5-cyanoindole)[433], poly (p-anisidine) [434], poly (o-dihydroxy benzene) [435], polythiophene [436, 437], polypyrrole [438, 439] and polyindole [440] were inspected as catalyst supports towards FAO . CP enhances the properties of the electrode-electrolyte interface and permits a facile flow of electronic charges during the oxidation of small organic molecules on Pt particles [441, 442]. The PdAu/Cnanocatalyst shows higher activities towards FAO [443]. Kim et al. [444] studied FA oxidation at Pt black catalysts modified by irreversibly adsorbed Bi. Yang et al. [445] prepared Pd catalysts supported on MWCNTs pretreated in a blend of sulfuric and 4-aminobenzene sulfonic acid, and demonstrated an enhanced FAO activity. Xu et al. [446] described a new class of N-doped graphene supported PtAu/Pt intermetallic core/dendritic shell nanocrystals for FAO. AuPd@Pd NCs achieved by Liu et al. [447] displayed higher catalytic characters for the FAO reaction. PdM nanodendrites/C catalysts (M = Co, Fe, Ni) showed enhanced catalytic activity for the oxidation of FA [448]. Li et al. [449] prepared Au@AuPd nanocrystals which showed highly electrocatalytic activity for formic acid oxidation.

The oxidation of FA mechanism has been studied by different electroanalytical methods combined with in-situ analysis techniques such as FTIR [65], DEMS [65, 450 - 454] and Raman spectroscopy [455].

In a recent publication, we combined the valuable characters of modified electrodes and metal (NPs) dispersion by the construction of nickel NPs at poly (1,5-diaminonaphthalene) modified glassy carbon electrode for electrocatalytic oxidation of some carbohydrates and biological compounds [148].

In this perspective, poly (1,5-diaminonaphthalene) (PDAN) films were prepared by electropolymerization at the surface of the glassy carbon electrode. Then, monometallic Pt or Pd and bimetallic Pd/Pt or Pt/Pd nanoparticles were deposited into the polymeric matrix by the electrochemical procedure. Suitability of these new composite NPs-modified polymeric glassy carbon electrodes toward the electrocatalytic oxidation of FA has been studied by

electrochemical and differential electrochemical mass spectroscopy (DEMS) measurements in order to shed light on the current efficiency for CO_2 formation during formic acid oxidation.

6.3 Experimental

6.3.1 Materials

1,5-diaminonaphthalene (DAN) (Sigma–Aldrich) and perchloric acid ($HClO_4$ 70%) purchased from Fluka and used without additional refinement. Palladium chloride ($PdCl_2$), chloroplatinic acid hexahydrate ($H_2PtCl_6.6H_2O$) and FA (HCOOH) obtained from (Sigma Aldrich). Sulfuric acid (H_2SO_4) obtained from Merck and finally, Millipore-Q water was always used.

6.3.2 Instruments

Electrochemical measurements were carried out using an EG&G potentiostat (model 273A) with LabVIEW software (National Instruments GmbH, Munich, Germany). The 3-compartments classical cell was used during the electrochemical measurements, which includes a glassy carbon electrode (GC) of 10.0 mm diameter as a working electrode (WE), a 1 cm^2 platinum sheet as a counter electrode and a reversible hydrogen electrode (RHE) used as a reference electrode (RE). The RE compartment is linked to the WE electrode compartment via a lugging capillary and separated by a roughened stopcock. The glassy carbon electrode was polished to a mirror-like surface with 0.50 and 0.02 µm alumina slurry then it was well cleaned in water. All experiments were conducted at room temperature (25° C ± 1) and carried out under argon atmosphere. All solutions are prepared with Millipore-Q water. Scanning Electron Microscope micrographs achieved by SEM Model QUANTA FEG 250 was equipped with an EDX unit. Differential electrochemical mass spectroscopy (DEMS) measurements were recorded using a quadrupole mass spectrometer (Balzer QMG-422) coupled with the dual thin layer flow through cell in which a hydrophobic Teflon membrane works as an interface between the electrolyte and the vacuum system [454].

6.3.3 Preparation of monometallic and bimetallic PDAN/GC modified electrodes

PDAN/GC modified electrode (PDAN/GC) was prepared according to the method reported by Abdel Azzem and coworkers [148] in which 1.50 mM of the DAN monomer dissolved in 1 M $HClO_4$ was electropolymerized at GC electrode using CV technique for 15

cycles in the potential window of 0.0 and 0.80 V at scan rate of 0.02 Vs^{-1}. The thickness of PDAN can be computed from the following equation [456]:

$$d = \frac{QM_w}{zFA\rho} \qquad (6.1)$$

where M_w is the molecular weight of 1,5-DAN (158.20 g mol^{-1}), F is the Faraday constant, ρ is the density of the monomer (1.5 g cm^{-3}) [457], A is the electrode area, z is the number of electrons involved (4) and Q is the overall oxidation charge associated with the polymer formation (Q_{PDAN} = 0.02815 C). The thickness of PDAN layer was determined to be ~ 0.1 µm for 1.0 cm diameter disc electrode**.**

Repetitive CVs for 25 scans in the potential range of − 0.35 and + 0.65V at a scan rate of 50 mV/s have been used for metal deposition [458]. Monometallic Pd or Pt catalyst was prepared by immersing the PDAN modified electrode in 0.10 M H_2SO_4 containing 2.50 mM $PdCl_2$ or 0.10 M $HClO_4$ containing 2.50 mM H_2PtCl_2, respectively. Depending on the order of metal deposition, Pt/Pd and Pd/Pt were prepared by sweeping the potential 12 cycles for each metal.

6.3.4 Determination of the active surface area by CO_{ads} oxidation

Active surface areas measurements of Pd/PDAN/GC, Pt/PDAN/GC, Pd/Pt/PDAN/GC and Pt/Pd/PDAN/GC modified electrodes were achieved by electrooxidation of the pre-adsorbed monolayer of CO at the electrode surface and simultaneous detection of CO_2 (oxidation product) by the mass spectrometer. The electrode potential was held at 0.06 V, then the CO saturated supporting electrolyte was injected in the DEMS cell. After the development of the CO monolayer, the solution was replaced with a supporting electrolyte under potential control, to keep the solution free of CO. The Faradaic and ionic currents were recorded during the positive potential sweep at scan rate 0.01 Vs^{-1} and flow rate 5.0 µL s^{-1}.

6.4 Results and discussion

6.4.1 Catalysts characterization

6.4.1.1 Scanning electron microscopy (SEM) and energy dispersive X-ray spectroscopy (EDX)

The response of an electrochemically-modified electrode is correlated to its physical morphology. The surface topographies of the obtained modified electrodes were examined using SEM (**Figure 6.1 A, B, C, and D**), which demonstrate significant modifications in the

surface structure of Pd/PDAN/GC, Pt/PDAN/GC, Pt/Pd/PDAN/GC, and Pd/Pt/PDAN/GC modified electrodes, respectively. The particle size of electrodeposited Pd (light-grey) and Pt (shiny particles) are in the range of 114.60 - 179.90 nm and 89.30 nm to 168.20 nm, respectively as shown in **Figure 6.1A** and **B**. **Figure 6.1C** shows good distributions for the Pd and Pt particles where the Pd is in the core and Pt in the outer shell over the whole surface of PDAN/GC modified electrode. Once the order of deposition is changed, i.e. Pt presumably in the core and Pd in the outer shell, the aggregated particle is formed (**Figure 6.1D**). The average particle size is 125.0 nm and 175.0 nm in **Figure 6.1C** and **D**, respectively.

The nanoparticles (NPs) sizes distribution histograms of the Pt/PDAN/GC and Pt/Pd/PDAN/GC catalysts were manually measured from SEM images of **Figure 6.1** (**B** and **C**) with more than 250 particles (Figure not shown). The average NPs sizes of Pt/PDAN/GC and Pt/Pd/PDAN/GC were 162.97 and 172.59 nm, respectively.

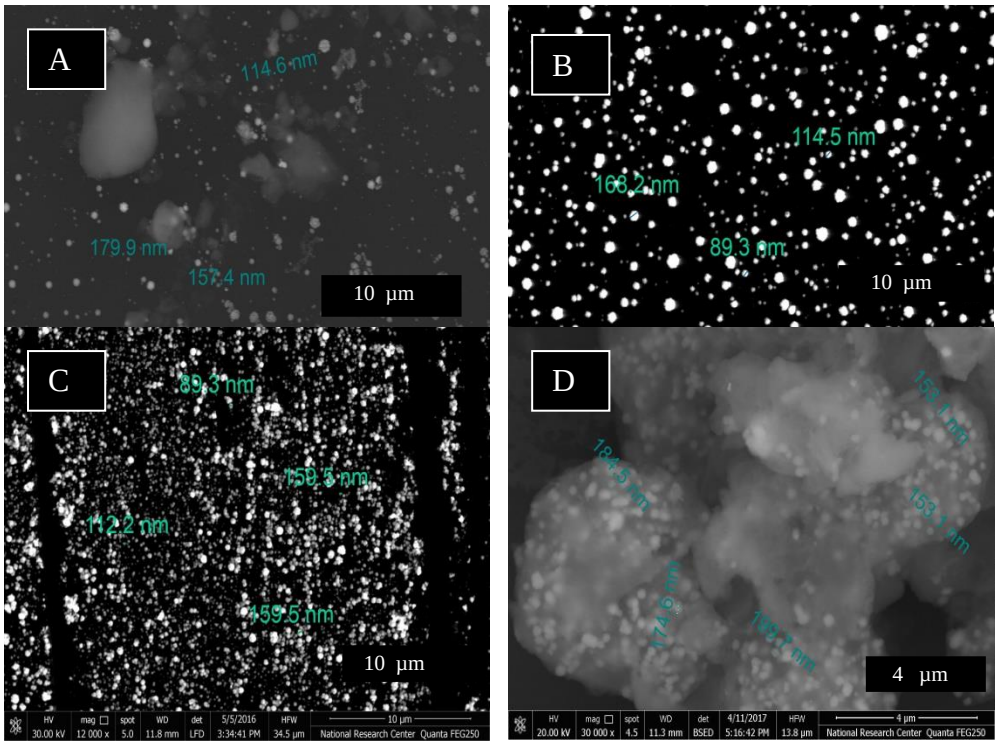

Figure 6.1: SEM micrographs of a freshly prepared modified electrodes, (A) Pd/PDAN/GC, (B) Pt/PDAN/GC, (C) Pt/Pd/PDAN/GC and (D) Pd/Pt/PDAN/GC.

The electroactive surface area was estimated from SEM image by counting the number of particles and using the average diameter. For **Figure 6.1B**, the calculated surface area is around 0.01 to 0.04 cm^2. Furthermore, the Pd and Pt NPs were dispersed in the PDAN film with

an atomic percentage of 4.7 % and 6.7 %, respectively according to the EDX analysis. Moreover, in the bimetallic system, EDX results reveal the presence of both dispersed metal nanoparticles in the order of 10 %.

6.4.1.2 Determination of the active surface area by CO_{ads} oxidation

After cleaning the four modified electrodes by scanning the potential between 0.05 and 1.50 V in the supporting electrolyte at a scan rate of 0.05 V s^{-1}, the potential was held at a potential between 0.04 and 0.07 V and the supporting electrolyte was substituted by a CO-saturated solution to form a CO adsorbed monolayer. After exchanging it again with supporting electrolyte the potential was swept in an anodic direction at a scan rate of 0.01 Vs^{-1}. So, the adsorbed CO was oxidized to CO_2. The active surface area of the supported catalysts was calculated according to the following equation:

$$A_{CO}^{i} = \frac{Q_{MS}}{K^{*}F\Gamma_{M}} \qquad (6.2)$$

where Q_{MS} is the integrated ionic charge of CO_2, F is the Faraday const. and Γ_M is the surface concentration of CO_{ads} monolayer (assuming Γ_M of 1.45 nmol /cm^2 corresponding to 280.0 µC/cm^2) and k* is the calibration constant measured by CO stripping on Pt polycrystalline at scan rate 10.0 mV/s and its value is 7.23 x 10^{-6}. The active surface area of the four catalysts estimated by CO stripping is given in **Table 6.1**.

Table 6.1: Active surface area of the studied electrodes determined from electrooxidation of pre-adsorbed CO. ($A_{geometric}$ = 0.282 cm^2)

Electrode	Real Surface Area (cm^2)	Q_{MS} (nC)
Pd/PDAN/GC	1.51	1.53
Pt/PDAN/GC	1.75	1.78
Pt/Pd/PDAN/GC	2.1	2.13
Pd/Pt/PDAN/GC	1.71	1.74

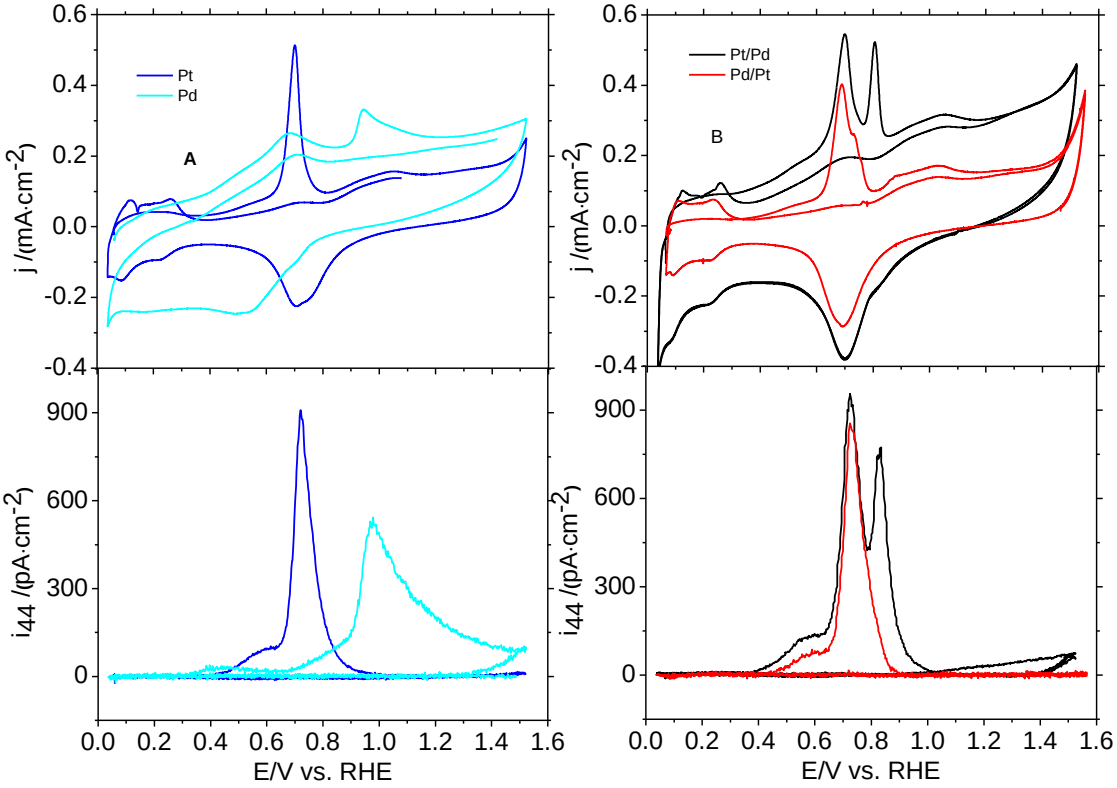

Figure 6.2: (A) monometallic and (B) bimetallic, Simultaneously recorded faradaic (upper) and corresponding ion current of CO_2 (m/z = 44) (lower) during the electrooxidation of pre-adsorbed CO at different modified electrodes in 0.50 M H_2SO_4 at scan rate 0.01 Vs^{-1} and flow rate 5.0 µL s^{-1}. (Current densities are referred to the true surface area as determined by CO_{ads})

The CV and in particular the shape of the MSCV for the Pt-modified electrode looks very comparable to that of polycrystalline Pt [65]. In particular, the pre-peak below 0.60 V is clearly visible. The catalytic activity of Pt/PDAN/GC and Pd/Pt/PDAN/GC electrodes towards CO_{ads} electrooxidation is similar. Pd nanoparticles show the lowest activity since the onset potential of CO oxidation is about 0.70 V, although a minor pre-peak is visible clearly at potentials lower than for Pt. The onset potential of CO_{ads} oxidation shifted to a less positive potential at Pt/Pd/PDAN/GC electrode compared to Pt/PDAN/GC electrode due to the synergistic effect of both metals. The presence of the second peak of CO oxidation at Pt/Pd/PDAN/GC at 0.80 V is ascribed to the oxidation of CO_{ads} at a second phase which is probably rich in Pd.

To compare the activities of different catalysts in terms of profitable efficiency, the current is generally normalized by the mass of loaded metal. Despite the fact that the mass-current density characterizes the economic efficiency of a catalyst, this does not consider the surface area of active metal sites. Electrochemical active surface area (ECSA) is an essential

parameter that shows the number of electrochemical active sites related to the mass of noble metal as follows [459, 460] :

$$\mathrm{ECSA} = \frac{Q}{sl} \qquad (6.3)$$

where Q is the coulombic charge of the metal oxide reduction peak; s is the proportionality constant that correlates charge with the area (0.405 mC cm^{-2}) and l is the electrocatalyst loading (gm^{-2}). The metal loading and ECSA of the modified electrodes were computed and listed in **Table 6.2**. Pt/Pd/PDAN/GC showed more active reaction centers and higher mass activity than the other electrocatalysts.

Table 6.2: Metal loading, electrochemical active surface area (ECSA) of the studied nanocatalysts electrodes.

Catalysts	**Metal Loading ($g.m^{-2}$)**	**ECSA ($m^2.g^{-1}$)**
Pd/ PDAN /GC	0.25	20.13
Pt/ PDAN /GC	0.28	56.16
Pd/Pt/ PDAN /GC	0.6	32.5
Pt/Pd/ PDAN /GC	0.4	90.43

6.4.1.3 Electrochemical behavior of the catalysts

The catalytic activities of the studied modified electrodes were examined by cyclic voltammetry technique. The CV of Pt/PDAN/GC electrode in 0.50 M H_2SO_4 in a potential range between - 0.10 and 1.60 V at a scan rate of 0.05 V s^{-1} as illustrated in **Figure 6.3** (blank line). The characteristic cathodic and anodic peaks of $H_{ads/des}$ and Pt Pt-oxide formation and its reduction peaks at Pt surface are obvious.

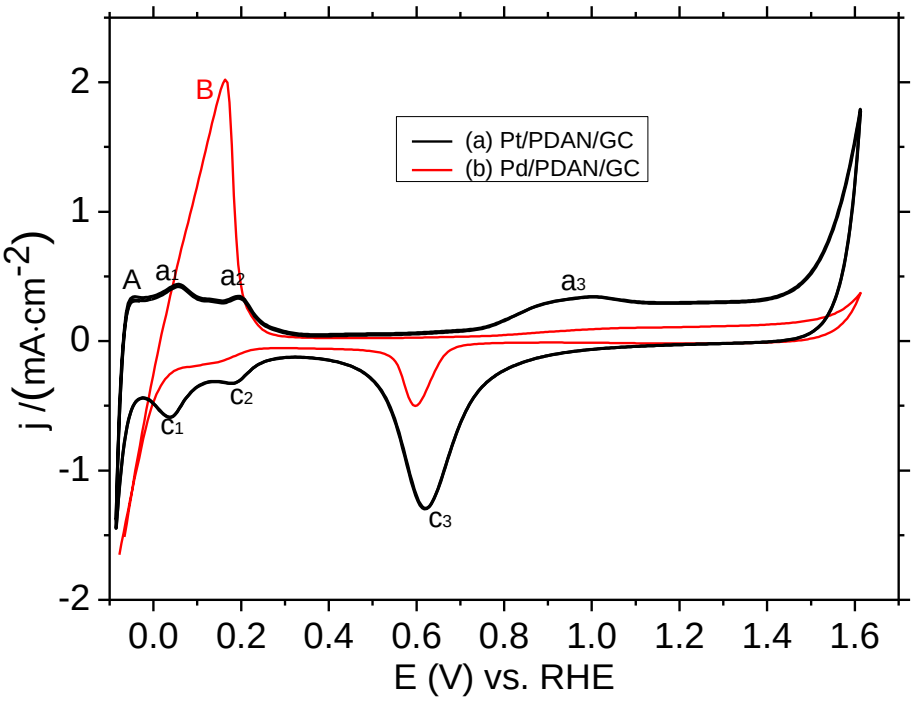

Figure 6.3: Cyclic voltammograms of Pt/PDAN/GC (black line), Pd/PDAN/GC (red line) modified electrode in an aqueous solution of 0.50 M H_2SO_4 at scan rate of 0.05 Vs^{-1}. (Current densities are referred to the true surface area as determined by CO_{ads})

Figure 6.3 (red line) shows a typical CV of the electrochemical profile of Pd/PDAN/GC modified electrode in 0.50 M H_2SO_4. For Pd/PDAN/GC, a large cathodic current below 0.05 V was observed which was attributed to the release of the dissolved hydrogen from the bulk of the Pd electrode [461]. The onset potential of oxide layer formation on palladium starts at nearly 0.75 V.

The specific surface area of Pd nanoparticles has been estimated from the amount of charge of Pd-oxide formation assuming the theoretical charge density is 420.0 $\mu C/cm^2$ [411].

The Pt/Pd/PDAN/GC modified electrode exhibited a drastic increase in the electrochemical response compared to that of Pd/Pt/PDAN/GC and monometallic modified electrodes as shown in **Figures 6.3** and **6.4.** These results indicate to the higher activity of Pt/Pd/PDAN/GC catalyst compared to the other catalysts.

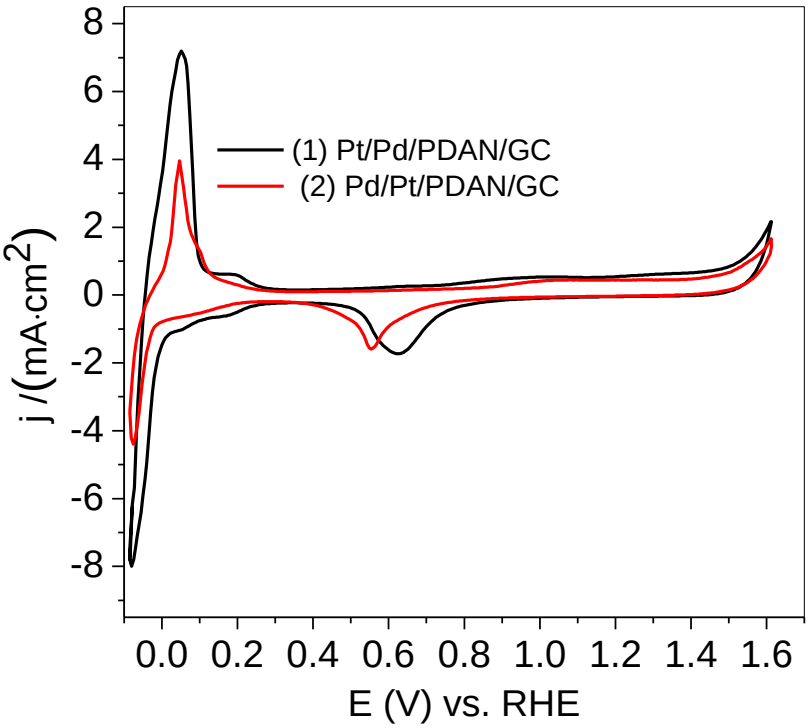

Figure 6.4: Cyclic voltammograms of Pt/Pd/PDAN/GC and Pd/Pt/PDAN/GC modified electrode in 0.50 M H_2SO_4 electrolyte at a scan rate of 0.05 Vs^{-1}. (Current densities are referred to the true surface area as determined by CO_{ads}).

6.4.2 Electrocatalytic activities of Pt/PDAN/GC, Pd/PDAN/GC, Pd/Pt/DAN/GC and Pt/Pd/PDAN/GC modified electrodes toward FAO

The electrocatalytic behaviors of GC electrode, PDAN, Pt/PDAN/GC, Pd/PDAN/GC, Pd/Pt/PDAN/GC and Pt/Pd/PDAN/GC modified electrodes toward FAO were assessed by CV techniques. No electrochemical responses were revealed neither at the GC electrode nor at PDAN/GC modified electrode in the presence of 0.01 M formic acid.

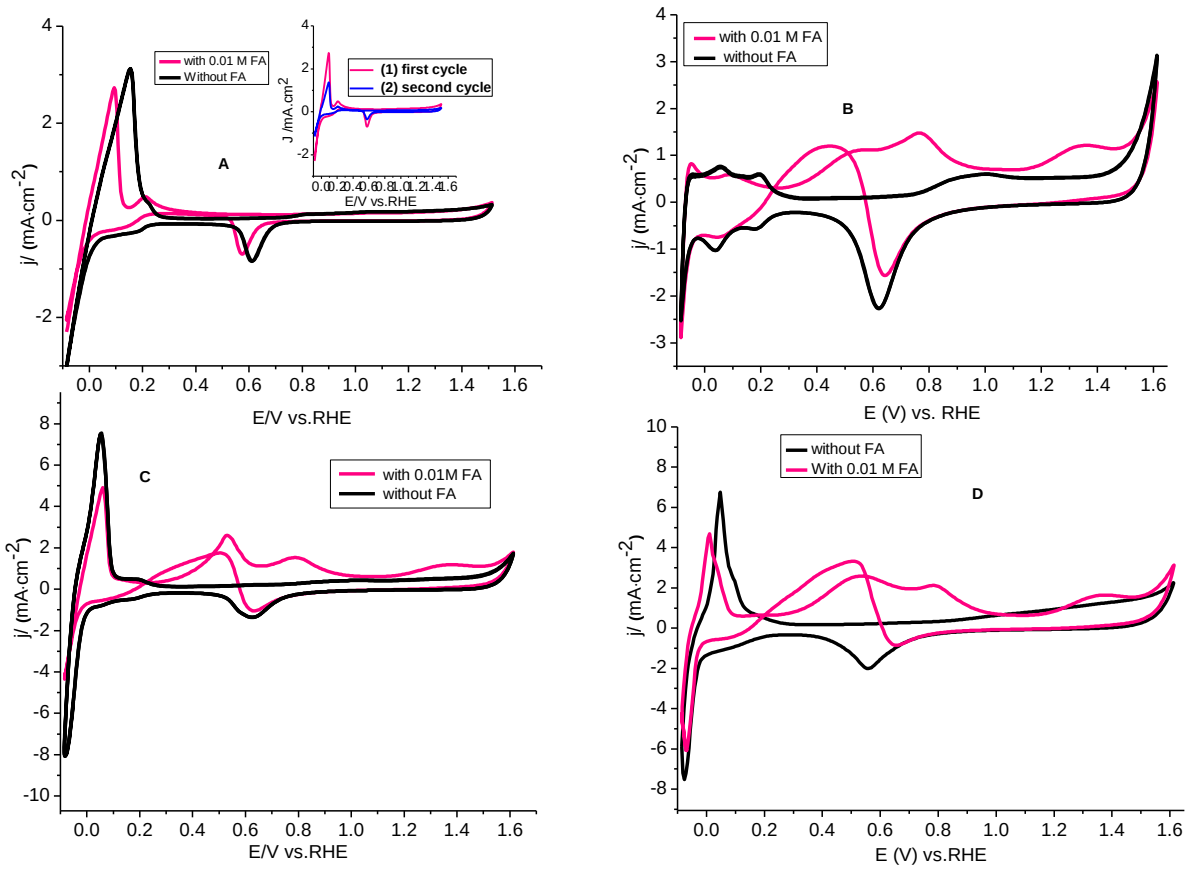

Figure 6.5: Cyclic voltammograms of (A) Pd/PDAN/GC, (B) Pt/PDAN/GC, (C) Pt/Pd/PDAN/GC and (D) Pd/Pt/PDAN/GC electrodes in absence and presence of 0.01 M formic acid in 0.50 M H_2SO_4 solution at a scan rate of 0.05 Vs^{-1}. The inset diagram shows the first (1) and second cycle (2) on Pd/PDAN/GC. (Current densities are referred to the true surface area as determined by CO_{ads}, cf. **Table 6.1**).

Figure 6.5 (A, B, C and **D**) presents CV profiles for the electrochemical responses of Pd/PDAN/GC, Pt/PDAN/GC, Pt/Pd/PDAN/GC and Pd/Pt/PDAN/GC electrodes respectively in the presence (Red line) and absence (Black line) of formic acid.

Pd/PDAN/GC is not really active for FAO (330 µA/cm^2), although the onset potential of FAO in the positive-going sweep is around 0.15 V and 0.20 V in the negative-going sweep as shown in **Figure 6.5A**. Nevertheless, the activity of Pd diminishes after the first sweep. The loss of the activity could be due to the intensely adsorbed reaction intermediates at Pd surface [462].

A characteristic oxidation behavior for FA developed at Pt/PDAN/GC, Pt/Pd/PDAN/GC and Pd/Pt/PDAN/GC electrodes are shown in **Figure 6.5B-D**. The mechanism of FAO has been investigated according to previous workers via two pathways [463

- 465]. The CV curves are split into three oxidation peaks during the positive scan (**Figure 6.5**), at approximately 0.53 and 0.78 V vs RHE, respectively. The first peak relates to the direct oxidation pathways of FAO *via* the dehydrogenation mechanism, involving the removal of two hydrogen atoms to form CO_2 [466]. The second peak (at ca. 0.78 V) is an indirect oxidation pathway of the dehydration reaction of FA [111, 466] via the oxidation of pre-adsorbed CO (CO_{ads}) formed from the "non-faradaic" dissociation of FA at a high potential and the third peak at ~ 1.40 V is visible in the oxygen region. The oxidation peak at 0.51 V vs RHE in the negative sweep, corresponding to the formic acid oxidation via the formate anion pathways [463, 467]. The oxidation reaction involves the removal of hydrogen to generate formate anions, and then these anions are oxidized to form CO_2.

In the low potential region (ca. 0.53 V), the Pt sites are partially poisoned by CO_{ads} from the dissociative adsorption stage. The measured current is then essentially originated from the FAO at the free Pt active sites throughout the direct dehydrogenation pathway. The peak current intensity in this potential range shows either the density of Pt active sites and/or the poisoning level of Pt surface by CO_{ads}. At high potential (ca. 0.78 V), in presence of oxygen active species at the surface, CO_{ads} is oxidized at 0.78 V. During the backward sweep, after the reduction of metal-oxides, an oxidation peak present at 0.44 V due to the electrocatalytic oxidation of FA at a clean and active surface [468].

The formation of adsorbed CO from FA on Pt surface demands the presence of three nearby Pt sites (with a certain atomic spacing) and any disturbance in this continuity could obstruct its adsorption [469]. In such a manner, the modification of Pt/PDAN/GC modified electrode with PdNPs has been accomplished in two methods. The first included the direct electrodeposition of PtNPs on PDAN/GC modified electrode then Pd was next deposited (Pd/Pt/PDAN/GC). The other included the electrodeposition of PdNPs on the PDAN/GC modified electrode then Pt was deposited (Pt/Pd/PDAN/GC).

As presented in **Figure 6.5D**, in the case of Pd/Pt/PDAN/GC there was a minor increment in the first peak (direct oxidation) of FAO beside a decrease in the second peak current (indirect oxidation) related with Pt/PDAN/GC electrode. This can be understood as far as the enormous increment in the surface area of Pt offering a lot of Pt active sites supporting the direct pathway of FAO. In parallel, the deposition of Pd onto PtNPs may help in a geometrical disturbance supporting the direct FAO. It was noticed that when the deposition order of PdNPs and PtNPs was inverted as in the case of Pt/Pd/PDAN/GC (**Figure 6.5C**), the

indirect peak current of FAO was smaller than the direct peak. The improvement of the catalytic activity of the direct FAO is due to the decrease of CO poisoning.

Keeping in mind the end goal to illustrate the level of catalytic improvement towards FAO, two functions are utilized; one is the ratio of the current intensities of the direct peak (I_p^d) to the indirect peak (I_p^{ind}), and the second is the ratio of I_p^d and the backward direct peak (I_p^b). The ratio of the two oxidation peaks, I_p^d/I_p^{ind}, (in the anodic scan direction) reveals the favored route of FAO [470]. This ratio improved from 0.72 at Pt/PDAN/GC to 1.20 at Pd/Pt/PDAN/GC electrode. At the Pt/Pd/PDAN/GC electrode, the I_p^d/I_p^{ind} ratio increased to 1.70 (i.e., about one time and half of Pd/Pt/PDAN/GC). Therefore, in the case of Pt/Pd/PDAN, the FAO shifted towards the direct pathway. Also, the (I_p^d/I_b) (forward peak/backward peak) ratio offers valuable knowledge about the catalytic tolerance of the electrode against the formation of carbonaceous species [458, 471]. A small I_p^d/I_b ratio reveals insignificant FAO to CO_2 and extra accumulation of carbonaceous species at the electrode surface. This I_p^d/I_b ratio improved from 0.77 at Pd/Pt/PDAN/GC to 0.90 at Pt/PDAN/GC electrode. This increase reveals an enhancement in the catalytic activity of the Pt/Pd/PDAN/GC electrode towards FAO, probably, through decreasing the CO adsorption and supporting the direct oxidation route. In the case of Pd/PDAN/GC, the ratio is nearly 3.87 and this value is high but in spite of that, this electrode loses its activity after the first cycle and might be due to intensely adsorbed intermediates of the reaction occurred on the Pd surface as mentioned before. Remarkably, at the Pt/Pd/PDAN/GC electrode, the ratio I_p^d/I_b was about 1.5, demonstrating a noteworthy tolerance of this electrode against the CO poisoning. This pronounced improvement in the catalytic activity of this electrode may be probably associated to the amount of disturbing the contiguity of the Pt sites required for CO adsorption [468]. The partial deposition of PtNPs on PdNPs in the Pt/Pd/PDAN/GC electrode could be considered as the main reason to diminish the possibility of surface poisoning and improve the catalytic activity towards the direct FAO [468]. Therefore, the presence of PDAN film loaded with Pt or Pd or Pt/Pd (layer by layer) nanoparticles arises to provide catalytic improvement for the direct FAO in terms of increasing oxidation current and promising shift in the potential. Also, a modified electrode composed of a bimetallic layer (Pt/Pd/PDAN/GC) provides the extreme response and higher electrochemical mass activity (MA) compared with the monometallic modified electrode (Pt/PDAN/GC or Pd/PDAN/GC) as shown in **Table 6.3**.

Interestingly, the electrodeposition of PtPd NPs onto the PDAN/GC (Pt/Pd/PDAN/GC) surface (**Figure 6.6**) resulted in a significant increase of I_p^d with a current depression in I_p^{ind}. In other words, at the same metal loading, the Pt/Pd/PDAN/GC has a higher electrocatalytic activity for FAO than that Pt/Pd/GC. The ratio between the direct and indirect FAO peak currents, I_p^d/I_p^{ind} (which measures the catalytic enhancement) increased from 0.26 to 1.79 for Pt/Pd/GC electrode and Pt/Pd/PDAN/GC electrode, respectively (see **Table 6.4**). Thus, FAO is shifted intensively towards the direct pathway.

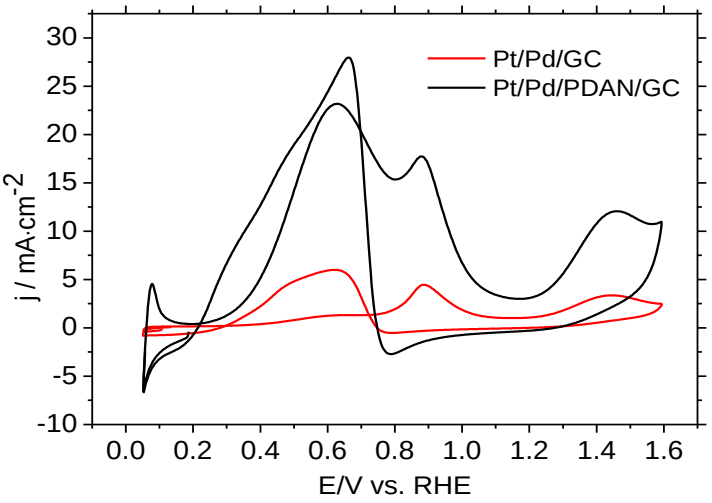

Figure 6.6: CV of 0.3 M formic acid in 0.50 M H_2SO_4 solution at (A) Pt/Pd/GC and (B) Pt/Pd/PDAN/GC at a scan rate of 0.05 Vs^{-1}.

Investigating the literature showed that Pt/Pd/PDAN/GC modified electrode has the highest electrochemical active surface area (ECSA) value (90.43 $m^2.g^{-1}$) and mass activity (MA) value (1825 $A.g^{-1}$) for FAO (see **Table 6.5**).

Table 6.3: CV characteristics of the electro-oxidation of Formic Acid at the studied catalysts.

catalyst	**E_{onset}* (from DEMS)**	$* E_p^d$	I_p^d **(mA.cm^{-2})**	I_p^{ind} **(mA.cm^{-2})**	I_p^b **(mA.cm^{-2})**	$\frac{I_p^d}{I_p^b}$	$\frac{I_p^d}{I_p^{ind}}$	**MA** (A.g^{-1})**
Pd/PDAN	0.11	0.22	0.31	-	0.08	3.87	-	380
Pt/PDAN	0.25	0.54	0.61	0.84	0.68	0.9	0.72	1071.42
Pd/Pt/PDAN	0.255	0.53	1.51	1.23	1.94	0.77	1.2	666.6
Pt/Pd/PDAN	0.188	0.528	2.83	1.66	1.89	1.5	1.7	1825

*V vs RHE ** 0.5 M FA

Table 6.4: Electrochemical data of FAO at Pt/Pd/GC and Pt/Pd/PDAN/GC catalysts.

Electrocatalyst	$\mathbf{I_p^d (mA.cm^{-2})}$	$\mathbf{I_p^{ind} (mA.cm^{-2})}$	$\mathbf{I_p^d/I_p^{ind}}$	$\mathbf{I_p^d/I_b}$
Pt/Pd/GC	1.17	4.5	0.26	0.2
Pt/Pd/PDAN/GC	23.7	13.2	1.79	0.92

Table 6.5. A comparison of the electrocatalytic activities reported for different catalysts toward FAO.

Modified electrode	**C_{FA} / M**	**Mass activity (A/g)**	**I_p^d (mA.cm^{-2})**	**ECSA (m^2 g^{-1})**	**Reference**
Pt-Pd/PFCA/GC	0.5	1225	44.1	53.3	[416]
PtPd/HPC500	0.5	126	0.169	49.6	[472]
Au@AuPd NCs	0.5	1250	71.24	62.68	[449]
Pd@Ni-B/C	0.5	400	71.2	43	[473]
PdAu/C	0.5	371	0.85	43	[474]
Commercial Pt/C	0.5	8.3	0.83	2.4	[475]
Pt/PANi/GC	0.3	1030	31	-	[476]
Pt/Pd/p1,5-DAN /GC	0.5	1825	73	90.43	This work

6.4.3 Parameters affecting the electrooxidation of formic acid

6.4.3.1 Effect of scan rate

CV for FAO at different modified electrodes and different sweep rates has been recorded as shown in **Figure 6.7**. Pt/Pd/ PDAN/GC electrode shows the highest catalytic activity since the anodic and cathodic current densities for FAO are higher than that of the other electrodes. Plotting the peak current densities at 0.65 V for Pt/Pd/ PDAN/GC modified electrode in the forward-going sweep as a function of the square root of sweep rate as displayed in **Figure 6.8**, the role of diffusion limitation can be elucidated. Since the diffusion rate for all catalysts is the same, such an evaluation only makes sense for the catalyst with the highest activity; for the others, the current will be limited to a larger extent by slow kinetics.

The diffusion coefficient for formic acid oxidation has been computed according to Randles- Sevcik equation [477]. For an irreversible system

$$j_p = 2.69\times10^5 D^{1/2} n^{3/2} \upsilon^{1/2} C \qquad (6.4)$$

where n is the number of electrons transferred, the peak current density j_p (direct) measured in mA cm^{-2}, the diffusion coefficient D in cm^2 s^{-1}, the FA concentration in the bulk solution, C_∞, in mol cm^{-3} and the scan rate (υ) in Vs^{-1}. (We can assume planar diffusion because the distance between the particles is small compared to the thickness of the Nernst diffusion layer)

The diffusion coefficient, D, which is a measurement of the mass-transport rate through the liquid nearby the electrode surface obtained from the slope of the linear relationship shown

in **Figure 6.7** is 9.02 x 10^{-6} cm^2/s for Pt/Pd/PDAN. This value is comparable to the values in literature for methanol (D =1.5 x 10^{-6} cm^2/s) and acetic acid (D =1.201 x 10^{-5} cm^2/s) in H_2SO_4 containing solutions [478 - 480]. Therefore, the linear relationship of **Figure 6.7** indicates that the reaction is largely diffusion controlled.

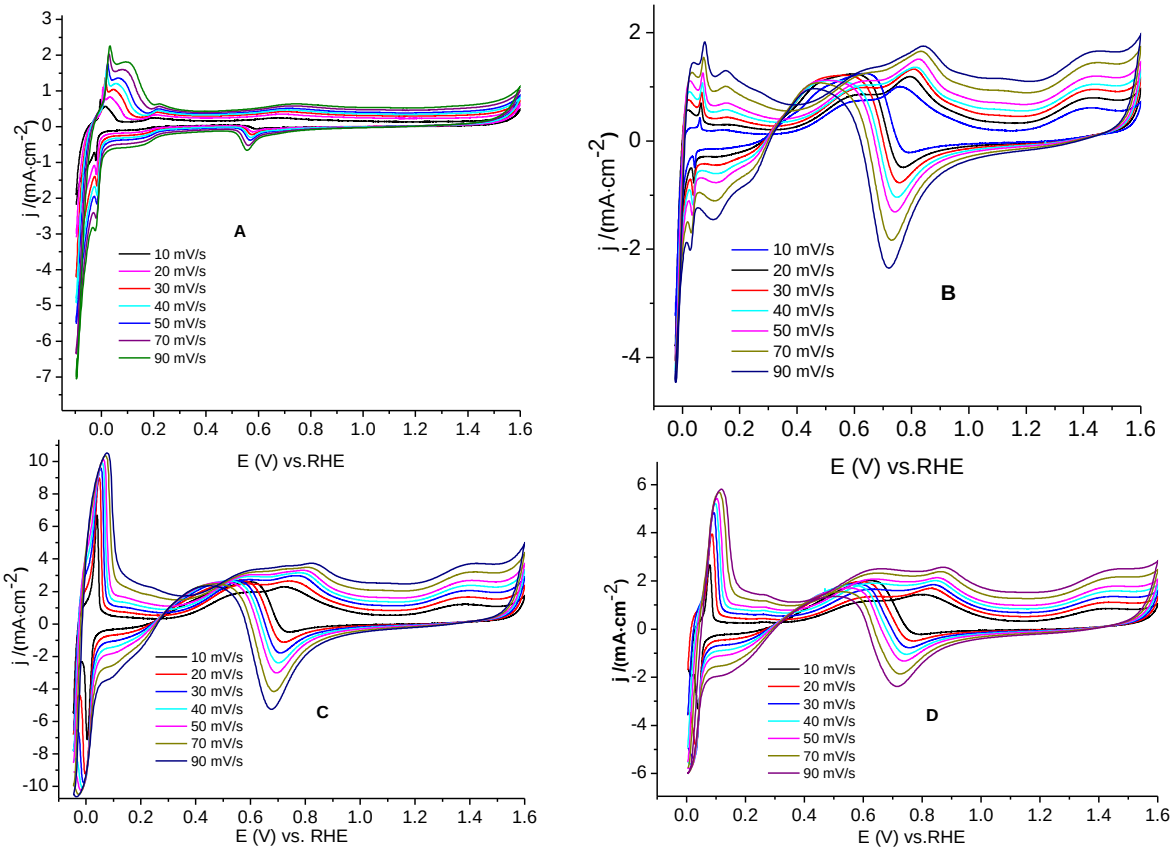

Figure 6.7: Cyclic voltammograms of (A) Pd/PDAN/GC, (B) Pt/PDAN/GC, (C) Pt/Pd/PDAN/GC and (D) Pd/Pt/PDAN/GC modified electrodes in 0.01 M HCOOH + 0.50 M H_2SO_4 solution at different sweep rates.

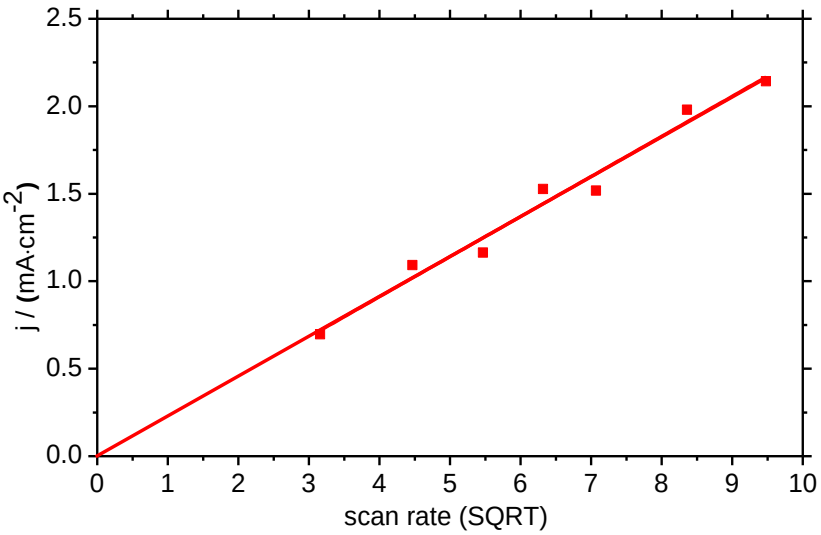

Figure 6.8: Current densities versus square root of sweep rate for FAO at Pt/Pd/PDAN/GC electrode in 0.01 M HCOOH + 0.50 M H_2SO_4 solution.

6.4.3.2 Effect of Formic acid concentration

To investigate the capacity of the Pd/PDAN/GC, Pt/PDAN/GC, Pd/Pt/PDAN/GC and Pt/Pd/PDAN/GC electrodes for FAO, different concentrations of FA were investigated by CV technique (Figure not shown). According to the investigation results, rising FA concentration by one decade (from 0.01 to 0.1 M) results in an increase of peak current densities in the forward and backward sweeps (**Figure 6.9A**). There is a direct proportionality concerning formic acid concentration and the corresponding direct anodic peak current densities. It was detected that anodic peak potential in the forward scan remains practically constant.

The reaction order of formic acid in the FAO reaction was investigated by plotting the logarithm of current versus the logarithm of FA concentration at the onset potentials of 0.23 V and 0.25 V for Pd/PDAN (**Figure 6.9B**), 0.47 V and 0.55 V for Pt/PDAN, Pd/Pt/PDAN and Pt/Pd/PDAN (Fig. 6.9C, D and E). The reaction order with respect to FA was calculated using **Equation 6.6** [4]:

$$\text{Rate} \equiv j = kC^n \qquad (6.5)$$

$$\log (j) = \log k + n \log C \qquad (6.6)$$

Where j is the current density, k is the reaction rate constant, C is the bulk concentration of FA, and n is the reaction order. The reaction order with respect to FA concentration has been calculated to be 0.02, 0.50, 0.80 and 0.70 for Pd/PDAN, Pt/PDAN, Pd/Pt/PDAN and Pt/Pd/PDAN, respectively. The fractional values of the reaction order indicate to the

electrooxidation reaction depends mainly on the adsorption steps [481, 482]. If the oxidation reaction was solely diffusion-limited as suggested by **Figure 6.8**, the reaction order would be unity according to the 1st Fick's law. The lower value of the reaction order shows that the reaction at least is not completely controlled by diffusion, only for the most active catalyst the reaction is approaching diffusion limitation.

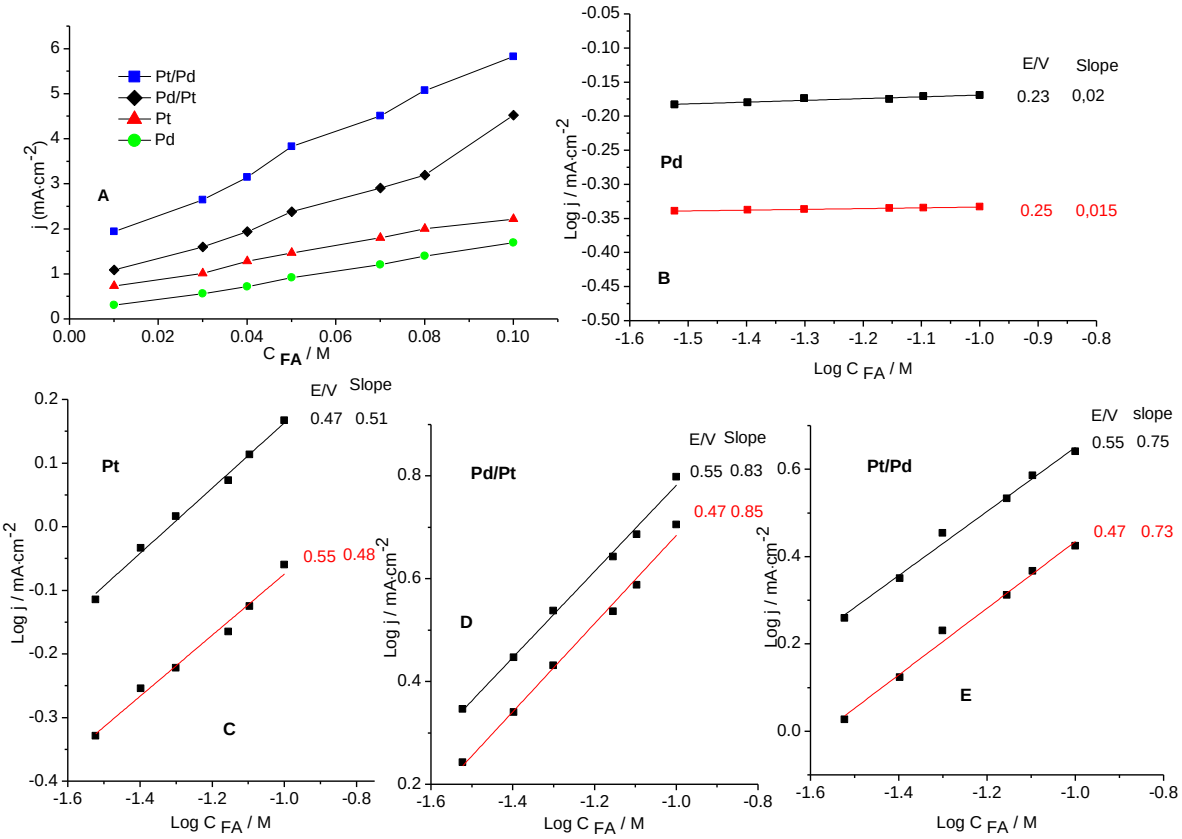

Figure 6.9: (A) Anodic peak current density (direct) in the forward sweep vs. FA concentration, Plot of the logarithm of current vs. logarithm of FA concentration at (B) Pd/PDAN/GC, (C) Pt/PDAN/GC (D) Pd/Pt/PDAN/GC and (E) Pt/Pd/PDAN/GC modified electrodes.

6.4.4 Differential Electrochemical Mass Spectroscopy (DEMS) measurements of FAO

FAO at different modified electrodes under electrolyte flow has been studied using DEMS. The recoded cyclic voltammograms of FAO and the related ionic signals for m/z = 44 (Evolution of CO_2) are shown in **Figure 6.10**. Since CO_2 is the only possible oxidation product, the ion currents correspond to the true oxidation rates; in particular, the onset potential can be detected more exactly than from the faradaic currents because it is difficult to separate the latter from pseudo capacitive currents. At 0.20 V the faradaic current starts to rise during the anodic

scan for all catalysts, leading to a broad peak with its maximum at 0.75 V followed by the second anodic peak in the oxygen region at 1.40 V. During the cathodic going sweep, an oxidation peak exists at 0.54 V after reduction of the whole oxides from the electrode surface. The ion current for CO_2 shows the rank of activity of Pt/Pd/PDAN/GC > Pt/PDAN/GC > Pd/Pt/PDAN/GC > Pd/PDAN/GC as already concluded from the faradaic currents, cf. **Figures 6.3** and **6.4**. The value of the current density of 140.0 $\mu A.cm^{-2}$ for formic acid oxidation at Pd/PDAN/GC modified electrode at 0.27 V is similar to the reported data in the literature for the oxidation of formic acid at Pd/GC considering the used surface area of 0.91 cm^2 [483].

The current efficiency with respect to CO_2 evolution (A_{CO_2}) was calculated using the following equation:

$$A_{CO_2} = \frac{2 \cdot Q_{CO_2}}{K^* \cdot Q_F} \qquad (6.7)$$

Here, 2 is the number of electrons transferred during the whole oxidation of one FA molecule, Q_{CO2} is the ionic charge of m/z = 44 and Q_f is the faradaic charge of FAO. The value of the current efficiencies are between 70 % and 100 %. Deviations from the expected value of 100 % arise from pseudo capacitive effects (charging of polymer and adsorption/ desorption of H and OH at the metal).

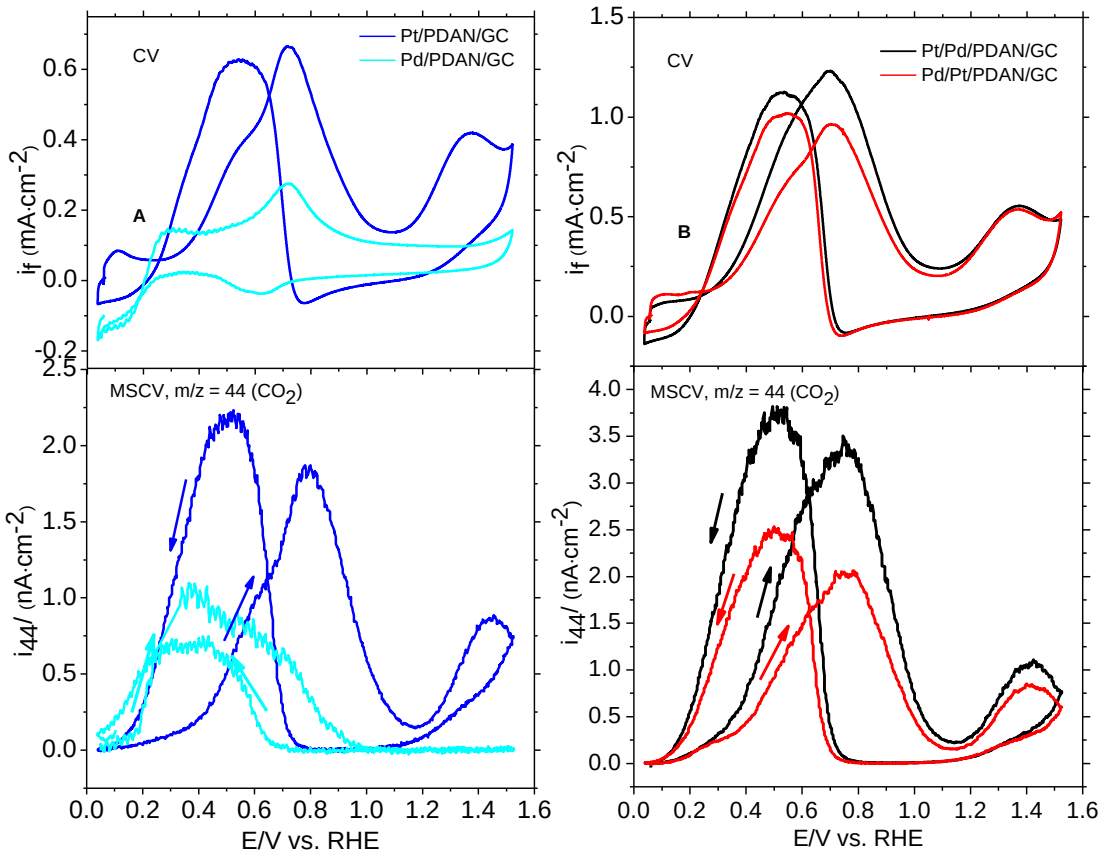

Figure 6.10: Simultaneously recorded faradaic and ion current of CO_2 (m/z = 44) during the electrooxidation of 0.01 M FA in 0.50 M H_2SO_4 at monometallic (A) and bimetallic (B) modified electrodes at a scan rate of 0.01 Vs^{-1} and electrolyte flow rate of 5.0 µL s^{-1}. (Current densities are referred to the true surface area as determined by CO_{ads})

Table 6.6: The integrated faradaic and ionic charges and the corresponding current efficiencies with respect to CO_2 results from the recorded CV and MSCV during the electrooxidation of formic acid at the studied catalysts at 10.0 mV/s in anodic and cathodic sweeps.

Electrodes	Q_f (mC/cm^2)		Q_i (nC/cm^2)		Eff %	
	Anodic	Cathodic	Anodic	Cathodic	Anodic	Cathodic
Pt/PDAN	17.5	21	57.35	76	97.82	108
Pd/PDAN	4.41	3.61	12.5	9.26	84.6	76.6
Pd/Pt/PDAN	26	26.9	76	98	87.2	108.2
Pt/pd/PDAN	38	55	137	202.6	107	109

6.5 Conclusion

Electrochemical preparation of mono- and bimetallic modified electrodes and their characterization have been reported in this manuscript. Pt, Pd, Pt/Pd and Pd/Pt at PDAN/GC modified electrodes were prepared by potentiodynamic technique in the corresponding metal ion-containing electrolyte. The recorded CVs show the characteristic profiles of the tested electrodes. DEMS coupled with dual thin layer flow-through cell has been used to determine the electrodes electroactive surface area by CO_{ads} oxidation and their electroactivity towards FA oxidation. The direct pathway of FAO (dehydrogenation) is the prevailing reaction at bimetallic modified electrodes since the dispersion of both metals disturbs the continuity of Pt sites which required to adsorb CO and in sequence the indirect pathway of FAO. DEMS results show that, however the Pd/PDAN/GC has the lowest onset oxidation potential during FAO, Pt/Pd/PDAN/GC has the highest rate of reaction among the electrodes under investigation. The current efficiency with respect to CO_2 production at bimetallic dispersed and Pt/PDAN/GC electrodes was close to 100 %. The modified electrode is a promising candidate as an electrocatalyst in FA fuel cell, but further studies on the electrode stability are required.

Chapter seven:

Comparative studies of ethylene glycol electrooxidation by Pt and Pd nanoparticles supported on different conducting polymers – a DEMS study

K.M. Hassan[a,*], A.S. Shatla[b,c], A.A. Abd-El-Latif [d,e], H. Baltruschat[c,] and M. Abdel-Azzem[b]

[a] Research Chemistry Laboratory, Physics and Mathematics Engineering Department, Faculty of Electronic Engineering, Menoufia University, Menof 23952 Egypt.
[b] Chemistry Department, Faculty of Science, Menoufia University, Shibin El-Kom, 32512 Egypt.
[c] Institute of Physical and Theoretical Chemistry, Bonn University, D-53117 Bonn, Germany.
[d] National Research Centre, Physical Chemistry Dept., 12311 Cairo, Egypt.
[e] Material Research Department (ECM), Center of Solar Energy and Hydrogen Research (ZSW), D-89081 Ulm, Germany

Published online: September 1, 2020

Reprinted (adapted) with permission from

K. M. Hassan, A. S. Shatla, A. A. Abd-El-Latif, H. Baltruschat and M. Abdel-Azzem, Journal of Electroanalytical Chemistry **2020**, 878, 114624.

Acknowledgment

The authors would like to appreciate the financial funding of Alexander von Humboldt (Project No. 30260067).

7.1 Abstract

The electrocatalysis of ethylene glycol oxidation (EGO) by platinum (Pt) or/and palladium (Pd) metal nanoparticles supported on three conducting polymers, poly-1,5-diaminonaphthalene (p-1,5-DAN), poly-1,8-diaminonaphthalene (p-1,8-DAN), and poly-1,2 diaminoanthraquinone (p-1,2-DAAQ) on a glassy carbon (GC) electrode was investigated at room temperature under a constant electrolyte flow using in situ differential electrochemical mass spectrometry (DEMS). The impact of the three different polymers as support materials on the catalytic activity of EGO was examined. During potentiodynamic measurements, both the faradaic current and the ionic signals corresponding to carbon dioxide (CO_2) formation were continuously monitored. For the different catalysts, it was found that EG adsorption was prevented at very low potentials due to blocking by the underpotential deposition of hydrogen species and dissociative adsorption was enhanced upon an increase in the potential. During EGO, CO_2 evolution was prohibited at the onset of OH_{ads} formation at the surface. A quantitative comparison of CO_2 formation was evaluated for these modified conducting polymers. The trend in the current efficiency with respect to CO_2 formation was found to be in the order of Pt/Pd/p-1,8-DAN/GC > Pt/Pd/p-1,5-DAN/GC > Pt/Pd/p-1,2-DAAQ/GC (shell–core). The current efficiency of CO_2 production at the Pt/Pd/p-1,8-DAN/GC electrode was recorded as 87.5%, which is higher than reported in the literature. The roles played by the three studied polymers are discussed in this study, in which P-1,8-DAN shows excellent behavior as an attractive material for supporting metal nanoparticles due to its high active surface area and high electrical conductivity.

7.2 Introduction

Hydrogen fuel cells have long been discussed as promising potential power sources because they are lightweight, show high reaction efficiency, are easy to transport and cheap to produce. However, the compact storage of hydrogen still remains a challenge.

Ethylene glycol (EG) as a pure aliphatic diol is a promising energy source for use in liquid fuel cells due to its low toxicity, remarkably high energy density, and high boiling point [484, 485]. Noble platinum (Pt) and Pt-based electrodes are perfect anodes for the electrooxidation of EG because Pt and its alloys are the most used catalysts for the electrooxidation of small organic molecules, however, they are high in cost and exhibit the high adsorption of catalytic oxidation products. The poisonous intermediates resulting from EG oxidation (EGO) and their slow kinetics still present a big challenge. To overcome this problem,

Pt was combined with other metal catalysts such as palladium (Pd), ruthenium (Ru), copper (Cu), and cobalt (Co) [486-489] to form bimetallic systems that show improved catalytic performance and a low yield of poisonous products. These metals have been used to modify anodes alongside support materials to achieve the immobilization of nanocatalysts, which significantly enhances their durability, activity, and stability compared to unsupported bulk metal catalysts [490]. The choice of a suitable polymeric film is an essential factor that affects electrocatalytic interactions, surface activity, and catalyst performance. Polymer supports have high surface areas and as such are excellent materials upon which to disperse a catalyst. The support can also reduce catalyst poisoning. For example, Chen et al. fabricated Pt–Co nanoclusters supported on polypyrrole sheets that showed improved catalytic activity toward EGO [491]. Besides this, polythiophene/MWCNTs have played an important role in the dispersion of Pt and Pt–Ru nanoparticles, showing increased electroactivity toward EGO [492]. Composite-supported Pt and bimetallic catalysts have also been studied in terms of their current efficiency with respect to their ability to produce carbon dioxide (CO_2) via the oxidation of C2 compounds such as ethanol [493, 494] using differential electrochemical mass spectrometry (DEMS). Wang et al. showed that the average current efficiency for CO_2 yield was 9.5% in the anodic direction and 2.6% in the cathodic direction [495]. Using a DEMS thin layer cell, it has been shown that the reaction pathway of alcohol oxidation (e.g., direct vs. indirect pathways, adsorbate formation) is largely influenced by catalyst structure, particle distribution, atomic surface composition, and convection [71, 496 - 498].

In this study, the combined activities of Pt and/or Pd nanoparticle composites on three different polymers support toward EGO were examined. In these electrocatalysts, three diamino derivatives were tested as the conducting polymers. Conducting polymers such as these have broad potential stability and excellent conducting properties. The three conducting polymers used in this study were supported on glassy carbon (GC) electrodes and named poly(1,5-diaminonaphthalene)/GC (p-1,5-DAN/GC), poly(1,8-diaminonaphthalene)/GC (p-1,8-DAN/GC), and poly(1,2-diaminoanthraquinone)/GC (p-1,2-DAAQ/GC) electrodes. In previous studies, these polymer supports have been used in the electrooxidation of small organic species [499 - 501]. These diamino polymer matrices have shown excellent behavior as attractive materials for hosting metal nanoparticles (MNPs) due to their large surface area, high electrical conductivity, and stability. Both Pt and Pd have been investigated in the form of monometallic as well as bimetallic systems as catalysts for EGO. A quantitative comparison of CO_2 formation from complete EGO was made using DEMS and the results were examined.

Besides this, the catalyst with the highest current efficiency value was found to have the optimal arrangement of MNPs.

7.3. Experimental

7.3.1 Materials

The 1,5-DAN, 1,8-DAN, 1,2-DAAQ monomers, EG, acetonitrile (99.8%), lithium perchlorate ($LiClO_4$, ≥ 99%), palladium chloride ($PdCl_2$), and chloroplatinic acid hexahydrate ($H_2PtCl_6.6H_2O$) were purchased from Sigma–Aldrich. Perchloric acid ($HClO_4$, 70%) was purchased from Fluka and used as received. Sulfuric acid (H_2SO_4) was procured from Merck. Aqueous solutions used in the study were prepared using 18.2 MΩ.cm Milli-Q Millipore water, with a total organic carbon content of <3 ppb. All electrolytes were purged with highly pure argon (99.999%, AIR LIQUIDE) prior to their use.

7.3.2 Instruments

The preparation of the catalysts was conducted using an EG&G potentiostat (Model 273A) in conjunction with the LabVIEW software, where the experiments were performed using a traditional three-electrode electrochemical cell. A GC electrode was used as a working electrode, a 1.0 cm^2 Pt sheet as a counter electrode, and Ag/Ag^+ or Ag/AgCl were used as reference electrodes. Electrochemical surface area (ECSA) measurements of the catalysts were made using DEMS, as previously reported by our group [499 - 501]. The current efficiency of CO_2 formation from EG was also measured by DEMS. All of the DEMS experiments were conducted at the University of Bonn using a dual thin-layer flow cell with a four-electrode design incorporating a GC electrode as the working electrode, a reversible hydrogen electrode (RHE) as the reference electrode, and two Pt wires as counter electrodes. The two wires were mounted at the inlet and outlet used to introduce the electrolyte to the vessel and were attached via resistances of 1.1 and 0.1 kΩ, respectively, to regulate the distribution of current in the thin-layer cell in addition to reducing the IR drop resistance [502]. First, the electrolyte was passed from the cell entrance to the working electrode, situated in the upper compartment of the thin-layer cell. There, the EG was oxidized at the bimetallic catalyst. The products from the reaction in the electrolyte diffused through six narrow capillaries into the lower compartment where the volatile components and gases were sucked through a 20 nm pore sized Teflon membrane to a vacuum inlet (10^{-5} mbar) mass spectrometer (Balzers quadrupole QMG-422).

The DEMS was calibrated as follows. The potential was kept between 40 and 70 mV after cleaning of the Pt (poly) electrode by cycling the potential limit from 0.05 to 1.5 V in the supporting electrolyte at 50 mV/s, after which the electrolyte was then replaced via the injection of CO saturated supporting electrolyte (10^{-3} mol L^{-1}) into the cell to form a monolayer of adsorbed CO on the electrode. Elimination of the bulk CO from the cell was achieved by introducing supporting electrolyte and the potential was scanned in the anodic direction at a rate of 10 mV/s and subsequently, the adsorbed CO was oxidized to CO_2. Due to 20% of non-faradaic charges present as a result of sulfate or bisulfate adsorption on the Pt electrode, the total charge from the faradaic current was corrected by a factor of 0.8 [172, 503].

7.3.3 Electrochemical preparation of differently modified electrodes

The formation of a 1,5-DAN polymer film was carried out in aqueous solution, as presented in our previous work [501]. The DAN monomer (1.50 mM) was dissolved in 1.0 M $HClO_4$ and electropolymerized using cyclic voltammetry (CV) at a GC electrode in the potential range of 0.0 – 0.80 V (vs. Ag/AgCl) for 15 scans at a sweep rate of 20 mV/s. Both the 1,8-DAN and 1,2-DAAQ polymers were also prepared using CV at a GC electrode in acetonitrile containing 0.1 M $LiClO_4$ [499, 500].

7.3.4 Electrodeposition of MNPs

Pt or Pd monometallic composites were prepared by cycling the modified electrode 25 times between −0.35 to +0.65 V (vs. Ag/AgCl) in a 0.1 M aqueous solution of $HClO_4$ containing 2.5 mM of H_2PtCl_6 or 2.5 mM of $PdCl_2$ at 50 mV/s. The procedure for the electrodeposition of Pt/Pd or Pd/Pt (shell–core) bimetallic composites was identical to the previously described monometallic deposition.

7.4 Results and discussion

7.4.1 Electrooxidation of EG at the different MNPs/p-1,5-DAN/GC catalysts

The electrooxidation of 0.01 M EG in 0.5 M H_2SO_4 supporting electrolyte was studied by DEMS on the four Pt/p-1,5-DAN/GC, Pd/p-1,5-DAN/GC, Pd/Pt/p-1,5-DAN/GC, and Pt/Pd/p-1,5-DAN/GC catalysts (**Figure 7.1a** and **b**) in which the faradaic current (I_F) and the corresponding ion current (I_{44}) for m/z = 44 (CO_2) are shown. The CVs are characterized by two broadening peaks in the anodic sweep and one peak in the cathodic sweep. The EGO process on the Pt/Pd/p-1,5-DAN/GC catalyst starts at about 0.55 V in the anodic scan (**Figure**

7.1a), resulting in the first wide peak associated with a maximum at 0.70 with a shoulder at 0.80 V, a broad peak in the oxygen adsorption region at 1.30 V, and one oxidation peak in the cathodic direction at 0.62 V. The mass spectrometric cyclic voltammetry (MSCV) (**Figure 7.1b**) is dominated by a single asymmetric peak, the position of which corresponds to the maximum of the wide faradaic current peak in the low potential area (0.70 V). This peak is mainly related to the electrooxidation of adsorbed carbon monoxide (CO_{ads}), which forms at low potential or in the previous cathodic sweep. Accordingly, the second peak (or shoulder) in the faradaic current at 0.80 V can be ascribed as EGO to an incompletely oxidized species [504]. The current decay at a potential of higher than 0.80 V originates from the growth of O-adsorbed species at the electrode surface. The slow eventual increase in the faradaic current at a potential of higher than 1.00 V can be attributed to incomplete EGO that takes places on the oxidized electrode surface since the MS signal barely increased in this potential region; only above 1.30 V was complete oxidation to CO_2 observed again. In the cathodic direction, the reaction began again at ∼0.79 V (faradaic current) combined with surface oxide reduction. Moreover, the faradaic current density goes through a maximum at 0.62 V vs. RHE and then decreases quickly, approaching zero current at ∼0.33 V. The CO_2 ion current begins to increase at ∼0.75 V and approaches a maximum at 0.63 V due to a delay of around two seconds between the faradaic current and MS detection at such low electrolyte flow rates. In spite of the coincidence between the main peaks, there are obvious differences between the faradaic current density and the CO_2 formation rate. The faradaic current density is higher in the cathodic than the anodic direction, while the opposite trend is observed in the production of CO_2. Hence, in the cathodic sweep, the formation of partial oxidation products of EG occurs to a much greater extent than in the anodic direction. The peak at 0.72 V in the MSCV matches the first component of the anodic peak potential in the CV, while the second component in the CV at 0.80 V is associated with a low ionic current, without the presence of any apparent peak for CO_2, which indicates that other oxidation species are formed at the surface at such a high potential.

It is clear from the CV and MSCV data that the Pt/Pd/p1,5-DAN/GC catalyst shows the highest electroactivity (in terms of oxidation current and onset potential (from MSCV) for EGO) than the other catalysts, from which it can be concluded that the Pd/p1,5-DAN/GC catalyst is not effective for EGO. **Equation 7.1** was used to calculate the current efficiency for CO_2 production and the obtained results are shown in **Table 7.1**:

$$A = \left(\frac{(z\, I_{MS} / K^*}{I_F}\right) 100 \qquad (7.1)$$

where z is the number of electrons transferred per evolved CO_2 molecule (ten electrons), I_{MS} and I_F are the ionic and faradaic current densities at their corresponding potentials, respectively, and K* is the calibration constant for the DEMS setup, calculated from the integrated ionic and faradaic charges during electrooxidation of a pre-adsorbed monolayer of CO_{ads} at a polycrystalline Pt electrode according to the relationship: $K^* = 2\ Q_i/Q_f$ [505].

Table 7.1: The current efficiencies corresponding to the evolved CO_2 during EGO on the different metal catalysts supported on p-1,5-DAN/GC electrode.

Catalysts	Q_F^A/ mA cm^{-2}	j_F^A / mA cm^{-2}	Q_F^C / mA cm^{-2}	j_F^C / mA cm^{-2}	Q_{44}^A/ nA cm^{-2}	j_{44}^A/ nA cm^{-2}	Q_{44}^C/ nA cm^{-2}	j_{44}^C/ nA cm^{-2}	Current eff. for CO_2			
									A_{44}^A		cycle	peak
									cycle	peak		
Pt/p-1,5 DAN	7.5	0.43	12.9	0.64	4.1	0.26	1.39	0.08	63.9	71.1	12.47	14.8
Pd/p-1,5-DAN	-		-		-		-		-		-	
Pd/Pt/p-1,5-DAN	3.85	0.18	5.64	0.24	2.3	0.115	0.59	0.03	68.9	75.1	12.17	14.7
Pt/Pd/p-1,5-DAN	12.2	0.72	16.7	0.93	8.6	0.53	2.5	0.147	81.6	86.6	17.2	18.5

The current efficiency with respect to CO_2 formation averaged over the anodic sweep at the Pt/Pd/p-1,5-DAN/GC electrode reaches ca. 81.6% and it decreases to 17% in the cathodic sweep direction. The current efficiency of the peak (86.6%) is higher than the average, confirming the above statement that the shoulder in the faradaic current is largely due to the oxidation of products other than CO_2. The catalytic activity of the studied metal deposited on modified electrodes toward EGO shows higher efficiency than that of Pt/Vulcan, PtRu/Vulcan, and Pt_3Sn, which show current efficiencies in the range of 3–5% at constant potential over a potential limit of 0.50–0.70 V at the same scan rate [495, 504]. According to the current efficiency values, the catalytic activity toward EGO is in the order of Pt/Pd/p-1,5-DAN/GC > Pd/Pt/p-1,5-DAN/GC > Pt/p-1,5-DAN/GC.

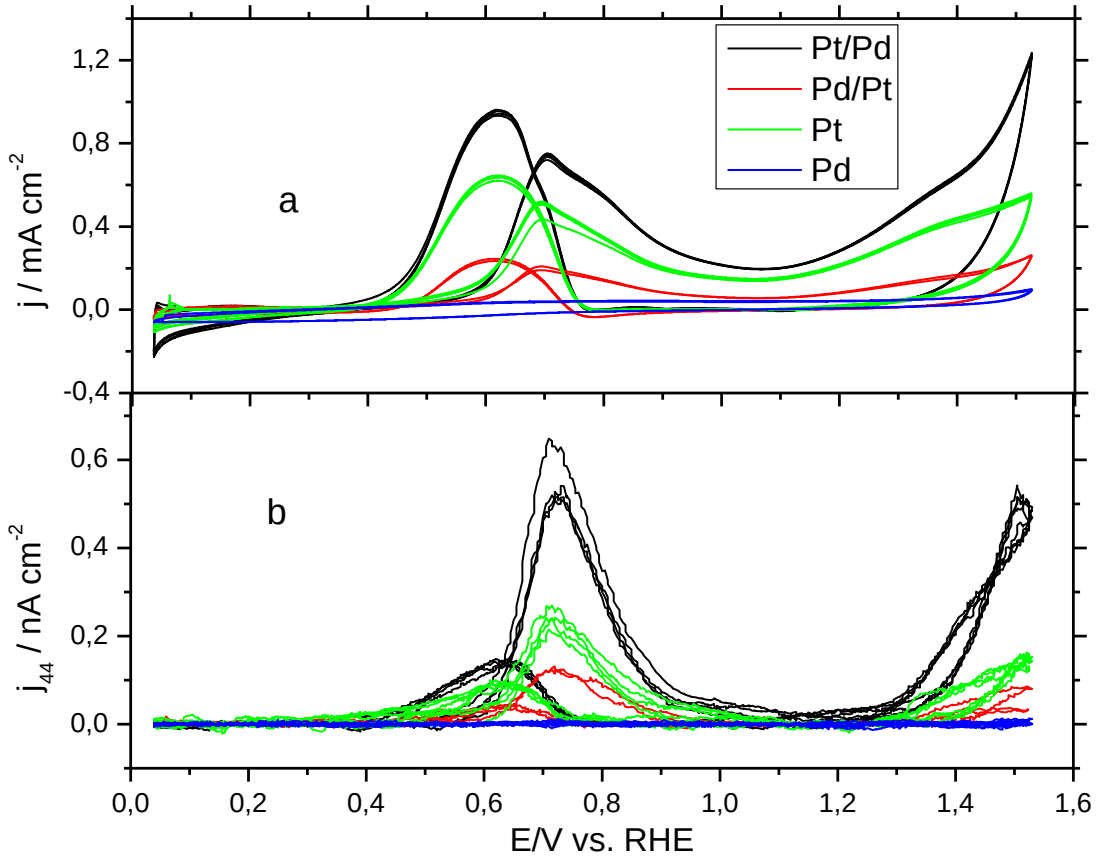

Figure 7.1: Simultaneously recorded CV (a) and the corresponding MSCV for CO_2 (m/z = 44) (b) in 0.01 M EG and 0.5 M H_2SO_4 at the different metal catalysts supported on p-1,5-DAN/GC at 10.0 mV/s and electrolyte flow rate 5.0 µl s^{-1}.

The ECSA, the onset potentials (E_{onset}), forward and reverse ionic current density (I_F and I_R) ratios (tolerance), and current efficiencies are shown in **Table 7.2**. The ratio between the forward and reverse current density is essentially an index of the catalytic enhancement, which is often used to evaluate the tolerance of a catalyst against partially oxidized species that have accumulated on its surface [489, 506, 507]. It is clear that the Pt/Pd/p-1,5-DAN/GC (shell–core) catalyst is more electroactive for EGO than the Pd/Pt/p-1,5-DAN/GC or Pt/p-1,5-DAN/GC composites. The Pt/Pd/modified electrode has the highest ECSA of 90.43 m^2/g [501], the lowest onset potential of 0.55 V vs. RHE, fewer intermediate oxidation products that form during the catalytic processes (higher ratio I_F/I_R), and higher current efficiency for CO_2 formation. The slightly more negative onset potential of the Pt/Pd/p-1,5-DAN/GC catalyst compared with the other catalysts (**Table 7.2**) reveals that EGO is more easily achieved on this surface. Its high ratio of CO tolerance suggests that there is a reasonably low amount of adsorbed carbonaceous material [508] resulting from incomplete EGO on the surface of this

catalyst. Glycolate [509], oxalate [510], and formate [509] intermediates have previously been determined to form during EGO at Pd-, Pt-, and Au-based modified electrodes. The increase in the current efficiency of CO_2 production at the Pt/Pd/p-1,5-DAN/GC electrode may indicate that the surface of the electrode is not blocked by the intermediates, since these are quickly oxidized in subsequent steps.

Table 7.2: EGO performance at the different catalysts supported on p-1,5-DAN/GC.

Catalysts	**ECSA [501] (m^2/g)**	**E^*_{onset} (V)**	**I_F^{MS} ($nA\ cm^{-2}$)**	**I_R^{MS} ($nA\ cm^{-2}$)**	**I_F/I_R**	**A^a_{CO2} %**
Pt/p-1,5-DAN/GC	56.16	0.58	0.269	0.097	2.77	63.9
Pd/p-1,5-DAN/GC	20.13	-	-	-	-	-
Pd/Pt/p-1,5-DAN/GC	32.5	0.57	0.127	0.043	2.95	68.9
Pt/Pd/p-1,5-DAN/GC	90.43	0.55	0.643	0.146	4.4	81.57

* vs. RHE

7.4.2 Electrooxidation of EG at the different MNPs/p-1,8-DAN/GC catalysts

Since it has the highest peak current density among all the catalysts, the bimetallic Pt/Pd/p-1,8-DAN/GC catalyst shows the best EGO (**Figure 7.2**), followed by the Pt/p-1,8-DAN/GC catalyst. The Pd/Pt/p-1,8-DAN/GC catalyst has a lower oxidative current density than the Pt/p-1,8-DAN/GC catalyst, but a worse performance than the Pt/Pd/p1,8-DAN/GC catalyst. When oxidizing EG, the Pt/Pd/p-1,8-DAN/GC catalyst exhibits three discrete characteristics. There is a central peak at 0.70 V, a less intense peak at 0.80 V, and a smooth shoulder at 1.36 V in the oxygen region. It can be seen that the Pd/p-1,8-DAN/GC catalyst is not active toward EGO. With increasing electrode potential, the anodic peak of EGO occurs at the same potential of 0.70 V for both the Pt/Pd/p-1,8-DAN/GC and Pd/Pt/p-1,8-DAN/GC catalysts, with currents densities of 184.1 and 114.8 μA cm^{-2}, respectively. In the negative sweep direction, reactivation of the electrode surface at around 0.62 V for Pt/Pd/p-1,8-DAN/GC gives rise to the formation of a reverse anodic peak, which is related to EGO and the elimination of intermediates partially oxidized during the anodic scan [511].On the other hand, in the MSCV, a peak at around 0.70 V resembles the faradaic current peak (0.70 V), with high ionic current observed at a high potential limit. CO oxidation occurs at 0.7 V, while partial EGO leads to the formation of a shoulder at 0.80 V. It is obvious that the anodic ionic current density is higher than the cathodic

current, whereas this behavior is reversed for the faradaic current. In the reverse scan, the EGO passes through a high faradaic current, whereas the corresponding ion current remains comparatively low due to the formation of more partially oxidized products than during the forward scan. The highest current value recorded at the Pt/Pd/p-1,8-DAN/GC catalyst reveals its excellent catalytic performance toward the oxidation of carbonaceous intermediates.

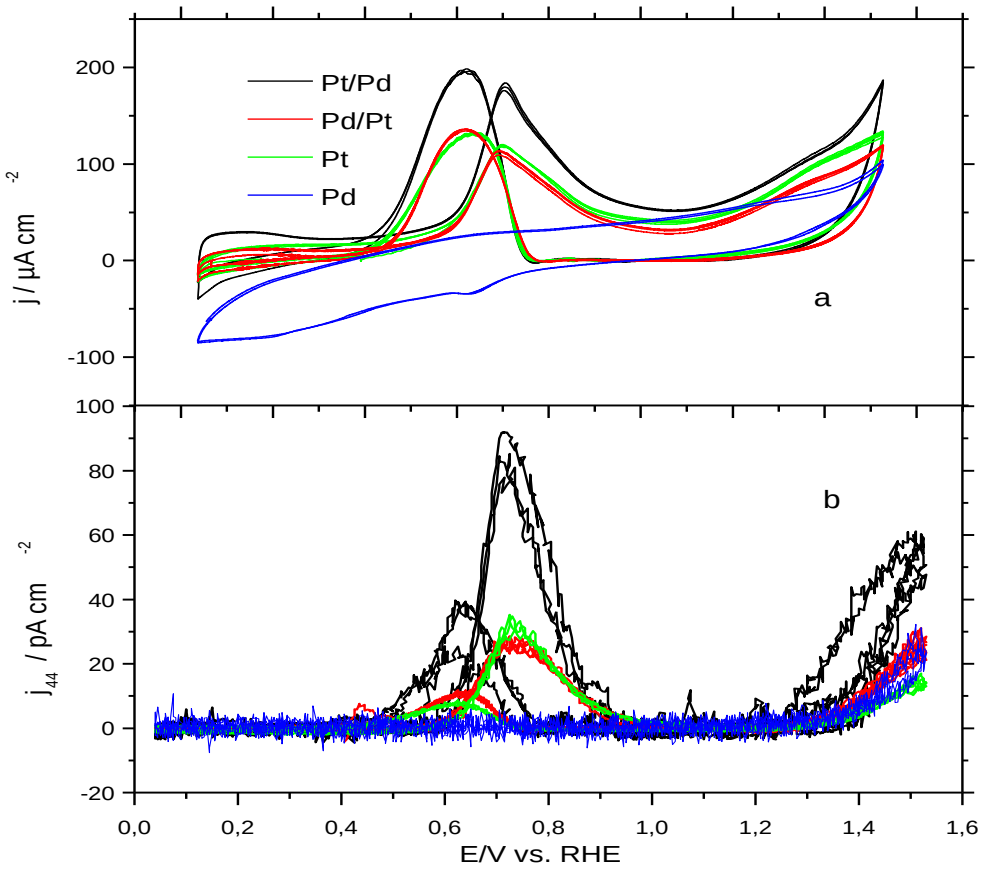

Figure 7.2: Simultaneously recorded CV (a) and the corresponding MSCV for CO_2 (m/z = 44) (b) in 0.01 M EG and 0.5 M H_2SO_4 at different metal catalysts supported on p-1,8-DAN/GC at 10.0 mV/s and electrolyte flow rate 5.0 µl s^{-1}.

Current efficiencies for CO_2 formation (A_{CO_2}) were determined using **Equation 7.1** and are presented in **Table 7.3**. The order of activity in terms of A_{CO_2} is Pt/Pd/p1,8-DAN/GC > Pt/p1,8-DAN/GC > Pd/Pt/p1,8-DAN/GC.

Table 7.3: Integrated ionic and faradaic charges and the current efficiencies with respect to CO_2, during EGO at different metal catalysts supported on p-1,8-DAN/GC at 10.0 mV/s.

Catalysts	Q_f / $(mC\ cm^{-2})$		Q_i / $(nC\ cm^{-2})$		A_{44}%	
	Anod.	Cath.	Anod.	Cath.	Anod.	Cath.
Pt/p1,8-DAN/GC	2.2	2.6	0.55	0.13	42.78	8.6
Pd/p1,8-DAN/GC	-	-	-	-	-	-
Pd/Pt/p1,8-DAN/GC	2.0	2.6	0.4	0.18	35.47	11.97
Pt/Pd/p1,8-DAN/GC	2.5	3.7	1.27	0.6	87.5	27.7

Table 7.4 outlines the performances of the catalysts according to their ECSAs, the onset potentials of EGO (E_{onset}), the peak ionic currents of the forward and reverse sweeps ($I_F^{MS}$and I_R^{MS}), the ratios of the forward primary and reverse oxidation peak current densities (I_F/I_R), and the current efficiencies for CO_2 production. The Pt/Pd/p-1,8-DAN/GC (shell–core) catalyst shows better electroactivity for EGO than Pd/Pt/p-1,5-DAN/GC or Pt/p-1,5-DAN/GC. The most pronounced advantage of using Pt/Pd/p-1,8-DAN/GC is that its ECSA of 157.58 m^2/g [500] increased relative to those of the other catalysts as a result of the order of metal deposition. The order of the catalysts based on the increasing onset potential for EGO is Pt/Pd/p-1,8-DAN/GC > Pt/p-1,8-DAN/GC > Pd/Pt/p-1,8-DAN/GC. The Pt/Pd/p-1,8-DAN/GC catalyst shows higher I_F/I_R ratios than the Pt/p-1,8-DAN/GC catalyst, exhibiting that the accumulation of remaining oxidation products during the electrocatalytic process is lower than on the pure Pt catalyst, where comparable catalysts that operate in the acidic medium have been reported in the literature [511]. The Pt/Pd/p-1,8-DAN/GC catalyst shows the highest I_F/I_R ratio, indicating that the modifier PtNPs (as a "shell") over the PdNPs (as a "core") in the Pt/Pd/p-1,8-DAN/GC catalyst are supported, prohibiting the promotion of oxidation products on the active platinum sites. The Pt/Pd/p-1,8-DAN/GC catalyst has a higher current efficiency than the other modified electrodes, which indicates that the intermediates resulting from EGO do not block the surface of the catalyst, leading to their oxidation in subsequent reaction steps.

Table 7.4: EGO performance at different catalysts supported on p-1,8-DAN/GC.

Catalysts	ECSA (m^2/g) [500]	E^*_{onset} (V)	I_F^{MS} / ($pA\ cm^{-2}$)	I_R^{MS} / ($pA\ cm^{-2}$)	I_F/I_R	A_{CO2}^a %
Pt/p-1,8-DAN/GC	17.13	0.43	32.26	9.55	3.37	42.78
Pd/p-1,8-DAN/GC	7.21	-	-	-	-	-
Pd/Pt/p-1,8-DAN/GC	25.69	0.47	26.35	11.52	2.28	35.47
Pt/Pd/p-1,8-DAN/GC	157.58	0.40	92.02	23.29	3.94	87.5

* vs. RHE

7.4.3 Electrooxidation of EG at the different MNPs/p-1,2-DAAQ/GC catalysts

Electrooxidation of 0.01 M EG in 0.5 M H_2SO_4 supporting electrolyte at the different catalysts supported at the p-1,2-DAAQ/GC modified electrodes was studied by DEMS. **Figure 7.3** shows the simultaneously recorded faradaic current density (I_F) and the corresponding ion current density (I_i) for m/z =` 44 (CO_2) during the electrooxidation of EG. Two peaks in the anodic scan and a single oxidation peak in the cathodic scan are observed in the CV. At Pt/Pd/p-1,2-DAAQ/GC, the EGO starts at around 0.30 V in the anodic scan, leading to the appearance of the main peak at around 0.65 V, followed by a broad peak at 1.30 V, and one oxidation peak in the cathodic sweep direction at 0.60 V. The faradaic current density at a potential of higher than 0.80 V is considerably reduced because of the increase in the amount of oxygen adsorbed and platinum oxide. The decrease in the faradaic current is paralleled by a decrease in the ionic current for CO_2, which reaches a baseline value at E > 1.00 V. At 1.10 V, the faradaic current begins to increase again, but the corresponding CO_2 signal initially remains at background levels followed by an obvious high signal at E > 1.30 V. In the cathodic direction, an oxidation peak is present at 0.60 V, which is greater than that in the anodic direction. At this peak potential, the higher reactivity in the cathodic direction is probably due to the lower coverage of CO_{ads} species, which blocks the electrode surface in the anodic sweep direction. While in the MSCV, the ion current density in the forward direction is greater than in the reverse direction, which can be attributed to the further oxidation of pre-formed partial oxidation products of EG at a lower potential.

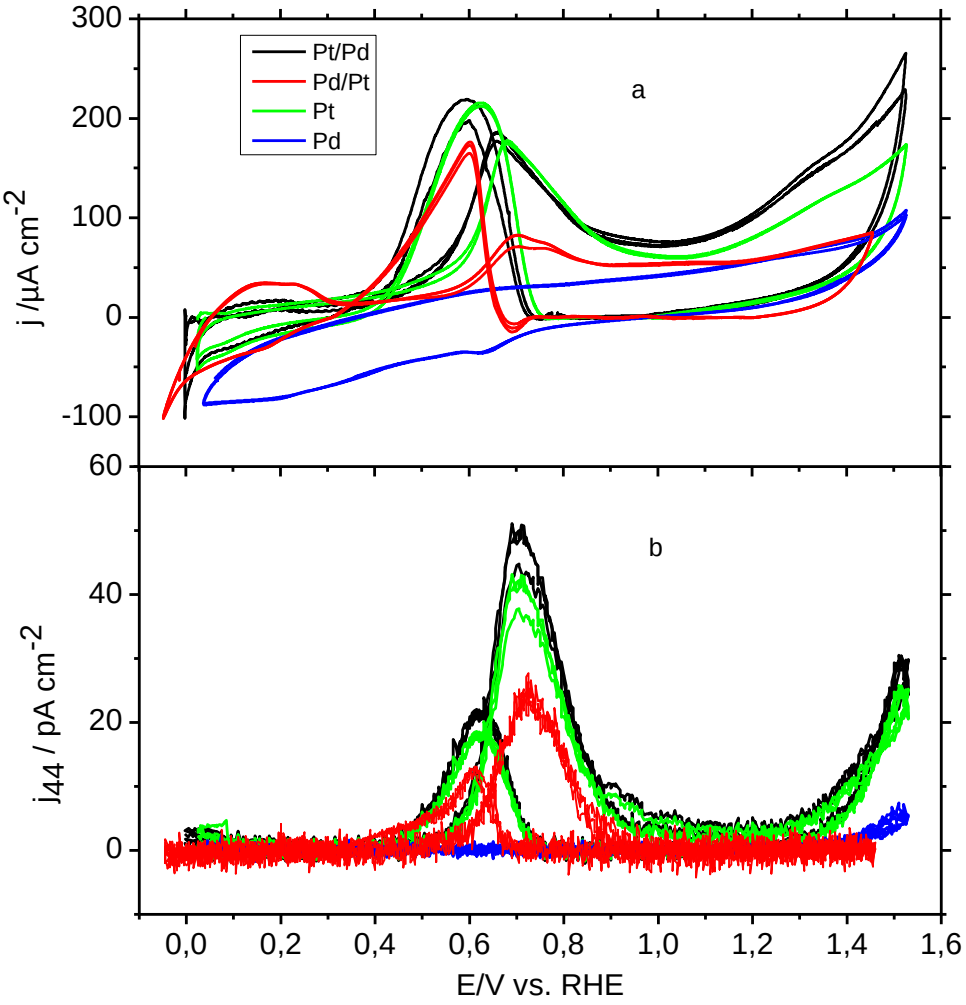

Figure 7.3: Simultaneously recorded CV (a) and the corresponding MSCV for CO_2 (m/z = 44) (b) in 0.01 M EG and 0.5 M H_2SO_4 at different metal catalysts supported on p-1,2-DAAQ/GC at 10.0 mV/s and electrolyte flow rate 5.0 µl s^{-1}.

Current efficiencies for CO_2 formation (A_{CO_2}) were determined using **Equation 7.1**. The current efficiencies with respect to CO_2 formation indicate that the catalytic activity for EGO is in the order of Pt/Pd/p-1,2-DAAQ/GC > Pt/p-1,2-DAAQ/GC > Pd/Pt/p-1,2-DAAQ/GC (**Table 7.5**).

Table 7.5: The integrated faradaic and ionic charges and the related current efficiencies with respect to CO_2 during the EGO at different catalysts supported on p-1,2-DAAQ/GC at 10.0 mV/s in both anodic and cathodic going sweeps.

Catalysts	Q_f / ($mC\ cm^{-2}$)		Q_i / ($nC\ cm^{-2}$)		A_{44}%	
	Anod.	Cath.	Anod.	Cath.	Anod.	Cath.
Pt/p-1,2-DAAQ/GC	2.6	4.2	0.71	0.25	31.5	6.8
Pd/p-1,2-DAAQ/GC	-	-	-	-	-	-
Pd/Pt/p-1,2-DAAQ/GC	0.525	2.0	0.425	0.18	24.2	2.7
Pt/Pd/p-1,2-DAAQ/GC	2.7	3.5	0.89	0.3	38.6	10.2

Different performances for the catalysts were observed (**Table 7.6**) in terms of their ECSAs, E_{onset} values, peak currents (0.70 V), ratios of the forward anodic peak to the reverse peak currents, and current efficiencies for CO_2 evolution. Pt/Pd/p-1,2-DAAQ/GC shows a higher ECSA value of 5.28 m^2/g [499] compared to the other metal catalysts. The onset potential for EGO is in the order of Pt/Pd/p-1,2-DAAQ/GC > Pt/p-1,2-DAAQ/GC > Pd/Pt/p-1,2-DAAQ/GC. For the Pt/Pd/p-1,2-DAAQ/GC catalyst, the I_F/I_R ratio, which is a measure of the catalytic tolerance to CO toxicity, has been reported to significantly increase. Its low I_F/I_R ratio suggests a lesser extent of EGO to CO_2 and the aggregation of incompletely oxidized carbonaceous species (e.g., CO) on the electrode surface[509].

Interestingly, the I_F/I_R (as presented in **Table 7.6**) value obtained at the Pt/Pd/p-1,2-DAAQ/GC catalyst is higher than for the other catalysts. In other words, the forward scan at the Pt/Pd/p-1,2-DAAQ/GC electrode surface results in the formation of fewer intermediate carbonaceous species than is observed at the Pt/p-1,2-DAAQ/GC electrode. The I_F/I_R value of ca. 2.31 also suggests the improved reversibility of the reaction at the Pt/Pd/p-1,2-DAAQ/GC catalyst [476]. As shown in **Table 7.7**, the high current efficiency at the Pt/Pd/p-1,2-DAAQ/GC catalyst compared to those of the other catalysts might be attributed to the presence of fewer intermediates at the surface of the catalyst and the fast EG oxidation in subsequent steps.

Table 7.6: EGO performances at different catalysts supported on p-1,2-DAAQ/GC.

Catalysts	ECSA (m^2/g) [499]	E_{onset} (V)	I_F^{MS} /($pA\ cm^{-2}$)	I_R^{MS} / ($pA\ cm^{-2}$)	I_F/I_R	A_{CO2}^a %
Pt/p-1,2-DAAQ/GC	3.95	0.34	41.25	18.54	2.22	31.5
Pd/p-1,2-DAAQ/GC	4.03	-	-	-	-	-
Pd/Pt/p-1,2-DAAQ/GC	4.23	0.4	31.94	14	2.28	24.2
Pt/Pd/p-1,2-DAAQ/GC	5.28	0.3	50.21	21.7	2.31	38.6

* vs. RHE

Table 7.7: EGO performances at the best catalysts:

Catalyst	ECSA (m^2/g)	Polymer Conductivity (S/cm)	E^*_{onset} (V)	A_{44}%	
				Anode	Cathode
Pt/Pd/p-1,5-DAN/GC	90.43 [501]	1.5×10^{-5} [512]	0.55	81.57	17.2
Pt/Pd/p1,8-DAN/GC	157.58 [500]	1×10^{-3} [513]	0.40	87.5	27.7
Pt/Pd/p-1,2-DAAQ/GC	5.28 [499]	-	0.30	38.6	10.2

* vs. RHE

7.5 Conclusion

In summary, it can be concluded that PtNPs (as a "shell") over PdNPs (as a "core") is the best arrangement of MNPs in catalysis toward EGO. Hence, it was worth comparing the most essential characteristics of the three best catalysts, Pt/Pd/p-1,5-DAN/GC, Pt/Pd/p-1,8-DAN/GC, and Pt/Pd/p-1,2-DAAQ/GC in order to shed light on the crucial roles of the supporting polymer in the activity of the catalysts toward EGO.

It was observed that using the p-1,8-DAN polymer as the host material, the ECSA (157.58 m^2/g) was 1.75 times greater compared to that of the p-1,5-DAN/GC polymer and 29.8 times greater compared to that of the p-1,2-DAAQ polymer. The current efficiencies for CO_2 evolution for the three catalysts were evaluated. It was found that EGO follows two pathways: (1) the EG molecules are dissociatively oxidized to CO_{ads} to form CO_2, and (2) intermediates are formed without C–C bond breakage, where carboxyl groups are the only possible products of the oxidation of the –OH groups in the EG molecules [137, 514]. The trend in the current efficiency for the CO_2 yield increased in the order of Pt/Pd/p-1,8-DAN/GC > Pt/Pd/p-1,5-DAN/GC > Pt/Pd/p-1,2-DAAQ/GC, which indicates that fewer intermediates accumulate at the

surface of the Pt/Pd/p-1,8-DAN/GC catalyst compared with at the other two catalysts and that EGO quickly proceeds in subsequent steps. The electrical conductivity of p-1,8-DAN (1×10^{-3} S cm^{-1}) [513] is around 60 times greater compared to that of p-1,5-DAN (1.5×10^{-5} S cm^{-1}) [512], hence leading to the enhanced performance and electroactivity of the Pt/Pd/p1,8-DAN/GC catalyst.

Chapter eight:

Summary and Outlook

This work addresses fundamental electrochemical processes for which adsorption phenomena play a large role. They are related to two important applications: the first one is electrical double-layer capacitors. As a model system for these, which should also help in a better understanding of processes in aprotic batteries served the adsorption of iodide and bromide adsorption on Au(111) | electrolyte interface in aprotic solvents such as PC, DMSO, and DG; This was studied using different techniques such as cyclic voltammetry, AC-Voltammetry, EIS, XPS, and ATR – SEIRAS. For comparison, the adsorption of iodide on the Au(111) electrode has been examined in an aqueous alkaline solution. From CV, the EDL region for Au(111) electrode in an aqueous solution containing non-specific adsorbed anions extends from -0.1 to 1.0 V vs. RHE. A wider range of potential can be reached in an organic solvent before solvent decomposition occurs. The Au(111) electrode is ideally polarizable within the potential region from –1.4 V to 0.63 V (vs. Ag|$AgNO_3$) in PC and from -1.4 to 0.5 V in DG and DMSO. Three pairs of peaks have been observed for iodine adsorption in aqueous solutions. The peaks observed in the organic medium resemble these though they are less sharp. The peak currents and charge of iodide adsorption in PC increase with the increase of concentration of iodide. Besides, the adsorption rate and capacitance C_{ad} increases with increasing the concentration of KI. They depend on the radius of the solvated cation of the supporting electrolyte, where the rate of adsorption increases in the order $K^+ > Na^+ > Li^+ > TBA^+$.

The effect of the type of solvent on the rate of iodide and bromide adsorption has been studied. As well, the adsorption rate of I^- and Br^- on Au(111) decreases in the order PC > DG > DMSO. The rate of iodide adsorption is higher than that of bromide adsorption due to the lower solvation energy of iodide. The adsorption rate of both halides depends on the electrode-solvent chemisorption interaction energy, which is directly dependent on the donor number of solvent, not on the dielectric constants of aprotic solvents. Furthermore, the adsorption rate and capacitance of iodide are increased when the water content increased from 35 ppm to 1100 ppm in PC and from 31 ppm to 1210 ppm in DMSO. XPS measurements confirm data obtained by CV and AC voltammetry, which reveal that the amount of adsorbed iodide on Au(111) in DMSO is less than in PC.

The pzc of Au(111) is determined in aprotic solvents such as PC, DMSO, DG, and ACN. The pzc values of the Au(111) electrode relative to DMFc(decamethylferrocene) changes as follows: ACN > DG > PC > DMSO. It is observed that the pzc values correlate neither with the dielectric constant of solvents nor with the solvent polarizability. Other factors like specific metal-solvent interactions and related to this will also play a role. The values of pzc are practically independent of the cation type. The strongly adsorbed anions like Br^- shifts pzc to more negative when compared with PF_6^-. The pzc in the presence of PF_6^- and ClO_4^- is quite similar due to the similarity of adsorption strength of both anions on Au(111) in ACN and PC. Water addition leads to disturbing of the interface structure of the roughened Au(111) electrode, and consequently, the pzc shifts to more positive potentials. The pzc value is dependent on the atomic arrangement of the electrode surface. The pzc values for Au(111) and roughened Au(111) electrode are determined in $LiClO_4$ containing acetonitrile ($E_{\sigma=0}$ = 0.21V and 0.0 V, respectively). By using ATR-SEIRAS, the bipolar CO vibration band of propylene carbonate is exhibited at 1800 cm^{-1}. Its intensity increases with going to negative potentials while shifting to lower wavenumbers because of the increasing field and better orientation of PC molecules. Stronger alignment of PC molecules in the direction of positive potentials has occurred in the presence of iodide, and this is attributed to shifting in pzc of gold film to -1.1 V vs $Ag|Ag^+$.

The second application is the fuel cell, for which the adsorption of carbon monoxide (CO) during formic acid and ethylene glycol oxidation plays a role. Conducting polymer is used as support for formic acid oxidation catalysts. Bimetallic catalysts supported on a conducting polymer were found to be more electroactive towards formic acid oxidation than catalysts without conducting polymer. Also, they are more electroactive than monometallic catalysts supported on conducting polymer towards the formic acid oxidation (FAO). The chemical composition and surface morphology of catalysts were characterized using scanning electron microscopy (SEM), energy-dispersive X-ray spectroscopy (EDX). The particle size distribution of Pt/Pd/PDAN/GC is in the range of 50 – 170 nm. Electroactive surface area Pt/Pd/p1,5-DAN/GC was determined through oxidation of pre-adsorbed CO in 0.5 M sulphuric acid using the DEMS technique. The direct dehydrogenation pathway of FAO is the favourable reaction at bimetallic modified electrodes since the presence of Pt as outer and Pd as core disturbs the continuity of Pt sites and consequently reduces poisoning by adsorbing CO which is responsible for the indirect dehydration pathway to occur. The determination of current efficiency for CO_2 production was conducted using DEMS and was close to 100%.

Electrooxidation of ethylene glycol (EGO) was also studied on different conducting polymers as support for the monometallic and bimetallic catalysts in acidic medium using the

DEMS technique. It was found that the binary catalyst is more electroactive than the monometallic catalyst towards EGO, regardless of the nature of the supported conducting polymer. Also, Pt/Pd showed higher activity than Pd/Pt. To prevail the vital role of the kind of supported conducting polymer towards the activity of EGO, three conducting polymers of p1,5-DAN, p1,8-DAN, and p1,2- DAAQ were used. It was found that Pt/Pd/p 1,8-DAN/GC shows a higher current efficiency (87.5 %) than Pt/Pd/p1,5-DAN/GC and Pt/Pd/p1,2-DAAQ/GC and this attributed to higher electric conductivity of p1,8-DAN and high electroactive surface area of Pt/Pd/p1,8-DAN/GC.

The following experiments would be interesting for future work:

1- The addition of third metal nanoparticles to binary nanoparticles catalyst is preferable to enhance the electrolytic activity of oxidation of small organic species.
2- Application of conducting polymers supported metal nanoparticles for oxygen reduction reaction in organic solvents.
3- Using other single-crystal electrodes such as Ag(111) to study the structure of metal | electrolyte interface and adsorption of halogens in organic solvents is better than Au(111) due to lack of lifting of reconstruction.
4- Mathematic modeling of the electrical double layer allows more investigation of the structure and effect of change in the double layer.
5- Study the characteristics of electrode | electrolyte interface on a single-crystal electrode in organic solvents using FTIR Reflection-Absorption spectroscopy.

Bibliography

[1] C. Wang, Z. Xie, and Z. Zhou, APL Materials 7:040701 (**2019**).

[2] K. M. Abraham and Z. Jiang, Journal of the Electrochemical Society 143:1 (**1996**).

[3] T. S. EG&G, Fuel Cell Handbook, U.S. Department of Energy, Office of Fossil Energy, National Energy Technology Laborator, Morgantown, West Virginia, **2004**.

[4] A. J. Bard and L. R. Faulkner, Electrochemical Methods: Fundamentals and Applications, John Wiley & Sons Inc., New York, Weinheim, **2001**.

[5] R. J. Forster, Keyes, T.E., Vos, J.G.,, Interfacial Supramolecular Assemblies, John Wiley & Sons Ltd.,, Chichester, England, **2003**.

[6] D. T. Sawyer, Sobkowiak, A., Roberts Jr., J. L., Electrochemistry for chemists, John Wiley & Sons Ltd., New York, **1995**.

[7] J. O. Bockris, B. E. Conway, and E. Yeager, comprehensive treatise of electrochemistry, plenum press, New york, **1980**.

[8] A. Hamelin, T. Vitanov, E. Sevastyanov, and A. Popov, Journal of Electroanalytical Chemistry and Interfacial Electrochemistry 145:225 (**1983**).

[9] D. V. Tripkovic, D. Strmcnik, D. van der Vliet, V. Stamenkovic, and N. M. Markovic, Faraday Discussions 140:25 (**2008**).

[10] A. N. Frumkin and O. A. Petrii, Electrochimica Acta 20:347 (**1975**).

[11] A. Hamelin, in modern aspects of electrochemistry, Vol. 16 (B. E. Conway, R. E. White, and J. O. Bockris, eds.), Plenum Press, New York, **1985**.

[12] J. Clavilier, R. Albalat, R. Gómez, J. M. Orts, J. M. Feliu, and A. Aldaz, Journal of Electroanalytical Chemistry 330:489 (**1992**).

[13] J. M. Feliu, J. M. Orts, R. Gómez, A. Aldaz, and J. Clavilier, Journal of Electroanalytical Chemistry 372:265 (**1994**).

[14] E. Herrero, J. M. Feliu, A. Wieckowski, and J. Clavilier, Surface Science 325:131 (**1995**).

[15] V. Climent, R. Gómez, and M. Feliu, Electrochimica Acta 45:629 (**1999**).

[16] R. Gomez, V. Climent, J. M. Feliu, and M. J. Weaver, Journal of Physical Chemistry B 104:597 (**2000**).

[17] R. Gomez, J. M. Feliu, A. Aldaz, and M. J. Weaver, Surface Science 410:48 (**1998**).

[18] U. W. Hamm, D. Kramer, R. S. Zhai, and D. M. Kolb, Journal of Electroanalytical Chemistry 414:85 (**1996**).

[19] C. Müller, S. Vesztergom, T. Pajkossy, and T. Jacob, Electrochimica Acta 188:512 (**2016**).

[20] L. A. Kibler, Preparation and Characterization of Noble Metals Single Crystal Electrodes, University of Ulm, **2003**.

[21] A. Zangwill, Physiscs at surfaces, Cambridge University Press, Cambridge, **1990**.

[22] G. A. Somorjai and Y. Li, Introduction to Surface Chemistry and Catalysis, John Wiley & Sons, Inc., Hoboken, New Jersey, **2010**.

[23] R. J. Needs, M. J. Godfrey, and M. Mansfield, Surface Science 242:215 (**1991**).

[24] R. J. Needs and M. Mansfield, Journal of Physics: Condensed Matter 1:7555 (**1989**).

[25] V. Heine and L. D. Marks, Journal of Electron Spectroscopy and Related Phenomena 38:229 (**1986**).
[26] V. Heine and L. D. Marks, Surface Science 165:65 (**1986**).
[27] L. Piccolo, D. Loffreda, F. J. Cadete Santos Aires, C. Deranlot, Y. Jugnet, P. Sautet, and J. C. Bertolini, Surface Science 566-568:995 (**2004**).
[28] D. M. Kolb and J. Schneider, Electrochimica Acta 31:929 (**1986**).
[29] D. M. Kolb, Progress in Surface Science 51:109 (**1996**).
[30] U. Harten, A. M. Lahee, J. P. Toennies, and C. Wöll, Physical Review Letters 54:2619 (**1985**).
[31] H. Melle and E. Menzel, Z. Naturforsch. 33a:282 (**1978**).
[32] F. Hanke and J. Björk, Physical Review B 87:235422 (**2013**).
[33] W. Schmickler and S. E., Interfacial Electrochemistry, springer, Berlin, **2010**.
[34] W. Schmickler, Interfacial Electrochemistry, Oxford University Press, New York, **1996**.
[35] S. Sharma and B. G. Pollet, Journal of Power Sources 208:96 (**2012**).
[36] J. W. Gosselink, International Journal of Hydrogen Energy 27:1125 (**2002**).
[37] Z.-B. Wang, G.-P. Yin, J. Zhang, Y.-C. Sun, and P.-F. Shi, Journal of Power Sources 160:37 (**2006**).
[38] C. M. Miesse, W. S. Jung, K.-J. Jeong, J. K. Lee, J. Lee, J. Han, S. P. Yoon, S. W. Nam, T.-H. Lim, and S.-A. Hong, Journal of Power Sources 162:532 (**2006**).
[39] Y. M. Zhu, S. Y. Ha, and R. I. Masel, Journal of Power Sources 130:8 (**2004**).
[40] M. A. F. Akhairi and S. K. Kamarudin, International Journal of Hydrogen Energy 41:4214 (**2016**).
[41] B. Braunchweig, D. Hibbitts, M. Neurock, and A. Wieckowski, Catalysis Today 202:197 (**2013**).
[42] K. Scott and A. K. Shukla, in Modern Aspects of Electrochemistry No. 40, Vol. 40 (R. E. White, C. G. Vayenas, and M. E. Gamboa-Aldeco, eds.), Springer New York, **2007**, p. 127.
[43] A. A. Abd-El-Latif, PhD thesis, Universität Bonn, Bonn, **2011**.
[44] S. Gilman, Journal of Physical Chemistry 68:70 (**1964**).
[45] Y. M. Zhu, H. Uchida, and M. Watanabe, Langmuir 15:8757 (**1999**).
[46] N. M. Markovic and P. N. Ross, Surface Science Reports 45:117 (**2002**).
[47] C. McCallum and D. Pletcher, Journal of Electroanalytical Chemistry 70:277 (**1976**).
[48] C.-S. Chen, F.-M. Pan, and H.-J. Yu, Applied Catalysis B: Environmental 104:382 (**2011**).
[49] F. Maillard, S. Schreier, M. Hanzlik, E. R. Savinova, S. Weinkauf, and U. Stimming, Physical Chemistry Chemical Physics 7:385 (**2005**).
[50] F. Maillard, E. R. Savinova, P. A. Simonov, V. I. Zaikovskii, and U. Stimming, Journal of Physical Chemistry B 108:17893 (**2004**).
[51] K. A. Friedrich, F. Henglein, U. Stimming, and W. Unkauf, Electrochimica Acta 45:3283 (**2000**).
[52] A. Lopez-Cudero, J. Solla-Gullon, E. Herrero, A. Aldaz, and J. M. Feliu, Journal of Electroanalytical Chemistry 644:117 (**2010**).
[53] L. M. Plyasova, I. Y. Molina, A. N. Gavrilov, S. V. Cherepanova, O. V. Cherstiouk, N. A. Rudina, E. R. Savinova, and G. A. Tsirlina, Electrochimica Acta 51:4477 (**2006**).

[54] E. Herrero, B. Alvarez , J. M. Feliu, S. Blais, Z. Radovic-Hrapovic, and G. Jerkiewicz, Journal of Electroanalytical Chemistry 567:139 (**2004**).
[55] J. Solla-Gullon, F. J. Vidal-Iglesias, E. Herrero, J. M. Feliu, and A. Aldaz, Electrochemistry Communications 8:189 (**2006**).
[56] J. Solla-Gullon, P. Rodriguez, E. Herrero, A. Aldaz, and J. M. Feliu, Physical Chemistry Chemical Physics 10:1359 (**2008**).
[57] S. Brimaud, S. Pronier, C. Coutanceau, and J. M. Léger, Electrochemistry Communications 10:1703 (**2008**).
[58] P. Urchaga, S. Baranton, T. W. Napporn, and C. Coutanceau, Electrocatalysis 1:3 (**2010**).
[59] C. Coutanceau, P. Urchaga, and S. Baranton, Electrochemistry Communications 22:109 (**2012**).
[60] G. Samjeské, H. Wang, T. Löffler, and H. Baltruschat, Electrochimica Acta 47:3681 (**2002**).
[61] K. Kunimatsu, H. Seki, W. G. Golden, J. G. Gordon, and M. R. Philpott, Langmuir 2:464 (**1986**).
[62] N. M. Markovic, B. N. Grgur, C. A. Lucas, and P. N. Ross, Journal of Physical Chemistry B 103:487 (**1999**).
[63] N. M. Markovic, C. A. Lucas, B. N. Grgur, and P. N. Ross, Journal of Physical Chemistry B 103:9616 (**1999**).
[64] A. Couto, M. C. Pérez, A. Rincón, and C. Gutiérrez, Journal of Physical Chemistry 100:19538 (**1996**).
[65] A. Cuesta, M. Escudero, B. Lanova, and H. Baltruschat, Langmuir 25:6500 (**2009**).
[66] H. Massong, H. Wang, G. Samjeske, and H. Baltruschat, Electrochimica Acta 46:701 (**2000**).
[67] G. Samjeské, X.-Y. Xiao, and H. Baltruschat, Langmuir 18:4659 (**2002**).
[68] H.-C. Wang and H. Baltruschat, ChemPhysChem 11:2798 (**2010**).
[69] V. S. Bagotzky, Y. B. Vassiliev, and O. A. Khazova, Journal of Electroanalytical Chemistry 81:229 (**1977**).
[70] R. Parsons and T. VanderNoot, Journal of Electroanalytical Chemistry 257:9 (**1988**).
[71] H. Wang, C. Wingender, H. Baltruschat, M. Lopez, and M. T. Reetz, Journal of Electroanalytical Chemistry 509:163 (**2001**).
[72] V. Grozovski, V. Climent, E. Herrero, and J. M. Feliu, Journal of Electroanalytical Chemistry 662:43 (**2011**).
[73] A. A. Abd-El-Latif and H. Baltruschat, Journal of Electroanalytical Chemistry 662:204 (**2011**).
[74] H. Wang and H. Baltruschat, Journal of Physical Chemistry C 111:7038 (**2007**).
[75] Q. Jiang, L. Jiang, S. Wang, J. Qi, and G. Sun, Catalysis Communications 12:67 (**2010**).
[76] D.-J. Guo and Z.-H. Jing, Journal of Power Sources 195:3802 (**2010**).
[77] M. A. Scibioh, S.-K. Kim, E. A. Cho, T.-H. Lim, S.-A. Hong, and H. Y. Ha, Applied Catalysis B: Environmental 84:773 (**2008**).
[78] L. Cao, F. Scheiba, C. Roth, F. Schweiger, C. Cremers, U. Stimming, H. Fuess, L. Q. Chen, W. T. Zhu, and X. P. Qiu, Angewandte Chemie-International Edition 45:5315 (**2006**).

[79] W. Huang, H. Wang, J. Zhou, J. Wang, P. N. Duchesne, D. Muir, P. Zhang, N. Han, F. Zhao, M. Zeng, J. Zhong, C. Jin, Y. Li, S.-T. Lee, and H. Dai, Nature Communications 6:10035 (**2015**).
[80] R. Chetty, S. Kundu, W. Xia, M. Bron, W. Schuhmann, V. Chirila, W. Brandl, T. Reinecke, and M. Muhler, Electrochimica Acta 54:4208 (**2009**).
[81] L. Li and Y. Xing, Journal of Physical Chemistry C 111:2803 (**2007**).
[82] S. Lu, H. Li, J. Sun, and Z. Zhuang, Nano Research 11:2058 (**2018**).
[83] H. Yang, C. Coutanceau, J. M. Leger, N. Alonso-Vante, and C. Lamy, Journal of Electroanalytical Chemistry 576:305 (**2005**).
[84] Z. Niu, D. Wang, R. Yu, Q. Peng, and Y. Li, Chemical Science 3:1925 (**2012**).
[85] X. Guo, D.-J. Guo, X.-P. Qiu, L.-Q. Chen, and W.-T. Zhu, Electrochemistry Communications 10:1748 (**2008**).
[86] Q. Lu, H. Wang, K. Eid, Z. A. Alothman, V. Malgras, Y. Yamauchi, and L. Wang, Chemistry - An Asian Journal 11:1939 (**2016**).
[87] D.-B. Huang, Q. Yuan, H.-H. Wang, and Z.-Y. Zhou, Chemical Communications 50:13551 (**2014**).
[88] Z. Peng and H. Yang, Journal of the American Chemical Society 131:7542 (**2009**).
[89] L. Wang, Y. Nemoto, and Y. Yamauchi, Journal of the American Chemical Society 133:9674 (**2011**).
[90] B. Lim, M. Jiang, T. Yu, P. H. C. Camargo, and Y. Xia, Nano Research 3:69 (**2010**).
[91] F. Zhan, T. Bian, W. Zhao, H. Zhang, M. Jin, and D. Yang, CrystEngComm 16:2411 (**2014**).
[92] F. Ren, C. Wang, C. Zhai, F. Jiang, R. Yue, Y. Du, P. Yang, and J. Xu, Journal of Materials Chemistry A 1:7255 (**2013**).
[93] K.-S. Lee, I.-S. Park, Y.-H. Cho, D.-S. Jung, N. Jung, H.-Y. Park, and Y.-E. Sung, Journal of Catalysis 258:143 (**2008**).
[94] J. J. Pietron, M. B. Pomfret, C. N. Chervin, J. W. Long, and D. R. Rolison, Journal of Materials Chemistry 22:5197 (**2012**).
[95] T. Saida, W. Sugimoto, and Y. Takasu, Electrochimica Acta 55:857 (**2010**).
[96] W. Li, Y. Bai, F. Li, C. Liu, K.-Y. Chan, X. Feng, and X. Lu, Journal of Materials Chemistry 22:4025 (**2012**).
[97] H. A. Gasteiger, N. Markovic, P. N. Ross, and E. J. Cairns, Journal of Physical Chemistry 97:12020 (**1993**).
[98] M. Watanabe and S. Motoo, Journal of Electroanalytical Chemistry 60:267 (**1975**).
[99] E. Urbanczyk, A. Jaron, and W. Simka, International Journal of Hydrogen Energy 43:17156 (**2018**).
[100] D. M. Han, Z. P. Guo, R. Zeng, C. J. Kim, Y. Z. Meng, and H. K. Liu, International Journal of Hydrogen Energy 34:2426 (**2009**).
[101] A. Capon and R. Parsons, Journal of Electroanalytical Chemistry 44:1 (**1973**).
[102] R. Parsons and T. VanderNoot, Journal of Electroanalytical Chemistry 257:9 (**1988**).
[103] T. D. Jarvi and E. M. Stuve, in Electrocatalysis (J. Lipkowski and P. N. Ross, eds.), Wiley-VCH, New York, **1998**, p. 75.
[104] E. Herrero and J. M. Feliu, Current Opinion in Electrochemistry 9:145 (**2018**).
[105] X. Chen, Y. Liu, and J. Wu, Molecular Catalysis 483:110716 (**2020**).

[106] X. Yu and P. G. Pickup, Journal of Power Sources 182:124 (**2008**).
[107] A. Boronat-Gonzalez, E. Herrero, and J. M. Feliu, Current Opinion in Electrochemistry 4:26 (**2017**).
[108] Y.-W. Rhee, S. Y. Ha, and R. I. Masel, Journal of Power Sources 117:35 (**2003**).
[109] A. Capon and R. Parsons, Journal of Electroanalytical Chemistry 45:205 (1973).
[110] S. G. Sun, J. Clavilier, and A. Bewick, Journal of Electroanalytical Chemistry and Interfacial Electrochemistry 240:147 (**1988**).
[111] A. Miki, S. Ye, and M. Osawa, Chemical Communications: 1500 (**2002**).
[112] H. Miyake, T. Okada, G. Samjeské, and M. Osawa, Physical Chemistry Chemical Physics 10:3662 (**2008**).
[113] M. R. Columbia and P. A. Thiel, Journal of Electroanalytical Chemistry 369:1 (**1994**).
[114] A. Cuesta, G. Cabello, M. Osawa, and C. Gutiérrez, ACS Catalysis 2:728 (**2012**).
[115] A. Cuesta, G. Cabello, C. Gutiérrez, and M. Osawa, Physical Chemistry Chemical Physics 13:20091 (**2011**).
[116] V. Grozovski, F. J. Vidal-Iglesias, E. Herrero, and J. M. Feliu, ChemPhysChem 12:1641 (**2011**).
[117] H.-F. Wang and Z.-P. Liu, Journal of Physical Chemistry C 113:17502 (**2009**).
[118] N. M. Markovic, H. A. Gasteiger, P. N. Ross, X. D. Jiang, I. Villegas, and M. J. Weaver, Electrochimica Acta 40:91 (**1995**).
[119] W. Y. Yuan, Y. Cheng, P. K. Shen, C. M. Li, and S. P. Jiang, Journal of Materials Chemistry A 3:1961 (**2015**).
[120] K. Jiang and W. B. Cai, Applied Catalysis B-Environmental 147:185 (**2014**).
[121] V. Mazumder, Y. Lee, and S. H. Sun, Advanced Functional Materials 20:1224 (**2010**).
[122] G. Samjeske and M. Osawa, Angewandte Chemie-International Edition 44:5694 (**2005**).
[123] H. Okamoto, W. Kon, and Y. Mukouyama, Journal of Physical Chemistry B 109:15659 (**2005**).
[124] J. Kim, C. Jung, C. K. Rhee, and T. h. Lim, Langmuir 23:10831 (**2007**).
[125] X. Yu and P. G. Pickup, Electrochemistry Communications 11:2012 (2009).
[126] J.-Y. Wang, H.-X. Zhang, K. Jiang, and W.-B. Cai, Journal of the American Chemical Society 133:14876 (**2011**).
[127] C. Xu, Q. Hao, and H. Duan, Journal of Materials Chemistry A 2:8875 (**2014**).
[128] S.-Y. Lee, N. Jung, J. Cho, H.-Y. Park, J. Ryu, I. Jang, H.-J. Kim, E. Cho, Y.-H. Park, H. C. Ham, J. H. Jang, and S. J. Yoo, ACS Catalysis 4:2402 (**2014**).
[129] S. Yang, C. Shen, Y. Tian, X. Zhang, and H.-J. Gao, Nanoscale 6:13154 (**2014**).
[130] B. T. Sneed, A. P. Young, D. Jalalpoor, M. C. Golden, S. Mao, Y. Jiang, Y. Wang, and C.-K. Tsung, ACS Nano 8:7239 (**2014**).
[131] K. Miyazaki, T. Matsumiya, T. Abe, H. Kurata, T. Fukutsuka, K. Kojima, and Z. Ogumi, Electrochimica Acta 56:7610 (**2011**).
[132] L. An and R. Chen, Journal of Power Sources 329:484 (**2016**).
[133] V. Livshits, M. Philosoph, and E. Peled, Journal of Power Sources 178:687 (**2008**).
[134] N. W. Maxakato, C. J. Arendse, and K. I. Ozoemena, Electrochemistry Communications 11:534 (**2009**).
[135] N. W. Maxakato, K. I. Ozoemena, and C. J. Arendse, Electroanalysis 22:519 (**2010**).
[136] A. Serov and C. Kwak, Applied Catalysis B: Environmental 97:1 (**2010**).

[137] H. Wang, Z. Jusys, and R. J. Behm, Electrochimica Acta 54:6484 (**2009**).
[138] K. Matsuoka, Y. Iriyama, T. Abe, M. Matsuoka, and Z. Ogumi, Electrochimica Acta 51:1085 (**2005**).
[139] P. A. Christensen and A. Hamnett, Journal of Electroanalytical Chemistry and Interfacial Electrochemistry 260:347 (**1989**).
[140] R. B. de Lima, V. Paganin, T. Iwasita, and W. Vielstich, Electrochimica Acta 49:85 (**2003**).
[141] C. Jin, Y. Song, and Z. Chen, Electrochimica Acta 54:4136 (**2009**).
[142] H. Kohlmuller, Journal of Power Sources 1:249 (**1976**).
[143] N. Dalbay and F. Kadirgan, Electrochimica Acta 36:353 (**1991**).
[144] L. Demarconnay, S. Brimaud, C. Coutanceau, and J. M. Léger, Journal of Electroanalytical Chemistry 601:169 (**2007**).
[145] H. Khatoon and S. Ahmad, Journal of Industrial and Engineering Chemistry 53:1 (**2017**).
[146] S. Iqbal and S. Ahmad, Journal of Industrial and Engineering Chemistry 60:53 (**2018**).
[147] P. M. Dziewonski and M. Grzeszczuk, Electrochimica Acta 55:3336 (**2010**).
[148] A. A. Hathoot, U. S. Yousef, A. S. Shatla, and M. Abdel-Azzem, Electrochimica Acta 85:531 (**2012**).
[149] E. Antolini, Applied Catalysis B: Environmental 88:1 (**2009**).
[150] S.-S. Li and C.-W. Chen, Journal of Materials Chemistry A 1:10574 (**2013**).
[151] M. A. A. Mohd Abdah, N. H. N. Azman, S. Kulandaivalu, and Y. Sulaiman, Materials & Design 186:108199 (**2020**).
[152] K. M. Molapo, P. M. Ndangili, R. F. Ajayi, G. Mbambisa, S. M. Mailu, N. Njomo, M. Masikini, P. Baker, and E. I. Iwuoha, Int. J. Electrochem. Sci. 7:11859 (2012).
[153] H. Laborde, J. M. Léger, and C. Lamy, Journal of Applied Electrochemistry 24:219 (**1994**).
[154] J.-H. Choi, Y.-M. Kim, J.-S. Lee, K.-Y. Cho, H.-Y. Jung, J.-K. Park, I.-S. Park, and Y.-E. Sung, Solid State Ionics 176:3031 (**2005**).
[155] S. Kim and S.-J. Park, Solid State Ionics 178:1915 (**2008**).
[156] M. Yaldagard, M. Jahanshahi, and N. Seghatoleslami, Applied Surface Science 317:496 (**2014**).
[157] R. Yan, X. Sun, X. Zhang, J. Zheng, and B. Jin, Nanotechnology 31:135703 (**2020**).
[158] M. L. Banon, V. Lopez, P. Ocon, and P. Herrasti, Synthetic Metals 48:355 (**1992**).
[159] A. Kelaidopoulou, E. Abelidou, A. Papoutsis, E. K. Polychroniadis, and G. Kokkinidis, Journal of Applied Electrochemistry 28:1101 (**1998**).
[160] S. Chemchoub, L. Oularbi, A. El Attar, S. A. Younssi, F. Bentiss, C. Jama, and M. El Rhazi, Materials Chemistry and Physics 250:123009 (**2020**).
[161] C. M. A. Brett and A. M. O. Brett, Electrochemistry: Principles, Methods and Applications, Oxford University Press, Oxford, **1993**.
[162] D. Pletcher, R. Greff, R. Peat, L. M. Peter, and J. Robinson, Instrumental Methods in Electrochemistry, Woodhead Publishing Limited, Cambridge, **2011**.
[163] A. J. Bard and P. R. U. e. M. Stratmann, Encyclopedia of Electrochemistry, Instrumentation and Electroanalytical Chemistry, Wiley-VCH, Weinheim, Germany, **2003**.

[164] R. R. Bruckenstein and J. Gadde, Journal of the American Chemical Society 93:793 (**1971**).
[165] O. Wolter and J. Heitbaum, Berichte der Bunsengesellschaft für Physikalische Chemie 88:2 (**1984**).
[166] Z. Jusys, H. Massong, and H. Baltruschat, Journal of the Electrochemical Society 146:1093 (**1999**).
[167] A. A. Abd-El-Latif and H. Baltruschat, in Encyclopedia of Applied Electrochemistry (G. Kreysa, K.-i. Ota, and R. Savinell, eds.), Springer New York Dordrecht Heidelberg London, **2014**, p. 507.
[168] H. Baltruschat, in Interfacial Electrochemistry (A. Wieckowski, ed.), Marcel Dekker, Inc., New York, Basel, **1999**, p. 577.
[169] H. Baltruschat, Journal of the American Society for Mass Spectrometry 15:1693 (2004).
[170] T. Hartung and H. Baltruschat, Langmuir 6:953 (**1990**).
[171] T. Hartung, U. Schmiemann, I. Kamphausen, and H. Baltruschat, Analytical Chemistry 63:44 (**1991**).
[172] H. Baltruschat and U. Schmiemann, Ber. Bunsenges. Phys. Chem. 97:452 (**1993**).
[173] C. J. Powell, Journal of Electron Spectroscopy and Related Phenomena 185:1 (**2012**).
[174] P. Christensen and A. Hamnett, Electrochimica Acta 45:2443 (**2000**).
[175] A. Bewick, K. Kunimatsu, and B. Stanley Pons, Electrochimica Acta 25:465 (**1980**).
[176] A. Bewick and K. Kunimatsu, Surface Science 101:131 (**1980**).
[177] M. Osawa, S.-G. Sun, P. A. Christensen, and A. Wieckowski, in In-situ Spectroscopic Studies of Adsorption at the Electrode and Electrocatalysis, Elsevier Science B.V., Amsterdam, **2007**, p. 209.
[178] A. Bewick, K. Kunimatsu, B. S. Pons, and J. W. Russell, Journal of Electroanalytical Chemistry and Interfacial Electrochemistry 160:47 (**1984**).
[179] P. Lange, V. Glaw, H. Neff, E. Piltz, and J. Sass, Vacuum 33:763 (**1983**).
[180] B. W. Johnson, J. Bauhofer, K. Doblhofer, and B. Pettinger, Electrochimica Acta 37:2321 (**1992**).
[181] E. Kretschmann, Zeitschrift für Physik A Hadrons and nuclei 241:313 (1971).
[182] J. Chalmers and E. P. R. Griffiths, Handbook of Vibrational Spectroscopy, John Wiley & Sons Ltd, Chichester, UK, **2003**.
[183] M. Fleischmann, P. J. Hendra, and A. J. McQuillan, Chemical Physics Letters 26:163 (**1974**).
[184] A. Hartstein, J. R. Kirtley, and J. C. Tsang, Physical Review Letters 45:201 (**1980**).
[185] A. Hatta, T. Ohshima, and W. Suetaka, Applied Physics A 29:71 (**1982**).
[186] M. Osawa, K.-I. Ataka, K. Yoshii, and Y. Nishikawa, Applied spectroscopy 47:1497 (**1993**).
[187] D. L. Jeanmaire and R. P. Van Duyne, Journal of Electroanalytical Chemistry and Interfacial Electrochemistry 84:1 (**1977**).
[188] M. G. Albrecht and J. A. Creighton, Journal of the American Chemical Society 99:5215 (**1977**).
[189] R. F. Aroca, D. J. Ross, and C. n. Domingo, Applied Spectroscopy 58:324A (**2004**).
[190] T. Wandlowski, K. Ataka, S. Pronkin, and D. Diesing, Electrochimica Acta 49:1233 (**2004**).

[191] M. Osawa, Bulletin of the Chemical Society of Japan 70:2861 (**1997**).
[192] M. Osawa, K.-I. Ataka, M. Ikeda, H. Uchihara, and R. Nanba, Analytical sciences 7:503 (**1991**).
[193] A. Hatta, Y. Suzuki, and W. Suëtaka, Applied Physics A 35:135 (**1984**).
[194] A. Hatta, Y. Chiba, and W. Suëtaka, Surface Science 158:616 (**1985**).
[195] A. Hatta, Y. Chiba, and W. Suëtaka, Applied surface science 25:327 (**1986**).
[196] K.-i. Ataka, T. Yotsuyanagi, and M. Osawa, Journal of Physical Chemistry 100:10664 (**1996**).
[197] H. Miyake, S. Ye, and M. Osawa, Electrochemistry Communications 4:973 (**2002**).
[198] Yan, Q.-X. Li, S.-J. Huo, M. Ma, W.-B. Cai, and M. Osawa, The Journal of Physical Chemistry B 109:7900 (**2005**).
[199] T. Kamata, A. Kato, J. Umemura, and T. Takenaka, Langmuir 3:1150 (**1987**).
[200] G.-Q. Lu, S.-G. Sun, L.-R. Cai, S.-P. Chen, Z.-W. Tian, and K.-K. Shiu, Langmuir 16:778 (**2000**).
[201] G.-Q. Lu, S.-G. Sun, S.-P. Chen, and L.-R. Cai, Journal of Electroanalytical Chemistry 421:19 (**1997**).
[202] M. Osawa, in Near-Field Optics and Surface Plasmon Polaritons (S. Kawata, ed.), Springer Berlin Heidelberg, Berlin, Heidelberg, **2001**, p. 163.
[203] M. Osawa and M. Ikeda, Journal of Physical Chemistry 95:9914 (**1991**).
[204] Y. Suzuki, M. Osawa, A. Hatta, and W. Suëtaka, Applied surface science 33:875 (**1988**).
[205] F. Neubrech, A. Pucci, T. W. Cornelius, S. Karim, A. Garce-a-Etxarri, and J. Aizpurua, Physical Review Letters 101:157403 (**2008**).
[206] F. Neubrech, C. Huck, K. Weber, A. Pucci, and H. Giessen, Chemical Reviews 117:5110 (**2017**).
[207] Y. Nishikawa, T. Nagasawa, K. Fujiwara, and M. Osawa, Vibrational Spectroscopy 6:43 (**1993**).
[208] P. Alonso-González, P. Albella, F. Neubrech, C. Huck, J. Chen, F. Golmar, F. Casanova, L. E. Hueso, A. Pucci, and J. Aizpurua, Physical review letters 110:203902 (**2013**).
[209] P. Dumas, R. Tobin, and P. Richards, Surface science 171:555 (**1986**).
[210] S. Pons, Journal of Electroanalytical Chemistry and Interfacial Electrochemistry 150:495 (**1983**).
[211] S. Pons, T. Davidson, and A. Bewick, Journal of the American Chemical Society 105:1802 (**1983**).
[212] b. C. Smith, fundamentals of fourier transform infrared spectroscopy, CRC Press, Boca Raton, **2011**.
[213] P. R. Griffiths and J. A. De Haseth, Fourier transform infrared spectrometry, John Wiley & Sons, **2007**.
[214] A. A. Michelson, London, Edinburgh, and Dublin Philosophical Magazine and Journal of Science 31:256 (**1891**).
[215] P. H. Reinsberg and H. Baltruschat, Electrochimica Acta 334:135609 (**2020**).
[216] C. Bondue, P. Reinsberg, A. A. Abd-El-Latif, and H. Baltruschat, Physical Chemistry Chemical Physics 17: 25593 (**2015**).

[217] N. M. Marković, R. R. Adžić, and V. B. Vešović, Journal of electroanalytical chemistry and interfacial electrochemistry 165:121 (**1984**).
[218] N. M. Marković, I. M. Tidswell, and P. N. Ross, Langmuir 10:1 (**1994**).
[219] C. N. Vanhuong, Journal of Electroanalytical Chemistry 194:131 (**1985**).
[220] D. Aurbach, M. Daroux, P. Faguy, and E. Yeager, Journal of Electroanalytical Chemistry and Interfacial Electrochemistry 297:225 (**1991**).
[221] A. Bard and L. Faulkner, Electrochemical Methods: Fundamentals and Applications, John Wiley & Sons, New York, **1980**.
[222] H. Schirmer and H. Baumgartel, Journal of Electroanalytical Chemistry 316:235 (**1991**).
[223] A. Hamelin, T. Vitanov, E. Sevastyanov, and A. Popov, Journal of Electroanalytical Chemistry 145:225 (**1983**).
[224] J. Clavilier, D. Armand, S. G. Sun, and M. Petit, Journal of Electroanalytical Chemistry 205:267 (**1986**).
[225] G. Valette and A. Hamelin, Journal of Electroanalytical Chemistry 45:301 (**1973**).
[226] A. Hamelin and J.-P. Bellier, Surface Science 78:159 (**1978**).
[227] A. Hamelin, M. L. Foresti, and R. Guidelli, Journal of Electroanalytical Chemistry 346:251 (**1993**).
[228] G. Beltramo and E. Santos, Journal of Electroanalytical Chemistry 556:127 (**2003**).
[229] J. Lipkowski, Z. C. Shi, A. C. Chen, B. Pettinger, and C. Bilger, Electrochimica Acta 43:2875 (**1998**).
[230] A. C. Chen, Z. C. Shi, D. Bizzotto, J. Lipkowski, B. Pettinger, and C. Bilger, Journal of Electroanalytical Chemistry 467:342 (**1999**).
[231] G. N. Salaita, D. A. Stern, F. Lu, H. Baltruschat, B. C. Schardt, J. L. Stickney, M. P. Soriaga, D. G. Frank, and A. T. Hubbard, Langmuir 2:828 (**1986**).
[232] H. Baltruschat, M. Martinez, S. K. Lewis, F. Lu, D. Song, D. A. Stern, A. Datta, and A. T. Hubbard, Journal of Electroanalytical Chemistry 217:111 (**1987**).
[233] F. Lu, G. N. Salaita, H. Baltruschat, and A. T. Hubbard, Journal of Electroanalytical Chemistry 222:305 (**1987**).
[234] R. J. Nichols, O. M. Magnussen, J. Hotlos, T. Twomey, R. J. Behm, and D. M. Kolb, Journal of Electroanalytical Chemistry 290:21 (**1990**).
[235] S. L. Yau, C. M. Vitus, and B. C. Schardt, Journal of the American Chemical Society 112:3677 (**1990**).
[236] R. Vogel, I. Kamphausen, and H. Baltruschat, Berichte der Bunsengesellschaft für Physikalische Chemie 96:525 (**1992**).
[237] B. M. Ocko, O. M. Magnussen, J. X. Wang, R. R. Adzic, and T. Wandlowski, Physica B-Condensed Matter 221:238 (**1996**).
[238] B. M. Ocko, J. Wang, and G. M. Watson, Journal of Physical Chemistry 98:897 (**1994**).
[239] R. Oelgeklaus, J. Rose, and H. Baltruschat, Journal of Electroanalytical Chemistry 376:127 (**1994**).
[240] S. Morin, H. Dumont, and B. E. Conway, Journal of Electroanalytical Chemistry 412:39 (**1996**).
[241] B. E. Conway, J. Barber, and S. Morin, Electrochimica Acta 44:1109 (**1998**).
[242] T. Langkau and H. Baltruschat, Electrochimica Acta 44:909 (**1998**).

[243] E. Sibert, R. Faure, and R. Durand, Journal of Electroanalytical Chemistry 515:71 (**2001**).
[244] V. Climent, B. A. Coles, and R. G. Compton, Journal of Physical Chemistry B 106:5988 (**2002**).
[245] T. Pajkossy and D. M. Kolb, Electrochemistry Communications 5:283 (**2003**).
[246] L. Siinor, K. Lust, and E. Lust, Journal of Electroanalytical Chemistry 601:39 (**2007**).
[247] D. Eberhardt, E. Santos, and W. Schmickler, Journal of Electroanalytical Chemistry 419:23 (**1996**).
[248] Z. Kerner and T. Pajkossy, Electrochimica Acta 47:2055 (**2002**).
[249] C. N. Vanhuong, Journal of Electroanalytical Chemistry 207:235 (**1986**).
[250] L. Falciola, P. R. Mussini, S. Trasatti, and L. M. Doubova, Journal of Electroanalytical Chemistry 593:185 (**2006**).
[251] P. Sebastian, V. Climent, and J. M. Feliu, Electrochemistry Communications 62:44 (**2016**).
[252] J. J. Segura, A. Elbourne, E. J. Wanless, G. G. Warr, K. Voitchovsky, and R. Atkin, Physical Chemistry Chemical Physics 15:3320 (**2013**).
[253] H. Li, F. Endres, and R. Atkin, Physical Chemistry Chemical Physics 15:14624 (**2013**).
[254] B. Roling, M. Drueschler, and B. Huber, Faraday Discussions 154:303 (**2012**).
[255] T. Pajkossy, C. Muller, and T. Jacob, Physical Chemistry Chemical Physics 20:21241 (**2017**).
[256] C. Siimenson, L. Siinor, K. Lust, and E. Lust, Ecs Electrochemistry Letters 4:H62 (**2015**).
[257] O. Oll, C. Siimenson, K. Lust, G. Gorbatovski, and E. Lust, Electrochimica Acta 247:910 (**2018**).
[258] S. Strbac, A. Hamelin, and R. R. Adzic, Journal of Electroanalytical Chemistry 362:47 (**1993**).
[259] X. P. Gao and M. J. Weaver, Journal of the American Chemical Society 114:8544 (**1992**).
[260] T. Yamada, N. Batina, and K. Itaya, Surface Science 335:204 (**1995**).
[261] K. Itaya, N. Batina, and T. Yamada, Journal of Physical Chemistry 99:8817 (**1995**).
[262] N. Nanbu, Y. Sasaki, and F. Kitamura, Electrochemistry Communications 5:383 (**2003**).
[263] M. Gnahm, T. Pajkossy, and D. M. Kolb, Electrochimica Acta 55:6212 (**2010**).
[264] M. R. Deakin, T. T. Li, and O. R. Melroy, Journal of Electroanalytical Chemistry and Interfacial Electrochemistry 243:343 (**1988**).
[265] N. Garcia-Araez, V. Climent, P. Rodriguez, and J. M. Feliu, Electrochimica Acta 53:6793 (**2008**).
[266] M. T. M. Koper and W. Schmickler, Chemical Physics 211:123 (**1996**).
[267] C. Hartnig and M. T. M. Koper, Journal of the American Chemical Society 125:9840 (**2003**).
[268] J. F. Reardon, Electrochimica Acta 32:1595 (**1987**).
[269] P. Reinsberg, A. A. Abd-El-Latif, and H. Baltruschat, Electrochimica Acta 273:424 (**2018**).
[270] P. Reinsberg, A. Weiss, P. P. Bawol, and H. Baltruschat, Journal of Physical Chemistry C 121:7677 (**2017**).

[271] B. Genorio, J. Staszak-Jirkovsky, R. S. Assary, J. G. Connell, D. Strmcnik, C. E. Diesendruck, P. P. Lopes, V. R. Stamenkovic, J. S. Moore, L. A. Curtiss, and N. M. Markovic, Journal of Physical Chemistry C 120:15909 (**2016**).
[272] T. A. Galloway, J. C. Dong, J. F. Li, G. Attard, and L. J. Hardwick, Chemical Science 10:2956 (**2019**).
[273] C. O. Laoire, S. Mukerjee, K. M. Abraham, E. J. Plichta, and M. A. Hendrickson, Journal of Physical Chemistry C 114:9178 (**2010**).
[274] C. J. Bondue, P. P. Bawol, A. A. Abd-El-Latif, P. Reinsberg, and H. Baltruschat, The Journal of Physical Chemistry C 121:8864 (**2017**).
[275] P. Verma, P. Maire, and P. Novak, Electrochimica Acta 55:6332 (**2010**).
[276] C. J. Bondue, P. Reinsberg, and H. Baltruschat, Electrochimica Acta 245:1035 (**2017**).
[277] Q. Yu and S. Ye, Journal of Physical Chemistry C 119:12236 (**2015**).
[278] C. J. Bondue, M. Hegemann, C. Molls, E. Thome, and H. Baltruschat, Journal of the Electrochemical Society 163:A1765 (**2016**).
[279] M. A. Schroeder, N. Kumar, A. J. Pearse, C. Liu, S. B. Lee, G. W. Rubloff, K. Leung, and M. Noked, ACS applied materials & interfaces 7:11402 (**2015**).
[280] P. Hegemann, M. Hegemann, L. Zan, and H. Baltruschat, Journal of Electrochemical Society 166:A245 (**2019**).
[281] S. Y. Ha, Y. W. Lee, S. W. Woo, B. Koo, J. S. Kim, J. Cho, K. T. Lee, and N. S. Choi, Acs Applied Materials & Interfaces 6:4063 (**2014**).
[282] D. Aurbach, A. Schechter, M. Moshkovich, and Y. Cohen, Journal of Electrochemical Society 148:A1004 (**2001**).
[283] T. Fukutsuka, K. Asaka, A. Inoo, R. Yasui, K. Miyazaki, T. Abe, K. Nishio, and Y. Uchimoto, Chemistry Letters 43:1788 (**2014**).
[284] N. Garcia-Araez, V. Climent, E. Herrero, J. Feliu, and J. Lipkowski, Journal of Electroanalytical Chemistry 576:33 (**2005**).
[285] N. Garcia-Araez, V. Climent, E. Herrero, J. Feliu, and J. Lipkowski, Journal of Electroanalytical Chemistry 591:149 (**2006**).
[286] J. Lipkowski and Z. Shi, Journal of Electroanalytical Chemistry 369:283 (**1994**).
[287] J. Albers, H. Baltruschat, and I. Kamphausen, Journal of Electroanalytical Chemistry 395:99 (**1995**).
[288] H. Baltruschat, U. Bringemeier, and R. Vogel, Faraday Discussions 94:317 (**1992**).
[289] A. M. Bittner, J. Wintterlin, B. Beran, and G. Ertl, Surface Science 335:291 (**1995**).
[290] C. A. Lucas, N. M. Markovic, and P. N. Ross, Surface Science 340:L949 (**1995**).
[291] A. Cuesta and D. M. Kolb, Surface Science 465:310 (**2000**).
[292] M. H. Holzle, U. Retter, and D. M. Kolb, Journal of Electroanalytical Chemistry 371:101 (**1994**).
[293] M. H. Hölzle, V. Zwing, and D. M. Kolb, Electrochimica Acta 40:1237 (**1995**).
[294] P. Berenz, S. Tillmann, H. Massong, and H. Baltruschat, Electrochimica Acta 43:3035 (**1998**).
[295] E. A. Abd El Meguid, P. Berenz, and H. Baltruschat, Journal of Electroanalytical Chemistry 467:50 (**1999**).
[296] T. Pajkossy, T. Wandlowski, and D. M. Kolb, Journal of Electroanalytical Chemistry 414:209 (**1996**).

[297] L. M. Dubova, Bagotskaya I. A., Sov. Electrochem 13:49 (**1977**).
[298] W. R. Fawcett and M. D. Mackey, Journal of the Chemical Society, Faraday Transactions 1: Physical Chemistry in Condensed Phases 69:634 (**1973**).
[299] W. R. Fawcett and A. J. Motheo, Electrochimica Acta 36:1971 (**1991**).
[300] M. D. Levi, A. V. Shlepakov, B. B. Damaskin, and I. A. Bagotskaya, Journal of Electroanalytical Chemistry and Interfacial Electrochemistry 138:1 (**1982**).
[301] V. V. Emets and B. B. Damaskin, Journal of Electroanalytical Chemistry 600:191 (**2007**).
[302] V. V. Emets and B. B. Damaskin, Russian Journal of Electrochemistry 47:121 (**2011**).
[303] V. V. Emets and B. B. Damaskin, Russian Journal of Electrochemistry 48:26 (**2012**).
[304] V. V. Emets and B. B. Damaskin, Russian Journal of Electrochemistry 50:201 (**2014**).
[305] A. V. Shlepakov, Bagotskaya I. A., Sov. Electrochem 18:23 (**1982**).
[306] V. V. Emets and A. A. Mel'nikov, Journal of Electroanalytical Chemistry 842:8 (**2019**).
[307] J. D. Roth and M. J. Weaver, Langmuir 8:1451 (**1992**).
[308] C. N. Van Huong, Journal of Electroanalytical Chemistry and Interfacial Electrochemistry 207:235 (**1986**).
[309] M. Väärtnou and E. Lust, Journal of Electroanalytical Chemistry 733:20 (**2014**).
[310] M. Väärtnôu and E. Lust, Journal of Electroanalytical Chemistry 445:165 (**1998**).
[311] M. Vaartnou and E. Lust, Journal of Electroanalytical Chemistry 578:273 (**2005**).
[312] O. Oll, M. Väärtnou, G. Gorbatovski, J. Zhao, C. Siimenson, L. Siinor, K. Lust, T. Romann, P. Pikma, and E. Lust, Electrochimica Acta 319:895 (**2019**).
[313] H. Ueda, K. Nishiyama, and S. Yoshimoto, Electrochemistry 86:217 (**2018**).
[314] A. S. Shatla, A. A. Abd-El-Latif, S. Ayata, D. Demir, and H. Baltruschat, Electrochimica Acta 334:135556 (**2020**).
[315] A. S. Shatla and H. Baltruschat, in preparation.
[316] Z. Shi, S. Wu, and J. Lipkowski, Electrochimica Acta 40:9 (**1995**).
[317] B. M. Jovic, V. D. Jovic, and D. M. Drazic, Journal of Electroanalytical Chemistry 399:197 (**1995**).
[318] N. J. Tao and S. M. Lindsay, Journal of Physical Chemistry 96:5213 (**1992**).
[319] J. Friedl, I. I. E. Markovits, M. Herpich, G. Feng, A. A. Kornyshev, and U. Stimming, ChemElectroChem 4:216 (**2017**).
[320] M. P. Soriaga, G. M. Berry, M. E. Bothwell, B. G. Bravo, G. J. Cali, J. E. Harris, T. Mebrahtu, S. L. Michelhaugh, and J. F. Rodriguez, Langmuir 5:707 (**1989**).
[321] M. P. Soriaga, B. G. Bravo, S. L. Michaelhaugh, J. L. Stickney, I. Villegas, and D. W. Suggs, Journal of Physical Chemistry 95:5245 (**1991**).
[322] C. A. Lucas, N. M. Markovic, and P. N. Ross, Physical Review B-Condensed Matter 55:7964 (**1997**).
[323] H. Ogasawara, Y. Sawatari, J. Inukai, and M. Ito, Journal of Electroanalytical Chemistry 358:337 (**1993**).
[324] G. J. Edens, X. Gao, and M. J. Weaver, Journal of Electroanalytical Chemistry and Interfacial Electrochemistry 375:357 (**1994**).
[325] S. Thomas, Y.-E. Sung, H. S. Kim, and A. Wieckowski, Journal of Physical Chemistry 100:11726 (**1996**).

[326] V. Gutman, donor-acceptor approach to molecular interactions Plenum Press, New York, **1978**.
[327] W. R. Fawcett and C. A. Foss, Journal of Electroanalytical Chemistry and Interfacial Electrochemistry 270:103 (**1989**).
[328] C. Reichardt, Chemical Reviews 94:2319 (**1994**).
[329] W. Schmickler, Chemical Physics Letters 237:152 (**1995**).
[330] V. Gutman, Chemistry of Coordination Compounds in Nonaqueous Solutions, Springer-Verlag, Wien. New York, **1968**.
[331] A. Frumkin, N. Polianovskaya, N. Grigoryev, and I. Bagotskaya, Electrochimica Acta 10:793 (**1965**).
[332] I. A. Bagotskaya, Chan Ngok Hay, Boitsov V. G., Kazarinov V. E. , Elektrokhimiya 24:265 (**1988**).
[333] S. Trasatti, Electrochimica Acta 32:843 (**1987**).
[334] V. V. Emets and B. B. Damaskin, Russian Journal of Electrochemistry 45:45 (**2009**).
[335] V. V. Emets and B. B. Damaskin, Journal of Electroanalytical Chemistry 491:30 (**2000**).
[336] W. Linert, R. F. Jameson, G. Bauer, and A. Taha, Journal of Coordination Chemistry 42:211 (**1997**).
[337] P. H. Reinsberg, A. Koellisch, and H. Baltruschat, Electrochimica Acta 313:223 (**2019**).
[338] G. Gritzner, Journal of Physical Chemistry 90:5478 (**1986**).
[339] C. F. Riadigos, R. Iglesias, M. A. Rivas, and T. P. Iglesias, Journal of Chemical Thermodynamics 43:275 (**2011**).
[340] W. M. Haynes, D. R. Lide, and T. J. Bruno, CRC Handbook of chemistry and physics, CRC press, Boca raton , Florida, **2016**.
[341] Z. Borkowska and G. Jarzabek, Journal of Electroanalytical Chemistry 353:1 (**1993**).
[342] J. Applequist, J. R. Carl, and K.-K. Fung, Journal of the American Chemical Society 94:2952 (**1972**).
[343] R. Schmid, Journal of solution chemistry 12:135 (**1983**).
[344] G. Valette, Journal of Electroanalytical Chemistry 138:37 (**1982**).
[345] D. C. Grahame, Chemical Reviews 41:441 (**1947**).
[346] Y. Hou, K. J. Aoki, J. Chen, and T. Nishiumi, Journal of Physical Chemistry C 118:10153 (**2014**).
[347] M. M. Waegele, C. M. Gunathunge, J. Li, and X. Li, Journal of Chemical Physics 151:160902 (**2019**).
[348] M. Arulepp, L. Permann, J. Leis, A. Perkson, K. Rumma, A. JÃ¤nes, and E. Lust, Journal of Power Sources 133:320 (**2004**).
[349] E. Lust, A. Janes, and M. Arulepp, Journal of Electroanalytical Chemistry 562:33 (**2004**).
[350] S. Trasatti, Journal of Electroanalytical Chemistry and Interfacial Electrochemistry 33:351 (**1971**).
[351] G. Valette, Journal of Electroanalytical Chemistry 139:285 (**1982**).
[352] S. Trasatti and E. Lust, in Modern Aspects of Electrochemistry, Vol. 33 (B. E. Conway, R. E. White, and J. O. M. Bockris, eds.), Plenum Press, New York, **1999**.
[353] R. Parsons, Croat. Chem. Acta 53:133 (**1980**).

[354] S. Trasatti, Journal of Electroanalytical Chemistry and Interfacial Electrochemistry 150:1 (**1983**).
[355] S. Trasatti, Materials Chemistry and Physics 12:507 (**1985**).
[356] A. Hamelin, Z. Borkowska, and J. Stafiej, Journal of Electroanalytical Chemistry and Interfacial Electrochemistry 189:85 (**1985**).
[357] G. Valette, Journal of Electroanalytical Chemistry 269:191 (**1989**).
[358] G. Valette, Journal of Electroanalytical Chemistry 260:425 (**1989**).
[359] G. Valette, Journal of Electroanalytical Chemistry 224:285 (**1987**).
[360] G. Valette and R. Parsons, Journal of Electroanalytical Chemistry 204:291 (**1986**).
[361] G. Valette and R. Parsons, Journal of Electroanalytical Chemistry 191:377 (**1985**).
[362] G. Valette, A. Hamelin, and R. Parsons, Z. Phys. Chem. 113:71 (**1978**).
[363] Z. Borkowska and A. Hamelin, Journal of Electroanalytical Chemistry and Interfacial Electrochemistry 241:373 (**1988**).
[364] G. Jarzabek and Z. Borkowska, Journal of Electroanalytical Chemistry and Interfacial Electrochemistry 226:295 (**1987**).
[365] E. Lust, in Encyclopedia of Electrochemistry (A. J. Bard and M. Stratman, eds.), Wiley, Weinheim, **2002**, p. pp 188.
[366] O. A. Petrii and I. G. Khomchenko, Journal of Electroanalytical Chemistry and Interfacial Electrochemistry 106:277 (**1980**).
[367] T. Biegler and R. Parsons, Journal of Electroanalytical Chemistry and Interfacial Electrochemistry 22:A4 (**1969**).
[368] Z. Borkowska and J. Stafiej, Journal of Electroanalytical Chemistry and Interfacial Electrochemistry 226:283 (**1987**).
[369] Z. Borkowska, Journal of Electroanalytical Chemistry and Interfacial Electrochemistry 244:1 (**1988**).
[370] R. Payne, Journal of the American Chemical Society 89:489 (**1967**).
[371] G. J. Hills and R. M. Reeves, Journal of Electroanalytical Chemistry and Interfacial Electrochemistry 38:1 (**1972**).
[372] G. J. Hills and R. M. Reeves, Journal of Electroanalytical Chemistry and Interfacial Electrochemistry 41:213 (**1973**).
[373] J. Taraszewska, Journal of Electroanalytical Chemistry and Interfacial Electrochemistry 121:215 (**1981**).
[374] V. V. Emets and B. B. Damaskin, Russian Journal of Electrochemistry 51:789 (**2015**).
[375] A. N. Frumkin, N. B. Grigoryev, and I. A. Bagotskaya, Dokl. Akad. Nauk SSSR 157:957 (**1964**).
[376] I. A. Bagotskaya, V. V. Emets, V. G. Boytsov, and V. E. Kazarinov, Electrokhimiya 24:1145 (**1988**).
[377] V. V. Emets and A. A. Mel'nikov, Russian Journal of Electrochemistry 54:1012 (**2018**).
[378] S. Amokrane, Z. Borkowska, and G. Jarzabek, Journal of Electroanalytical Chemistry 377:9 (**1994**).
[379] A. Shen and J. E. Pemberton, Journal of Electroanalytical Chemistry 479:21 (**1999**).
[380] E. Lust, in Encyclopedia of Interfacial Chemistry (K. Wandelt, ed.), Elsevier, Oxford, 2018, p. **316**.

[381] Y. Liu, Y.-X. Yuan, X.-R. Wang, N. Zhang, M.-M. Xu, J.-L. Yao, and R.-A. Gu, Journal of Electroanalytical Chemistry 728:10 (**2014**).
[382] M. T. Alam, M. M. Islam, T. Okajima, and T. Ohsaka, Journal of Physical Chemistry C 112:16600 (**2008**).
[383] M. T. Alam, M. Mominul Islam, T. Okajima, and T. Ohsaka, Electrochemistry Communications 9:2370 (**2007**).
[384] I. Noviandri, K. N. Brown, D. S. Fleming, P. T. Gulyas, P. A. Lay, A. F. Masters, and L. Phillips, The Journal of Physical Chemistry B 103:6713 (**1999**).
[385] E. Mostafa and H. Baltruschat, Journal of Solid State Electrochemistry 17:1861 (**2013**).
[386] V. D. Jovic and B. M. Jovic, Journal of Electroanalytical Chemistry 541:1 (**2003**).
[387] E. Panzram, H. Baumgärtel, B. Roelfs, C. Schröter, and T. Solomun, Berichte der Bunsengesellschaft für Physikalische Chemie 99:827 (**1995**).
[388] P. N. Ross and A. T. D'Agostino, Electrochimica Acta 37:615 (**1992**).
[389] V. V. Pavlishchuk and A. W. Addison, Inorganica Chimica Acta 298:97 (**2000**).
[390] V. J. Cunnane, G. Geblewicz, and D. J. Schiffrin, Electrochimica Acta 40:3005 (**1995**).
[391] S. Amokrane and J. P. Badiali, Journal of Electroanalytical Chemistry 266:21 (**1989**).
[392] S. Amokrane and J. P. Badiali, Journal of Electroanalytical Chemistry 297:377 (**1991**).
[393] S. Amokrane, Journal of Electroanalytical Chemistry 361:1 (**1993**).
[394] M. Morita, M. Goto, and Y. Matsuda, Journal of Applied Electrochemistry 22:901 (**1992**).
[395] E. R. Nightingale, Journal of Physical Chemistry 63:1381 (**1959**).
[396] D. C. Grahame, Journal of Electrochemical Society 98:343 (**1951**).
[397] A. Hamelin and L. Stoicoviciu, Journal of Electroanalytical Chemistry and Interfacial Electrochemistry 234:93 (**1987**).
[398] M. Landstorfer, C. Guhlke, and W. Dreyer, Electrochimica Acta 201:187 (**2016**).
[399] G. Valette, Journal of Electroanalytical Chemistry 122:285 (**1981**).
[400] H. Gerischer and C. W. Tobias, in Advances in Electrochemistry and Electrochemical Engineering, Vol. 10 (H. Gerischer and C.W.Tobias, eds.), Wiley, New York, **1977**, p. 213.
[401] A. F. Silva, Trends in interfacial electrochemisty, D. Reidel, Dordrecht, **1986**.
[402] G. Valette, Journal of Electroanalytical Chemistry 255:215 (**1988**).
[403] I. Hill, D. Irish, and G. Atkinson, Langmuir 2:752 (**1986**).
[404] C. T. Hsieh, W. Y. Chen, D. Y. Tzou, A. K. Roy, and H. T. Hsiao, International Journal of Hydrogen Energy 37:17837 (**2012**).
[405] B. Habibi and N. Delnavaz, International Journal of Hydrogen Energy 35:8831 (**2010**).
[406] Z. H. Wang and K. Y. Qu, Electrochemistry Communications 8:1075 (**2006**).
[407] M. D. Obradovic, A. V. Tripkovic, and S. L. Gojkovic, Electrochimica Acta 55:204 (**2009**).
[408] D. Zhao, Y. H. Wang, and B. Q. Xu, Journal of Physical Chemistry C 113:20903 (**2009**).
[409] N. Kristian, Y. L. Yu, P. Gunawan, R. Xu, W. Q. Deng, X. W. Liu, and X. Wang, Electrochimica Acta 54:4916 (**2009**).
[410] J. S. Huang, H. Q. Hou, and T. Y. You, Electrochemistry Communications 11:1281 (**2009**).
[411] M. Baldauf and D. M. Kolb, Journal of Physical Chemistry 100:11375 (**1996**).

[412] A. N. Golikand, E. Lohrasbi, M. G. Maragheh, and M. Asgari, Journal of Applied Electrochemistry 39:2421 (**2009**).
[413] V. Selvaraj, A. N. Grace, and M. Alagar, Journal of Colloid and Interface Science 333:254 (**2009**).
[414] B. Lim, M. J. Jiang, T. Yu, P. H. C. Camargo, and Y. N. Xia, Nano Research 3:69 (**2010**).
[415] G. Q. Chen, M. Y. Liao, B. Q. Yu, Y. H. Li, D. Wang, G. R. You, C. J. Zhong, and B. H. Chen, International Journal of Hydrogen Energy 37:9959 (**2012**).
[416] R. R. Yue, C. Q. Wang, F. X. Jiang, H. W. Wang, Y. K. Du, J. K. Xu, and P. Yang, International Journal of Hydrogen Energy 38:12755 (**2013**).
[417] R. Ojani, E. Hasheminejad, and J. B. Raoof, International Journal of Hydrogen Energy 39:8194 (**2014**).
[418] F. Z. Si, J. J. Ge, C. Y. Li, L. Liang, C. P. Liu, and W. Xing, International Journal of Hydrogen Energy 39:2489 (**2014**).
[419] H. A. Gasteiger, N. Markovic, P. N. Ross, and E. J. Cairns, Electrochimica Acta 39:1825 (**1994**).
[420] J. H. Choi, K. J. Jeong, Y. Dong, J. Han, T. H. Lim, J. S. Lee, and Y. E. Sung, Journal of Power Sources 163:71 (**2006**).
[421] S. Kang, J. Lee, J. K. Lee, S. Y. Chung, and Y. Tak, Journal of Physical Chemistry B 110:7270 (**2006**).
[422] A. V. Tripkovic, K. D. Popovic, R. M. Stevanovic, R. Socha, and A. Kowal, Electrochemistry Communications 8:1492 (**2006**).
[423] A. C. Chen and P. Holt-Hindle, Chemical Reviews 110:3767 (**2010**).
[424] B. D. Bath, H. S. White, and E. R. Scott, Analytical Chemistry 72:433 (**2000**).
[425] E. Antolini, Energy & Environmental Science 2:915 (**2009**).
[426] D. D. Sun, L. Si, G. T. Fu, C. Liu, D. M. Sun, Y. Chen, Y. W. Tang, and T. H. Lu, Journal of Power Sources 280:141 (**2015**).
[427] S. Zhang, Y. Y. Shao, G. P. Yin, and Y. H. Lin, Angewandte Chemie-International Edition 49:2211 (**2010**).
[428] R. Y. Wang, J. G. Liu, P. Liu, X. X. Bi, X. L. Yan, W. X. Wang, X. B. Ge, M. W. Chen, and Y. Ding, Chemical Science 5:403 (**2014**).
[429] K. M. Hassan, G. M. Elhaddad, and M. A. Azzem, Journal of Electroanalytical Chemistry 728:123 (**2014**).
[430] K. M. Hassan and M. A. Azzem, Journal of Applied Electrochemistry 45:567 (**2015**).
[431] M. Gholamian and A. Q. Contractor, Journal of Electroanalytical Chemistry 289:69 (**1990**).
[432] Z. Z. Zhu, Z. Wang, and H. L. Li, Applied Surface Science 254:2934 (**2008**).
[433] F. X. Jiang, R. Zhou, Z. Q. Yao, Y. K. Du, J. K. Xu, P. Yang, and C. Y. Wang, International Journal of Electrochemical Science 6:4114 (**2014**).
[434] R. H. Tammam and M. M. Saleh, Journal of Power Sources 246:178 (**2014**).
[435] F. Ren, R. Zhou, F. Jiang, W. Zhou, Y. Du, J. Xu, and C. Wang, Fuel Cells 12:116 (**2012**).
[436] R. Schrebler, M. A. Delvalle, H. Gomez, C. Veas, and R. Cordova, Journal of Electroanalytical Chemistry 380:219 (**1995**).

[437] V. Selvaraj, M. Alagar, and I. Hamerton, Applied Catalysis B-Environmental 73:172 (**2007**).
[438] I. Becerik and F. Kadirgan, Turkish Journal of Chemistry 25:373 (**2001**).
[439] V. Selvaraj, M. Alagar, and K. S. Kumar, Applied Catalysis B-Environmental 75:129 (**2007**).
[440] W. Q. Zhou, Y. K. Du, H. M. Zhang, J. K. Xu, and P. Yang, Electrochimica Acta 55:2911 (**2010**).
[441] B. Habibi and M. H. Pournaghi-Azar, International Journal of Hydrogen Energy 35:9318 (**2010**).
[442] F. X. Jiang, Z. Q. Yao, R. R. Yue, Y. K. Du, J. K. Xu, P. Yang, and C. Y. Wang, International Journal of Hydrogen Energy 37:14085 (**2012**).
[443] Y. Suo and I. M. Hsing, Electrochimica Acta 56:2174 (**2011**).
[444] B.-J. Kim, K. Kwon, C. K. Rhee, J. Han, and T.-H. Lim, Electrochimica Acta 53:7744 (**2008**).
[445] S. Yang, X. Zhang, H. Mi, and X. Ye, Journal of Power Sources 175:26 (**2008**).
[446] H. Xu, B. Yan, S. M. Li, J. Wang, C. Q. Wang, J. Guo, and Y. K. Du, Chemical Engineering Journal 334:2638 (**2018**).
[447] M. T. Liu, L. X. Chen, D. N. Li, A. J. Wang, Q. L. Zhang, and J. J. Feng, Journal of Colloid and Interface Science 508:551 (**2017**).
[448] Y. R. Ma, T. F. Li, H. Chen, X. J. Chen, S. H. Deng, L. Xu, D. M. Sun, and Y. W. Tang, Journal of Energy Chemistry 26:1238 (**2017**).
[449] D. N. Li, A. J. Wang, J. Wei, Q. L. Zhang, and J. J. Feng, International Journal of Hydrogen Energy 42:19894 **(**2017).
[450] H. Kita and H. W. Lei, Journal of Electroanalytical Chemistry 388:167 (**1995**).
[451] E. Casado-Rivera, Z. Gál, A. C. D. Angelo, C. Lind, F. J. DiSalvo, and H. D. Abruña, ChemPhysChem 4:193 (**2003**).
[452] S. Fierroa, L. Ouattara, E. H. Calderon, E. Passas-Lagos, H. Baltruschat, and C. Comninellis, Electrochimica Acta 54:2053 (**2009**).
[453] A. Kapałka, B. Lanova, H. Baltruschat, G. Fóti, and C. Comninellis, Journal of The Electrochemical Society 156:E149 (**2009**).
[454] A. A. Abd-El-Latif, C. J. Bondue, S. Ernst, M. Hegemann, J. K. Kaul, M. Khodayari, E. Mostafa, A. Stefanova, and H. Baltruschat, Trac-Trends in Analytical Chemistry 70:4 (**2015**).
[455] F. J. E. Scheijen, G. L. Beltramo, S. Hoeppener, T. H. M. Housmans, and M. T. M. Koper, Journal of Solid State Electrochemistry 12:483 (**2008**).
[456] U. Abaci, H. Y. Guney, and U. Kadiroglu, Electrochimica Acta 96:214 (**2013**).
[457] K. Jackowska, J. Bukowska, and M. Jamkowski, Journal of Electroanalytical Chemistry 388:101 (**1995**).
[458] B. Habibi and S. Mohammadyari, International Journal of Hydrogen Energy 40:10833 (**2015**).
[459] A. E. Fetohi, R. S. Amin, R. M. A. Hameed, and K. M. El-Khatib, Electrochimica Acta 242:187 (**2017**).
[460] R. M. Abdel Hameed, Journal of Colloid and Interface Science 505:230 (**2017**).
[461] R. F. Wang, S. J. Liao, and S. Ji, Journal of Power Sources 180:205 (**2008**).

[462] F. Koleli, A. Beytaroglu, D. Ropke, T. Ropke, and R. Aydin, International Journal of Chemical Reactor Engineering 9:16 (**2011**).
[463] W. Gao, J. A. Keith, J. Anton, and T. Jacob, Journal of the American Chemical Society 132:18377 (**2010**).
[464] V.-T. Nguyen, Q. C. Tran, N. D. Quang, N.-A. Nguyen, V.-T. Bui, V.-D. Dao, and H.-S. Choi, Journal of Alloys and Compounds 766:979 (**2018**).
[465] C. Jiang, H. Chen, C. Yu, S. Zhang, B. Liu, and J. Kong, Electrochimica Acta 54:1134 (**2009**).
[466] C. Venkateswara Rao, C. R. Cabrera, and Y. Ishikawa, Journal of Physical Chemistry C 115:21963 (**2011**).
[467] M. Osawa, K.-i. Komatsu, G. Samjeské, T. Uchida, T. Ikeshoji, A. Cuesta, and C. Gutiérrez, Angewandte Chemie International Edition 50:1159 (**2011**).
[468] G. A. El-Nagar, A. M. Mohammad, M. S. El-Deab, and B. E. El-Anadouli, Electrochimica Acta 94:62 (**2013**).
[469] C. A. Lucas, N. M. Markovic, and P. N. Ross, Surface Science 425:L381 (**1999**).
[470] M. K. Kumar, N. S. Jha, S. Mohan, and S. K. Jha, International Journal of Hydrogen Energy 39:12572 (**2014**).
[471] S. Zhang, Y. Y. Shao, G. P. Yin, and Y. H. Lin, Journal of Power Sources 195:1103 (**2010**).
[472] A. M. Baena-Moncada, G. M. Morales, C. Barbero, G. A. Planes, J. Florez-Montano, and E. Pastor, Catalysts 3 (**2013**).
[473] N. He, Y. Gong, Y. Yang, Y. Wang, C. Qin, R. Wang, J. Liu, and T. Qi, International Journal of Hydrogen Energy 43:3216 (**2018**).
[474] T. Szumelda, A. Drelinkiewicz, E. Lalik, R. Kosydar, D. Duraczynska, and J. Gurgul, Applied Catalysis B: Environmental 221:393 (**2018**).
[475] C. Zhu, D. Liu, Z. Chen, L. Li, and T. You, Journal of Colloid and Interface Science 511:77 (**2018**).
[476] M. G. Abd El-Moghny, H. H. Alalawy, A. M. Mohammad, A. A. Mazhar, M. S. El-Deab, and B. E. El-Anadouli, International Journal of Hydrogen Energy 42:11166 (**2017**).
[477] G.-C. C. Carvalho RC, Brett CM, Anal Bioanal Chem 398:1675 (**2010**).
[478] W. J. Albery, A. R. Greenwood, and R. F. Kibble, Transactions of the Faraday Society 63:360 (**1967**).
[479] D. G. Leaist and P. A. Lyons, Journal of Solution Chemistry 13:77 (**1984**).
[480] L. L. Van Loon, H. C. Allen, and B. E. Wyslouzil, The Journal of Physical Chemistry A 112:10758 (**2008**).
[481] R. K. Pandey, S. Patnaik, and V. Lakshminarayanan, Catalysis Letters 144:965 (**2014**).
[482] R. Jiang, D. T. Tran, J. P. McClure, and D. Chu, ACS Catalysis 4:2577 (**2014**).
[483] X.-G. Zhang, T. Arikawa, Y. Murakami, K. Yahikozawa, and Y. Takasu, Electrochimica Acta 40:1889 (**1995**).
[484] M. C. Halseid, Z. Jusys, and R. J. Behm, Journal of Electroanalytical Chemistry 644:103 (**2010**).
[485] A. Serov and C. Kwak, Applied Catalysis B-Environmental 97:1 (**2010**).

[486] T. R. Kumar, D. J. Yoo, A. R. Kim, and G. G. Kumar, New Journal of Chemistry 42:14386 (**2018**).
[487] H. Xu, C. F. Liu, P. P. Song, J. Wang, F. Gao, Y. P. Zhang, Y. Shiraishi, J. W. Di, and Y. K. Du, Chemistry-an Asian Journal 13:626 (**2018**).
[488] W. Hong, C. S. Shang, J. Wang, and E. K. Wang, Nanoscale 7:9985 (**2015**).
[489] Z. Liu, X. Y. Ling, X. Su, and J. Y. Lee, The Journal of Physical Chemistry B 108:8234 (**2004**).
[490] P. Sharma S, G. B, Journal of Power Sources 208:96 (**2012**).
[491] X. L. Chen, L. Zhang, J. J. Feng, W. P. Wang, P. X. Yuan, D. M. Han, and A. J. Wang, Journal of Colloid and Interface Science 530:394 (**2018**).
[492] V. Selvaraj and M. Alagar, Nanotechnology 19:045504 (**2008**).
[493] H. Wang, Z. Jusys, and R. J. Behm, Journal of Physical Chemistry B 108:19413 (**2004**).
[494] L. Zhao, S. Mitsushima, A. Ishihara, K. Matsuzawa, and K.-i. Ota, Chinese Journal of Catalysis 32:1856 (**2011**).
[495] H. Wang, Y. Zhao, Z. Jusys, and R. J. Behm, Journal of Power Sources 155:33 (**2006**).
[496] E. Mostafa, A. A. Abd-El-Latif, R. Ilsley, G. Attard, and H. Baltruschat, Physical Chemistry Chemical Physics 14:16115 (**2012**).
[497] U. Schmiemann, U. Müller, and H. Baltruschat, Electrochimica Acta 40:99 (**1995**).
[498] B. Lanova, H. Wang, and H. Baltruschat, Fuel Cells 6:214 (**2006**).
[499] A. A. Hathoot, K. M. Hassan, A. G. Ali, A. S. Shatla, H. Baltruschat, and M. Abdel-Azzem, RSC Advances 9:1849 (**2019**).
[500] K. M. Hassan, A. A. Hathoot, R. Maher, and M. Abdel Azzem, RSC Advances 8:15417 (**2018**).
[501] A. S. Shatla, K. M. Hassan, A. A. Abd-El-Latif, A. A. Hathoot, H. Baltruschat, and M. Abdel-Azzem, Journal of Electroanalytical Chemistry 833:231 (**2019**).
[502] H. Baltruschat, Journal of the American Society for Mass Spectrometry 15:1693 (**2004**).
[503] J. Willsau and J. Heitbaum, Electrochimica Acta 31:943 (**1986**).
[504] H. Wang, Z. Jusys, and R. J. Behm, Journal of Electroanalytical Chemistry 595:23 (**2006**).
[505] O. Wolter and J. Heitbaum, Berichte der Bunsengesellschaft für physikalische Chemie 88:6 (**1984**).
[506] Y. Li, W. Gao, L. Ci, C. Wang, and P. M. Ajayan, Carbon 48:1124 (**2010**).
[507] H. Gao, S. Liao, J. Zeng, and Y. Xie, Journal of Power Sources 196:54 (**2011**).
[508] J. Masud, M. T. Alam, Z. Awaludin, M. S. El-Deab, T. Okajima, and T. Ohsaka, Journal of Power Sources 220:399 (**2012**).
[509] Y. Kim, H. Kim, and W. B. Kim, Electrochemistry Communications 46:36 (**2014**).
[510] V. Bambagioni, M. Bevilacqua, C. Bianchini, J. Filippi, A. Marchionni, F. Vizza, L. Q. Wang, and P. K. Shen, Fuel Cells 10:582 (**2010**).
[511] H. J. Kim, S. M. Choi, S. Green, G. A. Tompsett, S. H. Lee, G. W. Huber, and W. B. Kim, Applied Catalysis B: Environmental 101:366 (**2011**).
[512] M. A. Azzem, U. S. Yousef, D. Limosin, and G. Pierre, Synthetic Metals 63:79 (**1994**).
[513] R. Singh, A. K. Bajpai, and A. K. Shrivastava, SN Applied Sciences 1:815 (**2019**).
[514] V. E. Kazarinov, Y. B. Vassiliev, and V. N. Andreev, Journal of Electroanalytical Chemistry and Interfacial Electrochemistry 147:247 (**1983**).

Publications:

1. K. M. Hassan, A.S. Shatla, A.A. Abd-El-Latif, H. Baltruschat, M. Abdel-Azzem, **Comparative studies of ethylene glycol electrooxidation on different conducting polymers supported Pt and Pd nanoparticles-DEMS study**, 878 (**2020**) 114624.
2. A. S. Shatla , A. A. Abd-El-Latif , S. Ayata , D. Demir and H. Baltruschat, **Iodide adsorption at Au(111) electrode in non-aqueous electrolyte: AC-voltammetry and EIS studies**, Electrochimica Acta 334 (**2020**) 135556.
3. A. S. Shatla, K.M. Hassan, A.A. Abd-El-Latif, A.A. Hathoot, H. Baltruschat, M. Abdel-Azzem, **Poly 1,5 diaminonaphthalene supported Pt, Pd, Pt/Pd and Pd/Pt nanoparticles for direct formic acid oxidation**, J. Electroanalytical Chemistry 833 (**2019**) 231-241.
4. A. Hathoot, K. M. Hassan, A. G. Ali, A. S. Shatla, H. Baltruschat and M. Abdel-Azzem, **Mono and dual hetero-structured M@poly-1,2 diaminoanthraquinone (M = Pt, Pd and Pt–Pd) catalysts for the electrooxidation of small organic fuels in alkaline medium**, RSC Adv., 9 (**2019**) 1849.
5. A. Hathoot, U. S. Yousef, A. S. Shatla, and M. Abdel-Azzem, **Voltammetric simultaneous determination of glucose, ascorbic acid and dopamine on glassy carbon electrode modified byNiNPs@poly 1,5-diaminonaphthalene**, Electrochimica Acta 85 (**2012**) 531-537.
6. A. S. Shatla, P. P. Bawol, H. Baltruschat, **Adsorption of iodide and bromide on Au(111) electrode in aprotic solvents**, submitted to ChemElectroChem.
7. A. S. Shatla, H. Baltruschat, **The pzc of Au(111) in aprotic solvents**, in preparation.

Conference contributions:

- **Poster**

1. A. S. Shatla , A. A. Abd-El-Latif , S. Ayata , D. Coban and H. Baltruschat, 68th Annual Meeting of the International Society of Electrochemistry, **27.08.2017 – 01.09.2017**, Providence, RI, USA.
2. A. S. Shatla, P. H. Reinsberg, A. A. Abd-El-Latif and H. Baltruschat, Electrochemistry 2018, **24.09.2018 – 26.09.2018**, Ulm, Germany.

3. A. S. Shatla, K.M. Hassan, A. A. Abd-El-Latif, A.A. Hathoot, H. Baltruschat, M. Abdel Azzem, Electrochemistry 2018, **24.09.2018 – 26.09.2018**, Ulm, Germany.
4. A. S. Shatla, P. P. Bawol, H. Baltruschat, 71th Annual Meeting of the International Society of Electrochemistry, **30.08.2020 – 04.09.2020**, Belgrade, Serbia.

- **Talk**

1. A. S. Shatla , P. H. Reinsberg, A. A. Abd-El-Latif and H. Baltruschat, 69th Annual Meeting of the International Society of Electrochemistry, **02.09.2018 – 07.09.2018**, Bologna, Italy.
2. A. S. Shatla, P.H. Reinsberg, I. Park, H. Baltruschat, December (2019), AGEF Meeting, **December 2019** (Duisburg) Germany.
3. A. S. Shatla and H. Baltruschat, International Workshop on Impedance Spectroscopy (IWIS) **03.12. - 04.12.2020**, Chemnitz, Germany.